

**Titre:** Aggregation of Electric Vehicles and Thermostatically Controlled  
Title: Loads for Providing Ancillary Services to the Smart Grid

**Auteur:** Sina Kiani  
Author:

**Date:** 2023

**Type:** Mémoire ou thèse / Dissertation or Thesis

**Référence:** Kiani, S. (2023). Aggregation of Electric Vehicles and Thermostatically Controlled  
Citation: Loads for Providing Ancillary Services to the Smart Grid [Thèse de doctorat,  
Polytechnique Montréal]. PolyPublie. <https://publications.polymtl.ca/10824/>

 **Document en libre accès dans PolyPublie**  
Open Access document in PolyPublie

**URL de PolyPublie:** <https://publications.polymtl.ca/10824/>  
PolyPublie URL:

**Directeurs de  
recherche:** Keyhan Sheshyekani, & Hanane Dagdougui  
Advisors:

**Programme:** Génie électrique  
Program:

**POLYTECHNIQUE MONTRÉAL**

affiliée à l'Université de Montréal

**Aggregation of electric vehicles and thermostatically controlled loads for  
providing ancillary services to the smart grid**

**SINA KIANI**

Département de génie électrique

Thèse présentée en vue de l'obtention du diplôme de *Philosophiæ Doctor*  
Génie électrique

Février 2023

**POLYTECHNIQUE MONTRÉAL**

affiliée à l'Université de Montréal

Cette thèse intitulée :

**Aggregation of electric vehicles and thermostatically controlled loads for  
providing ancillary services to the smart grid**

présentée par **Sina KIANI**

en vue de l'obtention du diplôme de *Philosophiæ Doctor*  
a été dûment acceptée par le jury d'examen constitué de :

**Issmail EL HALLAOUI**, président

**Keyhan SHESHYEKANI**, membre et directeur de recherche

**Hanane DAGDOUGUI**, membre et codirectrice de recherche

**Antoine LESAGE-LANDRY**, membre

**Rachid CHERKAOUI**, membre externe

**DEDICATION**

*To my ever supportive parents,  
To my love, Pegah*



## ACKNOWLEDGEMENTS

First and foremost, I would like to express my sincere gratitude to my advisors, Professor Keyhan Sheshyekani and Professor Hanane Dagdougui for their unwavering support, guidance, motivation, and insightful comments throughout my Ph.D. journey. It has been an honor to pursue this journey with both of you.

My sincere thanks go to Solutions Serafin Inc., and Mitacs for trusting me and providing financial and technical support for this project. This Ph.D. project could not be accomplished without your support and trust.

I also would like to express my gratitude to the members of the examination jury, Professor Rachid Cherkaoui, Professor Antoine Lesage-Landry, and Professor Issmail El Hallaoui for reading my thesis and providing their valuable feedback and constructive criticism.

Finally, I thank a lot my wife, my family, friends, and colleagues who have been a constant source of motivation and inspiration for me.

## RÉSUMÉ

Ces dernières années, la tendance à la transition énergétique s'est accentuée, notamment dans les secteurs résidentiel et du transport. L'adoption généralisée des véhicules électriques (EVs) dans le secteur des transports et le volume élevé de charges thermostatiques contrôlées (TCLs) dans le secteur du bâtiment révèlent la capacité de ces secteurs à réduire les émissions de gaz à effet de serre et à améliorer l'efficacité énergétique. Cependant, la pénétration non gérée des EVs et des TCLs à grande échelle peut avoir des impacts négatifs sur le réseau électrique existant, tels que les points de puissance, les fluctuations de puissance accrues, une qualité de puissance réduite et des violations des limites de tension, qui nécessitent des extensions de réseau coûteuses. En revanche, une population de EV et TCL bien gérée limite non seulement les expansions inutiles de réseau, mais offre également des opportunités potentielles pour soutenir le réseau électrique fonctionnant en tant que réseau intelligent (SG). Dans ce contexte, cette thèse traite le développement des modèles d'agrégation et d'optimisation centralisés et distribués efficaces pour exploiter le potentiel de flexibilité des populations TCL et EV à grande échelle. Les modèles proposés sont utilisés pour atteindre des objectifs spécifiques au niveau de l'utilisateur, de l'agrégateur et du réseau électrique tout en évitant d'éventuels effets négatifs sur l'intégrité du système.

Premièrement, un nouveau cadre d'agrégation centralisé a été développé pour la participation des TCLs à grande échelle au service de régulation de fréquence. Ce cadre d'agrégation est basé sur le modèle de représentation d'état (SSM) et il est réalisé en coordination avec le générateur conventionnel (CG). Le modèle proposé est caractérisé par une charge de communication réduite et une estimation précise de la capacité de régulation. Les résultats de la simulation montrent que l'agrégateur TCL basé sur le SSM peut contrecarrer avec succès les écarts de fréquence tout en soulageant le stress sur le CG.

Ensuite, un nouveau cadre d'agrégation de EV centralisé étendu basé sur le SSM a été proposé pour la participation des populations de EV à grande échelle dans les services de régulation de fréquence et de l'écrêtement de la charge de pointe. Le cadre proposé augmente la flexibilité de l'agrégateur de véhicules électriques (EVA) en permettant aux véhicules électriques de participer à des services auxiliaires avec des taux de charge/décharge réguliers et rapides. Cela permettra à l'EVA d'apporter des réponses rapides et efficaces à de graves déséquilibres entre la production et la consommation. Une approche de contrôle probabiliste est développée qui réduit la charge de communication de l'agrégateur EV. Les résultats de la simulation montrent que l'agrégateur de EV basé sur le SSM proposé peut décrire

avec précision le comportement agrégé d'une grande population de EV, leur permettant de participer efficacement aux services de régulation de fréquence et d'écrêtement de la charge de pointe.

Afin d'obtenir une agrégation coordonnée des TCLs et des EVs, un nouveau cadre d'agrégation centralisé unifié basé sur le SSM a été proposé. Afin d'effectuer la coordination avec une charge de communication minimale, deux signaux de commande distincts, à savoir le signal de commande TCL et le signal de commande EV sont développés. Le premier est communiqué à tous les TCLs tandis que le second est communiqué à tous les EVs. Les simulations sont menées pour un micro-réseau communautaire comprenant une grande population de TCL et de EV, un générateur conventionnel et un système de production éolienne. Il a été démontré que le cadre unifié proposé peut décrire avec précision le comportement agrégé d'une grande population de TCL et de EV et réaliser efficacement l'ajustement les écarts de fréquence. De plus, le cadre proposé réduit la dépendance excessive à une seule ressource, minimise le cycle court des TCLs, garantit les besoins énergétiques des EVs et respecte les contraintes énergétiques des batteries des EVs.

Finalement, un nouveau cadre distribué hiérarchique a été proposé pour la planification optimale de la recharge des véhicules électriques (EVCS). La structure hiérarchique de l'EVCS comprend l'opérateur du système de distribution (DSO) au niveau supérieur, les EVA au niveau intermédiaire et les EV au niveau inférieur. Un algorithme itératif à boucle unique est développé pour résoudre le problème EVCS en combinant l'algorithme d'optimisation ADMM et le modèle de flux de puissance de la ligne de distribution (DistFlow). En utilisant la structure à boucle unique, la variable primale de tous les agents est mise à jour simultanément à chaque itération, ce qui se traduit par un nombre réduit d'itérations et une convergence plus rapide. Bien que le cadre développé soit général et puisse être appliqué à tout problème d'optimisation convexe, il est utilisé pour fournir une minimisation des coûts de charge au niveau de EV, un écrêtement de la charge de pointe au niveau de EVA et une régulation de la tension au niveau de DSO. Afin d'améliorer encore les performances du cadre d'optimisation, un modèle de prévision de charge utilisant un réseau neuronal artificiel (ANN) est développé pour prédire la demande non-EV des bâtiments résidentiels. L'efficacité et l'optimalité du modèle EVCS proposé sont évaluées par des simulations numériques.

## ABSTRACT

In recent years, there has been a growing trend toward energy transition, particularly in the transportation and building sectors. The widespread adoption of Electric Vehicles (EVs) in the transportation sector, and the high volume of Thermostatically Controlled Loads (TCLs) in the building sector, provide these sectors with the capacity to reduce carbon emissions and improve energy efficiency. However, the unmanaged penetration of large-scale EVs and TCLs can lead to negative impacts on the existing electric network, such as high peak, increased power fluctuations, decreased power quality, and voltage limit violations, which require costly remedial actions and network expansions. By contrast, a well-managed EV fleet and TCL population not only limit unnecessary network expansions but also potentially offers opportunities to support the electric grid operating as the smart grid (SG) in different ways.

Within this concept, this thesis deals with the development of efficient centralized and distributed aggregation and optimization models to exploit the flexibility of large-scale TCL and EV populations in supporting the electric grid. The proposed models are employed to obtain specific user-level, aggregator-level, and grid-level objectives while preventing possible adverse effects on system integrity.

First, a new centralized aggregation framework is developed for the participation of large-scale TCLs in the frequency regulation service. The aggregation is based on the State Space Model (SSM) and is realized in coordination with the Conventional Generator (CG). The proposed aggregation framework is characterized by a low communication requirement and an accurate regulation capacity estimation. The simulation results show that the proposed SSM-based TCL aggregator can successfully counteract the frequency deviations while relieving the stress on the CG by mitigating the amount of required ramp adjustments.

Next, a new extended SSM-based centralized EV aggregation framework is proposed for the participation of large-scale EV populations in the frequency regulation and peak load shaving services. The proposed framework increases the flexibility of the EV aggregator (EVA) by enabling the EVs to participate in ancillary services with both regular and fast charging/discharging rates. This will help the EVA to provide prompt and efficient responses to severe generation-consumption imbalances. A probabilistic control approach is developed which reduces the communication burden of the EV aggregator. The simulation results show that the proposed SSM-based EV aggregator can accurately describe the aggregated behavior of a large population of EVs enabling them to efficiently participate in frequency regulation and peak load shaving services.

In order to achieve coordinated aggregation of TCLs and EVs, a new unified SSM-based centralized aggregation framework is proposed. In order to perform the coordination with minimum communication burden, two distinct control signals, namely the TCL-control signal and EV-control signal are constructed. The former is communicated to all individual TCLs while the latter is communicated to all individual EVs. The simulations are conducted for a community-level microgrid including a large population of TCLs and EVs, a conventional generator, and a wind generation system. It is shown that the proposed unified framework can accurately describe the aggregated behavior of a large population of TCLs and EVs and can efficiently counteract the frequency deviations. Moreover, the proposed framework reduces the excessive dependence on one type of resource, minimizes the short cycling of TCLs, guarantees the energy requirements of the EVs and respects the energy constraints of the EV batteries.

Finally, a new hierarchical distributed framework is proposed for optimal electric vehicle charging scheduling (EVCS). The hierarchical EVCS structure includes distribution system operator (DSO) at the top layer, EVAs at the middle layer, and EVs at the bottom layer. A single-loop iterative algorithm is developed to solve the EVCS problem by combining the alternating direction method of multipliers (ADMM) and the distribution line power flow model (DistFlow). Using the single-loop structure, the primal variable of all agents is updated simultaneously at every iteration resulting in a reduced number of iterations and faster convergence. While the developed framework is general and can be applied to any convex optimization problem, it is employed to provide charging cost minimization at the EV layer, peak load shaving at the EVA layer, and voltage regulation at the DSO layer. In order to further improve the performance of the optimization framework, a load forecasting model using artificial neural network (ANN) is developed to predict the non-EV load demand of residential buildings. Finally, the efficiency and the optimality of the proposed EVCS framework is evaluated by numerical simulations.

## TABLE OF CONTENTS

DEDICATION . . . . .	iii
ACKNOWLEDGEMENTS . . . . .	iv
RÉSUMÉ . . . . .	v
ABSTRACT . . . . .	vii
TABLE OF CONTENTS . . . . .	ix
LIST OF TABLES . . . . .	xiii
LIST OF FIGURES . . . . .	xiv
LIST OF SYMBOLS AND ABBREVIATIONS . . . . .	xvi
LIST OF APPENDICES . . . . .	xviii
CHAPTER 1 INTRODUCTION . . . . .	1
1.1 Context and Motivation . . . . .	1
1.2 Problem Definition . . . . .	2
1.3 Objectives . . . . .	3
1.4 Research Contributions . . . . .	4
1.5 Organization of the Thesis . . . . .	6
CHAPTER 2 LITERATURE REVIEW . . . . .	7
2.1 Thermostatically Controlled Loads . . . . .	7
2.1.1 Modeling individual TCL . . . . .	7
2.1.2 Control approache of TCLs . . . . .	9
2.1.3 TCL aggregation models . . . . .	9
2.1.4 State Space Model for TCL aggregation . . . . .	10
2.2 Electric Vehicles . . . . .	16
2.2.1 EV charging levels . . . . .	16
2.2.2 Modeling individual EV . . . . .	17
2.2.3 EV aggregation models . . . . .	19
2.2.4 State Space Model for EV aggregation . . . . .	21

2.2.5 Alternating Direction Method of Multipliers for EV aggregation . . .	25
2.3 Distribution network model . . . . .	32
CHAPTER 3 COHERENCE OF THE ARTICLES IN RELATION TO THE RESEARCH GOALS . . . . .	34
CHAPTER 4 ARTICLE 1: STATE SPACE MODEL OF AGGREGATED TCLS FOR FREQUENCY REGULATION WITH A LOW COMMUNICATION REQUIREMENT	36
4.1 Abstract . . . . .	36
4.2 Introduction . . . . .	36
4.3 Modeling Framework . . . . .	37
4.3.1 Individual TCL Model . . . . .	37
4.3.2 State Space Model of Aggregated TCLs . . . . .	38
4.4 Frequency Regulation . . . . .	40
4.4.1 Framework of Frequency Regulation with SSM . . . . .	40
4.4.2 Frequency Regulation with State Space Model . . . . .	40
4.4.3 Control Action of State Space Model . . . . .	43
4.5 Case Studies And Simulation Results . . . . .	45
4.6 Conclusion . . . . .	47
CHAPTER 5 ARTICLE 2: AN EXTENDED STATE SPACE MODEL FOR AGGREGATION OF LARGE-SCALE EVS CONSIDERING FAST CHARGING . . . . .	49
5.1 Abstract . . . . .	49
5.2 Introduction . . . . .	49
5.3 Modeling Framework . . . . .	53
5.3.1 Individual EV Model . . . . .	53
5.3.2 Extended EV State Space Model for EV Aggregator (EVA) . . . . .	55
5.4 EV-SSM Framework for Ancillary Services . . . . .	59
5.4.1 EV-SSM for Frequency Regulation . . . . .	60
5.4.2 EV-SSM for Peak Load Shaving . . . . .	61
5.4.3 Control Actions for EVA . . . . .	62
5.4.4 User-level implementation of probabilistic control signal . . . . .	65
5.5 Case Studies And Simulation Results . . . . .	66
5.5.1 EV population modeling . . . . .	66
5.5.2 EV-SSM for Frequency Regulation . . . . .	67
5.5.3 EV-SSM for Peak Load Shaving . . . . .	74
5.6 Conclusion . . . . .	79

CHAPTER 6	ARTICLE 3: A UNIFIED STATE SPACE MODEL FOR AGGREGATION AND COORDINATION OF LARGE-SCALE TCLS AND EVS FOR FREQUENCY REGULATION . . . . .	80
6.1	Abstract . . . . .	80
6.2	Introduction . . . . .	80
6.3	Modeling Framework . . . . .	82
6.3.1	Individual TCL Model . . . . .	82
6.3.2	Individual EV Model . . . . .	83
6.3.3	Unified State Space Model of Aggregated TCLs and EVs . . . . .	84
6.4	Frequency Regulation . . . . .	88
6.4.1	Framework of Frequency Regulation with SSM . . . . .	88
6.4.2	Frequency Regulation with State Space Model . . . . .	89
6.4.3	Control Actions for TCLs . . . . .	91
6.4.4	Control Actions for EVs . . . . .	92
6.5	Case Studies And Simulation Results . . . . .	94
6.6	Conclusion . . . . .	101
CHAPTER 7	ARTICLE 4: ADMM-BASED HIERARCHICAL SINGLE-LOOP FRAMEWORK FOR EV CHARGING SCHEDULING CONSIDERING POWER FLOW CONSTRAINTS . . . . .	102
7.1	Abstract . . . . .	102
7.2	Introduction . . . . .	102
7.3	System Modeling . . . . .	106
7.3.1	Distribution Network Model . . . . .	106
7.3.2	EV Charging Infrastructure Model . . . . .	107
7.4	EV Charging Scheduling Problem Formulation . . . . .	109
7.4.1	EVCS Optimization Problem . . . . .	109
7.4.2	Lossy DistFlow approximation . . . . .	111
7.4.3	ANN-based load forecasting model . . . . .	113
7.4.4	ADMM-based Hierarchical Single-loop EV Charging Scheduling (ADMM-HS-EVCS) . . . . .	114
7.5	Case studies and simulation results . . . . .	118
7.5.1	Case studies . . . . .	119
7.5.2	Simulation results . . . . .	121
7.6	Conclusion . . . . .	127
CHAPTER 8	GENERAL DISCUSSION . . . . .	128



CHAPTER 9 CONCLUSION AND RECOMMENDATIONS . . . . .	132
9.1 Concluding Remarks . . . . .	132
9.2 Future Work . . . . .	134
REFERENCES . . . . .	135
APPENDICES . . . . .	150

## LIST OF TABLES

Table 1.1	Comparison of decomposition methods for distributed approaches	3
Table 2.1	EV charging levels . . . . .	17
Table 4.1	Simulation Parameters . . . . .	45
Table 5.1	EV fleet parameters* . . . . .	67
Table 5.2	Simulation parameters* . . . . .	68
Table 5.3	EVA communication performance under scenario c (fleet No. 1)	73
Table 5.4	EVA computation performance under scenario c (fleet No. 1) .	73
Table 6.1	Simulation Parameters . . . . .	95
Table 6.2	Average number of switching actions . . . . .	98
Table 7.1	ANN input features . . . . .	114
Table 7.2	EV fleet parameters . . . . .	119
Table 7.3	Simulation parameters . . . . .	120
Table 7.4	Performance of the load forecasting model . . . . .	122
Table 7.5	Peak load shaving performance . . . . .	124
Table 7.6	Performance comparison of the proposed framework . . . . .	126

## LIST OF FIGURES

Figure 2.1	First order ETP model for a TCL . . . . .	8
Figure 2.2	Hysteresis cycle of a fixed-frequency TCL in cooling mode . .	10
Figure 2.3	The SSM structure for cooling TCLs . . . . .	11
Figure 2.4	Operating states of an individual EV . . . . .	18
Figure 2.5	Operation area of an individual EV and its corresponding power profile . . . . .	18
Figure 2.6	The SSM structure for EVs . . . . .	22
Figure 2.7	The definition of the constraint matrices . . . . .	30
Figure 2.8	Distribution line power flow model (DistFlow) . . . . .	32
Figure 4.1	State space of aggregated TCLs . . . . .	38
Figure 4.2	Framework of frequency regulation with SSM of aggregated TCLs	41
Figure 4.3	Flowchart of calculating frequency regulation coefficient . . . .	42
Figure 4.4	The wind and load power profiles adapted from [1] . . . . .	46
Figure 4.5	System frequency for scenarios a and b . . . . .	46
Figure 4.6	Power profiles of aggregated TCLs for scenarios a and b . . . .	47
Figure 4.7	Power profiles of conventional generator for scenarios a and b .	47
Figure 4.8	Indoor air temperature profiles of all TCLs for scenario b . . .	48
Figure 5.1	EV states and responding modes . . . . .	53
Figure 5.2	Structure of the state-bins and input vectors . . . . .	56
Figure 5.3	EV-SSM framework for ancillary services . . . . .	59
Figure 5.4	Structure of the probabilistic control signal . . . . .	65
Figure 5.5	Plug-in/plug-out time distributions for different EV fleets . . .	67
Figure 5.6	The wind and load power profiles adapted from [1] . . . . .	68
Figure 5.7	System frequency for scenarios a, b and c (fleet No. 1) . . . .	69
Figure 5.8	Power profile of the EVA for scenarios a, b and c (fleet No. 1)	70
Figure 5.9	Power profile of the CG for scenarios a, b and c (fleet No. 1) .	70
Figure 5.10	State distribution of EVs for scenario b (fleet No. 1) . . . . .	71
Figure 5.11	State distribution of EVs for scenario c (fleet No. 1) . . . . .	71
Figure 5.12	Connection session, switch state and SOC% for two EVs under scenario c (fleet No. 1) . . . . .	72
Figure 5.13	System frequency for scenario c considering different EV fleets	74
Figure 5.14	State distribution of EVs for scenario c . . . . .	75
Figure 5.15	Power profile of the EVA for scenarios d and e (fleet No. 1) . .	76

Figure 5.16	Power profile of the CG for scenarios d and e (fleet No. 1) . . .	76
Figure 5.17	Energy profile of the EVA for scenarios d and e (fleet No. 1) .	77
Figure 5.18	State distribution of EVs for scenario e with CG base power of 91% (fleet No. 1) . . . . .	77
Figure 5.19	Power profile of the CG for scenario e (91%) considering different EV fleets . . . . .	78
Figure 5.20	Energy profile of the EVA for scenario e (91%) considering different EV fleets . . . . .	78
Figure 6.1	Structure of the state-bins for TCLs . . . . .	85
Figure 6.2	Structure of the state-bins for EVs . . . . .	85
Figure 6.3	Framework of frequency regulation with coordinated SSM . .	89
Figure 6.4	The wind and load power profiles adapted from [1] . . . . .	96
Figure 6.5	System frequency for scenarios a, b, c and d . . . . .	96
Figure 6.6	Power profiles of aggregated TCLs for scenarios a and d . . . .	97
Figure 6.7	Power profiles of aggregated EVs for scenarios a and d . . . .	97
Figure 6.8	Power profiles of conventional generator for scenarios a, b, c and d	98
Figure 6.9	Number of TCLs with different switch states . . . . .	99
Figure 6.10	Number of EVs with different switch states . . . . .	99
Figure 6.11	Indoor air temperature profiles of all TCLs for scenario c . . .	100
Figure 6.12	SOC of all EVs for scenario c . . . . .	100
Figure 7.1	Distribution line power flow model (DistFlow) . . . . .	106
Figure 7.2	IEEE 13 bus test feeder with the proposed ADMM-HS-EVCS framework . . . . .	109
Figure 7.3	Left: predicted uncontrollable power balance of EVAs Right: wholesale electricity price . . . . .	121
Figure 7.4	Load forecasting regression plots using the three layer 10-24 architecture . . . . .	123
Figure 7.5	Daily EV charging costs . . . . .	123
Figure 7.6	Power profile of the network buses . . . . .	124
Figure 7.7	Power profile of the network lines . . . . .	126
Figure 7.8	Voltage profile of the network buses . . . . .	126

## LIST OF SYMBOLS AND ABBREVIATIONS

AC	Air-conditioning
ADMM	Alternating Direction Method of Multipliers
AET	Average Execution Time
ANN	Artificial Neural Network
ASTT	Average Signal Transmission Times
BRP	Balance Responsible Party
CG	Conventional Generator
CNS	Connecting State
COP	Coefficient of Performance
CS	Charging State
DR	Demand Response
DS	Discharging State
DSO	Distribution System Operator
DSR	Demand Side Resource
DVS	Driving State
EMS	Energy Management System
ETP	Equivalent Thermal Parameter
EV	Electric Vehicle
EVA	Electric Vehicle Aggregator
EVCS	Electric Vehicle Charging Scheduling
FCS	Fast Charging State
FDS	Fast Discharging State
FTCL	Fixed-frequency TCL
HESS	Hybrid Energy Storage Systems
HMM	Hidden Markov Model
HVAC	Heating, Ventilation and Air-conditioning
ICEV	Internal Combustion Engine Vehicle
ITCL	Inverter TCL
IS	Idle State
LM	Levenberg-Marquardt
MAPE	Mean Absolute Percentage Error
MLP	Multi-Layered Perceptron
MSTT	Maximum Signal Transmission Times

MTM	Markov Transition Matrix
PTA	Peak-to-Average
PTP	Peak-to-Peak
RB	Residential Building
RCS	Regular Charging State
RDS	Regular Discharging State
RES	Renewable Energy Source
RMSE	Root Mean Square Error
RPDS	Regularized Primal-Dual Sub-gradient
SAE	Society of Automotive Engineering
SG	Smart Grid
SOC	State of Charge
SPDS	Shrunk Primal-Dual Sub-gradient
SSM	State Space Model
TCL	Thermostatically Controlled Load
TSO	Transmission System Operator
V2G	Vehicle-to-Grid

**LIST OF APPENDICES**

Appendix A	Alternating Direction Method of Multipliers (ADMM) . . . . .	150
Appendix B	List of publications . . . . .	157

## CHAPTER 1 INTRODUCTION

### 1.1 Context and Motivation

The recent growing trend toward large scale integration of Renewable Energy Sources (RESs) and new loads (e.g., Electric Vehicles (EVs)) in Smart Grid (SG) can put the power systems at risk of operation with higher power production-consumption mismatch, lower inertial levels, and more uncertainties [2]. Therefore, the exploitation of flexibility for maintaining supply-demand balance in modern power systems is becoming highly attractive [3]. Traditionally, end-users are considered to be inelastic and thermal generators are in charge of maintaining the balance of supply and demand in real-time by adjusting their output power [4]. However, there are many situations where the thermal generators do not operate at their optimal operating points due to their thermal efficiency and economic issues [5]. More specifically, increasing the capacity of regulating generators is not economical due to their short up-time. Furthermore, the mechanical stress caused by fast-changing regulating signals will reduce their lifetime.

Nowadays, with the development of advanced communication structures within the smart grid context, Demand Response (DR) programs have become an attractive alternative to provide different ancillary services to the power system [6]. DR programs represent a way to exploit the flexibility of Demand Side Resources (DSRs), such as batteries, curtailable loads, deferrable loads, Thermostatically Controlled Loads (TCLs), and Electric Vehicles (EVs) [7]. Taking TCLs into account, the exploitation can be done by adopting a proper control framework to interrupt their regular operating cycle and force them to turn ON or OFF when required. As for EVs, various charging scheduling techniques can be used to coordinate their charging sessions and even force them to inject their energy back into the grid using vehicle-to-grid (V2G) technology, if required [8]. However, the power rate and the energy capacity of a single TCL or EV is not sufficient to effectively participate in grid-level ancillary services. Therefore, several TCLs and EVs need to be aggregated and coordinated so that the accumulated capacity can become high enough to provide considerable grid-level services [9]. Within this concept, an aggregator is defined as a middle agent who is in charge of controlling the smart interactions between the end-users and the power grid with the goal of achieving various user-level objectives (e.g., operation cost, comfort, etc.) and grid-level services (e.g., frequency regulation, voltage regulation, peak load shaving, etc.) [10]. The grid-level services can be offered to different stakeholders such as the Balance Responsible Party (BRP), the Distribution System Operator (DSO), or the Transmission System Operator (TSO).



## 1.2 Problem Definition

To date, various aggregation models have been proposed which can be generally categorized as centralized and distributed approaches [11]. In centralized approaches, a central entity, e.g., DSO, is responsible to collect and process the information of the whole system. Considering all decisions are made at a single location, centralized approaches are known to have better accuracy and controllability [12]. However, the communication and computation burden for data collecting, data processing, and control signal dispatching makes them less efficient, specially for large-scale populations. In order to improve both communication and computation efficiencies of centralized approaches, various control strategies have been developed majority of them focusing on employing some sort of reduced aggregation models. As an example of reduced aggregation model, State Space Model (SSM) was initially introduced for analyzing the aggregated response of flexible loads consisting of TCLs [13, 14]. Later, authors in [15] and [16] showed that it is possible to determine the parameters of the SSM-based TCL aggregator by observing the temperature dynamics of TCLs and utilize the TCL aggregator to regulate frequency and energy imbalances in power systems. Although there is extensive literature on SSM-based TCL aggregation models, using SSM for EV aggregation is an emerging research topic. In this thesis, we motivate the use of SSM to build accurate and efficient aggregation models which can be employed to aggregate large population of end-users containing TCLs, EVs, or a mix of both.

Although reduced aggregation models are successful in improving the efficiency of centralized approaches, they still suffer from a variety of security issues such as vulnerability to single point failure and end-user data privacy concerns. Alternatively, distributed approaches can be used to overcome the higher computational cost and communication burden of centralized approaches. Based on the configuration of the communication network, the distributed approaches are categorized into hierarchical and fully-distributed structures. These approaches decompose the main problem into several sub-problems and distribute them over several agents (e.g., DSO, aggregators, and end-users) with some possible coupling in the constraints or/and objective functions [17]. These small-scale sub-problems are solved simultaneously but independently by each agent through a distributed and iterative procedure. As a result, distributed approaches are not only immune to the single point failure, but also preserve the end-users' privacy since they do not require the private information of users to be shared with a higher-level agent. However, they may not lead to the global optimal solution because of the limited amount of shared information and its consequent uncertainty about the state of the whole system [18]. Table 1.1 shows some popular decomposition methods for distributed approaches which are categorized based on the structure (i.e., the type of coupling between

Table 1.1 Comparison of decomposition methods for distributed approaches

Algorithm	Coupling constraints & cost	Coupling constraints	Coupling cost	Strictly convex cost	Non-strictly convex cost
Gradient projection	-	-	✓	✓	-
Subgradient projection	-	-	✓	✓	✓
Dual decomposition	✓	✓	✓	✓	-
ADMM	✓	✓	✓	✓	✓

the agents) and characteristics (i.e., convexity level) of the problem [19–21]. As it is seen, gradient projection and dual decomposition algorithms only converge if the cost function of the optimization problem is strictly convex. However, some important optimization problems (e.g., linear programs) have convex but not strictly convex cost functions [22]. Furthermore, the conventional gradient and subgradient projection algorithms are not able to deal with optimization problems with coupling constraints. Therefore, in this thesis, the Alternating Direction Method of Multipliers (ADMM) is employed to develop a distributed EV aggregation model which can be applied to a wide range of user-level, aggregator-level, and grid-level optimization problems.

### 1.3 Objectives

The main goal of this thesis is to develop efficient centralized and distributed optimization models for the participation of TCLs and EVs in the ancillary service of the smart grid. The proposed models are used to obtain economical and/or technical user-level, aggregator-level, and grid-level objectives while preventing possible adverse effects on end-users' integrity. More specifically, the objectives of the thesis are listed as follows:

- Developing scalable centralized and distributed models which are applicable to a large population of TCLs and EVs integrated into aggregators.
- Designing accurate aggregation models that are computationally and communicationally efficient.
- Devising appropriate measures in order to avoid excessive wear and tear of TCLs and battery degradation of EVs caused by frequent switching between different operating states.

- Considering special operational characteristics of end-users, such as comfort constraints, parameter uncertainty, lock-out effect of TCLs, fast charging mode of EVs, and their V2G capability.
- Adopting the proposed aggregation models to provide various ancillary services including:
  - Frequency regulation: which refers to the actions that are performed to balance generation and consumption subsequent to large disturbances in the power system such as line/generation-unit outages or sudden load changes. The focus will be devoted to the primary regulation control which aims at counteracting frequency excursions following large disturbances.
  - Voltage regulation: which refers to the ability to maintain the system voltage within the permissible range for different load conditions.
  - Peak load shaving and valley filling: which refers to flattening the load curve and shifting the peak load demand to off-peak intervals.

#### 1.4 Research Contributions

This thesis is based on four journal and conference articles. The contributions achieved per each article are listed as follows:

Article 1: S. Kiani, K. Sheshyekani, and H. Dagdougui, "State Space Model of Aggregated TCLs for Frequency Regulation with a Low Communication Requirement," *2020 IEEE Power & Energy Society General Meeting (PESGM)*, 2020, pp. 1-5, doi: 10.1109/PESGM41954.2020.9281513.

- A new SSM-based aggregation model for the participation of large-scale TCLs in the frequency regulation service has been developed.
- The proposed aggregation model is characterized by a low communication requirement and an accurate regulation capacity estimation.
- The device wear and tear, the comfort requirement of end-users, and the short cycling of TCLs are considered.

Article 2: S. Kiani, K. Sheshyekani, and H. Dagdougui, "An Extended State Space Model for Aggregation of Large-scale EVs Considering Fast Charging," in *IEEE Transactions on Transportation Electrification*, doi: 10.1109/TTE.2022.3179311.

- An extended SSM-based aggregation model has been developed for the participation of large-scale EVs in frequency regulation and peak load shaving services.
- The extended SSM enables EVs to participate in ancillary services with both regular and fast charging/discharging rates by considering dedicated state-bins for each charging/discharging state. The extra flexibility offered by fast charging rates helps the EV aggregator (EVA) to provide prompt and efficient response to severe generation-consumption imbalances.
- Appropriate measures are taken into account in order to avoid excessive battery degradation of EVs caused by frequent switching to fast charging/discharging states.
- The proposed aggregation model is characterized by a low communication requirement and an accurate regulation capacity estimation.
- The performance of the proposed EV aggregator is evaluated for different driving behaviors and state of charge (SOC) levels of EV population.

Article 3: S. Kiani, K. Sheshyekani, and H. Dagdougui, "A unified state space model for aggregation and coordination of large-scale TCLs and EVs for frequency regulation," *Electric Power Systems Research*, vol. 195, p. 107181, 2021.

- A unified SSM-based aggregation and coordination model has been developed which enables TCLs and EVs to jointly participate in the frequency regulation service.
- Joint aggregation of TCLs and EVs reduces the excessive dependence on one type of resource.
- The proposed aggregation model is characterized by a low communication requirement and an accurate regulation capacity estimation.
- The short cycling of TCLs, the energy requirements of the EVs, and the capacity constraints of the EV batteries are considered.

Article 4: S. Kiani, K. Sheshyekani, and H. Dagdougui, "ADMM-Based Hierarchical Single-loop Framework for EV Charging Scheduling Considering Power Flow Constraints," in *IEEE Transactions on Transportation Electrification*, December 2022, submitted for publication.

- An ADMM-based trilayer distributed framework for optimal electric vehicle charging scheduling (EVCS) has been developed.

- A single-loop iterative algorithm is developed to solve the EVCS problem by combining ADMM and the distribution line power flow model (DistFlow).
- Using the single-loop structure, the primal variable of all agents are updated simultaneously at every iteration resulting in a reduced number of iterations and faster convergence.
- A load forecasting model using artificial neural network (ANN) is developed to predict the non-EV load demand of the residential buildings
- The proposed framework is employed to provide charging cost minimization at the EV layer, peak load shaving at the EVA layer, and voltage regulation at the DSO layer.

## 1.5 Organization of the Thesis

The thesis is organized as follows. Chapter 2 provides a literature review on the existing work on modeling TCLs and EVs as well as their aggregation methods. Furthermore, the underlying power system is taken into account using the distribution line power flow model (DistFlow). The structure of the research project as a whole and the coherence of the articles in relation to the research goals are presented in Chapter 3. In Chapter 4, a new SSM-based aggregation model for the participation of TCLs in the frequency regulation service is developed. The TCL aggregator broadcasts only one identical control signal to all individual TCLs which lowers the communication burden of the aggregation. Chapter 5 presents an extended SSM-based aggregation model for the participation of large-scale EVs in frequency regulation and peak load shaving services. Using the extended SSM, EVs are able to participate in ancillary services with both regular and fast charging/discharging rates. In Chapter 6, a unified SSM-based aggregation and coordination model is developed which enables TCLs and EVs to jointly participate in the frequency regulation service. The joint aggregation reduces the excessive dependence on one type of resource and increases the flexibility and capacity of the aggregator. In Chapter 7, an ADMM-based single-loop distributed framework for optimal electric vehicle charging scheduling is developed. Using the single-loop structure, the convergence performance of the distributed iterative algorithm is considerably improved. General discussion of the objectives and the achievements in this thesis is presented in Chapter 8. Finally, concluding remarks and the scope for further research are presented in Chapter 9.

## CHAPTER 2 LITERATURE REVIEW

In this chapter, a literature review on the individual modeling of TCLs and EVs as well as existing aggregation methods is presented. Furthermore, the distribution line power flow model (DistFlow) and its associated formulations will be revisited.

### 2.1 Thermostatically Controlled Loads

Thermostatically Controlled Loads (TCLs, such as electric water heaters, space heaters, refrigerators, ventilation, and air conditioning system) account for a major part of the total power consumption in the power systems [23]. More than 35% of the generated electricity in the USA is consumed by HVAC (heating, ventilation, and air-conditioning) units, and around 30%-40% of the peak power consumption is devoted to the air-conditioning (AC) loads in China [24,25]. TCLs are also considered great candidates for DR programs owing to their capacity for storing thermal energy and their ability to change their power consumption almost instantaneously according to given temperature set-points. Therefore, by adopting a proper controller, the local hysteresis cycle of TCLs can be interrupted in order to provide ancillary service to the power system without compromising end-users' comfort [26]. It is to be noted that this research is primarily focused on fixed-frequency TCLs (FTCLs) where power consumption is either zero or equal to the rated power. Investigating the inverter-based TCLs (ITCLs) with adjustable power consumption is out of the scope of the current study.

#### 2.1.1 Modeling individual TCL

The thermodynamic transition process of a fixed-frequency TCL can be mathematically described by the Equivalent Thermal Parameter (ETP) model. The simplified first order ETP model of a TCL is shown in Fig. 2.1 and described by (2.1). Temperature evolution is governed by heat gain, heat storage capacity, and heat loss due to the interaction with the surrounding environment.

$$C_a \frac{dT_a(t)}{dt} = \frac{(T_o(t) - T_a(t))}{R_a} + Q_a(t) \quad (2.1a)$$

$$Q_a(t) = \pm m(t) \cdot COP \cdot P_{tcl}^{rate} \quad (2.1b)$$

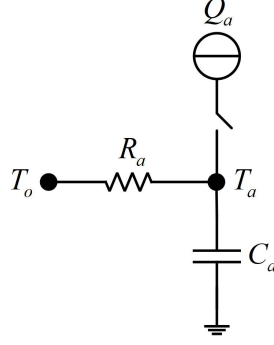


Figure 2.1 First order ETP model for a TCL

where signs  $+$  and  $-$  are used for heating and cooling TCLs, respectively. The inside air temperature is denoted by  $T_a(t)$  while the outside air temperature is given by  $T_o(t)$ . The thermal characteristics of the surrounding environment are specified by the thermal resistance  $R_a$  and the thermal capacitance  $C_a$ . The heat gain, the rated power, and the switch status of the TCL are represented by  $Q_a(t)$ ,  $P_{tcl}^{rate}$  and  $m(t)$ , respectively. Finally,  $COP$  is defined as the coefficient of performance of the TCL. In discrete time settings, (2.1a) can be rewritten as (2.2),

$$T_a(k+1) = e^{(-\Delta t/R_a C_a)} T_a(k) + (1 - e^{(-\Delta t/R_a C_a)}) (T_o(k) - R_a Q_a) \quad (2.2)$$

where  $\Delta t$  is the discretization time-step [24].

In order to maintain customer comfort, the hysteresis cycle of TCL is governed by a local controller around a specified temperature set-point,  $T_s$ , with a dead-band length of  $\delta$ . Therefore, the switch status for heating and cooling TCL can be determined by (2.3a) and (2.3b), respectively.

$$m(k+1) = \begin{cases} 0, & T_a(k) \geq T_s + \frac{\delta}{2} : OFF \\ 1, & T_a(k) \leq T_s - \frac{\delta}{2} : ON \\ m(k), & otherwise \end{cases} \quad (2.3a)$$

$$m(k+1) = \begin{cases} 1, & T_a(k) \geq T_s + \frac{\delta}{2} : ON \\ 0, & T_a(k) \leq T_s - \frac{\delta}{2} : OFF \\ m(k), & otherwise \end{cases} \quad (2.3b)$$

The time course evolution of inside air temperature,  $T_a$ , and power consumption,  $P$ , of a TCL in cooling mode are shown in Fig. 2.2. It is assumed that the inside air temperature is initially equal to the outside air temperature  $T_o$ . When the TCL turns on, the inside air temperature  $T_a$  decreases until it hits the lower limit  $T_{min} = T_s - \frac{\delta}{2}$ . At time  $t_1$ , the TCL turns off and the inside air temperature begins to increase naturally. At time  $t_2$ , the inside air temperature hits the upper limit  $T_{max} = T_s + \frac{\delta}{2}$  and TCL will turn on again to keep the inside air temperature within the given temperature dead band.

### 2.1.2 Control approach of TCLs

Generally, fixed-frequency TCLs can participate in DR programs using two main control approaches [26]. The first approach is known as ON-OFF toggling and involves changing the status of TCLs by direct ON/OFF switching control [16,27–39]. The second control approach is to slightly adjust the temperature set-point or the dead-band width of the hysteresis cycle without altering the percentage of ON and OFF TCLs [40–49].

Comparing both approaches, ON-OFF toggling can instantaneously change the switching status of TCLs and modify their power consumption. However, it is not able to retain this adjustment for a long period of time. This is due to the limitation of the temperature dead-band defined by each end-user. On the other hand, temperature set-point control is able to adjust the power consumption of TCLs for a longer period, but the regulation control may not be immediate [50]. Therefore, ON-OFF toggling is suitable for participating in short time-scale DR programs (e.g., frequency regulation service [27, 32]) while the temperature set-point adjustment may be utilized for longer time-scale DR programs (e.g., minimizing energy costs [46, 48]).

### 2.1.3 TCL aggregation models

In order to exploit the flexibility of TCLs, a number of aggregation models with different degrees of accuracy and complexity have been proposed in the literature. Studies began in 1979 by presenting a dynamic model for individual TCL by considering some external factors such as weather and human behavior [51]. The individual models were then statistically aggregated in order to obtain a model for a large number of similar TCLs. Later, authors in [52] developed an aggregated dynamic model for a homogeneous population of TCLs using stochastic diffusion models based on solving Fokker-Planck partial differential equations. Since the model was solved numerically without any closed-form analytic solution, authors



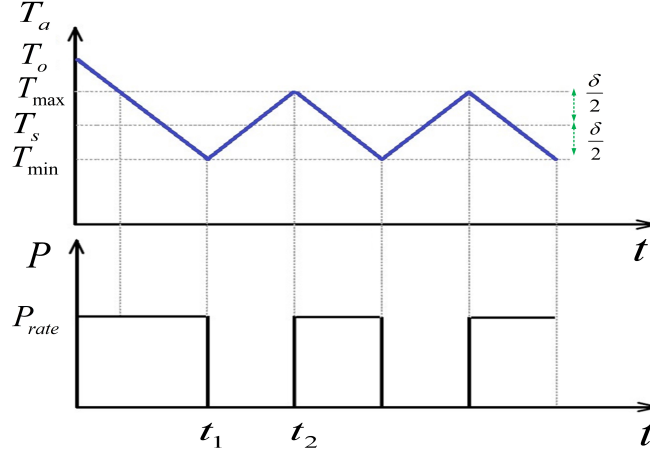


Figure 2.2 Hysteresis cycle of a fixed-frequency TCL in cooling mode

in [41] further extended it by deriving a closed-form solution for the coupled Fokker-Planck equations. However, improving the accuracy and reducing the complexity of the model still remained challenging.

The complexity of the aggregation model is mainly due to the non-linear characteristics of the devices. The common approach to simplify this non-linearity is to adopt a proper control model that can either describe only the aggregated output power of TCLs or the entire population dynamics. The former may be derived using Laplace transformation analysis [42] or different system identification techniques [41]. Since such output-oriented models describe TCLs as a black-box, it is difficult to monitor the impact of the control signals on the individual TCLs. On the other hand, using the population-based aggregation models, the TCLs' dynamics can be characterized by the evolution of probability density functions. This approach can be further simplified by adopting discrete temperature space and discrete-time settings and calculating the transition probability of TCLs between discrete states. Examples are the state queuing model [13, 14, 50], the transport model [40, 53, 54] and the State Space Model (SSM) [2, 6, 10, 15, 16, 18, 27, 28, 35, 37, 40, 53, 55–58].

#### 2.1.4 State Space Model for TCL aggregation

Compared to the conventional population-based TCL aggregation models, the SSM distributes TCLs into several state bins according to their indoor temperature and switching states and then controls the evolution of TCLs between different state bins. Therefore, the computational burden only depends on the number of state bins rather than the size of the TCL population. By adopting this model, the issue of heavy computational load when dealing with large-scale TCL populations can be effectively addressed [6].

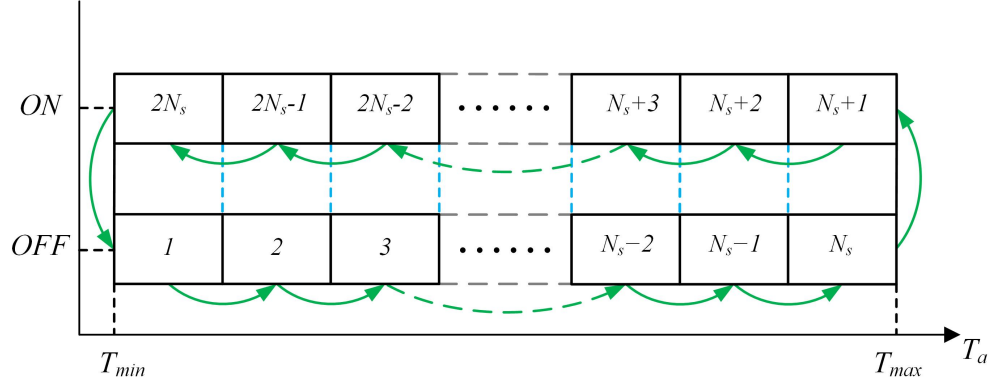


Figure 2.3 The SSM structure for cooling TCLs

In order to build the structure of the SSM, the temperature dead-band of each TCL is divided into a fixed number of temperature intervals with equal length. As fixed-frequency TCLs have only two operating states (ON or OFF), each temperature interval is further divided into two state-bins. The SSM structure for cooling TCLs is shown in Fig. 2.3 where the state bins are denoted by sequential numbers,  $1, 2, \dots, N_s, N_s + 1, \dots, 2N_s$ . The green arrows represent the natural transition of TCL between different state bins. Note that the number of state bins in ON and OFF states are equal ( $N_{ON} = N_{OFF} = N_s$ ). At any moment, the state distribution of TCLs can be defined by a state vector with a dimension of  $N_b = 2N_s$ . The structure of state vector  $\mathbf{x}(t)$  is given by (2.4),

$$\mathbf{x}(t) = [n_1(t), n_2(t), \dots, n_{N_s}(t), n_{N_s+1}(t), \dots, n_{2N_s}(t)]^T \quad (2.4)$$

where  $n_i(t)$  is the number of TCLs in the  $i$ th state bin at time  $t$ .

For an uncontrolled population of TCLs, their natural state transition can be formulated as (2.5),

$$\dot{\mathbf{x}} = \mathbf{G}\mathbf{x}(t) \quad (2.5)$$

where  $\mathbf{G}$  is a  $N_b \times N_b$  matrix. The element  $(l, q)$  in matrix  $\mathbf{G}$  (denoted by  $g_{lq}$ ) is the speed at which the TCLs in the state bin  $q$  move towards the state bin  $l$ . Assuming a very short time interval, the TCLs in one state bin will only move to the neighboring state bin or remain in the same state bin [37]. Therefore,  $\mathbf{G}$  is a large sparse matrix whose elements are given as below,

$$g_{lq} = \begin{cases} -\frac{1}{\Delta t_q}, & l = q, 1 \leq q \leq N_b \\ \frac{1}{\Delta t_q}, & l = q + 1, 1 \leq q \leq N_b - 1 \text{ or } l = 1, q = N_b \\ 0, & \text{otherwise} \end{cases} \quad (2.6)$$

where  $\Delta t_q$  is the time taken for a TCL to move from the start point of the state bin  $q$ ,  $t_q^{start}$ , to the start point of the state bin  $l$ ,  $t_l^{start}$ . Note that the start point of the state bin  $l$  has the same temperature as the end point of the state bin  $q$  ( $t_l^{start} = t_q^{end}$ ). Therefore,  $\Delta t_q$  can be calculated as follows,

$$\Delta t_q = \begin{cases} -R_a C_a \cdot \ln \left( \frac{T_o - COP \cdot P_{tcl}^{rate} \cdot R_a - T_q^{end}}{T_o - COP \cdot P_{tcl}^{rate} \cdot R_a - T_q^{start}} \right), & m(t) = 1 \\ -R_a C_a \cdot \ln \left( \frac{T_o - T_q^{end}}{T_o - T_q^{start}} \right), & m(t) = 0 \end{cases} \quad (2.7)$$

where  $m(t)$  is the switch state of the TCL [10, 18]. In discrete time setting (2.5) can be rewritten as follows,

$$\mathbf{x}(k+1) = \mathbf{A}\mathbf{x}(k) \quad (2.8a)$$

$$\mathbf{A} = \mathbf{I} + \mathbf{G}\Delta t \quad (2.8b)$$

where  $\mathbf{x}(k)$  is the state vector containing the number of the TCLs in each state bin at  $k$ th time interval.  $\mathbf{A}$  is a  $N_b \times N_b$  matrix whose elements are the transition probability of the TCLs between two neighboring state bins [37]. The structure of matrix  $\mathbf{A}$  is given by (2.9). Note that each element of the matrix  $\mathbf{A}$  can obtain a value between 0 and 1.

$$\mathbf{A} = \begin{bmatrix} 1 - \frac{\Delta t}{\Delta t_1} & 0 & \dots & \dots & 0 & \frac{\Delta t}{\Delta t_{N_b}} \\ \frac{\Delta t}{\Delta t_1} & 1 - \frac{\Delta t}{\Delta t_2} & 0 & \dots & \dots & 0 \\ \vdots & \vdots & \vdots & \vdots & \vdots & \vdots \\ \dots & 0 & \frac{\Delta t}{\Delta t_{q-1}} & 1 - \frac{\Delta t}{\Delta t_q} & 0 & \dots \\ \vdots & \vdots & \vdots & \vdots & \vdots & \vdots \\ 0 & \dots & \dots & 0 & \frac{\Delta t}{\Delta t_{N_b-1}} & 1 - \frac{\Delta t}{\Delta t_{N_b}} \end{bmatrix} \quad (2.9)$$

It is seen that  $\Delta t_q$  in (2.7) and consequently the matrix  $\mathbf{A}$  defined by (2.9) are dependent on the outside ambient temperature,  $T_o$ . In practice,  $T_o$  is not constant and the time varying characteristic of the ambient temperature needs to be properly taken into account by defining a variable transition matrix  $\mathbf{A}$  [28, 56]. However, for the sake of simplicity, the ambient temperature and consequently matrix  $\mathbf{A}$  are considered to be constant.

Note that the state transition formulation presented by (2.8) does not consider the effect of control signals. However, a certain number of TCLs participating in DR programs receive a control signal from the aggregator changing their ON/OFF states. This accordingly affects the final distribution of TCLs in the state bins [37]. In order to include the effect of controlled switching, SSM in (2.8) can be modified as follows,

$$\mathbf{x}(k+1) = \mathbf{A}.\mathbf{x}(k) + \mathbf{B}.\mathbf{u}(k) \quad (2.10)$$

where  $\mathbf{u} \in \mathbb{R}^{\frac{N_b}{2} \times 1}$  is the control input containing the number of ON and OFF TCLs in each temperature interval which are considered to be controlled by the TCL aggregator. The positive and negative elements of  $\mathbf{u}$  denote the number of TCLs in the corresponding temperature interval which are going to be turned ON or OFF, respectively. Note that the controlled TCLs only switch between corresponding ON and OFF bins of a certain temperature interval. Therefore,  $\mathbf{B} \in \mathbb{R}^{N_b \times \frac{N_b}{2}}$  can be constructed as follows [58]:

$$\mathbf{B} = \begin{bmatrix} -1 & & 0 \\ & \ddots & \\ 0 & & -1 \\ - & - & - \\ 0 & & 1 \\ & \ddots & \\ 1 & & 0 \end{bmatrix} \quad (2.11)$$

Finally, the aggregated power of the TCLs at the  $k$ th time interval is denoted by  $y(k)$  and given as follows,

$$y(k) = \mathbf{C}.\mathbf{x}(k) \quad (2.12a)$$

$$\mathbf{C} = P_{mean} \cdot [\underbrace{0, 0, \dots, 0}_{N_s}, \underbrace{1, 1, \dots, 1}_{N_s}] \quad (2.12b)$$

where  $P_{mean}$  is the mean value of the power consumption of TCLs. The State Space Model (SSM) of a population of controlled TCLs can be jointly described by equations (2.10), (2.11) and (2.12).

Note that theoretically, more state bins can lead to a more precise estimation of the aggregated power of the TCLs, but at the expense of more complex control structure. Therefore, the number of bins must be properly tuned as a trade-off between the accuracy and complexity of the aggregation. The SSM control algorithms for aggregated TCLs are presented in Chapters 4 and 5.

There are also some other aspects that need to be considered when designing an SSM-based TCL aggregation model, including the heterogeneity of TCL parameters, the identification method for the derivation of the transition matrix ( $\mathbf{A}$ ) and the lock-out effect of the TCLs. These aspects are further explained in the upcoming sections.

### Parameter heterogeneity

According to equations (2.1)-(2.3), the dynamics of TCLs can be characterized by the following parameters  $[R_a, C_a, COP, P_{tcl}^{rate}, T_s, \delta]$ . The SSM presented in the previous section is amenable to only a homogeneous population of TCLs, meaning that all TCL parameters are the same for the entire population. However, there is always a degree of parameter heterogeneity in TCL populations due to different building structures and device characteristics. If the effect of parameter heterogeneity is neglected, the resulting aggregation model error will be significant [26].

Several ideas have been proposed in the literature to handle the parameter heterogeneity of TCLs. Authors in [15, 16] take the number of state bins as a tuning variable for the heterogeneous populations, which is adjusted to achieve an acceptable modeling error. Other approaches consider clustering the heterogeneous TCLs into multiple homogeneous groups [10, 27, 32, 35, 55, 57, 59, 60]. For this purpose, first, a large number of parameter samples are generated based on the known distributions of the TCL parameters. Then, the standard k-mean algorithm (MATLAB function kmeans) is used to classify these parameters into few clusters. Each cluster is represented by a center as well as the number of parameters in that cluster.

Another approach to deal with parameter heterogeneity is to analytically derive the transition matrix  $\mathbf{A}$  for a heterogeneous population of TCLs using the probability density function of TCL parameters [16]. However, the matrix derivation process is quite complicated, particularly for heterogeneity of more than only one TCL parameter. Alternatively, the transition

matrix can also be identified using real or simulated state information of the TCL population. The matrix identification method is applicable to both homogeneous and heterogeneous populations. This method is presented in the following section.

### Identification of the transition matrix

The analytical approach for the calculation of the transition probability matrix using (2.9) assumes that all TCL parameters and the ambient temperature are known. Alternatively, the matrix  $\mathbf{A}$  can be identified by observing the real or simulated state information of all or a group of TCLs without knowing the details of their characteristic parameters.

This approach utilizes the Hidden Markov Model (HMM) parameter estimation method to calculate the state transition probabilities by observing the sequence of state information [16, 35]. The state information of TCLs includes the time series of indoor temperature and ON/OFF state of TCLs. As the TCLs in a heterogeneous population have different temperature set-points and temperature dead-bands, the indoor temperatures need to be first normalized by as follows [58],

$$T_{a,norm} = \frac{T_a - (T_s - 0.5\delta)}{\delta} \quad (2.13)$$

The HMM method (MATLAB function `hmmestimate`) can then be applied to the state information time series in order to identify the transition matrix. However, this method is not suitable for online applications due to the convergence problems caused by the large number of states. Therefore, in many studies, the identification of matrix  $\mathbf{A}$  is performed offline using measured historical points of the state information.

### Lock-out effect

Generally, the TCLs that are equipped with a compressor (e.g., AC units) cannot tolerate high switching frequencies. These TCLs need to spend a certain amount of time in OFF state, before being able to turn on again. This lock-out time is necessary to let them equalize the internal pressure of their compressors before starting again [2]. Therefore, the lock-out effect must be considered in the SSM in order to avoid the short cycling of TCLs. Several methods have been proposed to properly adjust the switching rate of TCLs in the SSM aggregation. For instance in [6, 18, 27, 37, 57], the dynamics of the locked TCLs are incorporated into the model by including dedicated lockout bins. Using this method, the TCLs in the ON bins do not move directly into OFF bins. Instead, they first flow into lockout bins and after a certain amount of time, they are released and passed to the OFF bins.

Another approach to deal with the lock-out effect is to keep the state bin structure unchanged while excluding the regulation capacity of the TCLs that are located at the state bins near the edge of the temperature dead-band. As these TCLs have been recently switched by their hysteresis temperature cycle, they can not be switched again by the DR control command for a certain amount of time [58].

## 2.2 Electric Vehicles

From the perspective of the transportation sector, Electric Vehicles (EVs) are considered as promising alternatives to internal combustion engine vehicles (ICEVs) owing to their lower energy costs and less carbon emissions [8]. The worldwide sale of EVs exceeded 8.5 million units in 2020 and is on track to reach more than a hundred million units by 2030 [61].

On one hand, large-scale penetration of unmanaged EVs introduces a significant load increase to the power system, resulting in adverse impacts such as high peaks, increased power fluctuations, decreased power quality and voltage limit violations, which requires costly network expansions.

On the other hand, EVs are considered as controllable loads that can be potentially used in DR programs [62]. It is reported that U.S. personal vehicles are in use only 4% of the time [63]. Assuming the same utilization rate for the EVs, when not in use, they can be kept connected to the grid to provide various ancillary services to the power systems. A well-managed population of EVs not only limits unnecessary network expansions, but also can enhance the resilience of the power system, facilitate the integration of renewable resources and lower the energy costs for the EV users [9]. For example, in the case of specific system component failures, the battery of EVs may be used as a backup energy storage to inject required energy back into the grid using the vehicle-to-grid (V2G) technology [64].

However, the main challenge when dealing with large-scale EV populations is to efficiently control their energy requirement without sacrificing the primary function of electric vehicles which is personal mobility [9].

### 2.2.1 EV charging levels

The Society of Automotive Engineering (SAE) defines the physical, electrical, performance and communication requirements for EV charging systems in North America [65]. According to the “SAE J1772” standard, the charging levels are classified into three categories based on the voltage, current, and rated power [66]. This classification is presented in Table 2.1. In level 1 and level 2 categories, an on-board charger is used to convert the AC power to DC

Table 2.1 EV charging levels

Type	Voltage/ Current/ Power	Charger type	Mile of range per hour of charging (RPH)	Time to fully charge
Level 1	120 V AC 12-16 A 1.44-1.92 kW	On-board	-5 RPH	-16 hours for 80-mile battery -40 hours for 200-mile battery
Level 2	208-240 V AC 12-80 A 2.5-19.2 kW	On-board	-12 RPH for 3.7 kW charger -25 RPH for 6.6 kW charger	-3.5 hours for 80-mile battery -8 hours for 200-mile battery
DC Fast Charging	480-600 V DC Up to 600 A Up to 350 kW	Off-board	-Up to 100 RPH for 24 kW charger -Up to 200 RPH for 50 kW charger	Depends on the power level of the charger and EV model. But normally takes 20-30 minutes to reach 80% of capacity

power while in the DC fast charging category, the AC/DC conversion is performed off-board inside the charging station and the DC power is directly delivered to the EV. The DC fast charging significantly reduces the charging time by using higher power rates to charge the EV battery. Note that the DC fast charging does not replace AC charging; but is an effective option when urgent energy is needed, specially during long distance travels [67].

### 2.2.2 Modeling individual EV

According to Fig. 2.4, it is assumed that each individual EV is either in Driving State (DVS) or in Connecting State (CNS). The EV plugs in as soon as it finishes its trip and plugs out right before its next trip. For a grid-connected EV, based on the power flow direction, three types of connecting states can be defined,

- Charging State (CS): EV receives energy from the grid.
- Idle State (IS): EV is plugged-in but does not have any power exchange with the grid.
- Discharging State (DS): EV injects energy to the grid (Vehicle-to-Grid or V2G)

Based on the above-mentioned connecting states, the state of charge (SOC) variation of a plugged-in EV in discrete form can be described as follows [62],

$$SOC(k+1) = SOC(k) + P_{ev}(k) \cdot \Delta t / Q_{ev} \quad (2.14)$$



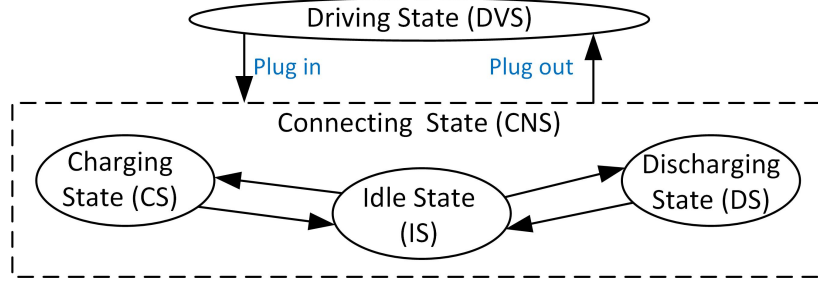


Figure 2.4 Operating states of an individual EV

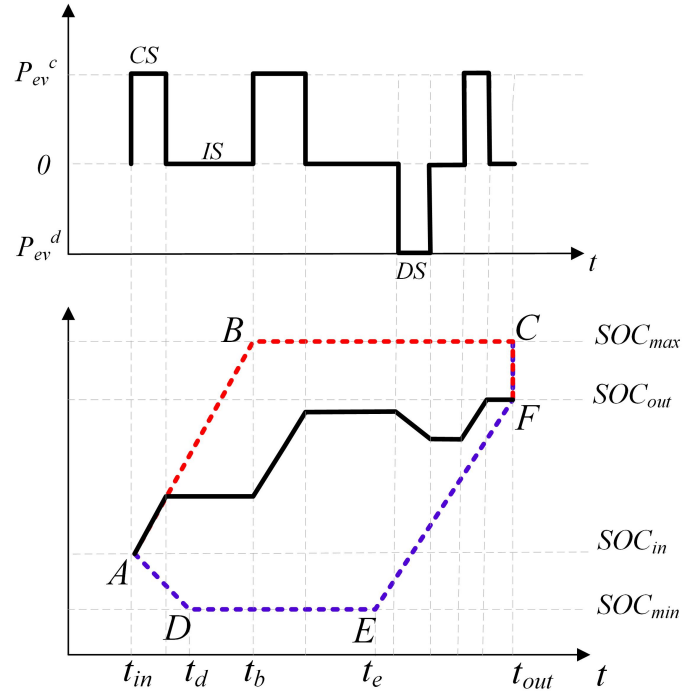


Figure 2.5 Operation area of an individual EV and its corresponding power profile

where  $k$  is the discrete time index,  $\Delta t$  is the time interval,  $Q_{ev}$  is the battery capacity and  $P_{ev}$  is the output power of the EV which can be defined as follows,

$$P_{ev}(k) = \begin{cases} P_{ev}^c \cdot \eta^c, & \text{CS: } P_{ev}^c > 0 \\ 0, & \text{IS} \\ P_{ev}^d / \eta^d, & \text{DS: } P_{ev}^d < 0 \end{cases} \quad (2.15)$$

where  $P_{ev}^c$  and  $P_{ev}^d$  are charging and discharging powers, respectively. Charging and discharging efficiencies are denoted by  $\eta^c$  and  $\eta^d$ , respectively.

For each individual plugged-in EV, the operation area can be defined as shown in Fig. 2.5 [68]. For simplicity, it is assumed that charging and discharging powers are equal to the rated power of the EV ( $P_{ev}^c = -P_{ev}^d = P_{ev}^{rate}$ ).  $t_{in}$  and  $t_{out}$  represent the plug-in and plug-out times, respectively. The initial and desired SOC values are shown by  $SOC_{in}$  and  $SOC_{out}$  while  $SOC_{min}$  and  $SOC_{max}$  represent the minimum and maximum allowable SOC values, respectively. The operation area is limited by the upper boundary defined by ‘A-B-C’ path, where the EV is charged with the rated charging power  $P_{ev}^c = P_{ev}^{rate}$  right after plugging into the power grid until  $SOC_{max}$  is achieved at time  $t_b$ . Then, the EV will switch to IS and remain idle until the plug-out time. The lower boundary is given by ‘A-D-E-F’ path, where the EV is discharged with the rated discharging power  $P_{ev}^d = -P_{ev}^{rate}$  right after plugging into the power grid until the SOC value drops to  $SOC_{min}$  at  $t_d$ . Then, it will switch to IS and remains idle until  $t_e$ . At time  $t_e$ , the EV will be forced to charge with the maximum possible charging rate in order to guarantee the desired SOC value of the EV when plugging out. This state is known as the forced-charging state and is shown by ‘E-F’ path in Fig. 2.5.

### 2.2.3 EV aggregation models

In Section 1.1, the flexibility potential of the EVs and the need for an efficient EV aggregator (EVA) have been emphasized. In this section, different EVA models will be studied and categorized according to their communication structure. The structure of an EVA model is closely related to the desired ancillary service. The examples are peak load shaving [69–73] and frequency regulation [74–78] services. Some studies have also considered the potential of aggregated EV for supporting the integration of wind and solar powers [79–81].

Generally, the EVA models are characterized by centralized or distributed structures. As discussed in Section 1.2, centralized structures are known to have better accuracy and controllability since all decisions are made only at one central location. In the existing literature, a number of centralized EVA models have been developed. The droop control method is used in [82] to control the charging and discharging power of EVs according to an individually broadcasted control signal. In [68], the EV charging and discharging processes are constrained by a laxity-SOC based heuristic smart charging strategy. Authors in [74] have proposed a queuing network to estimate the regulation capacity of the EVA for up and down regulations. A leader-follower game is proposed in [83], for the individual EVs and the EVA to determine optimal day-ahead frequency reserve scheduling. A scenario-based stochastic linear programming model is developed in [84] for EV charging scheduling (EVCS) using a rolling window approach.

Although centralized structure can be easily implemented, the communication and computation requirement for data measuring and processing, and control signal dispatching is very large, specially when dealing with a large population of EVs. In order to overcome this drawback, authors in [62, 64] have developed a centralized EVA based on the State Space Model (SSM). The SSM categorizes the EVs based on their operating states, describes their transition between different states and estimates the regulation capacity of the EVs. The proposed model improves the computational and communicational efficiencies of the centralized EVA [14]. The SSM for EV aggregation is further explained in Section 2.2.4.

Alternatively, distributed structures can be used to overcome the higher computational cost and communication burden of the centralized approaches [69, 85–89]. By adopting this approach, the main problem is decomposed into several sub-problems and distributed over several agents (e.g., DSO, EVA, and EVs) with some possible coupling in the constraints or/and objective functions. These small-scale sub-problems are solved simultaneously but independently by each agent through a distributed and iterative procedure. Depending on the configuration of the communication network, distributed approaches are divided into the bilayer and trilayer structures. The former consists of either EVA and EVs or DSO and EVAs while the latter includes all participating agents (e.g EVs, EVAs and DSO).

Considering the bilayer structure, authors in [90] have utilized a gradient projection algorithm to obtain the optimal charging profile of electric vehicles (EVs) for valley filling. A consensus-based primal-dual perturbation algorithm has been proposed in [91] which is applicable for EV charging coordination. In [92], a regularized primal-dual sub-gradient (RPDS) algorithm has been developed to solve a multi-agent optimization problem with coupled objectives and constraints. However, while the RPDS algorithm shows excellent convergence performance, it still has significant relative errors for optimal solutions. To improve on this, a novel shrunken primal-dual subgradient (SPDS) algorithm was introduced in [93]. The SPDS algorithm significantly reduced convergence errors by eliminating the need for regularization. A bilayer distributed structure has been established in [94] by using the lexicographic ordering method to transform the centralized formulation into two optimization phases. However, the two phases are solved sequentially (not in parallel), making practical implementation difficult. More recently, the alternating direction method of multipliers (ADMM) has gained attention due to its fast convergence, reasonable precision, and decomposability. In [89], the ADMM was used to solve the bilayer optimization problem, where the objectives were valley filling for EVA and charging cost minimization for EVs. Furthermore, a bilayer online ADMM has been proposed in [95], which is suitable for optimization problems with time-varying objectives and constraint sets. The bilayer ADMM formulation for the EV aggregation is further explained in section 2.2.5.

Considering the trilayer structure, in [96], an ADMM-based aggregation model has been developed to maximize the comfort of electric vehicle (EV) users. However, the optimization objectives for EVA and DSO layers are missing. In [97], a trilayer robust structure has been introduced to coordinate the DSO and EVAs and minimize the total operating cost of the system. Although effective in reducing operating costs, the model's inflexibility stems from the strict assumption on the DSO's objective function and its disregard of the EVAs' objective function. This issue has been addressed in [98] by incorporating the objectives and constraints of all agents. However, the method proposed in [98] has a significant communication load and a slow convergence rate. The trilayer structures proposed in [99–101] consist of two bilayer iterative procedures linked together hierarchically. However, these frameworks are slow and computationally inefficient due to the use of nested-loop hierarchical structures. As a remedy, the authors in [102] have proposed a hierarchical trilayer ADMM that solves the local optimization problems of all agents simultaneously in a single iterative loop. Nevertheless, this framework does not consider the distribution network model and power flow constraints.

#### 2.2.4 State Space Model for EV aggregation

The EV State Space Model is a centralized aggregation model which is characterized by high accuracy and computational efficiency but low real-time communication requirement [64]. The SSM distributes EVs into several state bins according to their SOC value and switching states and then controls the evolution of EVs between different state bins. Therefore, the computational burden only depends on the number of state bins rather than the size of the EV population.

In order to build the EV SSM structure, as shown in Fig. 2.6, the SOC range of EVs  $[SOC_{min}, SOC_{max}]$  is first divided into  $N_s$  equally spaced SOC intervals. Considering different switching states (i.e., CS, IS, and DS), each SOC interval is then divided into three state bins. At any moment, the state distribution of EVs can be defined by a state vector whose dimension is  $N_b = 3N_s$ . The structure of state vector  $\mathbf{x}(t)$  is given as follows:

$$\mathbf{x}(t) = [x_1(t), x_2(t), \dots, x_{N_s}(t), x_{N_s+1}(t), \dots, x_{2N_s}(t), x_{2N_s+1}(t), \dots, x_{3N_s}(t)]^T \quad (2.16)$$

where  $x_i(t)$  is the proportion of the EVs in the  $i$ th state bin at time  $t$ .

For an uncontrolled population of EVs, in discrete time setting, their state transition can be formulated as,

$$\mathbf{x}(k+1) = \mathbf{A}\mathbf{x}(k) \quad (2.17)$$

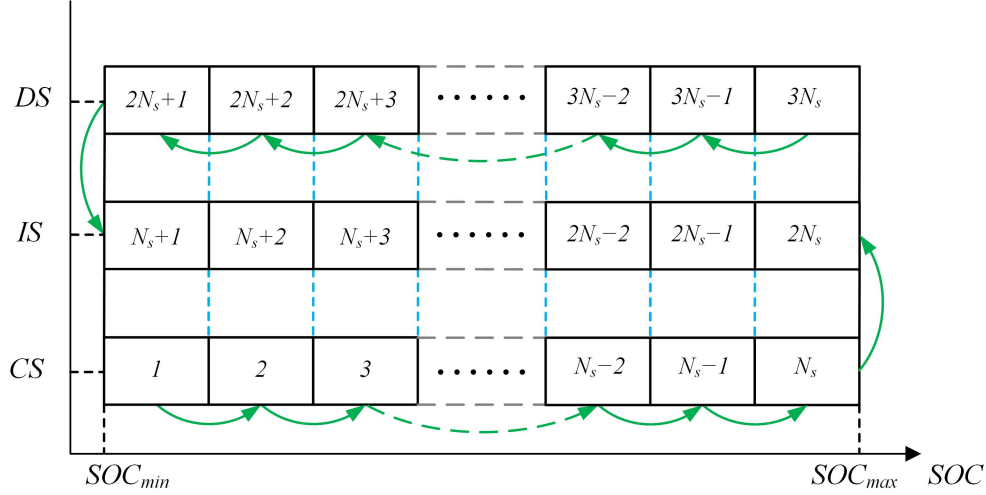


Figure 2.6 The SSM structure for EVs

where  $\mathbf{A}$  is a  $3N_s \times 3N_s$  Markov Transition Matrix (MTM) whose elements are the transition probability of the EVs between two neighboring state bins. The transition matrix  $\mathbf{A}$  can be obtained analytically by knowing the distributions of characteristic parameters (i.e.  $P_{ev}$  and  $Q_{ev}$ ). These parameters are different for each EV; however, their distributions can be statistically obtained from historical EV data. Alternatively, the matrix  $\mathbf{A}$  can be estimated by observing the real or simulated state information of all or a group of EVs without knowing the details of their characteristic parameters. Section 2.2.4 presents both analytical and estimation techniques for obtaining the state transition matrix.

Note that the state transition formulation presented by (2.17) does not consider the effect of control signals. However, a certain number of EVs who are participating in DR programs will receive a control signal from the aggregator changing their switching states and consequently their distribution in the state bins. The control signal may switch the EVs: (a) from CS to IS (CS→IS), (b) from IS to DS (IS→DS), (c) from DS to IS (DS→IS) or (d) from IS to CS (IS→CS). In order to include the effect of controlled switching, the SSM in (2.17) can be modified as follows:

$$\mathbf{x}(k+1) = \mathbf{A}\mathbf{x}(k) + \mathbf{B}\mathbf{u}(k) + \mathbf{C}\mathbf{v}(k) \quad (2.18)$$

where  $\mathbf{u}$  and  $\mathbf{v}$  are  $N_s \times 1$  input vectors which represent the effect of the controlled switching. The positive and the negative elements of  $\mathbf{u}$  denote the fraction of EVs in the corresponding SOC intervals which are about to take (CS→IS) and (IS→CS) switching actions, respectively. Likewise, the positive and the negative elements of  $\mathbf{v}$  refer to the fraction of EVs in the corresponding SOC intervals that will take (IS→DS) and (DS→IS) switching actions,

respectively.  $\mathbf{B}$  and  $\mathbf{C}$  are constant input matrices that are structured in a way that realizes the control action of the input vectors. These constant matrices are defined as follows:

$$\mathbf{B} = \begin{bmatrix} -\mathbf{I}_{N_s \times N_s} & \mathbf{I}_{N_s \times N_s} & \mathbf{O}_{N_s \times N_s} \end{bmatrix}^T \quad (2.19a)$$

$$\mathbf{C} = \begin{bmatrix} \mathbf{O}_{N_s \times N_s} & -\mathbf{I}_{N_s \times N_s} & \mathbf{I}_{N_s \times N_s} \end{bmatrix}^T \quad (2.19b)$$

The aggregated power of the EVs at the  $k$ th time step is denoted by  $y(k)$  and given by,

$$y(k) = \mathbf{D}\mathbf{x}(k) \quad (2.20a)$$

$$\mathbf{D} = P_{mean}N_{ev} \begin{bmatrix} -\mathbf{1}_{1 \times N_s} & \mathbf{O}_{1 \times N_s} & \mathbf{1}_{1 \times N_s} \end{bmatrix} \quad (2.20b)$$

where  $P_{mean}$  is the mean value of the power consumption of EVs,  $N_{ev}$  is the number of EVs in the aggregator [64]. Note that in this formulation, the power flow direction from the grid to EVs (charging) is represented as a negative value while the opposite (discharging) is considered as a positive value.

### Dynamic traveling behavior of EVs

In addition to control signals, the state distribution of EVs,  $\mathbf{x}$ , is also affected by the dynamic traveling behavior of EV users, specifically, the dynamic plug-in and plug-out events during the control horizon. At each time step, the variation of  $\mathbf{x}$  is calculated as follows [64]:

$$\Delta\mathbf{x}(k) = \frac{N_{in}(k)\mathbf{x}_{in}(k) - N_{out}(k)\mathbf{x}_{out}(k)}{N_{ev}(k) + N_{in}(k) - N_{out}(k)} \quad (2.21)$$

where  $N_{in}(k)$  and  $N_{out}(k)$  are the number of EVs plugged in and out during the  $k$ th time step, respectively.  $\mathbf{x}_{in} \in \mathbb{R}^{3N_s \times 1}$  is a state vector representing the state distribution of plugged-in EVs with  $\mathbf{x}_{out} \in \mathbb{R}^{3N_s \times 1}$  being a state vector representing the state distribution of plugged-out EVs during the  $k$ th time interval. Note that  $\mathbf{x}_{in}$  and  $\mathbf{x}_{out}$  are calculated in the same way as state vector  $\mathbf{x}$ , while only plugged-in and plugged-out EVs are taken into account and distributed among the state bins based on their SOC values and switch states. Considering the state distribution variation,  $\Delta\mathbf{x} \in \mathbb{R}^{3N_s \times 1}$ , (2.18) can be corrected as follows:

$$\mathbf{x}(k+1) = \mathbf{A}\mathbf{x}(k) + \mathbf{B}\mathbf{u}(k) + \mathbf{C}\mathbf{v}(k) + \Delta\mathbf{x}(k) \quad (2.22)$$

Finally, in order to account for the proportion of EVs in the forced-charging state described by ‘E-F’ path in Fig. 2.5, an extra element is added to the state distribution matrix ( $x_{3N_s+1}$ ). Matrix  $\mathbf{A}$  and  $\mathbf{D}$  are corrected accordingly,

$$A_{3N_s+1,3N_s+1} = 1 \quad (2.23a)$$

$$D_{3N_s+1} = P_{mean}N_{ev}[-1] \quad (2.23b)$$

Note that the EVs in the forced-charging state are uncontrollable and have no regulation capacity.

### Derivation of the transition matrix

As discussed in the previous section, the state transition matrix  $\mathbf{A}$  can be derived using either analytical or estimation methods as explained below.

**Analytical method:** In this method, it is assumed that the probability distribution functions of the characteristic parameters (i.e.,  $P_{ev}$  and  $Q_{ev}$ ) are known [64]. Let  $P(S_y | S_x)$  be the transition probability of EVs from SOC value  $S_x$  to SOC value  $S_y$ . For the EVs in CS and DS states, the transition probability is closely related to the characteristic parameters,

$$P(S_y | S_x) = p(\Delta S) = f(P_{ev}, Q_{ev}) \quad (2.24)$$

where  $\Delta S$  is the SOC variations of EVs during one time step and  $f(P_{ev}, Q_{ev})$  is the joint probability density function of parameters  $P_{ev}$  and  $Q_{ev}$ . Therefore, the transition probability of EVs from  $S_x$  to the  $n$ th state interval  $[S_n, S_{n+1})$  can be described by,

$$P(S_n \leq S_y < S_{n+1} | S_x) = \int_{S_n-S_x}^{S_{n+1}-S_x} p(\Delta S).d\Delta S, \quad n \in \{1, 2, \dots, N_s\} \quad (2.25)$$

As the EVs are considered to be uniformly distributed in each state interval, the transition probability of EVs from state interval  $m$  to  $n$  is calculated as below,

$$P(S_n \leq S_y < S_{n+1} | S_m \leq S_x < S_{m+1}) = A_{mn} = \int_{S_m}^{S_{m+1}} \int_{S_n-S_x}^{S_{n+1}-S_x} p(\Delta S).d\Delta S.dS_x, \quad (2.26)$$

$$n, m \in \{1, 2, \dots, N_s\}$$

This transition probability is denoted by  $A_{mn}$  and is equal to the element  $(m, n)$  of the state transition matrix  $\mathbf{A}$ . Note that for the EVs in the idle state (IS), the state transition probability is equal to zero [64].

**Estimation method:** Alternatively, the state transition matrix  $\mathbf{A}$  can be derived using the estimation method. To this aim, the Hidden Markov Model (HMM) toolbox of MATLAB can be employed to estimate the transition probabilities using a number of simulated or measured SOC sequences of the EVs [103]. The estimation accuracy of this method depends on the number of measured historical points of the state information.

### 2.2.5 Alternating Direction Method of Multipliers for EV aggregation

ADMM is a hierarchical multi-agent distributed algorithm that decomposes the large-scale convex optimization problem into smaller sub-problems, which are solved independently by each agent. This method converges to the optimal solution through the iterative exchange of incentive signals between the higher-level (e.g., EVA) and lower-level (e.g., EVs) agents [7]. Conventional ADMM provides privacy and security features while ensuring the convergence.

The general formulation of a bilayer ADMM for solving the EV aggregation optimization problem is presented in this section [89]. Considering a fixed number of EVs,  $i \in \{1, \dots, N_{ev}\}$ , the power profile of each EV can be defined by a vector,  $\mathbf{p}_i = [p_i(1), \dots, p_i(T)]^T$ , over the optimization time horizon,  $t \in \{1, \dots, T\}$ . The aggregated power profile of the EVs is also defined as a separate vector,  $\mathbf{p}_{eva} = [p_{eva}(1), \dots, p_{eva}(T)]^T$ . It is assumed that the positive elements of these vectors represent the energy consumption (i.e., charging) while the negative elements stand for feeding the energy back to the grid (i.e., V2G discharging).

Accordingly, the joint optimization problem of the EV aggregator (EVA) and the EVs is defined as follows:

$$\begin{aligned}
 & \underset{\mathbf{p}_{eva}, \mathbf{p}_i}{\text{minimize}} && F_{eva}(\mathbf{p}_{eva}) + \gamma \sum_{i=1}^{N_{ev}} F_i(\mathbf{p}_i) \\
 & \text{s.t.} && \mathbf{p}_{eva} = \sum_{i=1}^{N_{ev}} \mathbf{p}_i \\
 & && \mathbf{p}_{eva} \in \mathbb{P}_{eva} \\
 & && \mathbf{p}_i \in \mathbb{P}_i, \quad i \in \{1, \dots, N_{ev}\}
 \end{aligned} \tag{2.27}$$

where  $F_{eva}$  and  $\mathbb{P}_{eva}$  are the objective function and the constraint set of the EVA; and  $F_i$  and  $\mathbb{P}_i$  are the objective function and the constraint set of the EVs, respectively.  $\gamma$  is a scalar parameter that represents the trade-off between the global objective of the EVA and the local objective of the EVs.



According to (2.27), the aggregated power profile of the EVs is equal to the sum of all individual EV power profiles. Therefore, all individual optimization problems are coupled, and (2.27) can be reformulated as an *exchange* optimization problem [19]. To this aim, the EVA is redefined as agent 0 with the following power profile and objective function:

$$\mathbf{p}_0 = -\mathbf{p}_{eva} \quad (2.28a)$$

$$f_0(\mathbf{p}_0) = \begin{cases} F_{eva}(-\mathbf{p}_0), & \text{if } -\mathbf{p}_0 \in \mathbb{P}_{eva} \\ \infty, & \text{otherwise} \end{cases} \quad (2.28b)$$

The EVs are defined as agents  $i \in \{1, \dots, N_{ev}\}$  with the following objective functions:

$$f_i(\mathbf{p}_i) = \begin{cases} \gamma F_i(\mathbf{p}_i), & \text{if } \mathbf{p}_i \in \mathbb{P}_i \\ \infty, & \text{otherwise} \end{cases} \quad (2.29)$$

Therefore, the *exchange* form of the EV aggregation optimization problem is cast in the following form:

$$\begin{aligned} & \underset{\mathbf{p}_i}{\text{minimize}} && \sum_{i=0}^{N_{ev}} f_i(\mathbf{p}_i) \\ & \text{s.t.} && \sum_{i=0}^{N_{ev}} \mathbf{p}_i = 0 \end{aligned} \quad (2.30)$$

The *exchange* problem in (2.30) is equal to the original formulation of the EV aggregation problem in (2.27) and can be distributed between the EVA and the EVs using the ADMM formulation presented in the following way [89]:

1. For each EV  $i \in \{1, \dots, N_{ev}\}$ :

$$\begin{aligned} \mathbf{p}_i^{k+1} &:= \underset{\mathbf{p}_i}{\text{argmin}} \left( \gamma F_i(\mathbf{p}_i) + \frac{\rho}{2} \|\mathbf{p}_i - \mathbf{p}_i^k + \bar{\mathbf{p}}^k + \mathbf{u}^k\|_2^2 \right) \\ \text{s.t.} \quad & \mathbf{p}_i \in \mathbb{P}_i \end{aligned} \quad (2.31)$$

**Algorithm 1:** Bilayer ADMM algorithm

```

 $k \leftarrow 1$ ;
 $stop \leftarrow 0$ ;
while  $stop == 0$  do
  for  $i = 1 : N_{ev}$  do in parallel
    Calculate  $\mathbf{p}_i^{k+1}$  by (2.31) and send it to the EVA
  end
  Calculate  $\mathbf{p}_0^{k+1}$  by (2.32)
  Update  $\bar{\mathbf{p}}^{k+1}$  and  $\mathbf{u}^{k+1}$  by (2.33) and send it to all EVs
  Update primal and dual residuals by (2.34)
  if (2.35) is True then
     $stop \leftarrow 1$ ;
  end
   $k \leftarrow k + 1$ ;
end

```

2. For the EVA:

$$\begin{aligned}
 \mathbf{p}_0^{k+1} &:= \underset{\mathbf{p}_0}{\operatorname{argmin}} \left( F_{eva}(-\mathbf{p}_0) + \frac{\rho}{2} \|\mathbf{p}_0 - \mathbf{p}_0^k + \bar{\mathbf{p}}^k + \mathbf{u}^k\|_2^2 \right) \\
 \text{s.t.} \quad & -\mathbf{p}_0 \in \mathbb{P}_{eva}
 \end{aligned} \tag{2.32}$$

3. Incentive signal update by the EVA:

$$\mathbf{u}^{k+1} = \mathbf{u}^k + \bar{\mathbf{p}}^{k+1} \tag{2.33a}$$

$$\bar{\mathbf{p}}^{k+1} = \frac{1}{N_{ev} + 1} \sum_{i=0}^{N_{ev}} \mathbf{p}_i^{k+1} \tag{2.33b}$$

where  $k$  is the index of iteration,  $\rho$  is the augmented Lagrangian parameter (penalty parameter),  $\mathbf{u}^k$  denotes the scaled vector of the Lagrangian variable, and  $\bar{\mathbf{p}}$  is the average power profile of all agents. The detailed process of obtaining the ADMM solution is presented in Appendix A.

Using the ADMM algorithm, the original large-scale optimization problem in (2.27) is distributed between the EVA and the EVs. These small-scale sub-problems are solved independently by each agent in an iterative loop. The whole procedure of the bilayer ADMM is summarized in Algorithm 1. At each iteration  $k$ , (2.31) is solved by all EVs in parallel and the results are sent to the EVA. Next, the EVA solves (2.32) and updates  $\bar{\mathbf{p}}^{k+1}$  and  $\mathbf{u}^{k+1}$  by

(2.33) based on the received information from the EVs. The updated incentive signal is then sent back to all EVs. This iterative procedure between the EVA and the EVs continues until the ADMM converges to an optimal solution.

**Convergence criteria:** The convergence criteria of the ADMM can be determined based on the primal residual,  $\mathbf{r}$ , and the dual residual,  $\mathbf{s}_i$ , defined by (2.34) [19]. These two residuals converge to zero as ADMM proceeds.

$$\mathbf{r}^k = \bar{\mathbf{p}}^k \quad (2.34a)$$

$$\mathbf{s}_i^k = -\rho(N_{ev} + 1)(\mathbf{p}_i^k - \mathbf{p}_i^{k-1} + (\bar{\mathbf{p}}^{k-1} - \bar{\mathbf{p}}^k)) \quad (2.34b)$$

with  $\mathbf{s}^k = [\mathbf{s}_1^k, \dots, \mathbf{s}_{N_{ev}}^k]$  the stopping criteria are:

$$\|\mathbf{r}^k\|_2^2 \leq \epsilon_{pri} \quad (2.35a)$$

$$\|\mathbf{s}^k\|_2^2 \leq \epsilon_{dual} \quad (2.35b)$$

where  $\epsilon_{pri}$  and  $\epsilon_{dual}$  are the feasibility tolerances. Note that the primal residual reflects the mismatch of the coupling variables at each iteration while the dual residual describes the stability of the iterations. The detailed process of calculating the primal and dual residuals is presented in Appendix A.

Note that the ADMM converges to the optimal solution only if both cost functions and constraint sets of all agents are convex [19]. Therefore, the optimization problems of the EVA and the EVs must be properly formulated in order to accurately represent the real world behavior while being feasible and convex. In the following sections, some examples of the convex formulation of the EVA and EV optimization problems are presented.

### Convex formulation of the EVA optimization problem

The optimization problem of the EVA is defined based on the desired ancillary service or the global aggregation goal. Without the loss of generality, here we study the convex formulation of two commonly used EVA goals.

**1- Valley filling** Valley filling aims at filling the valleys of the fixed load demand using the aggregated power of the EVs in order to avoid new peaks in the power consumption curve. Therefore, the convex optimization problem of the EVA can be described as follows [102],

$$F_{eva} = \|\overline{\mathbf{p}_{unc}} - \mathbf{p}_{unc} - \mathbf{p}_{eva}\|_2^2 \quad (2.36a)$$

$$\text{s.t. } \underline{\mathbf{p}}_{eva} \leq \mathbf{p}_{eva} \leq \overline{\mathbf{p}}_{eva} \quad (2.36b)$$

where  $\mathbf{p}_{unc}$  is uncontrollable fixed load demand and  $\overline{\mathbf{p}_{unc}} = \frac{1}{T} \sum_{t=t_0}^{t_0+T-1} p_{unc}(t)$  is the temporal average of the uncontrollable load demand.  $\underline{\mathbf{p}}_{eva}$  and  $\overline{\mathbf{p}}_{eva}$  are respectively the minimum and maximum allowable power of the EVA during the optimization horizon.

**2- Cost minimization** The goal of EVA-level cost minimization is to optimize the charging behavior of the EVs in order to achieve the lowest total charging cost for the whole EV fleet [104]. Accordingly, the convex optimization problem of the EVA is described as follows [102]:

$$F_{eva} = \boldsymbol{\Omega}^T \mathbf{p}_{eva} \quad (2.37a)$$

$$\text{s.t. } \underline{\mathbf{p}}_{eva} \leq \mathbf{p}_{eva} \leq \overline{\mathbf{p}}_{eva} \quad (2.37b)$$

where  $\boldsymbol{\Omega}$  is the wholesale electricity price.

### Convex formulation of the EV optimization problem

The optimization problem of the EV is defined based on the desired individual goal, power limits, battery capacity limits, and the amount of energy required for personal mobility. Without losing any generality, here we assume that the EV's individual goal is to minimize the battery depreciation cost. This can be modeled using a quadratic cost function to reduce the number of switching actions between charging and discharging states. The battery capacity limits and the EV energy need can be defined using a series of inequality constraints that only depend on the EV's power profile ( $\mathbf{p}_i$ ) during the optimization horizon [89, 105]. Accordingly, the convex optimization problem of the  $i$ th EV reads [106],


	 <div> <div>1</div> <div>Connected</div> </div> <div> <div>0</div> <div>Not connected</div> </div>
Time slot	$\mathbf{t} = \begin{bmatrix} 1 & 2 & 3 & 4 & 5 & 6 & 7 & 8 & 9 & 10 & 11 & 12 \end{bmatrix}$
Connection matrix	$\mathbf{A} = \begin{bmatrix} 1 & 1 & 1 & 0 & 0 & 0 & 0 & 0 & 0 & 0 & 1 & 1 \end{bmatrix}$ $E_{req} = \underbrace{E_1}_{\text{slots 1-3}} + \underbrace{E_2}_{\text{slots 11-12}}$
Energy requirement	$\underline{\mathbf{R}} = \bar{\mathbf{R}} = \frac{1}{\eta \Delta t} E_{req}$
Input Matrix	$\mathbf{B} = \begin{bmatrix} 0 & 0 & 0 & 0 & 0 & 0 & 0 & 0 & 0 & 0 & 1 & 0 \\ 0 & 0 & 0 & 0 & 0 & 0 & 0 & 0 & 0 & 0 & 1 & 1 \\ 1 & 0 & 0 & 0 & 0 & 0 & 0 & 0 & 0 & 0 & 1 & 1 \\ 1 & 1 & 0 & 0 & 0 & 0 & 0 & 0 & 0 & 0 & 1 & 1 \\ 1 & 1 & 1 & 0 & 0 & 0 & 0 & 0 & 0 & 0 & 1 & 1 \end{bmatrix} \quad T_c=5$
Battery capacity limits	$\underline{\mathbf{S}} = \frac{1}{\eta \Delta t} \begin{bmatrix} E_{req} - E_{bat} \\ E_{req} - E_{bat} \\ E_{req} - E_{bat} \\ E_{req} - E_{bat} \\ E_{req} - E_{bat} \end{bmatrix}, \quad \bar{\mathbf{S}} = \frac{1}{\eta \Delta t} \begin{bmatrix} E_{req} \\ E_{req} \\ E_{req} \\ E_{req} \\ E_{req} \end{bmatrix}$

Figure 2.7 The definition of the constraint matrices

$$F_i = \alpha_i \|\mathbf{p}_i\|_2^2 \quad (2.38a)$$

$$\text{s.t. } \underline{\mathbf{p}}_i \leq \mathbf{p}_i \leq \bar{\mathbf{p}}_i \quad (2.38b)$$

$$\underline{\mathbf{R}}_i \leq \mathbf{A}_i \mathbf{p}_i \leq \bar{\mathbf{R}}_i \quad (2.38c)$$

$$\underline{\mathbf{S}}_i \leq \mathbf{B}_i \mathbf{p}_i \leq \bar{\mathbf{S}}_i \quad (2.38d)$$

where  $\alpha_i$  is the battery depreciation parameter.

The first set of constraints, (2.38b), defines the EV power limits during the optimization horizon. For a connected EV, its charging power is constrained by its upper,  $\bar{\mathbf{p}}_i$ , and lower,  $\underline{\mathbf{p}}_i$ , limits. If the EV is not connected,  $\bar{\mathbf{p}}_i = \underline{\mathbf{p}}_i = 0$ . The second set of constraints, (2.38c), defines the energy requirement of the EV during each connection session. Finally, the last set of constraints, (2.38d), represents the EV battery capacity limits for each individual time

slot during each connection session. The definition of  $\mathbf{A}_i$ ,  $\underline{\mathbf{R}}_i$ ,  $\overline{\mathbf{R}}_i$ ,  $\mathbf{B}_i$ ,  $\underline{\mathbf{S}}_i$  and  $\overline{\mathbf{S}}_i$  depends on the charging strategy and the driving behavior of the EVs. Therefore, in the remainder of this section, the following assumptions are made:

- The EV plugs into the charger at the arrival time and stays connected until departure time. During the connection session, the EV is able to be in charging, discharging (V2G), or idle states.
- The arrival time, departure time and consequently the connecting session of each EV are known.
- The required amount of energy ( $E_{req}$ ) for the connecting session is known. This is the difference between EV's desired energy level and its initial energy level when plugging in.

Based on these assumptions, the definition of the constraint matrices is presented in Fig. 2.7. Note that  $T_c$  is the total number of time slots that the EV is connected to the grid during the entire optimization horizon while  $E_{bat}$  is the effective energy capacity of the EV battery.

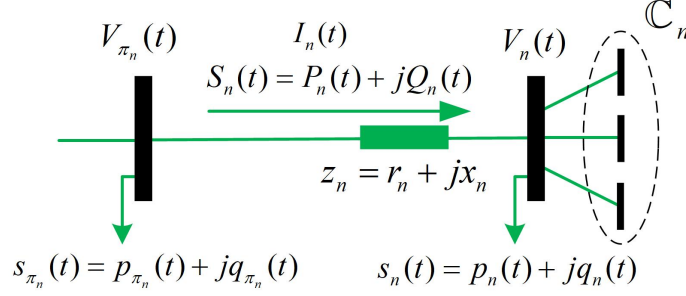


Figure 2.8 Distribution line power flow model (DistFlow)

### 2.3 Distribution network model

In order to achieve both optimal control of EV charging demand and effective management of the power grid, some studies directly integrate the power flow constraints into the EV aggregation model as a part of a unified framework. To this aim, the power flow constraints can be modeled using the distribution line power flow model (DistFlow) [107]. DistFlow is chosen as it has been proven to be suitable for modeling radial distribution networks, which is the typical network configuration to which EVs are connected.

Consider a radial distribution network which is modeled as a directed graph  $G = (\mathbb{N}, \mathbb{L})$ , where  $\mathbb{N} := \{1, \dots, N\}$  represents the set of network buses and  $\mathbb{L} := \{1, \dots, L\}$  represents the set of network lines ( $L = N - 1$ ) [107, 108]. The substation bus is indexed by  $n = 1$  and each bus  $n \in \mathbb{N} \setminus \{1\}$  has a unique parent bus  $\pi_n$  and a set of children buses  $\mathbb{C}_n$  as shown in Fig. 2.8. At each moment  $t \in \mathbb{T} := \{1, \dots, T\}$ , for each bus  $n \in \mathbb{N}$ , its voltage and apparent power are represented by  $V_n(t)$  and  $s_n(t) = p_n(t) + jq_n(t)$ , respectively. For each line  $(\pi_n, n) \in \mathbb{L}$ , its impedance and apparent power flow are denoted by  $z_n = r_n + jx_n$  and  $S_n(t) = P_n(t) + jQ_n(t)$ , respectively. In order to simplify the equations, we use the vector notation  $\mathbf{y} := (y(t), y(t+1), \dots, y(t+T-1))$  for all time dependent variables. The power flow and current of all lines as well as the voltage of all buses are related based on the physical power grid laws, as follows:

- Ohm's law:

$$\mathbf{V}_{\pi_n} - \mathbf{V}_n = \mathbf{z}_n \mathbf{I}_n \quad (2.39)$$

- Power flow:

$$\mathbf{S}_n = \mathbf{V}_{\pi_n} \mathbf{I}_n^* \quad (2.40)$$

- Power balance:

$$\mathbf{s}_n = \mathbf{S}_n - z_n |\mathbf{I}_n|^2 - \sum_{m \in \mathbb{C}_n} \mathbf{S}_m \quad (2.41)$$

Substituting from (2.39) and (2.40) in (2.41), the classic DistFlow equations is obtained [107],

$$\mathbf{P}_n = \mathbf{p}_n + r_n \mathbf{i}_n + \sum_{m \in \mathbb{C}_n} \mathbf{P}_m \quad (2.42a)$$

$$\mathbf{Q}_n = \mathbf{q}_n + x_n \mathbf{i}_n + \sum_{m \in \mathbb{C}_n} \mathbf{Q}_m \quad (2.42b)$$

$$\mathbf{v}_{\pi_n} - \mathbf{v}_n = 2(r_n \mathbf{P}_n + x_n \mathbf{Q}_n) - (r_n^2 + x_n^2) \mathbf{i}_n \quad (2.42c)$$

$$\mathbf{v}_n \mathbf{i}_n = \mathbf{P}_n^2 + \mathbf{Q}_n^2 \quad (2.42d)$$

where  $\mathbf{i}_n = |\mathbf{I}_n|^2$  and  $\mathbf{v}_n = |\mathbf{V}_n|^2$ . For the substation bus  $n = 1$ , the voltage is assumed to be constant, while for other buses, the voltage magnitude limits are given as follows:

$$\underline{\mathbf{V}} \leq \mathbf{V}_n \leq \overline{\mathbf{V}}, \quad n \in \mathbb{N} \setminus \{1\} \quad (2.43a)$$

$$\mathbf{V}_1 = \mathbf{V}_{ref} \quad (2.43b)$$



### CHAPTER 3 COHERENCE OF THE ARTICLES IN RELATION TO THE RESEARCH GOALS

The past two chapters have covered the present challenges surrounding the development of efficient aggregation and optimization models for the integration of TCLs and EVs in the ancillary services of smart grids. It is known that the centralized aggregation models have attracted a great deal of interest due to their superior accuracy and controllability. However, their heavy communication and computation burden can be a limiting factor, specially for large-scale TCL/EV populations. Sending an individualized control signal for each TCL or EV, implies a huge communication requirement between the aggregator and the end-users. In order to address this issue, a centralized aggregation model based on the State Space Model (SSM) is proposed in this thesis. Using the proposed model, first, some real-time processes are replaced with offline processes which alleviates the amount of real-time communication and computation; and second, only one identical probabilistic control signal is broadcasted to the population of end-users (e.g., TCLs or EVs), which further helps to lower the communication burden. In the following chapters, the employment of the proposed SSM-based aggregation model to manage large population of TCLs (Chapter 4 - article 1), EVs (Chapter 5 - article 2), or a mix of both (Chapter 6 - article 3) are studied.

In Chapter 4 (article 1), the proposed SSM model is utilized to provide frequency regulation service with a population of TCLs. The required power adjustment for frequency regulation is determined based on the estimated regulation capacity of the TCL population and monitored frequency deviation. The power adjustment is then translated to an identical control signal with a simple structure which is communicated to all individual TCLs. At the user level, the switching action of each individual TCL is determined locally based on the received identical control signal. The proposed probabilistic control reduces the communication requirement between the central aggregator and the individual TCLs.

In Chapter 5 (article 2), the SSM is employed to provide frequency regulation and peak load shaving services with a large-scale EV fleet. The conventional state-bin structure is extended to include dedicated bins for the fast charging EVs. Using the proposed model, the EVs are able to provide prompt and efficient responses to severe generation-consumption imbalances with both regular and fast charging rates. Although the extended EV-SSM benefits from the increased regulation flexibility, if not properly designed, it may lead to excessive degradation of the EV batteries caused by frequent switching to fast charging or fast discharging states. Therefore, appropriate measures are taken into account to ensure that the EVs spend the bare minimum of time in those states.

In Chapter 6 (article 3), a unified SSM is developed for the joint participation of both large-scale TCLs and EVs in the frequency regulation service. The collaborative participation of TCLs and EVs increases the regulation capacity of the aggregator while reducing the excessive dependence on one type of resource. This is of great importance specially for the EV population as it avoids excessive degradation of the EV batteries by reducing the total number of switching actions. In order to perform the coordination with minimum communication burden, two distinct control signals, namely TCL-control signal and EV-control signal are constructed. The former is communicated to all individual TCLs while the latter is communicated to all individual EVs. The probabilistic control method decreases the communication burden and probability of control error caused by transmitting numerous control signals to all TCLs and EVs individually.

Although the aforementioned aggregation models are successful in improving the computation and communication efficiency of the centralized approaches, they still suffer from a variety of security issues such as vulnerability to single point failure and end-user data privacy concerns. Alternatively, distributed approaches can be used to overcome the higher computational cost and communication burden of the centralized approaches. Distributed approaches decompose the main problem into several sub-problems and distribute them over several agents (e.g., end-users, aggregators, and DSO) with some possible coupling in the constraints or/and objective functions. These small-scale sub-problems are solved simultaneously but independently by each agent through a distributed and iterative procedure. As a result, distributed strategies are not only immune to single point failure, but also preserve the privacy of end-users since they do not require the private information of users to be shared with a higher-level agent.

In Chapter 7 (article 4), an ADMM-based distributed framework for optimal charging scheduling of EVs is proposed. In order to achieve both optimal control of the EV charging demand and effective management of the power grid, the power flow constraints are modeled using the distribution line power flow model (DistFlow). The proposed framework is general in the sense that any desired local objectives and constraints can be considered for the agents (e.g., EVs, EVAs, and DSO), as long as the optimization problems remain feasible and convex. In this study, it is assumed that the EV-ADMM is employed to provide charging cost minimization at the EV level, peak load shaving at the EVA level and voltage regulation at the DSO level. Furthermore, the communication structure is modeled by a single-loop iterative algorithm where the primal variable of all agents is updated simultaneously at every iteration resulting in a reduced number of iterations and faster convergence.

## CHAPTER 4    ARTICLE 1: STATE SPACE MODEL OF AGGREGATED TCLS FOR FREQUENCY REGULATION WITH A LOW COMMUNICATION REQUIREMENT

This chapter is the reproduction of the following peer-reviewed conference paper which has been published on 2020/08/02 [109].

– S. Kiani, K. Sheshyekani, and H. Dagdougui, "State Space Model of Aggregated TCLs for Frequency Regulation with a Low Communication Requirement," *2020 IEEE Power & Energy Society General Meeting (PESGM)*, 2020, pp. 1-5, doi: 10.1109/PESGM41954.2020.9281513.

### 4.1 Abstract

This paper presents a new control structure for participation of aggregated thermostatically controlled loads (TCLs) in the frequency regulation services. The aggregation is based on the state space model (SSM) of TCLs. The proposed structure is characterized by a low communication requirement and an accurate regulation capacity estimation. The TCL control center translates the estimated regulation capacity to an identical control signal with a simple structure which is communicated to all individual TCLs. Simulation results show that the proposed control structure can accurately describe the aggregated behaviour of a large population of TCLs. The frequency regulation is realized in coordination with conventional generators.

### 4.2 Introduction

Thermostatically Controlled Loads (TCLs) account for a large portion of consumption power and are widely distributed within the electrical grid. Owing to this fact, TCLs can be regarded as excellent candidates for providing frequency regulation services. This can be done by adopting a proper controller to interrupt their local hysteresis cycle and force them to switch between ON and OFF states when required. The efficient incorporation of TCLs in the frequency regulation services requires a reliable and fast control strategy which can respond to frequency deviations within seconds to one-minute intervals [18]. Furthermore, device wear and tear, customer comfort, short cycling and real-time communication requirement are among the issues that should be properly addressed.

Different aggregated TCL models have been proposed to estimate the regulation capacity and schedule the real-time power control for individual TCLs. The bin transition modeling

technique has been proposed in many studies (e.g., [10, 13, 15, 18, 28, 58]), to describe the aggregated dynamic behaviour of a population of TCL. This modeling approach is based on the temperature and switching evolution of the TCL population. A 2-D transition model based on the second-order TCL dynamics has been proposed in [28] to describe the aggregate behaviour of a population of TCLs. A modified version of transition matrices has been proposed in [13] to take into account the uncertainties of thermal parameters, ambient temperatures, and random customer behaviour. A hierarchical control framework has been presented in [58] which allows autonomous participation of TCLs in frequency regulation through broadcasting trigger frequencies to each individual TCL separately. This approach guarantees a fast response between each control time interval. Some studies [33, 38, 58] have used a temperature-priority-based control framework in which the TCLs are sorted based on their temperatures and prioritised in a way that the number of ON/OFF switching action for each TCL is minimized.

The above-mentioned approaches require a heavy data communication among the central controller and individual TCLs which can be a limiting factor for its large-scale implementation. To reduce the communication burden, a probability control method has been proposed in [10, 18] where the central controller sends an identical probabilistic control signal to all TCLs. Each individual TCL uses the same control signal to decide whether it participates in power regulation service or not.

Within the context alluded above, this paper presents a control structure for the participation of aggregated TCLs in frequency regulation service. The aggregation is done based on the State Space Model (SSM) of TCLs. This idea has been adopted from [64] where the SSM has been used for real-time aggregation of electric vehicles (EVs). The proposed control framework accommodates both TCLs and Conventional Generators (CGs) in frequency regulation services.

### 4.3 Modeling Framework

#### 4.3.1 Individual TCL Model

The thermodynamics of an individual TCL can be modeled with a discrete time difference equation as follows [58].

$$T(k+1) = aT(k) + (1-a)(T_a(k) - m(k)T_g) + \omega(k) \quad (4.1)$$

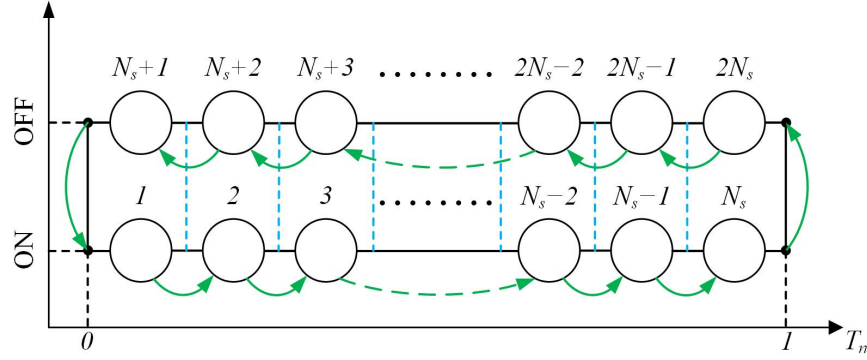


Figure 4.1 State space of aggregated TCLs

with  $a \triangleq e^{-\frac{\Delta t}{RC}}$  and  $T_g \triangleq \pm R \cdot COP \cdot P_{rate}$ , where signs - and + are used for cooling and heating devices respectively,  $T$  is the temperature of the heated/cooled zone,  $T_a$  denotes the ambient temperature,  $C$  and  $R$  are the thermal capacitance and resistance respectively,  $COP$  is the coefficient of performance,  $P_{rate}$  is the rated power of TCL,  $m$  is the switch status and  $\omega$  is the noise process. The time interval is denoted by  $\Delta t$  with  $k$  being the index of time steps.

To maintain customer comfort, the TCL is equipped with the local hysteresis temperature control which operates within a dead-band. TCL switch status  $m$  can be determined according to the following rules for heating mode:

$$m(k+1) = \begin{cases} 0, & T(k+1) \geq T_{set} + \frac{\delta_{db}}{2} : OFF \\ 1, & T(k+1) \leq T_{set} - \frac{\delta_{db}}{2} : ON \\ m(k), & otherwise \end{cases} \quad (4.2)$$

where  $T_{set}$  is the temperature reference and  $\delta_{db}$  is the dead-band width.

For TCL in cooling mode, the switch status is represented by (4.2) with opposite sign.

#### 4.3.2 State Space Model of Aggregated TCLs

To efficiently describe the dynamics of a TCL population over time, a common approach is the state-bin transition model which is simple and sufficiently accurate [15, 58]. As illustrated in Fig. 4.1, state distribution of a population of heating TCLs is described by definition of a finite number of state intervals. Since devices with different set-temperatures and dead-bands are involved, the first step is to normalize indoor temperature by  $T_n = (T - (T_{set} - 0.5\delta_{db})) / \delta_{db}$ ,  $T_n \in [0, 1]$ . The temperature dead-band is then divided into  $N_s$  equal intervals. As a TCL may be ON or OFF, each interval is divided into two state intervals. Thus, a

total of  $N_b = 2N_s$  state intervals can describe the state distribution of TCLs. At any time step, the current state-bin of a TCL can be found in the state space based on its normalized temperature ( $T_n$ ) and switch state ( $m$ ). A population of TCLs can be aggregated within the state space model (SSM) and expressed in the following form:

$$\begin{cases} \mathbf{x}(k+1) = \mathbf{A}\mathbf{x}(k) + \mathbf{B}\mathbf{u}(k) \\ y(k) = \mathbf{C}\mathbf{x}(k) \end{cases} \quad (4.3)$$

where  $\mathbf{x}$  is defined as a  $(2N_s \times 1)$  state vector, equivalent to the fraction of TCLs located in each state bin, indicating the state distribution of TCLs.  $\mathbf{u}$  is a  $(N_s \times 1)$  input vector which is used for updating the state vector  $\mathbf{x}$  at the end of each time interval.  $\mathbf{A}$  is a  $(2N_s \times 2N_s)$  transposed Markov transition matrix (MTM) which describes the transition probability of TCLs from one bin to another; and  $y$  is a  $(1 \times 1)$  output vector describing the output power of aggregated TCLs.  $\mathbf{B}$  is a  $(2N_s \times N_s)$  constant matrix and structured in a way to realize the control action of input vectors described above.  $\mathbf{C}$  is a  $(1 \times 2N_s)$  constant matrix and is used to obtain the output power of aggregated TCLs and structured as follows.

$$\begin{cases} \mathbf{B} = \begin{bmatrix} -\mathbf{I}_{N_s \times N_s} & \mathbf{I}_{N_s \times N_s} \end{bmatrix}^T \\ \mathbf{C} = P_{avg} N_{tcl} \begin{bmatrix} -\mathbf{1}_{1 \times N_s} & \mathbf{0}_{1 \times N_s} \end{bmatrix} \end{cases} \quad (4.4)$$

where  $P_{avg}$  is the average power consumption of the TCLs and  $N_{tcl}$  is the number of the TCLs in the aggregator.

In this study, according to [58] and [15], the matrix  $\mathbf{A}$  is generated offline from sequence of TCLs' past 500 states using the Hidden Markov Model (HMM) toolbox of MATLAB (*hmmestimate* function). Using identified matrix  $\mathbf{A}$ , the SSM predicts the state transition of aggregated TCLs within time interval  $T_f = 30s$  [58]. To increase the prediction accuracy, the SSM is updated with measured temperatures and switch status at each control sampling time ( $T_s = N_f T_f$ ) that is relatively long and is set to 2 minutes in this work. This "collect-and-correct" procedure results in significantly reduced communication requirement and accurate temperature forecasts [110].

Based on the SSM of aggregated TCLs, the TCLs' regulation capacity for both responding modes is given by (4.5).

$$\begin{cases} \Delta P_{tcl,l}(k) = \mathbf{C}_u \mathbf{x}(k) \\ \Delta P_{tcl,h}(k) = \mathbf{C}_l \mathbf{x}(k) \end{cases} \quad (4.5)$$

where  $\Delta P_{tcl,l}$  and  $\Delta P_{tcl,h}$  indicate the regulation capacity of responding modes ON→OFF and OFF→ON, respectively; and  $\mathbf{C}_u$  and  $\mathbf{C}_l$  are the constant matrices as given by (4.6).

$$\begin{cases} \mathbf{C}_u = P_{avg} N_{tcl} \begin{bmatrix} 0 & \mathbf{1}_{1 \times N_s - 2} & 0, & \mathbf{0}_{1 \times N_s} \end{bmatrix} \\ \mathbf{C}_l = P_{avg} N_{tcl} \begin{bmatrix} \mathbf{0}_{1 \times N_s}, & 0 & -\mathbf{1}_{1 \times N_s - 2} & 0 \end{bmatrix} \end{cases} \quad (4.6)$$

As the TCLs located at the bins near the edge of temperature dead-band have recently been switched by their hysteresis temperature control, they should not be switched again by the frequency regulation command. Thus, by setting  $\mathbf{C}_{u,1}$ ,  $\mathbf{C}_{u,N_s}$ ,  $\mathbf{C}_{l,N_s+1}$  and  $\mathbf{C}_{l,2N_s}$  to the zero, the short cycling of TCLs' compressor can be avoided.

Finally, the upper and lower boundaries of the output power of aggregated TCLs are obtained by (4.7).

$$\begin{cases} P_{tcl,u}(k) = y(k) + \Delta P_{tcl,l}(k) \\ P_{tcl,l}(k) = y(k) + \Delta P_{tcl,h}(k) \end{cases} \quad (4.7)$$

Theoretically, more bins can lead to a more precise estimation of regulation capacities, at the expense of more measurement accuracy [58,64]. In this study,  $N_s = 20$  is selected for the frequency regulation.

## 4.4 Frequency Regulation

### 4.4.1 Framework of Frequency Regulation with SSM

The framework of frequency regulation with SSM of aggregated TCLs is shown in Fig. 4.2. The SSM is built every  $T_f$  period and updated with measured data at each control sampling time  $T_s$ . The TCL control center calculates  $\mathbf{u}$  based on dispatch signals, which are derived from the power system control center where frequency deviation is monitored. Then  $\mathbf{u}$  is translated into the identical control signal  $\mathbf{u}_s$  and transmitted to all TCLs globally as introduced in Subsection 4.4.3.

### 4.4.2 Frequency Regulation with State Space Model

Neglecting local frequency differences caused by electromechanical transients and oscillations, the system is naturally governed by the physics of motion where frequency deviations are mainly caused by generation-consumption power imbalances [64] as given by (4.8).

$$\Delta P_g(t) + \Delta P_{tcl}(t) - \Delta P_d(t) = 2H \cdot d\Delta f(t)/dt + D \cdot \Delta f(t) \quad (4.8)$$

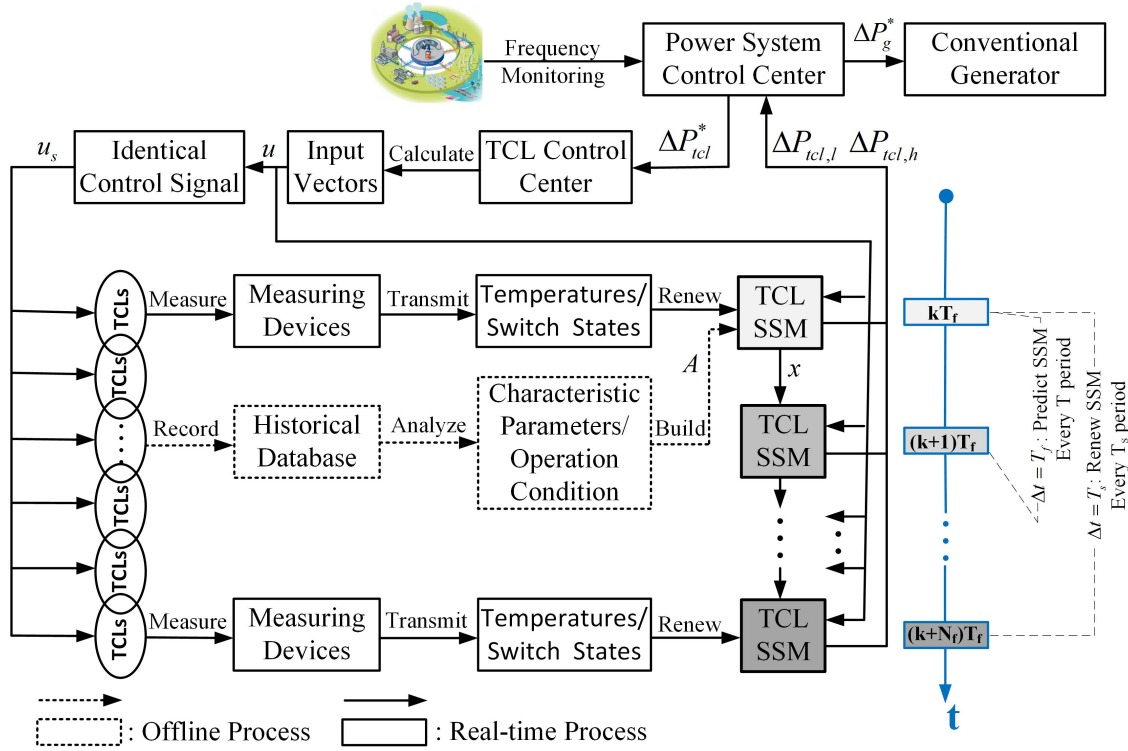


Figure 4.2 Framework of frequency regulation with SSM of aggregated TCLs

where  $\Delta f(t)$  is the system frequency deviation from the nominal value;  $H$  is the system inertia constant;  $D$  is the total load damping coefficient;  $\Delta P_g(t)$  is the output power deviation of conventional generator (CG); and  $\Delta P_{tcl}(t)$  is the output power deviation of aggregated TCLs.  $\Delta P_d(t)$  accounts for the variation of both load and wind powers. It is noted that in our calculations, the wind power is regarded as a negative load. The frequency deviation can be analytically obtained by (4.9).

$$\begin{cases}
 \Delta f(k+1) = (\Delta f(k) - \Psi_1) \cdot \exp(-D \cdot \Delta t / (2H)) + \Psi_2 \\
 \Psi_1 = (\Delta P_g(k) - \Delta P_d(k) + \Delta P_{tcl}(k+1)) / D + \Psi_0 \\
 \Psi_2 = (\Delta P_g(k+1) - \Delta P_d(k+1) + \Delta P_{tcl}(k+1)) / D + \Psi_0 \\
 \Psi_0 = 2H(\Delta P_g(k+1) - \Delta P_d(k+1) - \Delta P_g(k) + \Delta P_d(k)) / D^2 \Delta t
 \end{cases} \quad (4.9)$$

At each time step  $k$ , based on the calculated frequency deviation  $\Delta f(k)$ , frequency regulation coefficient  $\lambda(k)$  is obtained following the flowchart shown in Fig. 4.3, where  $\Delta f_{max}$  is the maximum allowable frequency deviation,  $\lambda^{(1)}$  is an arbitrary value,  $\zeta$  is the required tolerance and  $\Delta P_r(k)$  is the required power adjustment defined by (4.10).



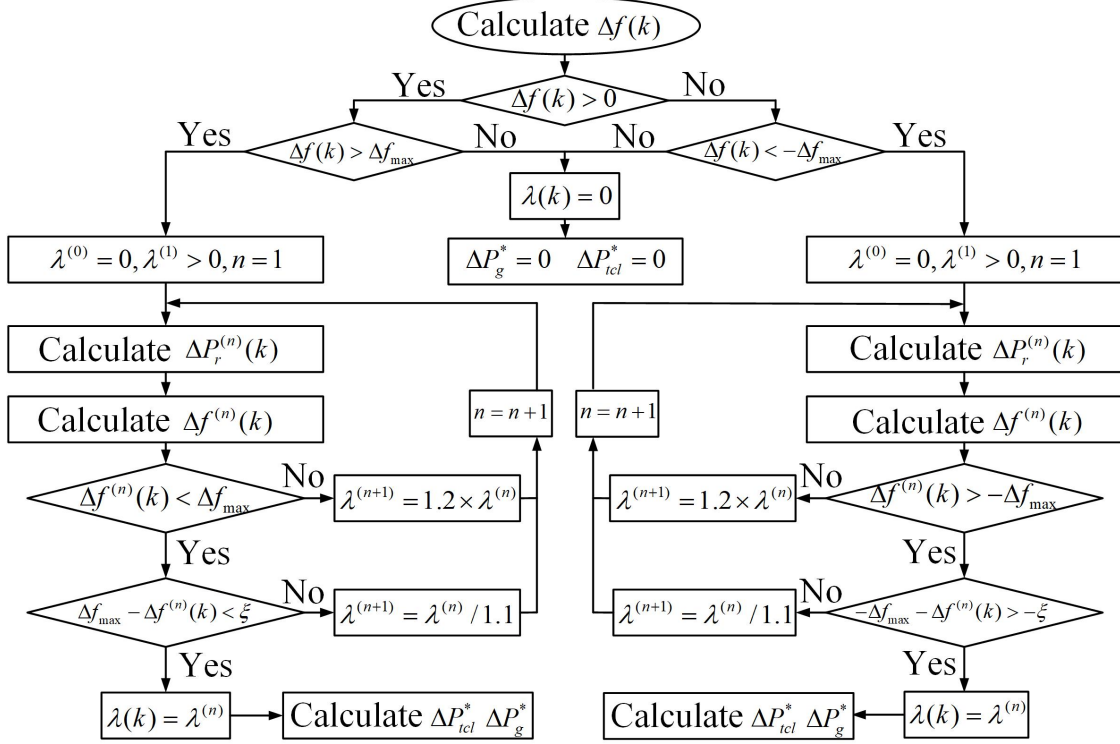


Figure 4.3 Flowchart of calculating frequency regulation coefficient

$$\Delta P_r(k) = \begin{cases} \lambda(k)(\Delta f(k) - \Delta f_{max}), & \Delta f(k) > \Delta f_{max} \\ 0, & -\Delta f_{max} \leq \Delta f(k) \leq \Delta f_{max} \\ \lambda(k)(\Delta f(k) + \Delta f_{max}), & \Delta f(k) < -\Delta f_{max} \end{cases} \quad (4.10)$$

For  $\Delta f(k) > 0$ , if frequency deviation is less than the maximum allowable deviation,  $\lambda(k) = 0$  and  $\Delta P_r(k) = 0$ ; otherwise,  $\lambda(k) = \lambda^{(n)}(k)$  and accordingly,  $\Delta P_r(k) = \Delta P_r^{(n)}(k)$  can be achieved when  $\Delta f_{max} - \zeta < \Delta f^{(n)} < \Delta f_{max}$  is satisfied. In the same way, if  $\Delta f(k) \leq 0$ ,  $\Delta P_r(k)$  can also be obtained according to the procedure shown in Fig. 4.3.

During the frequency regulation, as TCL aggregator has lower responding time compared to CG [58],  $\Delta P_r(k)$  is first allocated to TCL aggregator, and if not sufficient, the remaining power is compensated by CG.

The output power variation limits of CG are determined by its ramp rate and generation capacity as given by (4.11).

$$\begin{cases} \Delta P_{g,l}(k) = \max(\underline{P}_g - P_g(k), -r_g \Delta t) \\ \Delta P_{g,h}(k) = \max(\overline{P}_g - P_g(k), r_g \Delta t) \end{cases} \quad (4.11)$$

where  $P_g(k)$  is the output power of CG;  $\overline{P}_g$  and  $\underline{P}_g$  are the maximum and minimum output power limits of CG, respectively;  $r_g$  is the ramp rate of CG and  $\Delta P_{g,l}(k)$  and  $\Delta P_{g,h}(k)$  are the regulation capacity of CG for under frequency and over frequency, respectively.

The target power changes of the CG and the TCL aggregator can be obtained from the regulation capacity of the CG described by (4.11) and the estimated regulation capacity of the TCL aggregator described by (4.5) in Subsection 4.3.2. For  $\Delta P_r(k) > 0$  and  $\Delta P_r(k) < 0$ , the target power changes of the TCL aggregator and the CG can be determined by (4.12) and (4.13), respectively. And if  $\Delta P_r(k) = 0$ , then  $\Delta P_{tcl}^*(k) = 0$  and  $\Delta P_g^*(k) = 0$ .

$$\begin{cases} \Delta P_{tcl}^*(k) = -\min(\Delta P_r(k), -\Delta P_{tcl,h}(k)) \\ \Delta P_g^*(k) = -\min(\max(\Delta P_r(k) + \Delta P_{tcl,h}(k), 0), \Delta P_{g,h}(k)) \end{cases} \quad (4.12)$$

$$\begin{cases} \Delta P_{tcl}^*(k) = -\max(\Delta P_r(k), -\Delta P_{tcl,l}(k)) \\ \Delta P_g^*(k) = -\max(\min(\Delta P_r(k) + \Delta P_{tcl,l}(k), 0), \Delta P_{g,l}(k)) \end{cases} \quad (4.13)$$

The above process, realizes the required power adjustment for frequency regulation by coordinating TCL aggregator and CG.

#### 4.4.3 Control Action of State Space Model

Based on the target power change of TCL aggregator and regulation capacity of both responding modes, the input vector  $\mathbf{u}$  and control signal  $\mathbf{u}_s$  are determined to realize the frequency regulation with SSM.

##### Determine input vector $\mathbf{u}$

For the case of under frequency in the system ( $\Delta P_{tcl}^*(k) > 0$ ),  $\mathbf{u}$  is determined by (4.14); therefore, the initially ON TCLs located in the state-bin with a higher temperature are more likely to be switched OFF. For the case of over frequency in the system ( $\Delta P_{tcl}^*(k) < 0$ ),  $\mathbf{u}$  is determined by (4.15); therefore, the initially OFF TCLs located in the state-bin with a lower temperature are more likely to be switched ON. And, if  $\Delta P_{tcl}^*(k) = 0$ , then  $\mathbf{u} = \mathbf{O}$ .

$$\begin{cases} x_u^* = \min(\Delta P_{tcl}^*, \Delta P_{tcl,l}) / (P_{avg} N_{tcl}) \\ u_{N_s+1-j} = \max\left(\min\left(x_u^* - \sum_{h=1}^{j-1} x_{N_s+1-h}, x_{N_s+1-j}\right), 0\right) \end{cases} \quad (4.14)$$

$$\begin{cases} x_u^* = \max(\Delta P_{tcl}^*, \Delta P_{tcl,h}) / (P_{avg} N_{tcl}) \\ u_j = \min\left(\max\left(x_u^* + \sum_{h=1}^{j-1} x_{N_s+h}, -x_{N_s+j}\right), 0\right) \end{cases} \quad (4.15)$$

where  $j \in \{1, 2, \dots, N_s\}$ .

### Determine identical control signal $\mathbf{u}_s$

$\mathbf{u}$  can be translated into the real control signal  $\mathbf{u}_s$ . For  $\Delta P_{tcl}^*(k) > 0$  and  $\Delta P_{tcl}^*(k) < 0$ ,  $\mathbf{u}_s$  is determined by (4.16) and (4.17), respectively. In addition, if  $\Delta P_{tcl}^*(k) = 0$ , there is no need to switch TCLs. Thus,  $\mathbf{u}_s = \mathbf{O}$ .

$$\begin{cases} u_{s,j} = \min(u_j / x_j, 1) \\ u_{s,N_s+1} = 1 \end{cases} \quad (4.16)$$

$$\begin{cases} u_{s,j} = \min(-u_j / x_{N_s+j}, 1) \\ u_{s,N_s+1} = -1 \end{cases} \quad (4.17)$$

$u_{s,j}$  is a vector element which takes a value between  $[0, 1]$  and denotes the switching probability, meaning that a portion, or all of the TCLs located in the corresponding state-bin need to switch between ON and OFF. An additional element  $u_{s,N_s+1}$  is added to  $\mathbf{u}_s$  to determine the direction of switching command. When  $u_{s,N_s+1}$  is 1,  $\mathbf{u}_s$  realizes the control actions of ON→OFF and vice versa when  $u_{s,N_s+1}$  is -1. At each control cycle, TCLs find their location in  $\mathbf{u}_s$  based on their indoor temperature and switch state. Then, their local controllers will generate a random number subjected to a uniform distribution of  $U(0, 1)$  and calculate the response probability. If the random number is less than the corresponding  $u_{s,j}$ , the TCL will change its switch state. Otherwise, the TCL will retain its current status. In the proposed control strategy, there is only one global control signal in every dispatch period, which reduces the communication requirements between central controller and TCLs. The error of probabilistic control can be neglected in the presence of a large population of TCLs [64].

Table 4.1 Simulation Parameters

TCL Parameters		
Parameter	Meaning	Value*
$C$	Thermal capacitance [kWh/°C].	U(8,12)
$R$	Thermal resistance [°C/kW]	U(1.5,2.5)
$COP$	Coefficient of performance [-]	3
$P_{rate}$	Rated power [kW]	U(6,8)
$T_{set}$	Temperature reference [°C]	U(15,20)
$\delta_{db}$	Temperature dead-band width [°C]	2
$T_a$	Ambient temperature [°C]	5
Frequency Regulation Parameters		
Parameter	Meaning	Value*
$D$	Total load damping coefficient [MW/Hz].	20
$H$	System inertia constant [MW.s/Hz]	120
$f$	Frequency reference [Hz]	60
$\Delta f_{max}$	Allowable frequency deviation [Hz]	0.2
$r_g$	Generation ramp rate of CG [MW/min]	50
$\underline{P}_g/\overline{P}_g$	Min/Max output power limits of CG [MW]	0/500

\*U( $\alpha, \beta$ ) represents the uniform distribution, and ( $\alpha, \beta$ ) is the variation range. The data of TCL parameters derives from [58] and the data of frequency regulation parameters derives from [64].

#### 4.5 Case Studies And Simulation Results

We consider a system involving a population of 10,000 TCLs and a conventional generator with the parameters listed in Table 4.1. A wind generation system with the output power profile shown in Fig. 4.4 is also connected to the system. We assume a load power profile as shown in Fig. 4.4. The wind power is the main source of power fluctuations and hence frequency deviations. The following frequency regulation scenarios are studied:

- 1) *Scenario a*: The CG is the only resource for the frequency regulation and TCLs are not participating.
- 2) *Scenario b*: The frequency regulation is first realized by TCL aggregator, and if not sufficient, the CG will also contribute.

The frequency profiles for *Scenarios a* and *b* are compared in Fig. 4.5. It is seen that TCLs' participation can improve the frequency deviation and keep it within the desired dead-band. The simulation results validate the effectiveness of using TCL aggregator for frequency regulation.

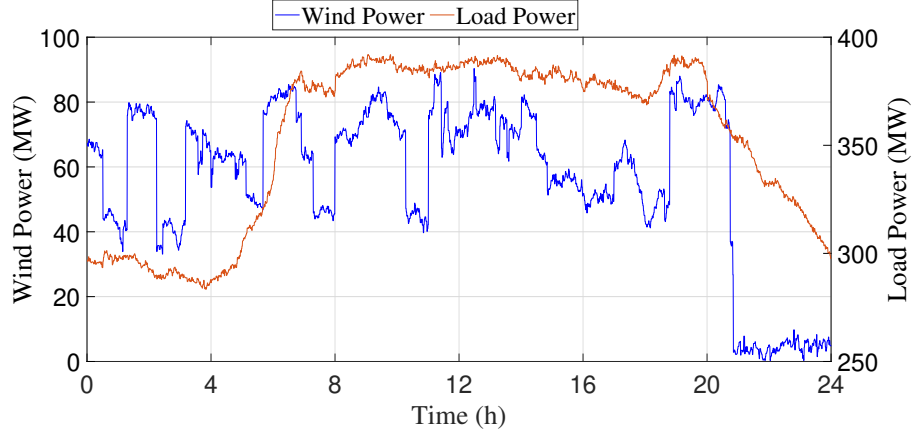


Figure 4.4 The wind and load power profiles adapted from [1]

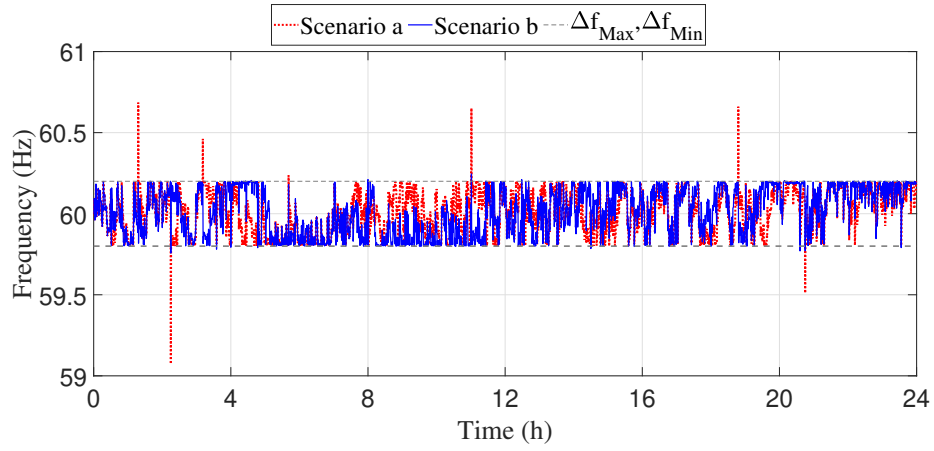


Figure 4.5 System frequency for scenarios a and b

The power response of the aggregated TCLs and the CG for both *Scenarios* are shown in Fig. 4.6 and Fig. 4.7, respectively. During the regulation period for *Scenario b*, when TCLs lose their regulation capacity due to huge frequency deviation, the power output of aggregated TCLs hits its lower and upper limits. Meanwhile, the CG compensates the remaining required power by adjusting its output power. The simulation results show that the proposed control structure can relieve the stress on the CG by mitigating the amount of required ramp adjustments. By relieving the stress on the CG, the economic and environmental benefits can be achieved.

Fig. 4.6, also compares the power profiles of TCLs utilizing SSM modeling and individual modeling for *Scenario b*. It is observed that the power of aggregated TCLs can track the power of the individual TCL model with a high accuracy.

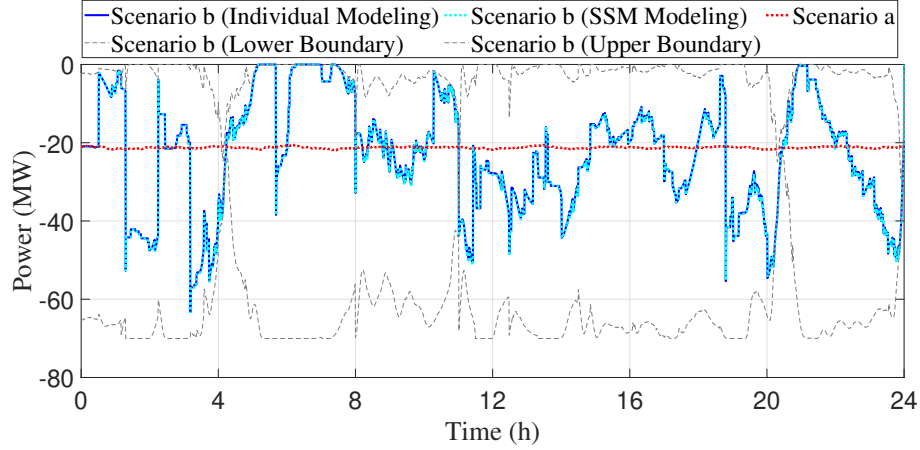


Figure 4.6 Power profiles of aggregated TCLs for scenarios a and b

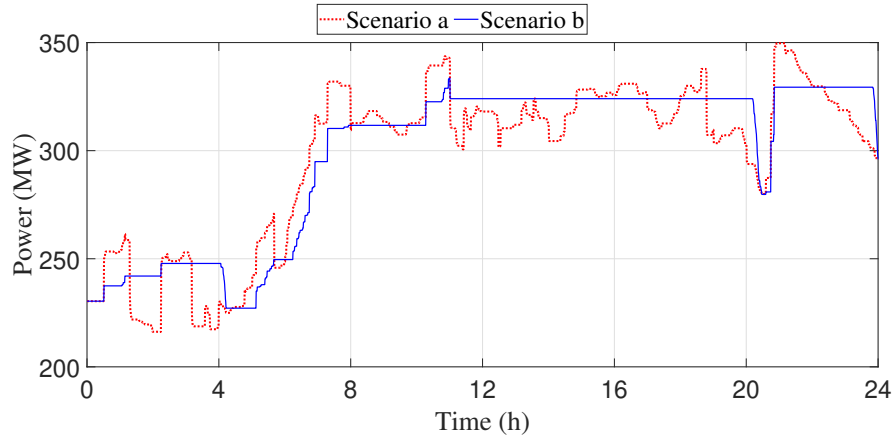


Figure 4.7 Power profiles of conventional generator for scenarios a and b

The indoor air temperatures of all TCLs for *Scenario b* are shown in Fig. 4.8. It is obvious that, during the frequency regulation, TCLs' indoor temperatures are always kept within  $[T_{set} - \delta_{db}, T_{set} + \delta_{db}]$  which guarantees the end users' comfort requirements.

## 4.6 Conclusion

A new control structure for the participation of aggregated TCLs in the frequency regulation services has been proposed. In the proposed control framework, the required power adjustment for frequency regulation is realized by coordinating the TCL aggregator and the Conventional Generators (CGs) giving the priority to the TCLs. The proposed control strategy broadcasts the same control signal to all TCLs. This control signal is calculated based

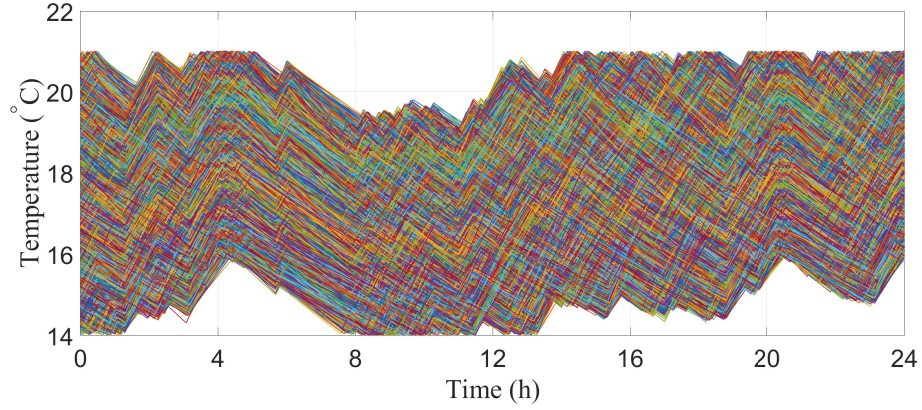


Figure 4.8 Indoor air temperature profiles of all TCLs for scenario b

on the local temperature and switch states of all TCLs. This strategy provides frequency regulation with a significantly reduced communication requirement. Furthermore, the short cycling is minimized and the end users' comfort is guaranteed. Simulations have been carried out for a typical system involving 10000 TCLs and a CG. It was found that the proposed control strategy can efficiently exploit the TCLs to counteract the frequency deviations. The role of CG in compensating the inefficient reserve power of TCLs has been demonstrated. It has also been shown that the participation of TCLs will not affect the end users' comfort.

## CHAPTER 5    ARTICLE 2: AN EXTENDED STATE SPACE MODEL FOR AGGREGATION OF LARGE-SCALE EVS CONSIDERING FAST CHARGING

This chapter is the reproduction of a peer-reviewed article which has been published in IEEE Transactions on Transportation Electrification on 2022/05/30 [111].

- S. Kiani, K. Sheshyekani, and H. Dagdougui, "An Extended State Space Model for Aggregation of Large-scale EVs Considering Fast Charging," in *IEEE Transactions on Transportation Electrification*, doi: 10.1109/TTE.2022.3179311.

### 5.1 Abstract

This paper presents an extended state space model for aggregation of large-scale electric vehicles (EVs) for frequency regulation and peak load shaving in power systems. The proposed model systematically deals with the fast-charging of EVs as an effective solution for immediate charging requirements. Furthermore, the proposed extended state space model increases the flexibility of the EV aggregator (EVA) by enabling the EVs to participate in ancillary services with both regular and fast charging/discharging rates. This will help the EVA to provide prompt and efficient response to severe generation-consumption imbalances. A probabilistic control approach is developed which reduces the communication burden of the EV aggregator. Furthermore, the uncertainties related to EV users behaviour are modeled in real time. The simulations are conducted for a typical power system including a large population of EVs, a conventional generator and a wind generation system. It is shown that the proposed aggregation model can accurately describe the aggregated behaviour of a large population of EVs enabling them to efficiently participate in frequency regulation and peak load shaving services. Finally, the performance of EVA is evaluated for different driving behaviors and SOC levels of EV population.

### 5.2 Introduction

Recently, the electrification in transportation has become a growing trend owing to the decreased battery costs of electric vehicles (EVs), their environmental benefits, and cheaper electricity prices compared to escalating fossil fuel prices [112]. The worldwide sale of EVs exceeded 8.5 million units in 2020 and is on track to reach more than hundred million units by 2030 [61].



With the recent developments of the EV charging technologies, the fast charging solutions where the EVs are being charged with higher power rates are becoming more popular. Adopting fast charging rate will bring benefits to the EV users by significantly reducing their charging time when immediate charging is required. However, large penetration of unmanaged EVs, specially with fast charging rate, can lead to negative impacts on the existing transmission and distribution network [113], such as high peak, increased power fluctuations, decreased power quality and voltage limit violations which require costly network expansions [114,115]. By contrast, a well-managed EV population not only limits the unnecessary network expansions but also potentially offers opportunities to support the electric grid operating as the smart grid [116]. For example, in the case of specific system component failures, the battery of EVs may be used as a backup energy storage to inject required energy into the grid using the vehicle-to-grid (V2G) technology [8].

In general, the EV integration can be realized to provide various ancillary services to the power grid including peak load shaving and frequency regulation. In peak load shaving, the energy stored in the EV batteries during the off-peak periods is used to provide additional electricity supply during the peak periods [117]. The frequency regulation service is also of particular importance for modern power systems due to the proliferation of intermittent renewable energy sources (RESs) [118]. The rapid ramping rate of the EV batteries enables them to be used for generation-consumption balancing. This can be done by controlling the bidirectional power flow between their batteries and the grid so that the frequency excursions are counteracted on a real-time basis [119].

However, the energy capacity and the power rate of a single EV is not sufficient to accomplish the desired functionality in the ancillary service. By aggregating and coordinating multiple EV batteries, the accumulated capacity can become high enough to provide considerable regulation capacity to the power grid [8]. The EV Aggregator (EVA) can be thought of as a proxy between EV population and the power grid which is responsible to manage the smart interactions, so that the direct interaction of the grid-operator with the large-scale EV population is eliminated [120].

To date, different EVA models have been proposed which can be generally categorized as centralized and distributed schemes [11]. In a centralized scheme, the information of the whole system needs to be collected and processed in one location. On the contrary, distributed scheme decomposes the main problem into several sub-problems and distributes them over several agents (e.g., EVs and EVAs) [102]. These small-scale sub-problems are solved independently by each agent lowering the computation load of the aggregation.

Centralized aggregation schemes are known to have better accuracy and optimized solution because all decisions are made only at one central location. In existing literature, a number of control approaches are developed for centralized aggregation schemes. The droop control method is used in [82] to control the charging and discharging power of EVs according to the frequency signal by broadcasting an individual control signal for each EV. In [68], the EV charging and discharging processes are constrained by a laxity-SOC based heuristic smart charging strategy. Authors in [74] proposed a queuing network to estimate the regulation capacity of EVA for up and down regulations. A leader-follower game is proposed in [83], for the individual EVs and the EVA to determine optimal day-ahead frequency reserve scheduling.

Although centralized structure can be easily implemented with good controllability and predictability [18], the communication and computation requirement for data measuring, data processing and control signal dispatching is very huge for central operator, specially when dealing with a large population of EVs. In order to overcome this drawback, authors in [62,64] developed a centralized EVA with the State Space transitions Model (SSM). The SSM was initially introduced as a reduced aggregation model for analyzing the aggregated response of flexible loads consisting of thermostatically controlled loads (TCLs) [13,14]. Later, authors in [15] and [16] showed that it is possible to determine the parameters of the SSM-based TCL aggregator by observing the temperature dynamics of TCLs and utilize the TCL aggregator to regulate frequency and energy imbalances in power systems. Although there is an extensive literature for SSM-based TCL aggregation models, using SSM for EV aggregation is an emerging research topic. Compared to the conventional population-based centralized EV aggregation models which consider the dynamics of all individual EVs, the SSM-based EVA in [64], distributes the large population of EVs into a fixed number of state-bins and then controls their transition between different bins. By doing so, the computational burden of the EVA only depends on the number of state bins rather than the size of EV population. Furthermore, authors in [62] have implemented a progressive state recovery strategy in EV-SSM in order to mitigate the impact of regulation service on the charging preferences of the EVs.

Though the SSM-based EVAs developed so far are successful in reducing the computational burden of the EVA, they do not utilize the flexibility of EV population to its full potential due to negligence of fast charging rates. In fact, considering both regular and fast charging rates can provide EVA with greater flexibility by allowing the EVs to participate in ancillary services with both charging rates [121]. Moreover, the EV aggregation model must appropriately address the immediate energy requirement of EVs when they need to be fast-charged in short connection sessions. To the best of authors' knowledge, the fast charging state has not been so far included in the SSM-based EVA. Furthermore, all previously developed SSM-

based EVAs were only focused on providing frequency regulation service. Even though there have been some relevant studies on EV aggregation techniques for jointly offering different ancillary services, the EV-SSM has never been utilized to provide peak load shaving. In practice, having a dual-use SSM-based EVA makes it easier to switch between frequency regulation and peak load shaving services as needed. In [122], it is shown that using aggregated EVs for frequency regulation on a daily basis and for peak load shaving on high demand days, leads to higher economic and environmental benefits than using it for either of the two services alone. Furthermore, with a dual-use aggregation model, EVA can exploit the full benefit of EV-SSM including improved computational and communication efficiencies, for both services.

Within this context, the key contributions of this paper with respect to the state of the art are summarized as follows:

- 1) A new extended SSM is proposed which enables the EVA to participate in regulation service with both regular and fast charging/discharging rates by considering dedicated state-bins for each charging/discharging state. This requires proper formulation of EV-SSM, appropriate definition of input and output matrices and calculation of regulation capacity for different responding modes. The extra flexibility offered by fast charging rates helps the EVA to provide prompt and efficient response to severe generation-consumption imbalances. Moreover, appropriate measures are taken into account in the designed controller in order to avoid excessive battery degradation of EVs caused by frequent switching to fast charging/discharging states.
- 2) The urgent charging demand of EVs when they need to be fast-charged in short connection sessions is modeled by categorizing them in a separate uncontrolled state (forced fast charging state). This classification is necessary as the EVs in this state are uncontrollable and their regulation capacity must be excluded from the rest of the EV fleet.
- 3) The proposed EV-SSM, in combination with the proposed probabilistic control method, reduces the bi-directional communication burden between EVA and EVs in both directions. On the one hand, reduced EV data measurement decreases measurement signal communication instances. On the other hand, the probabilistic control approach reduces the communication burden of the EVA even further by broadcasting only one global probabilistic control signal to all EVs.
- 4) The proposed EVA is utilized to provide both frequency regulation and peak load shaving services. The dual-use aggregation model makes it easier for the EVA to switch between the two services as needed.

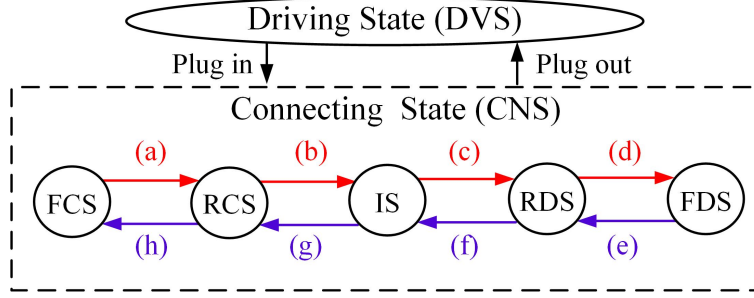


Figure 5.1 EV states and responding modes

5) The performance of EVA and the quality of provided ancillary services are evaluated for different driving behaviors and SOC levels of the EV population. Moreover, various evaluation metrics are defined to validate the effectiveness of the proposed EVA modeling in improving computational and communicational efficiencies.

### 5.3 Modeling Framework

#### 5.3.1 Individual EV Model

As shown in Fig. 5.1, each individual EV is assumed to be either in Driving State (DVS) or in Connecting State (CNS). The EV plugs in as soon as it finishes its trip and plugs out right before its next trip. For a plugged-in EV, based on the power flow direction with the grid, five types of connecting states are defined [123]:

- 1) *Fast Charging State (FCS)*: EV receives energy from the grid with fast charging rate.
- 2) *Regular Charging State (RCS)*: EV receives energy from the grid with regular charging rate.
- 3) *Idle State (IS)*: EV is plugged-in without any power exchange with the grid.
- 4) *Regular Discharging State (RDS)*: EV injects energy to the grid with regular discharging rate (V2G).
- 5) *Fast Discharging State (FDS)*: EV injects energy to the grid with fast discharging rate (V2G).

Based on the above-mentioned connecting states, using single battery model for energy management system (EMS), the state of charge (SOC) variation of a plugged-in EV can be described as follows [62].

$$SOC(k+1) = \begin{cases} SOC(k) - (P^{fast}/\eta^d).(\Delta t/Q), & m(k) = 2 : \text{FDS} \\ SOC(k) - (P^{reg}/\eta^d).(\Delta t/Q), & m(k) = 1 : \text{RDS} \\ SOC(k), & m(k) = 0 : \text{IS} \\ SOC(k) + (P^{reg}.\eta^c).(\Delta t/Q), & m(k) = -1 : \text{RCS} \\ SOC(k) + (P^{fast}.\eta^c).(\Delta t/Q), & m(k) = -2 : \text{FCS} \end{cases} \quad (5.1)$$

where  $m$  is the switch status of the EV;  $Q$  is the battery capacity;  $P^{fast}$  and  $P^{reg}$  are fast and regular charging powers, respectively; and  $\eta^c$  and  $\eta^d$  are charging and discharging efficiencies, respectively.

In order to characterize the battery constraints and the charging process of the EV, it is assumed that the EV changes its switch status when one of the following events happens:

- The EV switches to RCS right after plugging into the power grid.
- The EV switches to IS when the SOC reaches its maximum or minimum values ( $SOC^{max}$  and  $SOC^{min}$ ).
- The EV switches to RCS from the moment that the remaining connection duration begins to be smaller than the required time for charging the EV ( $t^{req}$ ). This state is called forced-RCS and is necessary to guarantee the desired SOC value when plugging out. When the EV switches to forced-RCS, it is considered to be uncontrollable and remains in this state until the end of connection session.
- The EV switches to FCS if the total connection session is not enough to charge the EV to the desired SOC value with regular charging rate. This state is called forced-FCS and helps the EV to be charged with the maximum possible charging rate in short connection sessions. The EVs in forced-FCS are also considered to be uncontrollable and remain in this state until the end of their connection session.

Therefore, the switch status of the EV is determined as follows:

$$m(k+1) = \left\{ \begin{array}{ll} -1, & c(k+1) - c(k) = 1: \text{ Plug-in} \\ 0, & SOC(k+1) \geq SOC^{max} : \text{ Fully charged} \\ 0, & SOC(k+1) \leq SOC^{min} : \text{ Fully discharged} \\ -1, & \left. \begin{array}{l} t^{req}(k+1) \leq t^{out} - t^{in} \ \& \\ t^{out} - (k+1)\Delta t \leq t^{req}(k+1) \end{array} \right\} : \text{ Forced-RCS} \\ -2, & t^{req}(k+1) \geq t^{out} - t^{in} : \text{ Forced-FCS} \\ m(k), & \text{ Otherwise} \end{array} \right\} \quad (5.2)$$

where  $c$  is the connecting status of the EV and is defined by (5.3) based on the plug-in and plug-out times,

$$c(k+1) = \left\{ \begin{array}{ll} 1, & t^{in} \leq (k+1)\Delta t \leq t^{out} : \text{ Connected} \\ 0, & \text{ Otherwise} : \text{ Not connected} \end{array} \right. \quad (5.3)$$

and  $t^{req}$  is defined as the required time which is needed to charge EV to its desired SOC value ( $SOC^{out}$ ) with regular charging rate before plug-out time. At any moment,  $t^{req}$  is calculated as,

$$t^{req}(k+1) = (SOC^{out} - SOC(k+1)) \cdot (Q / (P^{reg} \cdot \eta^c)) \quad (5.4)$$

The local charging cycle of a connected EV can be interrupted by the controller with eight basic responding modes (e.g. a-h) as shown in Fig. 5.1. Note that more complex responding modes can be achieved by combining these basic responding modes. For instance, FCS→RDS response can be regarded as the combination of responding modes (a), (b) and (c); while FDS→FCS response refers to the combination of (e), (f), (g) and (h).

### 5.3.2 Extended EV State Space Model for EV Aggregator (EVA)

The EV State Space Model (EV-SSM) distributes the population of EVs into several state-bins according to their switch status and SOC value and then controls their evolution between different bins. In order to build the EV-SSM, first, the SOC range is divided into  $N_s$  equally spaced intervals and then, according to the connecting states (FCS, RCS, IS, RDS and FDS), each SOC interval is further divided into five state-bins. As the EVs in forced-RCS and forced-FCS states are uncontrollable and have no regulation capacity, they need to be

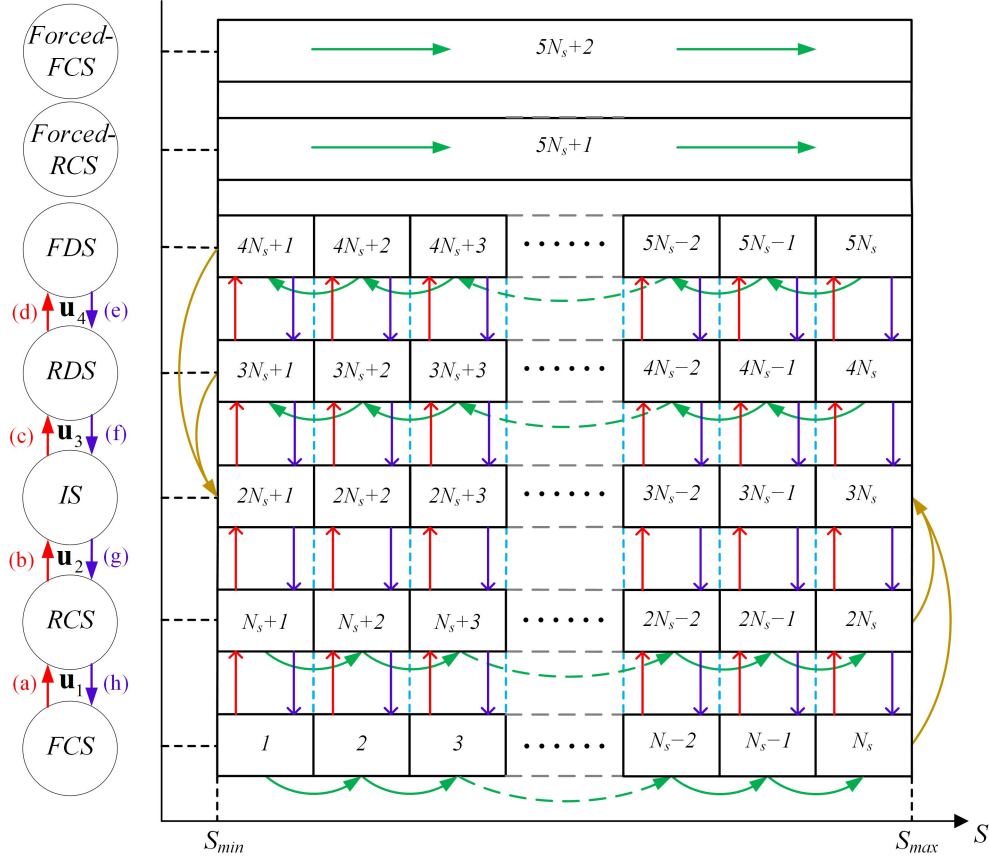


Figure 5.2 Structure of the state-bins and input vectors

handled separately. Therefore, two extra state-bins are considered which account for the fraction of EVs in forced-charging states. Thus, at any moment, the state distribution of EVs can be described by state vector  $\mathbf{x} \in \mathbb{R}^{(5N_s+2) \times 1}$ . The structure of the state-bins is illustrated in Fig. 5.2. The green arrows represent the natural state transition while the yellow arrows indicate the SOC boundary transitions. The controlled state transitions are shown by red and blue arrows.

The EV population is aggregated by the State Space Model as follows:

$$\begin{cases} \mathbf{x}(k+1) = \mathbf{A}\mathbf{x}(k) + \mathbf{B}\mathbf{u}(k) + \boldsymbol{\omega}(k) \\ y(k) = \mathbf{C}\mathbf{x}(k) \end{cases} \quad (5.5)$$

$$\mathbf{u}(k) = [\mathbf{u}_1(k) \quad \mathbf{u}_2(k) \quad \mathbf{u}_3(k) \quad \mathbf{u}_4(k)]^T$$

$$\mathbf{B} = [\mathbf{B}_1 \quad \mathbf{B}_2 \quad \mathbf{B}_3 \quad \mathbf{B}_4]$$

where  $y$  is a scalar value describing the output power of the EVA.  $\mathbf{A} \in \mathbb{R}^{(5N_s+2) \times (5N_s+2)}$  is transposed Markov Transition Matrix (MTM) whose elements are the transition probability of EVs between the state-bins.  $\mathbf{u}_1, \mathbf{u}_2, \mathbf{u}_3, \mathbf{u}_4 \in \mathbb{R}^{N_s \times 1}$  are input vectors which represent the effect of the controlled switching.

As shown in Fig. 5.2,  $\mathbf{u}_1$  represents the responding modes (a) and (h),  $\mathbf{u}_2$  corresponds to the responding modes (b) and (g),  $\mathbf{u}_3$  refers to the responding modes (c) and (f) and finally  $\mathbf{u}_4$  is associated with the responding modes (d) and (e). The positive elements of these four input vectors (e.g., red arrows), define the fraction of EVs in the corresponding SOC interval which are due to be switched toward decreasing the charging power (responding modes (a) and (b)) or increasing the discharging power (responding modes (c) and (d)). Contrariwise, the negative elements (e.g., blue arrows) define the fraction of EVs in the corresponding SOC interval which are going to take switching actions toward decreasing the discharging power (responding modes (e) and (f)) or increasing the charging power (responding modes (g) and (h)).

$\mathbf{B}_1, \mathbf{B}_2, \mathbf{B}_3$  and  $\mathbf{B}_4$  are constant input matrices which are structured in a way that realizes the control action of input vectors.  $\mathbf{C}$  is a constant output matrix which is used to obtain the output power of the EVA. These constant matrices are defined as follows,

$$\begin{aligned} & \begin{cases} \mathbf{B}_1 = \begin{bmatrix} -\mathbf{I}_{N_s \times N_s} & \mathbf{I}_{N_s \times N_s} & \mathbf{O}_{N_s \times N_s} & \mathbf{O}_{N_s \times N_s} & \mathbf{O}_{N_s \times N_s} & \mathbf{O}_{2 \times N_s} \end{bmatrix}^T \\ \mathbf{B}_2 = \begin{bmatrix} \mathbf{O}_{N_s \times N_s} & -\mathbf{I}_{N_s \times N_s} & \mathbf{I}_{N_s \times N_s} & \mathbf{O}_{N_s \times N_s} & \mathbf{O}_{N_s \times N_s} & \mathbf{O}_{2 \times N_s} \end{bmatrix}^T \\ \mathbf{B}_3 = \begin{bmatrix} \mathbf{O}_{N_s \times N_s} & \mathbf{O}_{N_s \times N_s} & -\mathbf{I}_{N_s \times N_s} & \mathbf{I}_{N_s \times N_s} & \mathbf{O}_{N_s \times N_s} & \mathbf{O}_{2 \times N_s} \end{bmatrix}^T \\ \mathbf{B}_4 = \begin{bmatrix} \mathbf{O}_{N_s \times N_s} & \mathbf{O}_{N_s \times N_s} & \mathbf{O}_{N_s \times N_s} & -\mathbf{I}_{N_s \times N_s} & \mathbf{I}_{N_s \times N_s} & \mathbf{O}_{2 \times N_s} \end{bmatrix}^T \end{cases} \quad (5.6) \\ & \mathbf{C} = N_{ev}(k) \begin{bmatrix} P_{avg}^{fast} & P_{avg}^{reg} & P_{avg}^{reg} & P_{avg}^{reg} & P_{avg}^{fast} & P_{avg}^{reg} & P_{avg}^{fast} \end{bmatrix} \\ & \odot \begin{bmatrix} -\mathbf{1}_{1 \times N_s} & -\mathbf{1}_{1 \times N_s} & \mathbf{O}_{1 \times N_s} & \mathbf{1}_{1 \times N_s} & \mathbf{1}_{1 \times N_s} & -1 & -1 \end{bmatrix} \end{aligned}$$

where the number of connected EVs are given by  $N_{ev}$ ; and  $P_{avg}^{reg}$  and  $P_{avg}^{fast}$  are the average regular charging rate and average fast charging rate of the EVs, respectively. As the EVs in the forced-charging state bins (e.g., forced-RCS and forced-FCS) are uncontrollable, the last two rows of the input matrices are set to zero. In addition, the power consumption of these EVs are added to the output power of the EVA by the last two elements of matrix  $\mathbf{C}$ .

The effect of dynamic traveling behaviour of EVs are represented by the noise vector  $\boldsymbol{\omega}$  in (5.5). Therefore, the matrix  $\mathbf{x}$  is being updated in accordance to the dynamic plug-in and plug-out of the EVs during the control horizon [64]. The noise vector  $\boldsymbol{\omega}$ , is calculated as follows,



$$\omega(k) = \frac{N_{ev}^{in}(k)\mathbf{x}^{in}(k) - N_{ev}^{out}(k)\mathbf{x}^{out}(k)}{N_{ev}(k) + N_{ev}^{in}(k) - N_{ev}^{out}(k)} \quad (5.7)$$

where  $N_{ev}^{in}(k)$  and  $N_{ev}^{out}(k)$  are the number of EVs plugged in and out during  $k$ th time interval, respectively.  $\mathbf{x}^{in} \in \mathbb{R}^{(5N_s+2) \times 1}$  is a state vector representing the state distribution of plugged-in EVs while  $\mathbf{x}^{out} \in \mathbb{R}^{(5N_s+2) \times 1}$  being a state vector representing the state distribution of plugged-out EVs during  $k$ th time interval. It is worth noting that  $\mathbf{x}^{in}$  and  $\mathbf{x}^{out}$  are calculated in the same way as state vector  $\mathbf{x}$ , except that instead of considering all available EVs, only plugged-in and plugged-out EVs are taken into account and distributed among the state bins based on their SOC values and switch states.

Based on the EV-SSM, the regulation capacity of the EVA for different responding modes are estimated as follows,

$$\begin{aligned} \mathbf{y}'(k) &= \mathbf{C}' \mathbf{x}(k) \\ \mathbf{y}'(k) &= [y_a(k) \ y_b(k) \ y_c(k) \ y_d(k) \ y_e(k) \ y_f(k) \ y_g(k) \ y_h(k)]^T \\ \mathbf{C}' &= [\mathbf{C}_a \ \mathbf{C}_b \ \mathbf{C}_c \ \mathbf{C}_d \ \mathbf{C}_e \ \mathbf{C}_f \ \mathbf{C}_g \ \mathbf{C}_h]^T \end{aligned} \quad (5.8)$$

where the matrices  $\mathbf{C}_{a-h}$  are given as below,

$$\begin{cases} \mathbf{C}_a = P_{avg}^{fast} N_{ev}(k) \begin{bmatrix} \mathbf{1}_{1 \times N_s} & \mathbf{O}_{1 \times N_s} & \mathbf{O}_{1 \times N_s} & \mathbf{O}_{1 \times N_s} & \mathbf{O}_{1 \times N_s} & 0 & 0 \end{bmatrix} \\ \mathbf{C}_b = P_{avg}^{reg} N_{ev}(k) \begin{bmatrix} \mathbf{1}_{1 \times N_s} & \mathbf{1}_{1 \times N_s} & \mathbf{O}_{1 \times N_s} & \mathbf{O}_{1 \times N_s} & \mathbf{O}_{1 \times N_s} & 0 & 0 \end{bmatrix} \\ \mathbf{C}_c = P_{avg}^{reg} N_{ev}(k) \begin{bmatrix} \mathbf{1}_{1 \times N_s} & \mathbf{1}_{1 \times N_s} & \mathbf{1}_{1 \times N_s} & \mathbf{O}_{1 \times N_s} & \mathbf{O}_{1 \times N_s} & 0 & 0 \end{bmatrix} \\ \mathbf{C}_d = P_{avg}^{fast} N_{ev}(k) \begin{bmatrix} \mathbf{1}_{1 \times N_s} & \mathbf{1}_{1 \times N_s} & \mathbf{1}_{1 \times N_s} & \mathbf{1}_{1 \times N_s} & \mathbf{O}_{1 \times N_s} & 0 & 0 \end{bmatrix} \\ \mathbf{C}_e = P_{avg}^{fast} N_{ev}(k) \begin{bmatrix} \mathbf{O}_{1 \times N_s} & \mathbf{O}_{1 \times N_s} & \mathbf{O}_{1 \times N_s} & \mathbf{O}_{1 \times N_s} & -\mathbf{1}_{1 \times N_s} & 0 & 0 \end{bmatrix} \\ \mathbf{C}_f = P_{avg}^{reg} N_{ev}(k) \begin{bmatrix} \mathbf{O}_{1 \times N_s} & \mathbf{O}_{1 \times N_s} & \mathbf{O}_{1 \times N_s} & -\mathbf{1}_{1 \times N_s} & -\mathbf{1}_{1 \times N_s} & 0 & 0 \end{bmatrix} \\ \mathbf{C}_g = P_{avg}^{reg} N_{ev}(k) \begin{bmatrix} \mathbf{O}_{1 \times N_s} & \mathbf{O}_{1 \times N_s} & -\mathbf{1}_{1 \times N_s} & -\mathbf{1}_{1 \times N_s} & -\mathbf{1}_{1 \times N_s} & 0 & 0 \end{bmatrix} \\ \mathbf{C}_h = P_{avg}^{fast} N_{ev}(k) \begin{bmatrix} \mathbf{O}_{1 \times N_s} & -\mathbf{1}_{1 \times N_s} & -\mathbf{1}_{1 \times N_s} & -\mathbf{1}_{1 \times N_s} & -\mathbf{1}_{1 \times N_s} & 0 & 0 \end{bmatrix} \end{cases} \quad (5.9)$$

Note that the last two elements of these matrices are set to zero in order to exclude the power contribution of forced-charging EVs from regulation capacities.

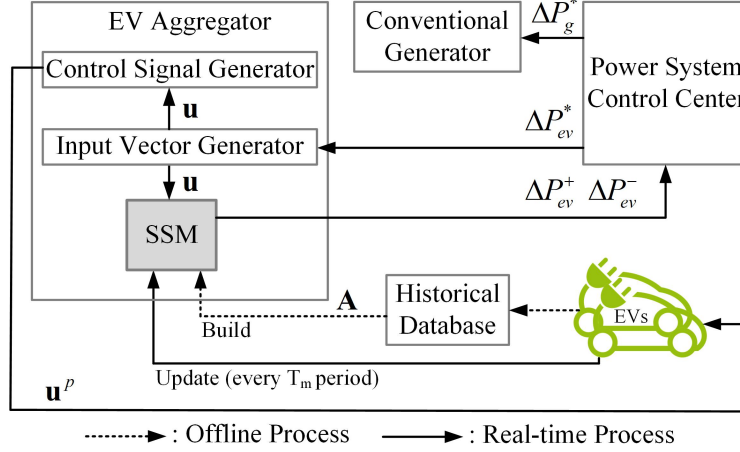


Figure 5.3 EV-SSM framework for ancillary services

#### 5.4 EV-SSM Framework for Ancillary Services

EV-SSM framework for ancillary services is shown in Fig. 5.3. The transition matrix  $\mathbf{A}$  is identified offline using the Hidden Markov Model toolbox of MATLAB (hmmestimate function), assuming that the full state information from all EVs is available. This function is used to calculate the maximum likelihood estimate of the transition probabilities for the sequence of EV states over the specific time [103].

In order to cover the entire SOC range, according to EV characteristics, 1200 history states of the uncontrolled EVs in different connecting states are used for matrix identification. Once the transition matrix is identified, it is used to build the SSM and update the state vector every  $\Delta t = 15s$ . The SSM is also updated with the measured data every  $T_m = N_m \Delta t$  period, which is set to 8 minutes in this work. The measuring period is a choice parameter which is determined as a trade-off between the estimation accuracy of the SSM and the communication burden [110]. At each control cycle (e.g. 15 s), based on the EV-SSM, the capacity of EVA for increasing and decreasing its output power are estimated. Theoretically, more state-bins can lead to a more precise estimation of these capacities, but at the expense of more complex control structure [58]. In this study, we choose  $N_s = 20$  for building the state-bin structure. According to the estimated capacities of the EVA and the required regulation power needed for a specific ancillary service, the power system control center calculates the regulated power of the EVA and the conventional generator. For the case of frequency regulation, the required regulation power is determined based on real-time frequency deviation, while for peak load shaving, it is calculated using the power equilibrium equation in real-time. Then, the EVA generates the input vectors for updating the EV-SSM. Finally, the input vectors are translated into a probabilistic control signal which is communicated to all EVs globally.

It is worth mentioning that the proposed EV-SSM reduces the bi-directional communication burden between EVA and EVs in both directions. On the one hand, the EV data, including the SOC and switch states, is measured and transmitted to the EVA every 8 minutes. While waiting for the next measurement signal, the SSM estimates the SOC and switch states of the EVs using the identified transition matrix at each control cycle (e.g. 15s). This process reduces the measurement signal communication instances by a factor of 32. On the other hand, the probabilistic control approach reduces the communication burden of the EVA even further by broadcasting only one global probabilistic control signal to all EVs rather than dispatching individual control signals to each EV separately.

It is also to be noted that the EVA must provide rewards to EV owners for the provided flexibility as well as the additional battery degradation cost caused by V2G operations. In this study, it is assumed that the EVA contracts with EV users to reimburse them for their participation in ancillary services.

The application of the proposed SSM framework for frequency regulation and peak load shaving services and the probabilistic control approach for those ancillary services are presented in the following subsections.

#### 5.4.1 EV-SSM for Frequency Regulation

The frequency deviation of the system,  $\Delta f(t)$ , is mainly caused by generation-consumption mismatch [124] and is calculated as follows,

$$\Delta P_g(t) + \Delta P_{ev}(t) + \Delta P_w(t) - \Delta P_l(t) = 2H.d\Delta f(t)/dt + D.\Delta f(t) \quad (5.10)$$

where  $\Delta P_g(t)$ ,  $\Delta P_{ev}(t)$ ,  $\Delta P_w(t)$ , and  $\Delta P_l(t)$  are the power deviation of conventional generator (CG), EVA, wind generation, and load, respectively. The system inertia constant and total load damping coefficient are denoted by  $H$  and  $D$ , respectively. At each control cycle, based on the system frequency deviation  $\Delta f(k)$ , the required regulation power  $\Delta P_{req}(k)$  is calculated by (5.11) where  $\Delta f_{max}$  is the maximum allowable frequency deviation and  $\beta(k)$  is the frequency regulation coefficient which is obtained following the procedure presented in [64].

$$\Delta P_{req}(k) = \begin{cases} \beta(k)(\Delta f(k) - \Delta f_{max}), & \Delta f(k) > \Delta f_{max} \\ 0, & -\Delta f_{max} \leq \Delta f(k) \leq \Delta f_{max} \\ \beta(k)(\Delta f(k) + \Delta f_{max}), & \Delta f(k) < -\Delta f_{max} \end{cases} \quad (5.11)$$

The frequency regulation strategy with EV-SSM tends to allocate  $\Delta P_{req}(k)$  to the EVA and CG by considering their response times and regulation capacities.

As the EVA has faster response compared to the CG [125],  $\Delta P_{req}(k)$  is first allocated to EVA. If the provided regulation power by EVA is not sufficient to bring back the frequency to the permissible range, the remaining power will be allocated to the CG. To do so, first, based on the different EV responding modes, the regulation capacity of the EVA for increasing or decreasing its output power is estimated as follows.

$$\begin{cases} \Delta P_{ev}^+(k) = y_a(k) + y_b(k) + y_c(k) + y_d(k) & : \text{Inc} \\ \Delta P_{ev}^-(k) = y_e(k) + y_f(k) + y_g(k) + y_h(k) & : \text{Dec} \end{cases} \quad (5.12)$$

Then, the regulation capacities of the CG are determined by its ramp rate and power limits as,

$$\begin{cases} \Delta P_g^+(k) = \min(P_g^{max} - P_g(k), r_g \Delta t) & : \text{Inc} \\ \Delta P_g^-(k) = \max(P_g^{min} - P_g(k), -r_g \Delta t) & : \text{Dec} \end{cases} \quad (5.13)$$

where  $P_g(k)$  is the CG output power;  $r_g$  is the CG ramp rate; and  $P_g^{max}$  and  $P_g^{min}$  are the CG generation limits.

Finally, in order to realize the power allocation strategy, the regulated power of the EVA and the CG are determined by (5.14) and (5.15) for  $\Delta P_{req}(k) > 0$  and  $\Delta P_{req}(k) < 0$ , respectively; and if  $\Delta P_{req}(k) = 0$ , there is no need for regulation, so  $\Delta P_{ev}^*(k) = \Delta P_g^*(k) = 0$ .

$$\begin{cases} \Delta P_{ev}^*(k) = -\min(\Delta P_{req}(k), -\Delta P_{ev}^-(k)) \\ \Delta P_g^*(k) = -\min(\max(\Delta P_{req}(k) + \Delta P_{ev}^-(k), 0), \Delta P_g^-(k)) \end{cases} \quad (5.14)$$

$$\begin{cases} \Delta P_{ev}^*(k) = -\max(\Delta P_{req}(k), -\Delta P_{ev}^+(k)) \\ \Delta P_g^*(k) = -\max(\min(\Delta P_{req}(k) + \Delta P_{ev}^+(k), 0), \Delta P_g^+(k)) \end{cases} \quad (5.15)$$

#### 5.4.2 EV-SSM for Peak Load Shaving

The proposed EV-SSM can also be adopted to provide effective peak load shaving service. In this case, the power system control center issues a reference power trajectory to EVA and the aggregated EVs follow the reference power trajectory in real-time through the control signal broadcasted by the EVA. This load following strategy is an efficient algorithm for continuous

regulation which allows EVA to provide a long period of peak load shaving service by forcing the EVs to be charged at off-peak periods so that the stored energy in the EV batteries support the grid during the on-peak periods.

The required regulation power needed for following the load curve is determined by power equilibrium equation as follows,

$$\Delta P_{req}(k) = \Delta P_g(k) + \Delta P_{ev}(k) + \Delta P_w(k) - \Delta P_l(k) \quad (5.16)$$

One peak load shaving approach is to increase the base power generation set point of the CG. Doing so, the extra power produced by CG during the off-peak periods is translated to  $\Delta P_{req}(k)$  and is first allocated to EVA using (5.12)-(5.15) in real-time. This extra energy is stored in the battery of EVs. During the peak periods, when the load increases, the required amount of power is first provided by the EVA and if not sufficient the CG will increase its power set point. The main challenge here is to obtain an optimal flattened load curve with proper adjustment of the base power generation of the CG. This approach will be discussed further in Subsection 5.5.3. Note that instead of using (5.16) for real-time peak load shaving, the reference power trajectory can also be provided by the power system control center in longer time intervals, e.g., every 5 minutes [54]. In this case, various interpolation techniques (e.g., cubic spline interpolation) may be used to derive a more detailed reference power trajectory that can provide EVA with a reference power value every control cycle, e.g., every 15s.

### 5.4.3 Control Actions for EVA

Based on the regulated power of the EVA and the regulation capacity of the different responding modes, the input vector  $\mathbf{u}$  and the probabilistic control signal  $\mathbf{u}^p$  are calculated.

#### Determining the input vector ( $\mathbf{u}$ )

If  $\Delta P_{ev}^*(k) > 0$ , input vector reference values are determined by (5.17); and then input vectors are calculated by (5.18). In this situation, the EVA first calculates the regulation capacity of available EVs being switched from FCS to RCS (responding mode (a)). If this adjustment is not enough, all, or some of the EVs will be switched directly to IS instead of RCS (responding modes (a)+(b)). In case further power adjustment is still required, direct switching to RDS (responding modes (a)+(b)+(c)) or further to FDS (responding modes (a)+(b)+(c)+(d)) will be considered. In all above-mentioned responding modes, the switching priority is given to the EVs located in the state-bin with a higher SOC value.

$$\begin{cases} x_{u_1}^* = \min(\Delta P_{ev}^*, y_a) / (P_{avg}^{fast} N_{ev}) \\ x_{u_2}^* = \min(\Delta P_{ev}^* - y_a, y_b) / (P_{avg}^{reg} N_{ev}) \\ x_{u_3}^* = \min(\Delta P_{ev}^* - y_a - y_b, y_c) / (P_{avg}^{reg} N_{ev}) \\ x_{u_4}^* = \max(\Delta P_{ev}^* - y_a - y_b - y_c, 0) / (P_{avg}^{fast} N_{ev}) \end{cases} \quad (5.17)$$

$$\begin{cases} u_{1,N_s+1-j} = \max\left(\min\left(x_{u_1}^* - \sum_{h=1}^{j-1} x_{N_s+1-h}, (x_{N_s+1-j})\right), 0\right) \\ u_{2,N_s+1-j} = \max\left(\min\left(x_{u_2}^* - \sum_{h=1}^{j-1} (x_{2N_s+1-h} + u_{1,N_s+1-h})\right), \right. \\ \quad \left. (x_{2N_s+1-j} + u_{1,N_s+1-j})\right), 0 \\ u_{3,N_s+1-j} = \max\left(\min\left(x_{u_3}^* - \sum_{h=1}^{j-1} (x_{3N_s+1-h} + u_{2,N_s+1-h})\right), \right. \\ \quad \left. (x_{3N_s+1-j} + u_{2,N_s+1-j})\right), 0 \\ u_{4,N_s+1-j} = \max\left(\min\left(x_{u_4}^* - \sum_{h=1}^{j-1} (x_{4N_s+1-h} + u_{3,N_s+1-h})\right), \right. \\ \quad \left. (x_{4N_s+1-j} + u_{3,N_s+1-j})\right), 0 \end{cases} \quad (5.18)$$

where  $j \in \{1, 2, \dots, N_s\}$ .

If  $\Delta P_{ev}^*(k) < 0$ , input vector reference values are determined by (5.19); and then input vectors are calculated by (5.20). In this situation, the EVA first calculates the regulation capacity of available EVs being switched from FDS to RDS (responding mode (e)). If this adjustment is not enough, all, or some of the EVs will be switched directly to IS instead of RDS (responding modes (e)+(f)). In case further power adjustment is still required, direct switching to RCS (responding modes (e)+(f)+(g)) or further to FCS (responding modes (e)+(f)+(g)+(h)) will be considered. In all above-mentioned responding modes, the switching priority is given to the EVs located in the state-bin with a lower SOC value.

$$\begin{cases} x_{u_4}^* = \max(\Delta P_{ev}^*, y_e) / (P_{avg}^{fast} N_{ev}) \\ x_{u_3}^* = \max(\Delta P_{ev}^* - y_e, y_f) / (P_{avg}^{reg} N_{ev}) \\ x_{u_2}^* = \max(\Delta P_{ev}^* - y_e - y_f, y_g) / (P_{avg}^{reg} N_{ev}) \\ x_{u_1}^* = \min(\Delta P_{ev}^* - y_e - y_f - y_g, 0) / (P_{avg}^{fast} N_{ev}) \end{cases} \quad (5.19)$$

$$\left\{ \begin{array}{l} u_{4,j} = \min \left( \max \left( (x_{u_4}^* + \sum_{h=1}^{j-1} x_{4N_s+h}), (-x_{4N_s+j}) \right), 0 \right) \\ u_{3,j} = \min \left( \max \left( (x_{u_3}^* + \sum_{h=1}^{j-1} (x_{3N_s+h} - u_{4,h})) \right. \right. \\ \quad \left. \left. , (-x_{3N_s+j} + u_{4,j}) \right), 0 \right) \\ u_{2,j} = \min \left( \max \left( (x_{u_2}^* + \sum_{h=1}^{j-1} (x_{2N_s+h} - u_{3,h})) \right. \right. \\ \quad \left. \left. , (-x_{2N_s+j} + u_{3,j}) \right), 0 \right) \\ u_{1,j} = \min \left( \max \left( (x_{u_1}^* + \sum_{h=1}^{j-1} (x_{N_s+h} - u_{2,h})) \right. \right. \\ \quad \left. \left. , (-x_{N_s+j} + u_{2,j}) \right), 0 \right) \end{array} \right. \quad (5.20)$$

where  $j \in \{1, 2, \dots, N_s\}$ .

Finally, if  $\Delta P_{ev}^*(k) = 0$ , there is no need for control actions; therefore,  $\mathbf{u} = \mathbf{O}$ .

### Determining the probabilistic control signal ( $\mathbf{u}^p$ )

Input vector,  $\mathbf{u}$ , can be translated into the probabilistic control signal,  $\mathbf{u}^p$ . For  $\Delta P_{ev}^*(k) > 0$  and  $\Delta P_{ev}^*(k) < 0$  the probabilistic control signal is determined by (5.21) and (5.22), respectively. If  $\Delta P_{ev}^*(k) = 0$ , there is no need to switch EVs; thus,  $\mathbf{u}^p = \mathbf{O}$ .

$$\left\{ \begin{array}{l} u_{1,j}^p = \min \left( (u_{1,j}/x_j), 1 \right) \\ u_{2,j}^p = \min \left( (u_{2,j}/(x_{N_s+j} + u_{1,j})), 1 \right) \\ u_{3,j}^p = \min \left( (u_{3,j}/(x_{2N_s+j} + u_{2,j})), 1 \right) \\ u_{4,j}^p = \min \left( (u_{4,j}/(x_{3N_s+j} + u_{3,j})), 1 \right) \\ u_{1,N_s+1}^p = u_{2,N_s+1}^p = u_{3,N_s+1}^p = u_{4,N_s+1}^p = 1 \end{array} \right. \quad (5.21)$$

$$\left\{ \begin{array}{l} u_{4,j}^p = \min \left( (-u_{4,j}/x_{4N_s+j}), 1 \right) \\ u_{3,j}^p = \min \left( (-u_{3,j}/(x_{3N_s+j} - u_{4,j})), 1 \right) \\ u_{2,j}^p = \min \left( (-u_{2,j}/(x_{2N_s+j} - u_{3,j})), 1 \right) \\ u_{1,j}^p = \min \left( (-u_{1,j}/(x_{N_s+j} - u_{2,j})), 1 \right) \\ u_{1,N_s+1}^p = u_{2,N_s+1}^p = u_{3,N_s+1}^p = u_{4,N_s+1}^p = -1 \end{array} \right. \quad (5.22)$$

where  $j \in \{1, 2, \dots, N_s\}$ .

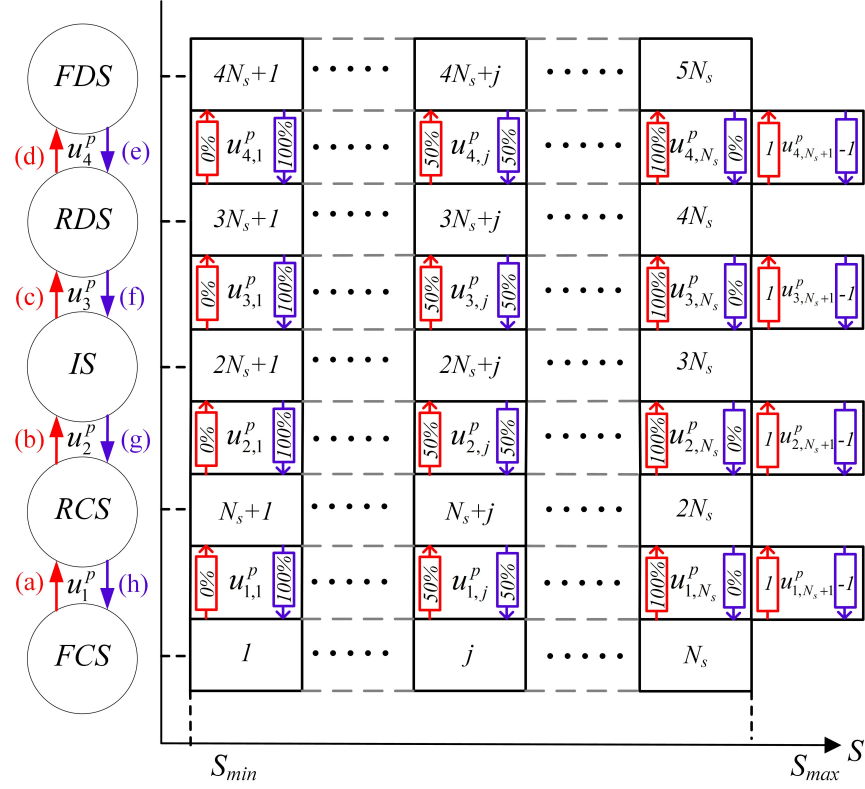


Figure 5.4 Structure of the probabilistic control signal

As shown in Fig. 5.4,  $u_{1,j}^p$ ,  $u_{2,j}^p$ ,  $u_{3,j}^p$  and  $u_{4,j}^p$  are vector elements taking values between  $[0, 1]$ . These vector elements are the percentage of EVs in the  $j$ th SOC interval which need to be switched between the connecting states associated to each vector. The additional elements  $u_{1,N_s+1}^p$ ,  $u_{2,N_s+1}^p$ ,  $u_{3,N_s+1}^p$  and  $u_{4,N_s+1}^p$  are added in order to control the direction of switching command. When the direction element is 1, the sequence of switching is FCS→RCS→IS→RDS→FDS (red arrows). Contrariwise, the direction element of -1 determines the switching sequence of FDS→RDS→IS→RCS→FCS (blue arrows).

#### 5.4.4 User-level implementation of probabilistic control signal

The probabilistic control signal ( $\mathbf{u}^p$ ) is communicated to all EVs globally. Each EV finds its corresponding elements in the received control signal according to its SOC value (see Fig. 5.4). For example, the EV located in the  $j$ th SOC interval considers  $u_{n,j}^p$ ,  $n \in \{1, 2, 3, 4\}$  elements which are regarded as the response probabilities. For any of these four elements, local controller of the EV will generate a random number  $\alpha_n$  with a uniform distribution of  $U(0, 1)$ . According to (5.23), if the response probability is greater than the generated random number, the EV will switch to the corresponding state. Otherwise, the EV will



stay in the current state. Note that the direction of switching is always determined by  $u_{n,N_s+1}^p, n \in \{1, 2, 3, 4\}$  elements of the probabilistic control signal.

$$\begin{cases} \text{If } \alpha_n < u_{n,j}^p, & \text{Switch} \\ \text{Otherwise,} & \text{Stay} \end{cases} \quad (5.23)$$

## 5.5 Case Studies And Simulation Results

### 5.5.1 EV population modeling

In this study, it is assumed that there are 10,000 EVs in the area covered by the EVA. In general, due to the probabilistic nature of Markov Transition Matrix (MTM) and broadcasted control signal ( $\mathbf{u}^p$ ), the prediction accuracy of EV-SSM significantly improves with higher numbers of EVs [64]. This subsequently reduces the tracking error of EVA output power, resulting in more efficient participation in ancillary services.

The driving behavior and the energy requirement of EVs in the population are modeled by defining distribution functions for their plug-in time, plug-out time, initial SOC when plugging in and desired SOC when plugging out. These distribution functions are listed in Table 5.1 and illustrated in Fig. 5.5 for three different EV fleets. We consider EV fleet No. 1 as the base case fleet where its distribution functions are determined by analyzing the daily personal travel behavior across the U.S. in [126,127]. In order to study the effect of different driving behavior and SOC level of EV population, in addition to the base case EV fleet No. 1, we have considered two more cases namely EV fleet No. 2 and EV fleet No. 3. This approach is consistent with the studies in [128,129] where the EVs are classified into different categories based on their travel patterns. We have adjusted the driving pattern of EVs in these two populations by modifying the distribution functions for plug-in time, plug-out time, initial SOC and desired SOC. Specifically, the EVs in fleet No. 2 spend more time in travelling compared to the base case EV fleet, consuming more energy. This is modeled by increasing the mean value of plug-in time and decreasing the mean value of plug-out time distribution functions, each by two hours; as well as increasing the mean value of desired SOC and decreasing the mean value of initial SOC distribution functions, each by 5%. In contrast, the EVs in fleet No. 3 spend less time in travelling compared to the base case EV fleet, consuming less energy. This is modeled by decreasing the mean value of plug-in time and increasing the mean value of plug-out time distribution functions, each by two hours; as well as decreasing the mean value of desired SOC and increasing the mean value of initial SOC distribution functions, each by 5%.

Table 5.1 EV fleet parameters\*

Parameter	Description	Fleet No. 1 (Base case)	Fleet No. 2	Fleet No. 3
$SOC^{in}$	SOC when plugging in	$N(0.3,0.05) \in [0.2,0.4]$	$N(0.25,0.05) \in [0.15,0.35]$	$N(0.35,0.05) \in [0.25,0.45]$
$SOC^{out}$	SOC when plugging out	$N(0.8,0.03) \in [0.7,0.9]$	$N(0.85,0.03) \in [0.75,0.95]$	$N(0.75,0.03) \in [0.65,0.85]$
$t^{in}$	Plug-in time [h]	$N(-6.5,3.4) \in [0.0,5.5]$ $N(17.5,3.4) \in [5.5,24]$	$N(-4.5,3.4) \in [0.0,7.5]$ $N(19.5,3.4) \in [7.5,24]$	$N(-8.5,3.4) \in [0.0,3.5]$ $N(15.5,3.4) \in [3.5,24]$
$t^{out}$	Plug-out time [h]	$N(8.9,3.4) \in [0.0,20.9]$ $N(32.9,3.4) \in [20.9,24]$	$N(6.9,3.4) \in [0.0,18.9]$ $N(30.9,3.4) \in [18.9,24]$	$N(10.9,3.4) \in [0.0,22.9]$ $N(34.9,3.4) \in [22.9,24]$

\* $N(\mu, \sigma) \in (\alpha, \beta)$  represents the normal distribution,  $\mu$  is the mean value,  $\sigma$  is the standard deviation, and  $(\alpha, \beta)$  is the variation range.

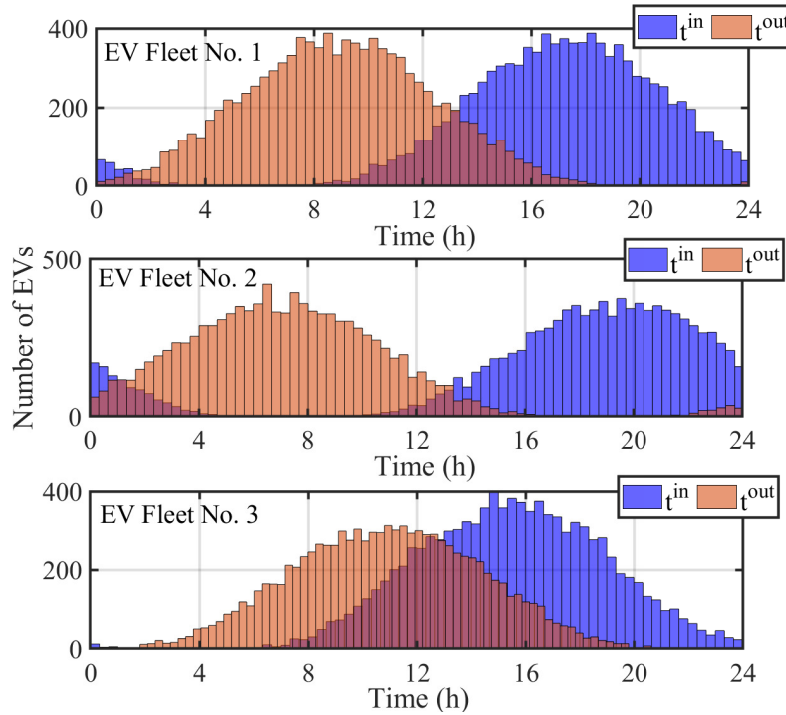


Figure 5.5 Plug-in/plug-out time distributions for different EV fleets

### 5.5.2 EV-SSM for Frequency Regulation

The proposed EV-SSM is used to provide frequency regulation service for a system involving population of 10,000 EVs, a wind generation system and a conventional generator with the parameters listed in Table 5.2. The power profiles of the wind generation system and the load are shown in Fig. 5.6. It is to be noted that the wind system is the main source of power fluctuations and hence frequency deviations.

Table 5.2 Simulation parameters\*

EV Parameters		
Parameter	Description	Value
$P^{reg}$	Regular charging power [kW]	U(5,7)
$P^{fast}$	Fast charging power [kW]	U(48,52)
$\eta^c/\eta^d$	Charging/discharging efficiency	U(0.88,0.95)
$Q$	Battery capacity [kWh]	U(20,30)
$SOC^{max}$	Maximum SOC value	0.95
$SOC^{min}$	Minimum SOC value	0.15

CG and Grid Parameters		
Parameter	Description	Value
$D$	Total load damping coefficient [MW/Hz]	20
$H$	System inertia constant [MW.s/Hz]	120
$f$	Frequency reference [Hz]	60
$\Delta f_{max}$	Allowable frequency deviation [Hz]	0.2
$r_g$	CG generation ramp rate [MW/min]	50
$P_g^{max}$	CG maximum power limit [MW]	500
$P_g^{min}$	CG minimum power limit [MW]	0

\*U( $\alpha, \beta$ ) represents the uniform distribution, and ( $\alpha, \beta$ ) is the variation range. The data of EV and grid is adapted from [64].

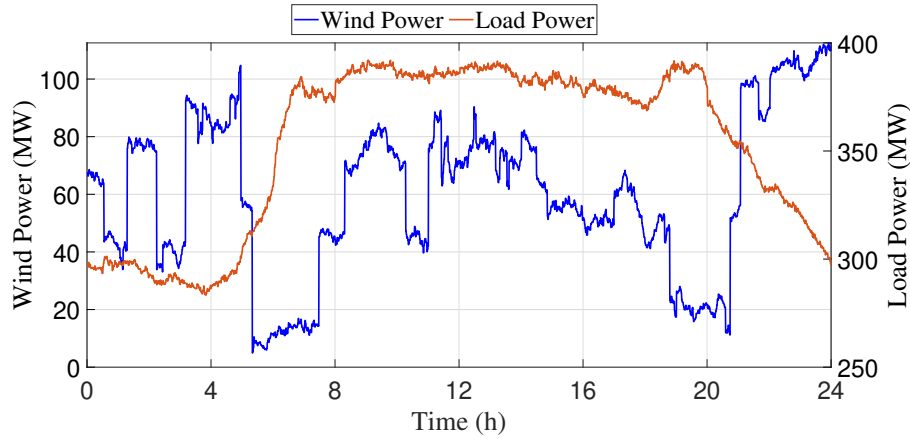


Figure 5.6 The wind and load power profiles adapted from [1]

### The effect of EVA participation

The following frequency regulation scenarios are defined in order to study the influence of EVA participation while taking into account various power levels in the EV-SSM structure:

- *Scenario a*: the CG is the only resource for the frequency regulation and the EVA is not involved.

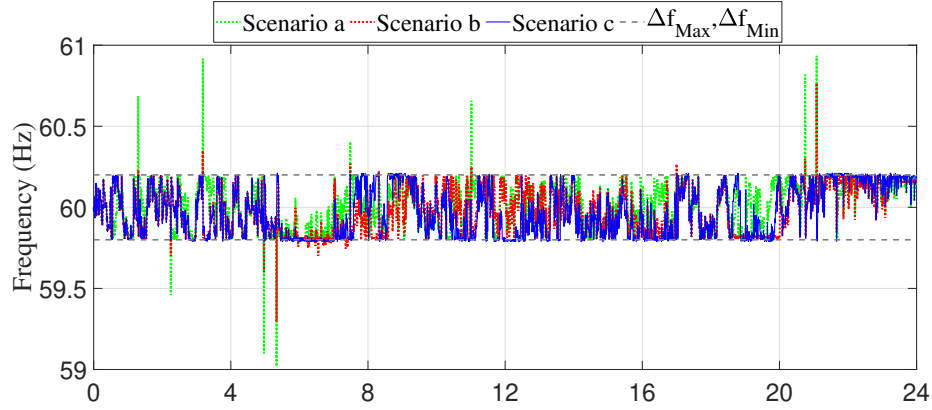


Figure 5.7 System frequency for scenarios a, b and c (fleet No. 1)

- *Scenario b*: the frequency regulation is first realized by EVA, and if the provided regulation is not sufficient, the CG will also contribute. In this scenario, only regular charging and discharging rates are considered for the EVs.
- *Scenario c*: similar to *Scenario b*, except the fact that both regular and fast charging/discharging rates are considered for the EVs.

Considering base case EV fleet (fleet No. 1), the frequency profile for different scenarios are compared in Fig. 5.7. It is seen that in *Scenario b*, the participation of EVA improves the frequency regulation. Moreover, in *Scenario c*, the system frequency is kept within the permissible range even after the severe power fluctuations in the system. This is due to the increased regulation capacity of EVA by considering the fast charging/discharging rates.

For the same EV fleet, the power profiles of the EVA and the CG for different scenarios are shown in Fig. 5.8 and Fig. 5.9, respectively. It is seen that in *Scenario a*, it is only the responsibility of the CG to limit the frequency deviations by making ramp adjustments to its output power. Therefore, the power profile of the EVA is not affected by frequency regulation commands. In *Scenarios b* and *c*, the EVA is the first resource to respond to the frequency regulation command. During the regulation period, when the EVA runs out of the regulation capacity, the CG will contribute to compensate the remaining required power. Considering the increased regulation capacity of EVA in *Scenario c*, the required ramp adjustments of CG is further reduced which decreases the stress on the CG. In order to verify this observation, the total ramp adjustment provided by the CG during the entire day is calculated for each scenario. It is found that for *Scenario a*, the total ramp adjustment is 1026.98 MW which is reduced to 327.25 MW and 292.43 MW in *Scenarios b* and *c*, respectively.

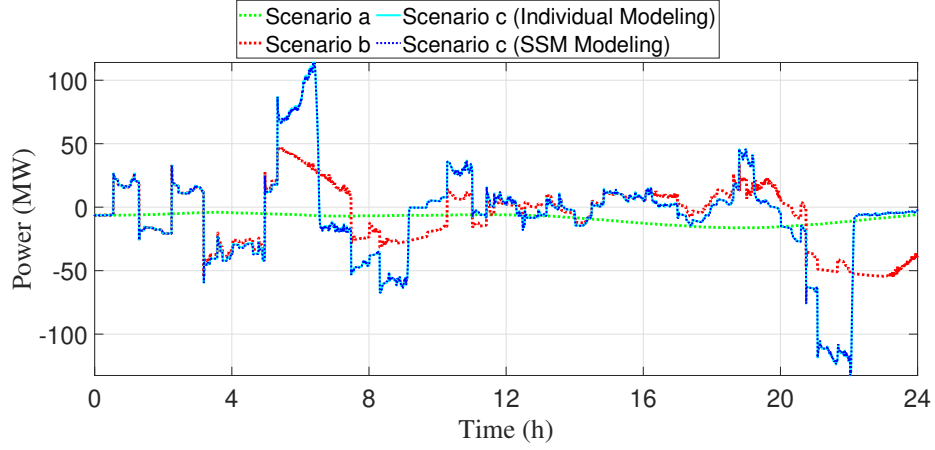


Figure 5.8 Power profile of the EVA for scenarios a, b and c (fleet No. 1)

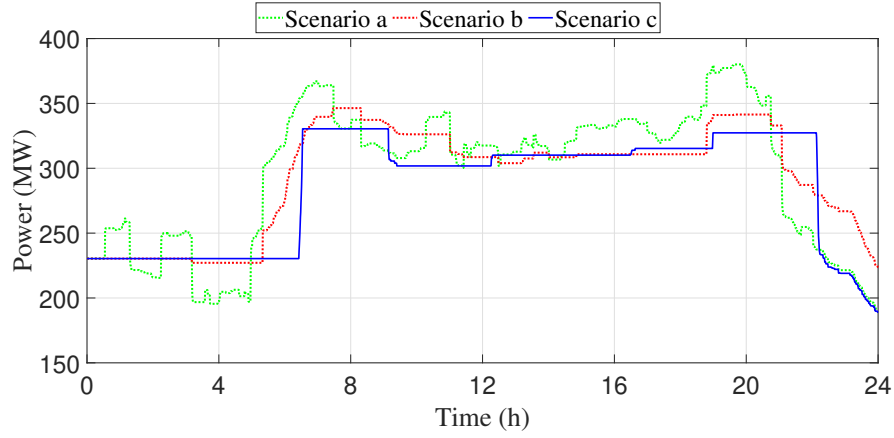


Figure 5.9 Power profile of the CG for scenarios a, b and c (fleet No. 1)

Fig. 5.8 also shows the aggregated power profile associated with the individual modeling of EVs for *Scenario c*. Note that in the EVA individual modeling, each individual EV is modeled separately using (5.1)-(5.4) and the aggregated power profile is derived by adding all individual EV power profiles using (5.24), instead of using SSM formulation in (5.5).

$$P_{agg}^{ind}(k) = \sum_{j=1}^{N_{ev}} P_{ev,j}(k) \quad (5.24)$$

As shown in Fig. 5.8, the aggregated power profile of individual modeling and that of SSM-based EVA modeling for *Scenario c* are perfectly matched, indicating that the proposed EVA model can accurately track the power adjustment command.

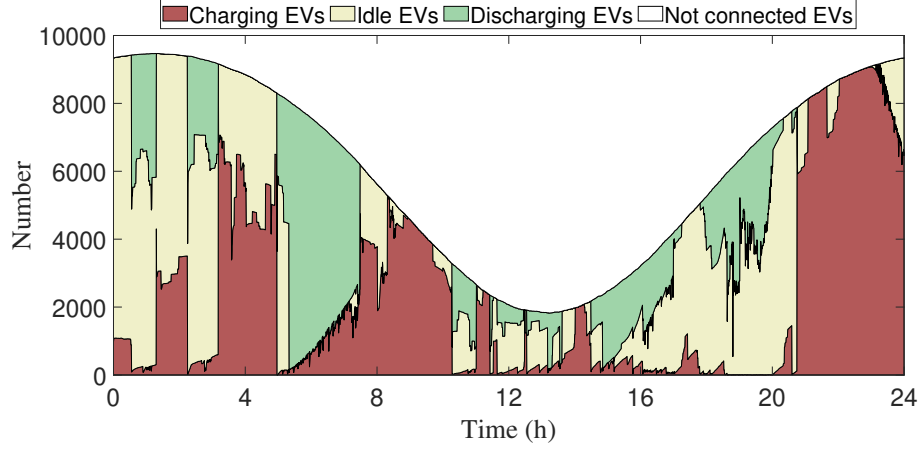


Figure 5.10 State distribution of EVs for scenario b (fleet No. 1)

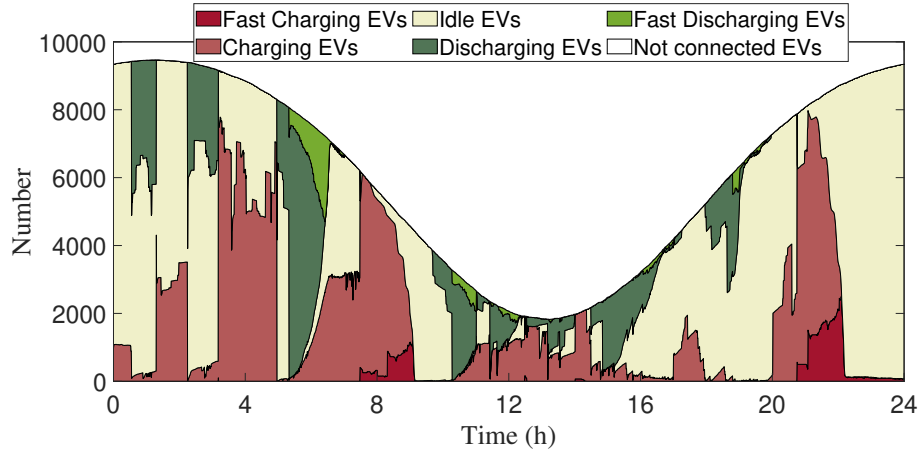


Figure 5.11 State distribution of EVs for scenario c (fleet No. 1)

The distribution of EVs between different connecting states during the frequency regulation with *Scenarios b* and *c* are shown in Fig. 5.10 and Fig. 5.11, respectively. The EVA in *Scenario b* runs out of regulation capacity when all none-forced-charging EVs are already switched to regular charging/discharging states. Comparing both figures, it is seen that *Scenario c* gives more flexibility for EVA to participate in frequency regulation when the severe wind power fluctuation happens in the system (e.g., 6h-9h AM and 21h-22h PM). This enhanced flexibility is realized by switching the EVs to fast charging/discharging states when required. When there is no available EV to respond to the regulation command with both regular and fast rates, the conventional generator will contribute.

To study the controlled charging/discharging behavior of individual EVs, the connection session ( $c$ ), the switch state ( $m$ ) and the *SOC* profile of two randomly chosen EVs from fleet

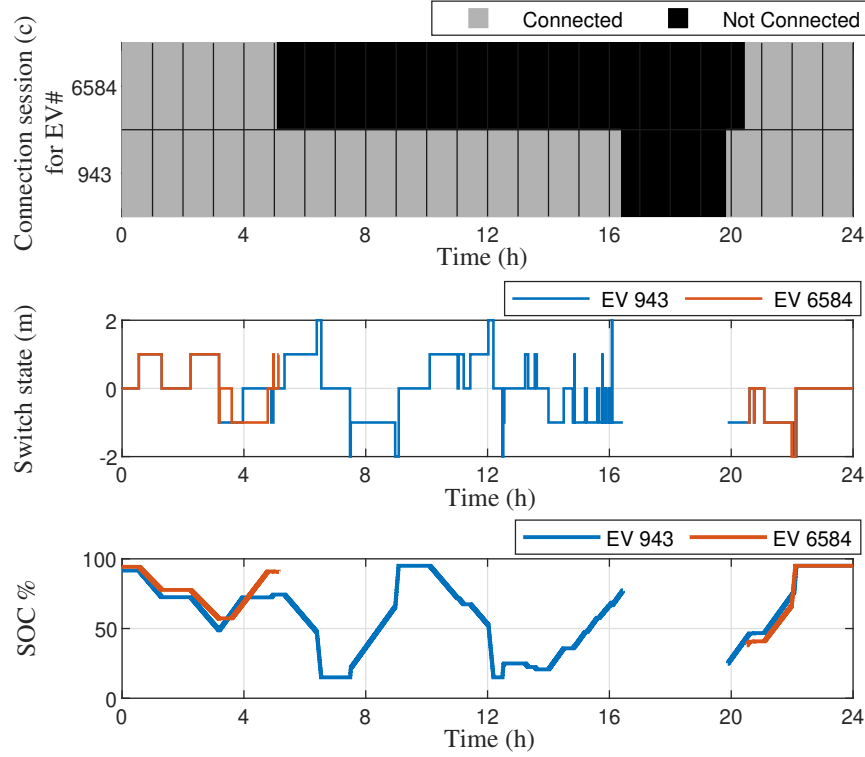


Figure 5.12 Connection session, switch state and SOC% for two EVs under scenario c (fleet No. 1)

No. 1 under *Scenario c* are shown in Fig. 5.12. Note that the connection session of each EV is derived directly from plug-in and plug-out distribution functions. It is seen that the EV 943 spends more time in the connected state than the EV 6584, giving it more opportunities to participate in regulation service by taking multiple switching actions between different charging and discharging states. During the regulation period, the SOC profile of both EVs remain within the permissible range (i.e. [15%, 95%]), respecting the SOC constraint of the EV batteries. Meanwhile, both EVs are charged to their desired SOC value before plugging out in order to meet the energy requirement condition for their next trip. It is worth noting that the EVs only spend the bare minimum of time in fast charging/discharging states. According to (5.17)-(5.20) in section 5.4.3, the fast charging/discharging states are the last state that EVs are switched "to" and the first state that EVs are switched "from" when responding to power regulation command. This strategy is needed to avoid excessive battery degradation of EVs caused by frequent switching to fast charging/discharging states.

Table 5.3 EVA communication performance under scenario c (fleet No. 1)

	Metric	Indiv. Modeling	SSM Modeling
Measurement Signal	ASTT	10,000	312.5
Control Signal	ASTT	97.17	1
	MSTT	8,568	1

Table 5.4 EVA computation performance under scenario c (fleet No. 1)

	Indiv. Modeling	SSM Modeling
Average Execution Time (s)	1.581	0.00143

To verify the effectiveness of the proposed EV-SSM in relieving the communication burden, the maximum signal transmission times (MSTT) and the average signal transmission times (ASTT) per dispatch period are calculated for control and measurement signals and compared for individual and SSM modelings in Table 5.3. It is seen that the ASTT of the measurement signal for SSM modeling is 32 times less than that for individual modeling. This is due to the fact that in SSM modeling, EV data measurements are carried out and transmitted to EVA every 32 control cycles. Furthermore, the EVA in individual modeling transmits an average of 97.17 individual control signals to EVs at each control cycle, whereas SSM modelling sends only one global control signal per control cycle. Comparing the MSTT values, it is seen that the MSTT of the control signal for the individual model is significantly higher than for the SSM modeling indicating higher communication burden where sudden load change is required. Therefore, it is concluded that the proposed EV-SSM can considerably relieve the bi-directional communication burden between EVA and EVs in both directions.

In order to evaluate the computational efficiency of the proposed EV-SSM, the average execution times (AET) for simulating the EVA with SSM modeling and the individual modeling are compared in Table 5.4. It is seen that with the SSM modeling, the AET per dispatch period is significantly reduced since the computational efficiency is mostly related to the number of state bins rather than the size of EV population. Note that the simulation is processed on a laptop with 1.8 GHz Intel Core i7-8550U CPU and 16.00 GB RAM.

### The effect of EV population characteristics

In the previous section, it has been shown that for EV fleet No .1, the *Scenario c* performs better in regulating system frequency putting less stress on the conventional generator compared to other scenarios. However, the driving behavior of EVs and their energy requirement



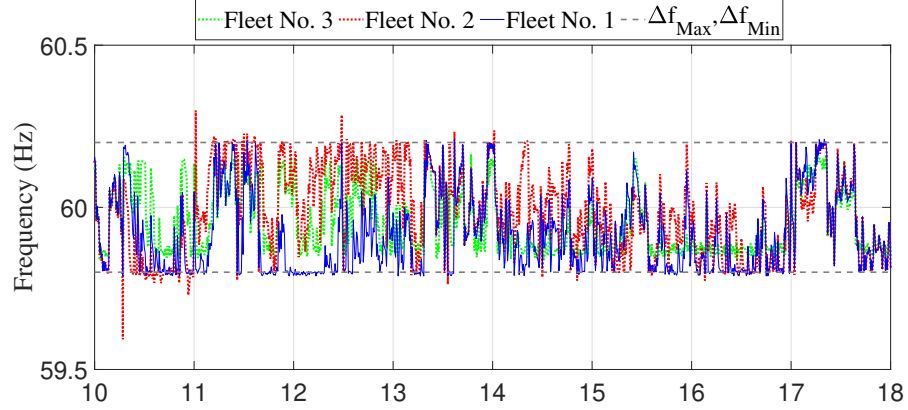
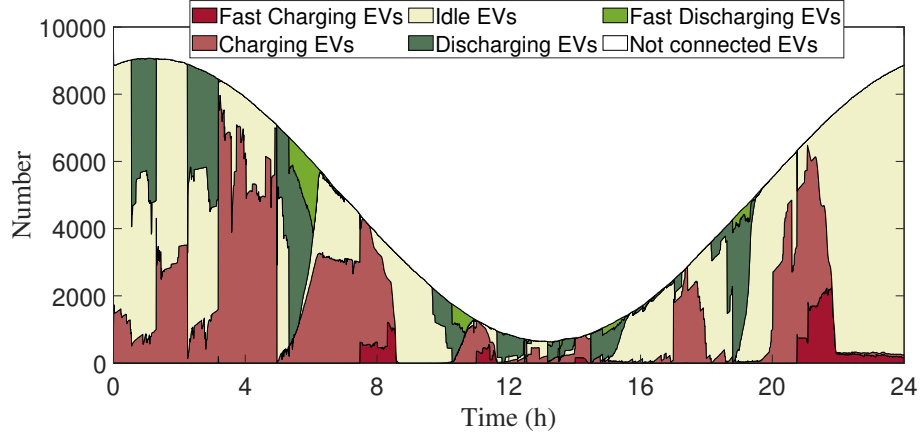


Figure 5.13 System frequency for scenario c considering different EV fleets

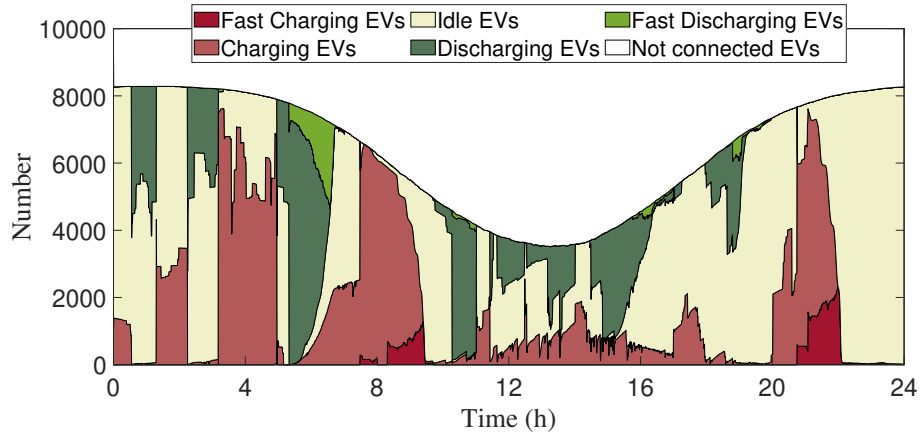
also affect the quality of frequency regulation service. Therefore, the system frequency for *Scenario c* considering different EV fleets are compared in Fig. 5.13; while the state distribution of EVs for fleet No. 2 and fleet No. 3 are shown in Fig. 5.14 (a) and (b), respectively. It is seen that the increased connection availability and less energy requirement of the EVs in fleet No. 3 (see Fig. 5.14 (b)) leads to better frequency regulation where the frequency is well kept below the limits all the time. However, in EV fleet No. 2, there are multiple occasions where the system frequency violates the predefined limits due to the following reasons: first, the EVs spend more time in traveling and are less available to be connected to the grid (see Fig. 5.14 (a)); and second, they need to be charged to higher SOC values within their limited connection period in order to support their extended travel time. These two factors reduce the regulation flexibility of the EV population resulting in a low-quality frequency regulation service. Comparing Fig. 5.14 (a) and (b) also shows that the reduced connection availability of EVs in fleet No. 2 between 10h and 15h forces more EVs to be switched to fast charging/discharging states. This is reasonable since during this period, there are not enough EVs available in fleet No. 2, to respond to frequency regulation commands using only regular charging/discharging rates.

### 5.5.3 EV-SSM for Peak Load Shaving

The proposed EV-SSM is also adopted to provide peak load shaving service for the system with the same number of EVs and a conventional generator with the same parameters. However, the wind and the load power profiles are scaled to be four times smaller to make the power contribution of EVs comparable with the load consumption profile.



(a) Fleet No. 2



(b) Fleet No. 3

Figure 5.14 State distribution of EVs for scenario c

### The effect of EVA participation

The following peak load shaving scenarios are defined in order to study the influence of EVA participation while taking into account various power levels in the EV-SSM structure:

- *Scenario d*: the CG is the only resource in the grid to follow the load and wind power profiles; and the EVA is not involved.
- *Scenario e*: the required power for peak shaving is offered by coordinating the EVA with the CG. In this scenario, both regular and fast charging/discharging rates are considered for the EVs.

Considering base case EV fleet (fleet No. 1), the power profiles of the EVA and the CG, and the energy profile of the EVA for *Scenarios d* and *e* are shown in Fig. 5.15, Fig. 5.16 and

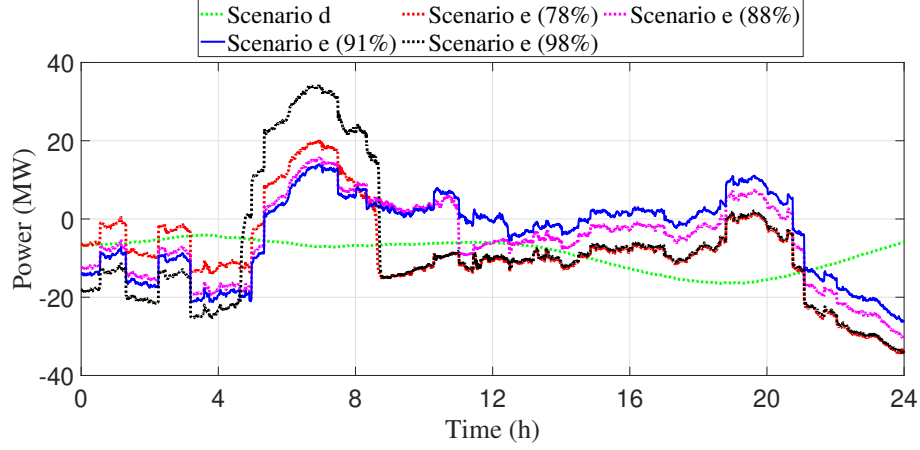


Figure 5.15 Power profile of the EVA for scenarios d and e (fleet No. 1)

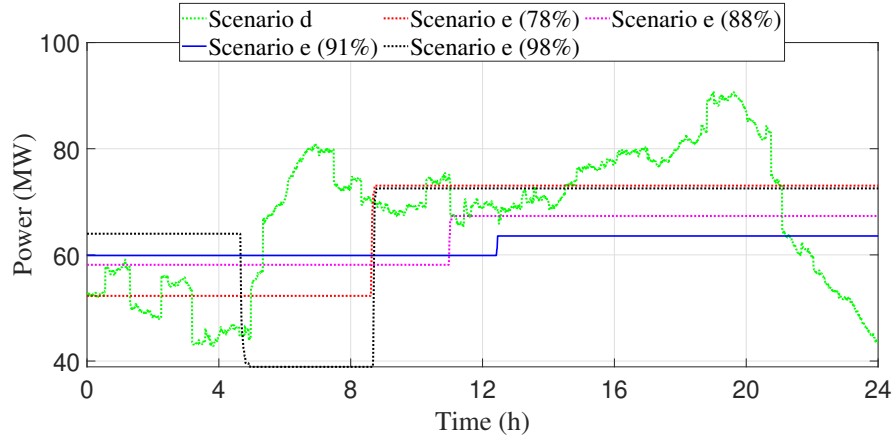


Figure 5.16 Power profile of the CG for scenarios d and e (fleet No. 1)

Fig. 5.17, respectively. For *Scenario e*, the performance of peak shaving has been studied by gradually increasing the base power generation of the CG. It has been found that the optimal flattened load curve is obtained with *Scenario e* when the base power generation of the CG is about 91% of the mean value of the load curve. For any base power below this amount (e.g. 88%), during the off-peak period, the EVA is not able to charge the aggregated EVs to reach the maximum amount of energy. Thus, the EVA runs out of energy shortly during the on-peak period and the CG has to contribute more. On the other hand, for higher CG base powers (e.g. 98%), the energy profile of the EVA hits its upper boundary (see Fig. 5.17) and all EVs switch to idle state after reaching their maximum SOC. This situation must be avoided as it results in rapid power reduction of the CG below the initial base power which affects the performance of peak shaving. Therefore, the optimal flattened load curve

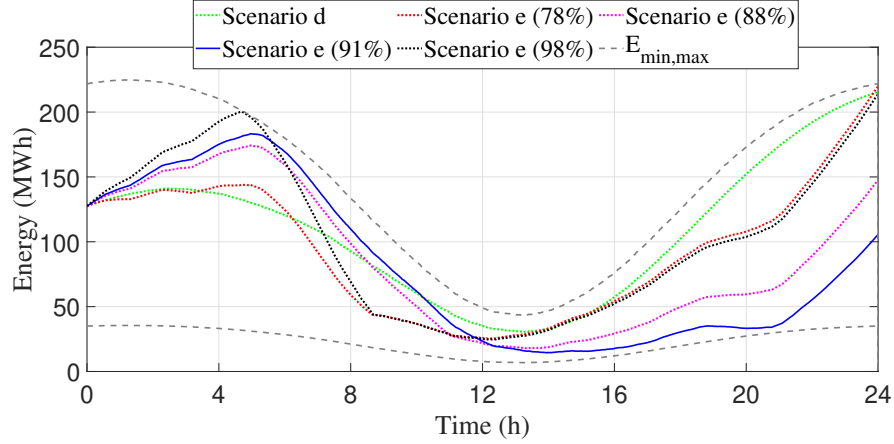


Figure 5.17 Energy profile of the EVA for scenarios d and e (fleet No. 1)

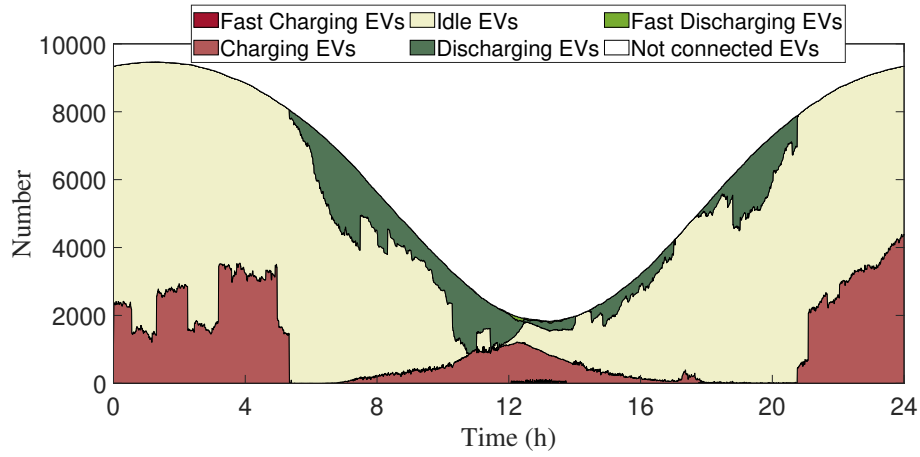


Figure 5.18 State distribution of EVs for scenario e with CG base power of 91% (fleet No. 1)

is obtained by adjusting the base power generation of the CG so that the peak energy of the EVA be slightly below its upper boundary without actually hitting it.

For the same EV fleet, the distribution of EVs between different connecting states during the peak load shaving with *Scenario e (91%)* is shown in Fig. 5.18. It is seen that the EVs gradually switch from the charging states toward the idle and the discharging states as the load consumption starts increasing. Note that some EVs are in the forced-charging states in the on-peak period and can not be switched to idle or discharging states. It is also to be noted that in peak load shaving service, due to the gradual load consumption variation, the contribution of EVA is mostly realized by regular charging/discharging rates of EVs even with the presence of fast charging.

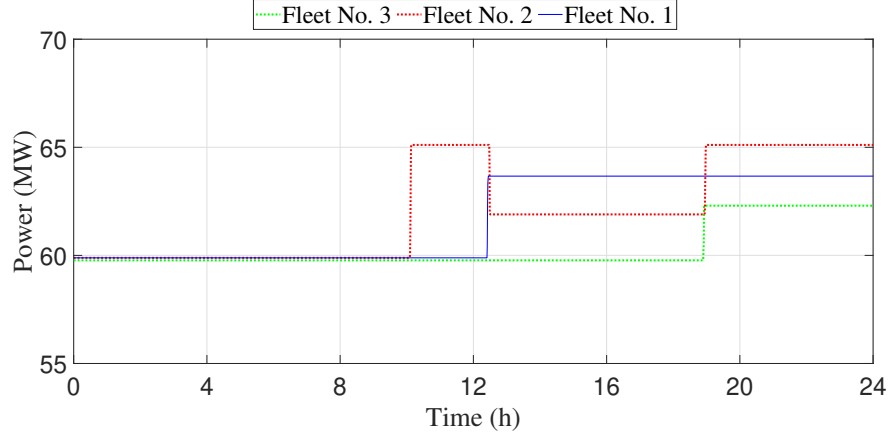


Figure 5.19 Power profile of the CG for scenario e (91%) considering different EV fleets

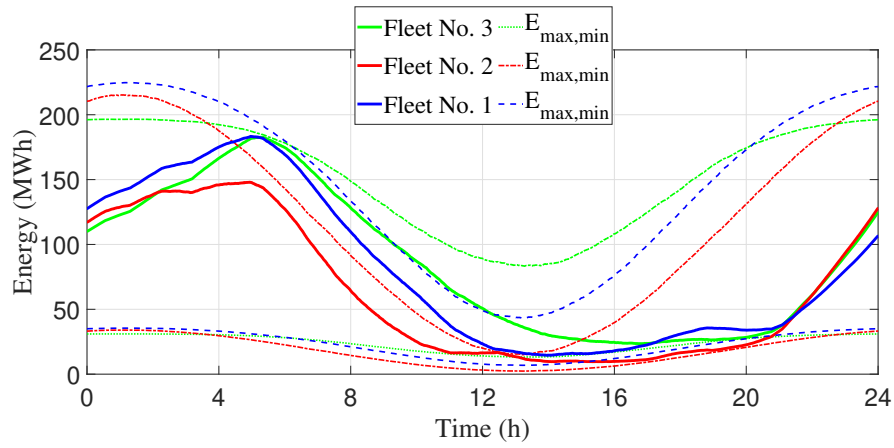


Figure 5.20 Energy profile of the EVA for scenario e (91%) considering different EV fleets

### The effect of EV population characteristics

In order to study the influence of EV population characteristics on the quality of peak load shaving service, the power profile of CG and energy profile of EVA for scenario e(91%) considering different EV fleets are compared in Fig. 5.19 and Fig. 5.20, respectively. It is seen that the maximum amount of energy in batteries of EV fleet No. 3 during the day (e.g, 7h-20h) is considerably higher compared to the other fleets due to their increased connection availability and less energy requirement. This helps the EVA to better contribute to peak load shaving resulting in smoother power profile of the CG as shown in Fig. 5.19. On the contrary, with EV fleet No. 2, the maximum amount of energy in EV batteries is far lower during the day, specially around noon. This increases the chance of EVA energy limits being exceeded by actual EVA energy profile resulting in more fluctuations in power profile of the CG in Fig. 5.19.

## 5.6 Conclusion

A new extended SSM-based EV aggregator has been proposed for the participation of large-scale population of EVs in frequency regulation and peak load shaving services. The urgent energy demand of fast-charging EVs has been modeled and the flexibility of EV aggregator is enhanced by enabling the EVs to participate in ancillary services with both regular and fast charging/discharging rates.

From the simulation results, it has been found that the proposed aggregation model can efficiently counteract the frequency excursions while reducing the stress on the conventional generator by decreasing its total ramp adjustments from 1026.98 MW to 292.43 MW. The frequency regulation service is achieved by accurate estimation of EVA regulation capacity with improved communicational and computational efficiencies. In particular, compared to individual modeling, the average signal transmission times (ASTT) of the control and measurement signals have been reduced by a factor of 97.17 and 32, respectively. In addition, using the proposed SSM, the maximum signal transmission times (MSTT) of the control signal has been reduced from 8568 to 1. Investigating the effectiveness of the proposed EVA for peak load shaving service, it has been found that the optimal flattened load curve can be obtained when the base power generation of the CG is about 91% of the mean value of the load curve. The performance of the proposed method has also been evaluated for three distinct EV fleets with different driving behaviors and SOC levels. It has been demonstrated that for the EV fleets with lower energy demand where the EVs spend more time being connected to the grid, the performance of both frequency regulation and peak load shaving services are improved.

In the future work, we will study the participation of the proposed EVA model in electricity markets. In particular, we will investigate how the EVA and end-users can provide ancillary services while maximizing their profits and minimizing the battery degradation due to V2G operations. Furthermore, the extension of state space model for aggregation of EVs with hybrid energy storage system, where a secondary energy storage is utilized to absorb power transients, is currently under investigation.

## CHAPTER 6    ARTICLE 3: A UNIFIED STATE SPACE MODEL FOR AGGREGATION AND COORDINATION OF LARGE-SCALE TCLS AND EVS FOR FREQUENCY REGULATION

This chapter is the reproduction of a peer-reviewed article which has been published in *Electric Power Systems Research* on 2021/06/01 [130].

- S. Kiani, K. Sheshyekani, and H. Dagdougui, “A unified state space model for aggregation and coordination of large-scale TCLs and EVs for frequency regulation,” *Electric Power Systems Research*, vol. 195, p. 107181, 2021.

### 6.1 Abstract

This paper presents a unified state space model for aggregation and coordination of large-scale thermostatically controlled loads (TCLs) and electric vehicles (EVs) to jointly participate in the frequency regulation of power systems. The proposed approach is characterized by low communication requirements and an accurate regulation capacity estimation. In order to perform the coordination with minimum communication burden, two distinct control signals, namely TCL-control signal and EV-control signal are developed. The former is communicated to all individual TCLs while the latter is communicated to all individual EVs. The simulations are conducted for a community-level microgrid including a large population of TCLs and EVs, a conventional generator and a wind generation system. It is shown that the proposed control structure can accurately describe the aggregated behaviour of a large population of TCLs and EVs and can efficiently counteract the frequency deviations. Moreover, the proposed control structure reduces the excessive dependence on one type of resource, minimizes the short cycling of TCLs, guarantees the energy requirements of the EVs and respects the energy constraints of the EV batteries.

### 6.2 Introduction

Demand Side Resources (DSRs) such as Thermostatically Controlled Loads (TCLs) and Electric Vehicles (EVs) can provide various ancillary services to the power grid via changing their nominal energy consumption [26, 123]. This is of particular importance for modern power systems due to the proliferation of intermittent renewable energy sources [83, 131]. TCLs can provide frequency regulation services by adopting a proper controller to interrupt their regular operating cycle and force them to switch to ON or OFF states when required [58].

As for EVs, the vehicle-to-grid (V2G) technology facilitates control of EV-grid bidirectional power flow to enhance system flexibility and frequency regulation capacity [8]. However, the efficient incorporation of TCLs and EVs in the frequency regulation services requires a reliable and fast control strategy which can respond to frequency deviations within seconds to one-minute intervals [18].

To date, different aggregation models have been proposed to estimate the regulation capacity and schedule the real-time power control for individual TCLs. The bin transition modeling technique has been proposed in many studies (e.g., [15, 58]), to describe the aggregated dynamic behaviour of a population of TCLs. This modeling approach is based on the temperature and switching evolution of the TCL population. A hierarchical control framework has been presented in [58] which allows autonomous participation of TCLs in frequency regulation through broadcasting trigger frequencies to each individual TCL separately. This approach guarantees a fast response between each control time interval. Some studies [33, 38, 58] have used a temperature-priority-based control framework in which the TCLs are sorted based on their temperatures and prioritised in a way that the number of ON/OFF switching actions for each TCL are minimized.

The regulation potential of an EV population is also exploited in the literature with various aggregation models. In order to control the real-time power of a population of EVs, the droop control [82], the least laxity [68], and the optimization [118] algorithms have been proposed. The droop control method in [82] regulates the charging and discharging power of EVs according to the frequency signal. In [68], the EV charging/discharging processes are constrained by both the laxity and the SOC merit orders. Authors in [74] proposed a queuing network to estimate the capacity of EVs for up/down regulations in frequency regulation service.

However, the above-mentioned approaches require a heavy data communication among the central controller and the end users (i.e., individual TCLs and EVs) which can be a limiting factor for large-scale implementation. To solve this issue, the State Space transitions Model (SSM) has been proposed in [10, 18, 62, 64] which introduce a reduced aggregation model resulting in less communication burden. However, these studies have used a single type of DSR which implies excessive dependence on one type of resource with less flexibility related to consumers behavior.

Although there are some studies investigating the integration of different types of DSRs, to the best of authors' knowledge, integrating TCLs and EVs has not been so far included in the SSM-based aggregators. The main interest for the SSM-based aggregation is its ability for providing regulation service with high accuracy and low communication burden. Therefore,



in order to take advantage of these benefits, we propose a unified SSM-based aggregation and coordination approach which enables large-scale TCLs and EVs to jointly participate in frequency regulation service with more flexibility, low communication burden and high accuracy.

Comparing with the related studies introduced earlier, the merits of the proposed aggregation method are summarized as follows:

- 1) The proposed unified SSM enables the TCLs and EVs to jointly participate in regulation service. This helps to increase the flexibility and capacity of DSR aggregator for prompt and efficient responding to generation-consumption variations.
- 2) The proposed aggregation-coordination approach is characterized by a low communication requirement because of the following reasons: First, the SSM replaces some real-time processes with offline processes which alleviates the amount of real-time communication; and second, the DSR controller uses a probabilistic control method to send control command to end-users which further helps to minimize the communication burden. Using this method, each individual TCL or EV uses the same control signal to decide whether it participates in frequency regulation service.
- 3) Using both TCLs and EVs as DSR resources reduces the excessive dependence on one type of resource. This is of great importance specially for EV population as it avoids excessive battery degradation of the EVs by reducing the total number of switching actions.

Simulations are done for a community-level microgrid including large number of TCLs and EVs, a conventional generator and a wind generation unit.

## 6.3 Modeling Framework

### 6.3.1 Individual TCL Model

The thermodynamic transition process of a TCL is mathematically described by the Equivalent Thermal Parameter (ETP) model. In discrete time settings, the ETP model is given as follows [58].

$$T(k+1) = a_{tcl}T(k) + (1 - a_{tcl})(T_a(k) - m_{tcl}(k)T_g) \quad (6.1)$$

with  $a_{tcl} \triangleq e^{\frac{-\Delta t}{R_{tcl}C_{tcl}}}$  and  $T_g \triangleq \pm R_{tcl}.COP.P_{tcl}^{rate}$ , where signs - and + are used for heating and cooling TCLs respectively. The inside air temperature and the switch status of the TCL are denoted by  $T$  and  $m_{tcl}$ , respectively. The descriptions of the other parameters are given

in Table 6.1. The time interval is denoted by  $\Delta t$  with  $k$  being the index of time interval. In order to maintain customer comfort, the hysteresis cycle of the TCL is governed by a local controller around a specified temperature reference  $T_{tcl}^{set}$  with dead-band of length  $\delta_{tcl}^{db}$ . Therefore, TCL switch status,  $m_{tcl}$ , can be determined according to the following rules for the heating mode:

$$m_{tcl}(k+1) = \begin{cases} 0, & T(k+1) \geq T_{tcl}^{set} + \frac{\delta_{tcl}^{db}}{2} : \text{OFF} \\ 1, & T(k+1) \leq T_{tcl}^{set} - \frac{\delta_{tcl}^{db}}{2} : \text{ON} \\ m_{tcl}(k), & \text{otherwise} \end{cases} \quad (6.2)$$

For the cooling TCL, the ON/OFF switching actions in (6.2) are in reverse. The local hysteresis cycle of the TCL can be interrupted by the controller in order to force the TCL to either (a) switch from ON to OFF (ON→OFF); or (b) switch from OFF to ON (OFF→ON).

### 6.3.2 Individual EV Model

Each individual EV is assumed to be plugged-in as soon as it finishes its trip and plugged-out right before its next trip. For a grid-connected EV, based on the power flow direction, three types of connecting states can be defined [123]:

- 1) *Charging State (CS)*: EV receives energy from the grid with rated power.
- 2) *Idle State (IS)*: EV is plugged-in without power exchange with the grid.
- 3) *Discharging State (DS)*: EV injects energy to the grid with rated power (Vehicle-to-Grid or V2G).

Based on the above-mentioned connecting states, the state of charge (*SOC*) variation of a connected EV can be described as follows [62].

$$SOC(k+1) = \begin{cases} SOC(k) - (P_{ev}^{rate}(k)/\eta_{ev}^d) \cdot (\Delta t/Q_{ev}), & m_{ev}(k) = 1 : \text{DS} \\ SOC(k), & m_{ev}(k) = 0 : \text{IS} \\ SOC(k) + (P_{ev}^{rate}(k)\eta_{ev}^c) \cdot (\Delta t/Q_{ev}), & m_{ev}(k) = -1 : \text{CS} \end{cases} \quad (6.3)$$

where  $m_{ev}$  is the switch status of the EV and is determined by (6.4). The descriptions of the other parameters are given in Table 6.1.

$$m_{ev}(k+1) = \begin{cases} -1, & c_{ev}(k+1) - c_{ev}(k) = 1: \text{Plug-in} \\ 0, & c_{ev}(k+1) - c_{ev}(k) = -1: \text{Plug-out} \\ 0, & SOC(k+1) \geq SOC^{max}: \text{Fully charged} \\ 0, & SOC(k+1) \leq SOC^{min}: \text{Fully discharged} \\ -1, & t_{ev}^{out} - (k+1)\Delta t \leq t_{ev}^{req}(k+1): \text{FCS} \\ m_{ev}(k), & \text{Otherwise} \end{cases} \quad (6.4)$$

In the equation above,  $c_{ev}$  is the connecting status of the EV and is 1 when the EV is connected and zero when the EVs is not connected to the grid. Not that the EV may switch to forced-charging state (FCS) to guarantee the desired SOC value when plugging out. In order to characterize the EV in FCS mode,  $t_{ev}^{req}$  is defined as the required time which is needed to charge EV to its desired SOC value,  $SOC^{out}$ , before plug-out time.  $t_{ev}^{req}$  is calculated as,

$$t_{ev}^{req}(k+1) = (SOC^{out} - SOC(k+1)) \cdot (Q_{ev} / (P_{ev}^{rate} \cdot \eta_{ev}^c)) \quad (6.5)$$

The local charging cycle of the EV can be interrupted by the controller in order to force the EV to either (a) switch from CS to IS (CS→IS) or (b) switch from IS to DS (IS→DS) or (c) switch from DS to IS (DS→IS) or (d) switch from IS to CS (IS→CS). Note that the CS→DS switching can be regarded as the combination of responding modes (a) and (b); while DS→CS switching is regarded as the combination of responding modes (c) and (d).

### 6.3.3 Unified State Space Model of Aggregated TCLs and EVs

The State Space Model (SSM) distributes the population of TCLs and EVs into several state-bins according to their operating conditions (e.g. switch status, indoor temperature of TCLs and SOC value of EVs) and then, controls their evolution between different bins [15].

Since TCLs in the heterogeneous population have different  $T_{tcl}^{set}$  and  $\delta_{tcl}^{db}$ , the first step is to normalize indoor temperature by  $T_n = (T - (T_{tcl}^{set} - 0.5\delta_{tcl}^{db})) / \delta_{tcl}^{db}$ ,  $T_n \in [0, 1]$ . Then, the normalized temperature dead-band is divided into  $N_{tcl}^s$  equal temperature intervals. As TCLs have two switch states (ON and OFF), each temperature interval is divided into two state-bins. Thus, at any moment, the state distribution of TCLs can be described by state vector  $\mathbf{x}_{tcl} \in \mathbb{R}^{2N_{tcl}^s \times 1}$ , whose elements represent the fraction of TCLs in the corresponding state-bin [18]. Fig. 6.1 illustrates the structure of the state-bins for a heating TCL. The green arrows represent the natural transition of TCL between different bins.

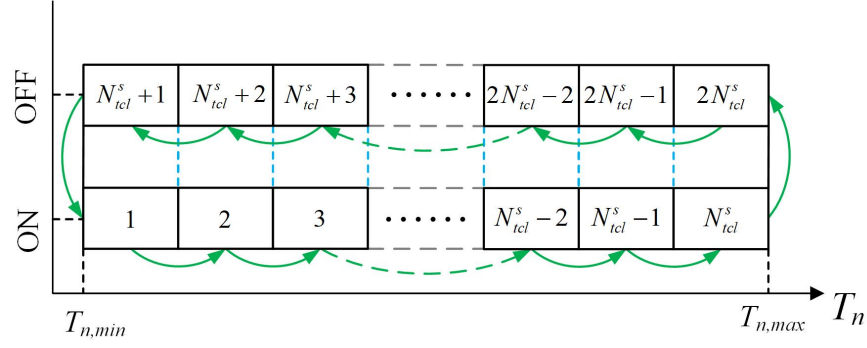


Figure 6.1 Structure of the state-bins for TCLs

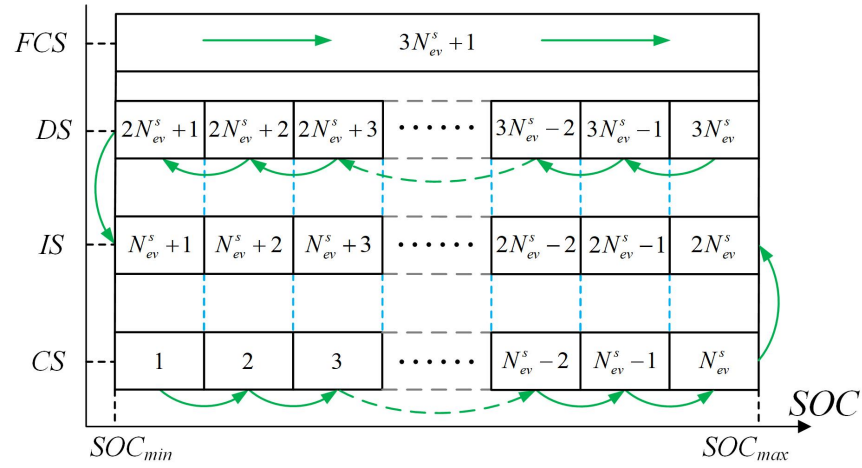


Figure 6.2 Structure of the state-bins for EVs

For the EVs, the SOC range is divided into  $N_{ev}^s$  equally spaced intervals. According to the connecting states (CS, IS and DS) of the EVs, each SOC interval is divided into three state-bins. As the EVs in forced-charging state are uncontrollable and have no regulation capacity, they need to be handled separately. Therefore, an extra state-bin is considered which accounts for the fraction of EVs in FCS mode. Thus, at any moment, the state distribution of EVs can be described by state vector  $\mathbf{x}_{ev} \in \mathbb{R}^{(3N_{ev}^s + 1) \times 1}$ . The structure of the state-bins for an EV is illustrated in Fig. 6.2.

The TCL and EV populations are aggregated by the State Space Model as follows:

$$\begin{aligned}
& \begin{cases} \mathbf{x}(k+1) = \mathbf{A}\mathbf{x}(k) + \mathbf{B}\mathbf{u}(k) + \boldsymbol{\omega}(k) \\ \mathbf{y}(k) = \mathbf{C}\mathbf{x}(k) \end{cases} \\
& \mathbf{x}(k) = [\mathbf{x}_{tcl}(k) \quad \mathbf{x}_{ev}(k)]^T \\
& \mathbf{u}(k) = [\mathbf{u}_{tcl}(k) \quad \mathbf{u}_{ev}(k) \quad \mathbf{v}_{ev}(k)]^T \\
& \boldsymbol{\omega}(k) = [\boldsymbol{\omega}_{tcl}(k) \quad \boldsymbol{\omega}_{ev}(k)]^T \\
& \mathbf{y}(k) = [y_{tcl}(k) \quad y_{ev}(k)]^T \\
& \mathbf{A} = \begin{bmatrix} \mathbf{A}_{tcl} & \mathbf{O} \\ \mathbf{O} & \mathbf{A}_{ev} \end{bmatrix}, \mathbf{B} = \begin{bmatrix} \mathbf{B}_{tcl} & \mathbf{O} & \mathbf{O} \\ \mathbf{O} & \mathbf{B}_{ev}^u & \mathbf{B}_{ev}^v \end{bmatrix}, \mathbf{C} = \begin{bmatrix} \mathbf{C}_{tcl} & \mathbf{O} \\ \mathbf{O} & \mathbf{C}_{ev} \end{bmatrix}
\end{aligned} \tag{6.6}$$

where  $y_{tcl}$  and  $y_{ev}$  are scalar values describing the aggregated power of TCLs and EVs, respectively.  $\mathbf{A}_{tcl} \in \mathbb{R}^{2N_{tcl}^s \times 2N_{tcl}^s}$  and  $\mathbf{A}_{ev} \in \mathbb{R}^{(3N_{ev}^s+1) \times (3N_{ev}^s+1)}$  are transposed Markov Transition Matrices (MTMs) whose elements are the transition probability of TCLs and EVs between the state-bins [37].  $\mathbf{u}_{tcl} \in \mathbb{R}^{N_{tcl}^s \times 1}$ ,  $\mathbf{u}_{ev} \in \mathbb{R}^{N_{ev}^s \times 1}$  and  $\mathbf{v}_{ev} \in \mathbb{R}^{N_{ev}^s \times 1}$  are input vectors which represent the effect of the controlled switching. The positive and the negative elements of  $\mathbf{u}_{tcl}$  define the fraction of TCLs in the corresponding temperature interval which are going to be turned ON and OFF, respectively. The positive and the negative elements of  $\mathbf{u}_{ev}$  denote the fraction of EVs in the corresponding SOC intervals which are due to take (CS→IS) and (IS→CS) switching actions, respectively. Likewise, the positive and the negative elements of  $\mathbf{v}_{ev}$  refer to the fraction of EVs in the corresponding SOC intervals for (IS→DS) and (DS→IS) switching actions, respectively.  $\mathbf{B}_{tcl}$ ,  $\mathbf{B}_{ev}^u$  and  $\mathbf{B}_{ev}^v$  are constant matrices which are structured in a way that realizes the control action of input vectors.  $\mathbf{C}_{tcl}$  and  $\mathbf{C}_{ev}$  are constant matrices and are used to obtain the output power of the aggregated TCLs and EVs, respectively. These constant matrices are defined as follows,

$$\begin{cases} \mathbf{B}_{tcl} = \begin{bmatrix} -\mathbf{I}_{N_{tcl}^s \times N_{tcl}^s} & \mathbf{I}_{N_{tcl}^s \times N_{tcl}^s} \end{bmatrix}^T \\ \mathbf{C}_{tcl} = P_{tcl}^{avg} N_{tcl} \begin{bmatrix} -\mathbf{1}_{1 \times N_{tcl}^s} & \mathbf{O}_{1 \times N_{tcl}^s} \end{bmatrix} \end{cases} \tag{6.7}$$

$$\begin{cases} \mathbf{B}_{ev}^u = \begin{bmatrix} -\mathbf{I}_{N_{ev}^s \times N_{ev}^s} & \mathbf{I}_{N_{ev}^s \times N_{ev}^s} & \mathbf{O}_{N_{ev}^s \times N_{ev}^s} & \mathbf{O}_{1 \times N_{ev}^s} \end{bmatrix}^T \\ \mathbf{B}_{ev}^v = \begin{bmatrix} \mathbf{O}_{N_{ev}^s \times N_{ev}^s} & -\mathbf{I}_{N_{ev}^s \times N_{ev}^s} & \mathbf{I}_{N_{ev}^s \times N_{ev}^s} & \mathbf{O}_{1 \times N_{ev}^s} \end{bmatrix}^T \\ \mathbf{C}_{ev} = P_{ev}^{avg} N_{ev}(k) \begin{bmatrix} -\mathbf{1}_{1 \times N_{ev}^s} & \mathbf{O}_{1 \times N_{ev}^s} & \mathbf{1}_{1 \times N_{ev}^s} & -1 \end{bmatrix} \end{cases} \tag{6.8}$$

where  $P_{tcl}^{avg}$  and  $P_{ev}^{avg}$  are the average rated power of the TCLs and EVs, respectively. The number of connected TCLs and EVs are given by  $N_{tcl}$  and  $N_{ev}$ , respectively. As the EVs in the FCS bin are uncontrollable, the last row of the matrices  $\mathbf{B}_{ev}^u$  and  $\mathbf{B}_{ev}^v$  are set to zero. Also,  $C_{ev,(3N_{ev}^s+1)}$  is set to  $-1$  to indicate the power consumption of the EVs in the FCS bin. The effect of noise processes are represented by  $\boldsymbol{\omega}_{tcl}$  and  $\boldsymbol{\omega}_{ev}$  in (6.6). Assuming sun exposure and door opening are insignificant to have major effects on temperature trajectories of the TCLs,  $\boldsymbol{\omega}_{tcl}$  can be set to zero. However, the effect of random traveling behavior of EVs,  $\boldsymbol{\omega}_{ev}$ , cannot be neglected. Therefore, the matrix  $\mathbf{x}_{ev}$  is updated in accordance to the plug-in and plug-out of the EVs during the control horizon [64].  $\boldsymbol{\omega}_{ev}$  is calculated as follows,

$$\boldsymbol{\omega}_{ev}(k) = \frac{N_{ev}^{out}(k) \left( \mathbf{x}_{ev}(k) - \mathbf{x}_{ev}^{out}(k) \right) - N_{ev}^{in}(k) \left( \mathbf{x}_{ev}(k) - \mathbf{x}_{ev}^{in}(k) \right)}{N_{ev}(k) + N_{ev}^{in}(k) - N_{ev}^{out}(k)} \quad (6.9)$$

where  $N_{ev}^{in}(k)$  and  $N_{ev}^{out}(k)$  are the predicted number of EVs plugged in and out during  $k$ th time interval, respectively with  $\mathbf{x}_{ev}^{in} \in \mathbb{R}^{(3N_{ev}^s+1) \times 1}$  being a state vector representing the state distribution of plugged-in EVs, which is derived from the distribution of plug-in SOC values.  $\mathbf{x}_{ev}^{out} \in \mathbb{R}^{(3N_{ev}^s+1) \times 1}$  is a state vector representing the state distribution of plugged-out EVs, which is obtained from the distribution of plug-out SOC values.

Based on the SSM and different responding modes, the regulation capacity of the aggregated TCLs and EVs for Up and Down regulations are estimated as follows,

$$\begin{cases} \Delta \mathbf{P}^l(k) = \mathbf{C}' \mathbf{x}(k) & : \text{Up regulation} \\ \Delta \mathbf{P}^h(k) = \mathbf{C}'' \mathbf{x}(k) & : \text{Down regulation} \end{cases} \quad (6.10)$$

$$\begin{aligned} \Delta \mathbf{P}^l(k) &= \begin{bmatrix} \Delta P_{tcl}^l(k) & \Delta P_{ev}^l(k) \end{bmatrix}^T \\ \Delta \mathbf{P}^h(k) &= \begin{bmatrix} \Delta P_{tcl}^h(k) & \Delta P_{ev}^h(k) \end{bmatrix}^T \\ \mathbf{C}' &= \begin{bmatrix} \mathbf{C}_{tcl}^{u,a} & \mathbf{O} \\ \mathbf{O} & \mathbf{C}_{ev}^{u,a} + \mathbf{C}_{ev}^{u,b} \end{bmatrix}, \mathbf{C}'' = \begin{bmatrix} \mathbf{C}_{tcl}^{l,b} & \mathbf{O} \\ \mathbf{O} & \mathbf{C}_{ev}^{l,c} + \mathbf{C}_{ev}^{l,d} \end{bmatrix} \end{aligned} \quad (6.11)$$

where  $\mathbf{C}_{tcl}^{u,a}$ ,  $\mathbf{C}_{tcl}^{l,b}$ ,  $\mathbf{C}_{ev}^{u,a}$ ,  $\mathbf{C}_{ev}^{u,b}$ ,  $\mathbf{C}_{ev}^{l,c}$  and  $\mathbf{C}_{ev}^{l,d}$  are the constant matrices as given below,

$$\begin{aligned}
& \begin{cases} \mathbf{C}_{tcl}^{u,a} = P_{tcl}^{avg} N_{tcl} \begin{bmatrix} 0 & \mathbf{1}_{1 \times N_{tcl}^s - 1} & \mathbf{0}_{1 \times N_{tcl}^s} \end{bmatrix} \\ \mathbf{C}_{tcl}^{l,b} = P_{tcl}^{avg} N_{tcl} \begin{bmatrix} \mathbf{0}_{1 \times N_{tcl}^s} & -\mathbf{1}_{1 \times N_{tcl}^s - 1} & 0 \end{bmatrix} \end{cases} \\
& \begin{cases} \mathbf{C}_{ev}^{u,a} = P_{ev}^{avg} N_{ev}(k) \begin{bmatrix} \mathbf{1}_{1 \times N_{ev}^s} & \mathbf{0}_{1 \times N_{ev}^s} & \mathbf{0}_{1 \times N_{ev}^s} & 0 \end{bmatrix} \\ \mathbf{C}_{ev}^{u,b} = P_{ev}^{avg} N_{ev}(k) \begin{bmatrix} \mathbf{1}_{1 \times N_{ev}^s} & \mathbf{1}_{1 \times N_{ev}^s} & \mathbf{0}_{1 \times N_{ev}^s} & 0 \end{bmatrix} \\ \mathbf{C}_{ev}^{l,c} = P_{ev}^{avg} N_{ev}(k) \begin{bmatrix} \mathbf{0}_{1 \times N_{ev}^s} & \mathbf{0}_{1 \times N_{ev}^s} & -\mathbf{1}_{1 \times N_{ev}^s} & 0 \end{bmatrix} \\ \mathbf{C}_{ev}^{l,d} = P_{ev}^{avg} N_{ev}(k) \begin{bmatrix} \mathbf{0}_{1 \times N_{ev}^s} & -\mathbf{1}_{1 \times N_{ev}^s} & -\mathbf{1}_{1 \times N_{ev}^s} & 0 \end{bmatrix} \end{cases} \quad (6.12)
\end{aligned}$$

As the TCLs with state-bin near the edge of temperature dead-band have recently been switched by their hysteresis temperature control, they should be locked and not be switched again by the controller in order to avoid short cycling. This is done by setting  $\mathbf{C}_{tcl,1}^{u,a}$  and  $\mathbf{C}_{tcl,2N_{tcl}^s}^{l,b}$  to zero. Furthermore, the last elements of matrices  $\mathbf{C}_{ev}^{u,a}$ ,  $\mathbf{C}_{ev}^{u,b}$ ,  $\mathbf{C}_{ev}^{l,c}$  and  $\mathbf{C}_{ev}^{l,d}$  are set to zero in order to exclude the power contribution of forced-charging EVs from regulation capacities.

Finally, the upper and lower boundaries of the aggregated power of TCLs and EVs are obtained as follows,

$$\begin{aligned}
P_{tcl}^u(k) &= y_{tcl}(k) + \Delta P_{tcl}^l(k), & P_{tcl}^l(k) &= y_{tcl}(k) + \Delta P_{tcl}^h(k) \\
P_{ev}^u(k) &= y_{ev}(k) + \Delta P_{ev}^l(k), & P_{ev}^l(k) &= y_{ev}(k) + \Delta P_{ev}^h(k)
\end{aligned} \quad (6.13)$$

## 6.4 Frequency Regulation

### 6.4.1 Framework of Frequency Regulation with SSM

The SSM is utilized to provide the frequency regulation service as shown in Fig. 6.3. The transition matrix  $\mathbf{A}$  is identified offline using the Hidden Markov Model (HMM) toolbox of MATLAB (hmmestimate function), assuming that the full state information from all population is available [15, 58]. This function calculates the maximum likelihood estimate of the transition probabilities of a hidden Markov model for sequence with known states. It is to be noted that in our modeling, the last 1200 history states of the TCLs and EVs are used for matrix identification. The transition matrix is used to build the SSM every  $T_f = 30s$ . The SSM is updated with the measured data every  $T_s = N_f T_f$  period, which is set to 8 minutes in this work. So the end-users' measured data is transmitted to the aggregator each 480s rather than 30s which reduces the amount of communication requirement. The renewing period is a choice parameter which is determined as a trade-off between the estimation accuracy and

the communication burden [110]. At each control cycle, based on the SSM, the Up and Down regulation capacities for the TCLs and EVs are estimated. Theoretically, more state-bins can lead to a more precise estimation of regulation capacities, at the expense of more complex control structure [58]. In this study, the state-bin structure is constructed by assuming  $N_{tcl}^s = N_{ev}^s = 20$ . According to the estimated regulation capacities and the frequency deviation, the power system control center calculates target power change for the aggregated TCLs, the aggregated EVs and the conventional generator. Then, the TCL/EV control center calculate the input vectors for updating the state vector. Finally, the input vectors are translated into two distinct control signals, namely TCL-control signal and EV-control signal. The former is communicated to all individual TCLs while the latter is communicated to all individual EVs. This further decreases the communication burden and probability of control error caused by transmitting numerous control signals to all TCLs and EVs individually. The structure of control signals will be discussed further in subsections 6.4.3 and 6.4.4.

Neglecting electromechanical transients, the frequency deviation is mainly caused by generation-consumption power imbalances as follows [124],



$$\begin{cases} \Delta P_g(t) + \Delta P_{DR}(t) - \Delta P_d(t) = 2H.d\Delta f(t)/dt + D.\Delta f(t) \\ \Delta P_{DR}(t) = \Delta P_{tcl}(t) + \Delta P_{ev}(t) \end{cases} \quad (6.14)$$

where  $\Delta P_{tcl}(t)$ ,  $\Delta P_{ev}(t)$  and  $\Delta P_g(t)$  are the power deviation of aggregated TCLs, EVs and conventional generator (CG), respectively. The system inertia constant is denoted by  $H$  while  $D$  represents the total load damping coefficient.  $\Delta P_d(t)$  accounts for the variation of both load and wind powers. It is noted that in our calculations, the wind power is regarded as a negative load. In discrete time settings, the frequency deviation can be obtained as follows,

$$\begin{cases} \Delta f(k+1) = (\Delta f(k) - \phi_1) \cdot \exp(-D.\Delta t/(2H)) + \phi_2 \\ \phi_1 = (\Delta P_g(k) - \Delta P_d(k) + \Delta P_{DR}(k+1))/D + \phi_0 \\ \phi_2 = (\Delta P_g(k+1) - \Delta P_d(k+1) + \Delta P_{DR}(k+1))/D + \phi_0 \\ \phi_0 = 2H(\Delta P_g(k+1) - \Delta P_d(k+1) - \Delta P_g(k) + \Delta P_d(k))/D^2\Delta t \end{cases} \quad (6.15)$$

At each control cycle, based on the system frequency deviation  $\Delta f(k)$ , the required power adjustment  $\Delta P_{adj}(k)$  is calculated by (6.16) where  $\Delta f_{max}$  is the maximum allowable frequency deviation and  $\lambda(k)$  is the frequency regulation coefficient which is obtained following the iterative procedure presented in [64].

$$\Delta P_{adj}(k) = \begin{cases} \lambda(k)(\Delta f(k) - \Delta f_{max}), & \Delta f(k) > \Delta f_{max} \\ 0, & -\Delta f_{max} \leq \Delta f(k) \leq \Delta f_{max} \\ \lambda(k)(\Delta f(k) + \Delta f_{max}), & \Delta f(k) < -\Delta f_{max} \end{cases} \quad (6.16)$$

As the CG has higher responding time compared to the EVs and TCLs [58],  $\Delta P_{adj}(k)$  is first allocated to TCLs and EVs, giving the priority to TCLs. If the provided regulation power is not sufficient, the remaining power is compensated by the CG. The regulation capacity of the CG for Up and Down regulations are determined by its ramp rate and power limits as,

$$\begin{cases} \Delta P_g^l(k) = \max(P_g^{min} - P_g(k), -r_g\Delta t) & : \text{Up regulation} \\ \Delta P_g^h(k) = \min(P_g^{max} - P_g(k), r_g\Delta t) & : \text{Down regulation} \end{cases} \quad (6.17)$$

where  $P_g(k)$  is the output power of the CG;  $r_g$  is the ramp rate of the CG; and  $P_g^{max}$  and  $P_g^{min}$  are the maximum and minimum output power limits of the CG, respectively.

For  $\Delta P_{adj}(k) > 0$  and  $\Delta P_{adj}(k) < 0$ , the target power changes of the aggregated TCLs,

the aggregated EVs and the CG can be determined by (6.18) and (6.19), respectively. If  $\Delta P_{adj}(k) = 0$ , then  $\Delta P_{tcl}^*(k) = \Delta P_{ev}^*(k) = \Delta P_g^*(k) = 0$ .

$$\begin{cases} \Delta P_{tcl}^*(k) = -\min(\Delta P_{adj}(k), -\Delta P_{tcl}^h(k)) \\ \Delta P_{ev}^*(k) = -\min(\max(\Delta P_{adj}(k) + \Delta P_{tcl}^h(k), 0), -\Delta P_{ev}^h(k)) \\ \Delta P_g^*(k) = -\min(\max(\Delta P_{adj}(k) + \Delta P_{tcl}^h(k) + \Delta P_{ev}^h(k), 0), \Delta P_g^h(k)) \end{cases} \quad (6.18)$$

$$\begin{cases} \Delta P_{tcl}^*(k) = -\max(\Delta P_{adj}(k), -\Delta P_{tcl}^l(k)) \\ \Delta P_{ev}^*(k) = -\max(\min(\Delta P_{adj}(k) + \Delta P_{tcl}^l(k), 0), -\Delta P_{ev}^l(k)) \\ \Delta P_g^*(k) = -\max(\min(\Delta P_{adj}(k) + \Delta P_{tcl}^l(k) + \Delta P_{ev}^l(k), 0), \Delta P_g^l(k)) \end{cases} \quad (6.19)$$

### 6.4.3 Control Actions for TCLs

Based on the target power change of the aggregated TCLs and the regulation capacity of both TCL responding modes, the input vector ( $\mathbf{u}_{tcl}$ ) and control signal ( $\mathbf{u}_{tcl}^s$ ) are determined.

#### Determine input vector ( $\mathbf{u}_{tcl}$ )

If  $\Delta P_{tcl}^*(k) = 0$ , there is no need for control actions. Therefore,  $\mathbf{u}_{tcl} = \mathbf{0}$ . If  $\Delta P_{tcl}^*(k) > 0$  (e.g. under frequency in the system),  $\mathbf{u}_{tcl}$  is determined by (6.20). Therefore, the ON TCLs will be switched OFF, giving the priority to the TCLs located in the state-bin with a higher temperature. If  $\Delta P_{tcl}^*(k) < 0$  (e.g. over frequency in the system),  $\mathbf{u}_{tcl}$  is determined by (6.21). Therefore, the OFF TCLs will be switched ON, giving the priority to the TCLs located in the state-bin with a lower temperature.

$$\begin{cases} x_{tcl}^{u*} = \min(\Delta P_{tcl}^*, \Delta P_{tcl}^l) / (P_{tcl}^{avg} N_{tcl}) \\ u_{tcl, N_{tcl}^s + 1 - j} = \max\left(\min\left(x_{tcl}^{u*} - \sum_{h=1}^{j-1} x_{tcl, N_{tcl}^s + 1 - h}\right), (x_{tcl, N_{tcl}^s + 1 - j})\right), 0 \end{cases} \quad (6.20)$$

$$\begin{cases} x_{tcl}^{u*} = \max(\Delta P_{tcl}^*, \Delta P_{tcl}^h) / (P_{tcl}^{avg} N_{tcl}) \\ u_{tcl, j} = \min\left(\max\left(x_{tcl}^{u*} + \sum_{h=1}^{j-1} x_{tcl, N_{tcl}^s + h}\right), (-x_{tcl, N_{tcl}^s + j})\right), 0 \end{cases} \quad (6.21)$$

where  $j \in \{1, 2, \dots, N_{tcl}^s\}$ .

### Determine identical control signal ( $\mathbf{u}_{tcl}^s$ )

$\mathbf{u}_{tcl}$  can be translated into the real control signal  $\mathbf{u}_{tcl}^s$  as follows: For  $\Delta P_{tcl}^*(k) > 0$  and  $\Delta P_{tcl}^*(k) < 0$ ,  $\mathbf{u}_{tcl}^s$  is determined by (6.22) and (6.23), respectively. In addition, if  $\Delta P_{tcl}^*(k) = 0$ , there is no need to switch TCLs. Thus,  $\mathbf{u}_{tcl}^s = \mathbf{O}$ .

$$\begin{cases} u_{tcl,j}^s = \min \left( (u_{tcl,j} / x_{tcl,j}), 1 \right) \\ u_{tcl,N_{tcl}^s+1}^s = 1 \end{cases} \quad (6.22)$$

$$\begin{cases} u_{tcl,j}^s = \min \left( (-u_{tcl,j} / x_{tcl,N_{tcl}^s+j}), 1 \right) \\ u_{tcl,N_{tcl}^s+1}^s = -1 \end{cases} \quad (6.23)$$

$u_{tcl,j}^s$  is a vector element which takes a value between  $[0, 1]$  and denotes the switching probability, meaning that a portion, or all of the TCLs located in the corresponding temperature interval need to switch between ON and OFF. An additional element  $u_{tcl,N_{tcl}^s+1}^s$  is added to  $\mathbf{u}_{tcl}^s$  to determine the direction of switching command. When  $u_{tcl,N_{tcl}^s+1}^s$  is 1,  $\mathbf{u}_{tcl}^s$  realizes the control action of ON→OFF and vice versa when  $u_{tcl,N_{tcl}^s+1}^s$  is -1. At each control cycle, the TCLs find their location in the received control signal  $\mathbf{u}_{tcl}^s$  based on their indoor temperature and switch state. Then, their local controllers will generate a random number subjected to a uniform distribution of  $U(0, 1)$  and calculate the response probability. If the random number is less than the corresponding  $u_{tcl,j}^s$ , then the TCL will switch. Otherwise, the TCL will stay in its current status. Note that at every dispatch period, only one global control signal is generated and broadcasted to all TCLs. This probabilistic control strategy avoids generating and distributing different control signals to heterogeneous TCLs individually which reduces the communication requirements between the TCL control center and the TCLs. The error of probabilistic control can be neglected in the presence of a large population of TCLs [64].

#### 6.4.4 Control Actions for EVs

Similar to the aggregated TCLs, based on the target power change of the aggregated EVs and the regulation capacity of the different EV responding modes, the input vectors ( $\mathbf{u}_{ev}$  and  $\mathbf{v}_{ev}$ ) and the control signals ( $\mathbf{u}_{ev}^s$  and  $\mathbf{v}_{ev}^s$ ) are determined.

### Determine input vectors ( $\mathbf{u}_{ev}$ and $\mathbf{v}_{ev}$ )

If  $\Delta P_{ev}^*(k) = 0$ , there is no need for control actions. Therefore,  $\mathbf{u}_{ev} = \mathbf{v}_{ev} = \mathbf{O}$ . If  $\Delta P_{ev}^*(k) > 0$  (e.g. under frequency in the system),  $\mathbf{u}_{ev}$  is determined by (6.24), and then  $\mathbf{v}_{ev}$  is determined

by (6.25). Therefore, the EVs in CS mode will be switched to IS mode and if not sufficient, the EVs in IS mode will be switched to DS mode. In all above-mentioned switching actions, the priority will be given to the EVs located in the state-bin with a higher SOC value.

$$\begin{cases} x_{ev}^{u*} = \min \left( \Delta P_{ev}^*, \Delta P_{ev}^{u,a} \right) / \left( P_{ev}^{avg} N_{ev} \right) \\ u_{ev, N_{ev}^s + 1 - j} = \max \left( \min \left( (x_{ev}^{u*} - \sum_{h=1}^{j-1} x_{ev, 2N_{ev}^s + 1 - h}), (x_{ev, N_{ev}^s + 1 - j}) \right), 0 \right) \end{cases} \quad (6.24)$$

$$\begin{cases} x_{ev}^{v*} = \max \left( \Delta P_{ev}^* - \Delta P_{ev}^{u,a}, 0 \right) / \left( P_{ev}^{avg} N_{ev} \right) \\ v_{ev, N_{ev}^s + 1 - j} = \max \left( \min \left( (x_{ev}^{v*} - \sum_{h=1}^{j-1} (x_{ev, 2N_{ev}^s + 1 - h} + u_{ev, N_{ev}^s + 1 - h})) \right. \right. \\ \left. \left. , (x_{ev, 2N_{ev}^s + 1 - j} + u_{ev, N_{ev}^s + 1 - j}) \right), 0 \right) \end{cases} \quad (6.25)$$

where  $j \in \{1, 2, \dots, N_{ev}^s\}$  and  $\Delta P_{ev}^{u,a}(k) = \mathbf{C}_{ev}^{u,a} \mathbf{x}_{ev}(k)$ .

If  $\Delta P_{ev}^*(k) < 0$  (e.g. over frequency in the system),  $\mathbf{v}_{ev}$  is determined by (6.26), and then  $\mathbf{u}_{ev}$  is determined by (6.27). Therefore, the EVs in DS mode will be switched to IS mode and if not sufficient, the EVs in IS mode will be switched to CS mode. In all above-mentioned switching actions, the priority will be given to the EVs located in the state-bin with a lower SOC value.

$$\begin{cases} x_{ev}^{v*} = \max \left( \Delta P_{ev}^*, \Delta P_{ev}^{l,c} \right) / \left( P_{ev}^{avg} N_{ev} \right) \\ v_{ev, j} = \min \left( \max \left( (x_{ev}^{v*} + \sum_{h=1}^{j-1} x_{ev, 2N_{ev}^s + h}), (-x_{ev, 2N_{ev}^s + j}) \right), 0 \right) \end{cases} \quad (6.26)$$

$$\begin{cases} x_{ev}^{u*} = \min \left( \Delta P_{ev}^* - \Delta P_{ev}^{l,c}, 0 \right) / \left( P_{ev}^{avg} N_{ev} \right) \\ u_{ev, j} = \min \left( \max \left( (x_{ev}^{u*} + \sum_{h=1}^{j-1} (x_{ev, N_{ev}^s + h} - v_{ev, h})), (-x_{ev, N_{ev}^s + j} + v_{ev, j}) \right), 0 \right) \end{cases} \quad (6.27)$$

where  $j \in \{1, 2, \dots, N_{ev}^s\}$  and  $\Delta P_{ev}^{l,c}(k) = \mathbf{C}_{ev}^{l,c} \mathbf{x}_{ev}(k)$ .

### Determine identical control signals ( $\mathbf{u}_{ev}^s$ and $\mathbf{v}_{ev}^s$ )

$\mathbf{u}_{ev}$  and  $\mathbf{v}_{ev}$  can be translated into the real control signals  $\mathbf{u}_{ev}^s$  and  $\mathbf{v}_{ev}^s$ , respectively. For  $\Delta P_{ev}^*(k) > 0$ ,  $\mathbf{u}_{ev}^s$  and  $\mathbf{v}_{ev}^s$  are determined by (6.28). For  $\Delta P_{ev}^*(k) < 0$ ,  $\mathbf{u}_{ev}^s$  and  $\mathbf{v}_{ev}^s$  are determined by (6.29). In addition, if  $\Delta P_{ev}^*(k) = 0$ , there is no need to switch EVs. Thus,  $\mathbf{u}_{ev}^s = \mathbf{v}_{ev}^s = \mathbf{O}$ .

$$\begin{cases} u_{ev,j}^s = \min \left( (u_{ev,j} / x_{ev,j}), 1 \right) \\ u_{ev,N_{ev}^s+1}^s = 1 \\ v_{ev,j}^s = \min \left( (v_{ev,j} / (x_{ev,N_{ev}^s+j} + u_{ev,j})), 1 \right) \\ v_{ev,N_{ev}^s+1}^s = 1 \end{cases} \quad (6.28)$$

$$\begin{cases} v_{ev,j}^s = \min \left( (-v_{ev,j} / x_{ev,2N_{ev}^s+j}), 1 \right) \\ v_{ev,N_{ev}^s+1}^s = -1 \\ u_{ev,j}^s = \min \left( (-u_{ev,j} / (x_{ev,N_{ev}^s+j} - v_{ev,j})), 1 \right) \\ u_{ev,N_{ev}^s+1}^s = -1 \end{cases} \quad (6.29)$$

where  $j \in \{1, 2, \dots, N_{ev}^s\}$ .

$u_{ev,j}^s$  and  $v_{ev,j}^s$  are vector elements which take values between  $[0, 1]$ .  $u_{ev,j}^s$  donates the percentage of EVs in  $j$ th SOC interval which need to be switched between CS and IS. An additional element  $u_{ev,N_{ev}^s+1}^s$  is added to  $\mathbf{u}_{ev}^s$  to determine the direction of switching command. When  $u_{ev,N_{ev}^s+1}^s$  is 1,  $\mathbf{u}_{ev}^s$  realizes the control actions of CS→IS and vice versa when  $u_{ev,N_{ev}^s+1}^s$  is -1. In a similar fashion,  $v_{ev,j}^s$  donates the percentage of EVs in  $j$ th SOC interval which need to be switched between IS and DS. An additional element  $v_{ev,N_{ev}^s+1}^s$  is added to  $\mathbf{v}_{ev}^s$  to determine the direction of switching command. When  $v_{ev,N_{ev}^s+1}^s$  is 1,  $\mathbf{v}_{ev}^s$  realizes the control actions of IS→DS and vice versa when  $v_{ev,N_{ev}^s+1}^s$  is -1. At each control cycle, the EVs find their location in the received control signals  $\mathbf{u}_{ev}^s$  and  $\mathbf{v}_{ev}^s$  based on their SOC value and connecting state. Then, their local controllers will generate a random number subjected to a uniform distribution of  $U(0, 1)$  and calculate the response probability. If the random number is less than the corresponding elements ( $u_{ev,j}^s$  or  $v_{ev,j}^s$ ), the EV will change its switch state. Otherwise, the EV will stay in its current status. Similar to the aggregated TCLs, the probabilistic control strategy reduces the communication requirements between the EV control center and the EVs.

## 6.5 Case Studies And Simulation Results

We consider a community-level microgrid which is powered by a conventional generator with the parameters listed in Table 6.1 and a wind generation system with the output power profile shown in Fig. 6.4. The wind power is the main source of power fluctuations and hence frequency deviations. Uncontrollable loads with the power profile shown in Fig. 6.4 account for the power consumption in the system. The community involves populations of

Table 6.1 Simulation Parameters

TCL Parameters		
Parameter	Description	Value*
$C_{tcl}$	TCL thermal capacitance [kWh/°C]	U(8,12)
$R_{tcl}$	TCL thermal resistance [°C/kW]	U(1.5,2.5)
$COP$	TCL coefficient of performance [-]	3
$P_{tcl}^{rate}$	TCL rated power [kW]	U(6,8)
$T_{tcl}^{set}$	TCL temperature reference [°C]	U(15,20)
$\delta_{tcl}^{db}$	TCL temperature dead-band width [°C]	2
$T_a$	Ambient temperature [°C]	5
EV Parameters		
Parameter	Description	Value*
$P_{ev}^{rate}$	EV rated power [kW]	U(5,7)
$\eta_{ev}^c/\eta_{ev}^d$	EV charging/discharging efficiency	U(0.88,0.95)
$Q_{ev}$	EV battery capacity [kWh]	U(20,30)
$SOC^{in}$	SOC of EV when plugging in	N(0.3,0.05) ∈ [0.2,0.4]
$SOC^{out}$	SOC of EV when plugging out	N(0.8,0.03) ∈ [0.7,0.9]
$t_{ev}^{in}$	EV plug-in time [h]	N(-6.5,3.4) ∈ [0.0,5.5]
		N(17.5,3.4) ∈ [5.5,24]
$t_{ev}^{out}$	EV plug-out time [h]	N(8.9,3.4) ∈ [0.0,20.9]
		N(32.9,3.4) ∈ [20.9,24]
$SOC^{max}$	EV maximum SOC value	0.95
$SOC^{min}$	EV minimum SOC value	0.15
Frequency Regulation Parameters		
Parameter	Description	Value
$D$	Total load damping coefficient [MW/Hz]	20
$H$	System inertia constant [MW.s/Hz]	120
$\Delta f_{max}$	Allowable frequency deviation [Hz]	0.2
$r_g$	CG generation ramp rate [MW/min]	50
$P_g^{max}$	CG maximum power limit [MW]	500
$P_g^{min}$	CG minimum power limit [MW]	0

\*U( $\alpha, \beta$ ) represents the uniform distribution, and ( $\alpha, \beta$ ) is the variation range.  
N( $\mu, \sigma$ ) ∈ ( $\alpha, \beta$ ) represents the normal distribution,  $\mu$  is the mean value,  $\sigma$  is the standard deviation, and ( $\alpha, \beta$ ) is the variation range. The data of TCL parameters is adapted from [58] and the data of EV and frequency regulation parameters is adapted from [126,127].

10,000 TCLs, 10,000 EVs which are aggregated by TCL/EV control center. It is assumed that the initial temperatures of the TCLs are uniformly distributed within the temperature dead-band.

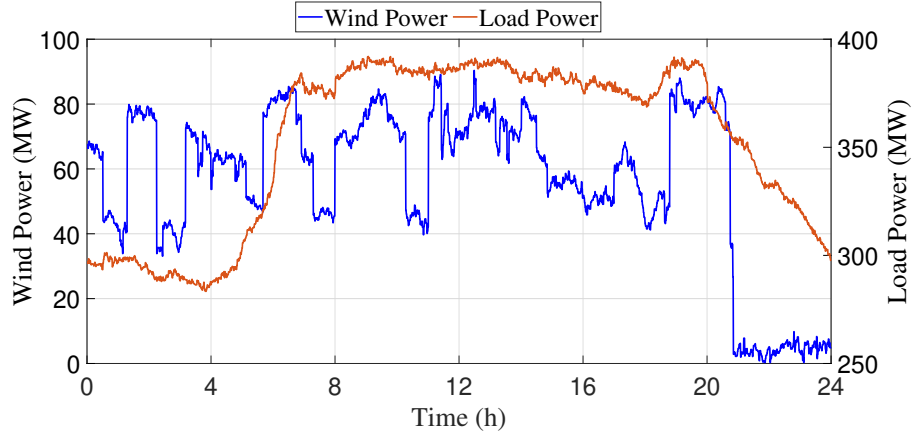


Figure 6.4 The wind and load power profiles adapted from [1]

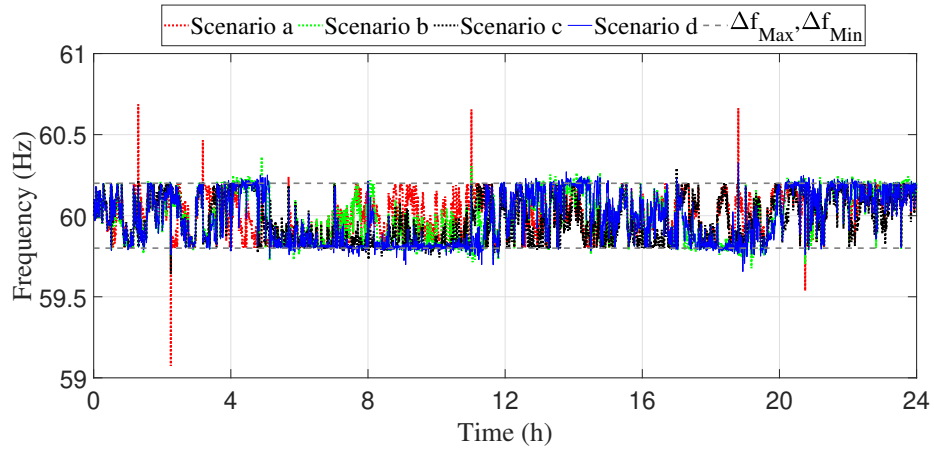


Figure 6.5 System frequency for scenarios a, b, c and d

The following frequency regulation scenarios are studied:

- 1) *Scenario a*: The CG is the only resource for the frequency regulation, the TCLs and EVs are not involved.
- 2) *Scenario b*: The frequency regulation is first realized by the aggregated TCLs, and if not sufficient, the CG will also contribute. In this scenario, the EVs are not involved.
- 3) *Scenario c*: The frequency regulation is first realized by the aggregated EVs, and if not sufficient, the CG will also contribute. In this scenario, the TCLs are not involved.
- 4) *Scenario d*: The frequency regulation is first realized by the aggregated TCLs, then by the aggregated EVs and if not sufficient, the CG will contribute.

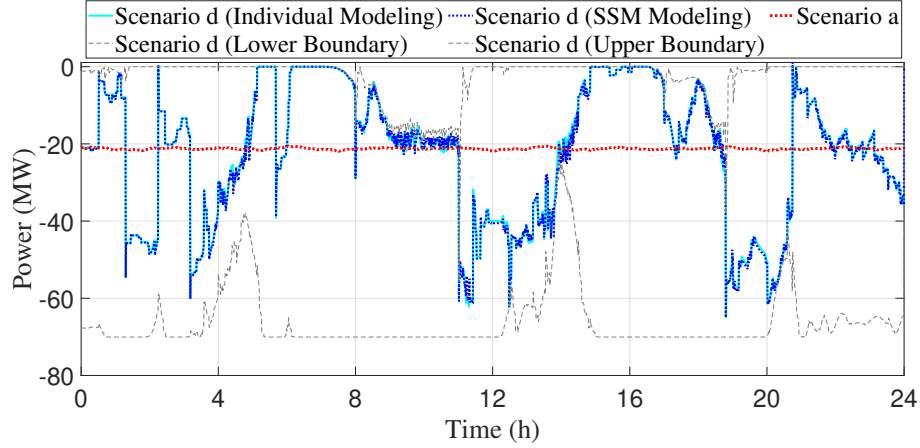


Figure 6.6 Power profiles of aggregated TCLs for scenarios a and d

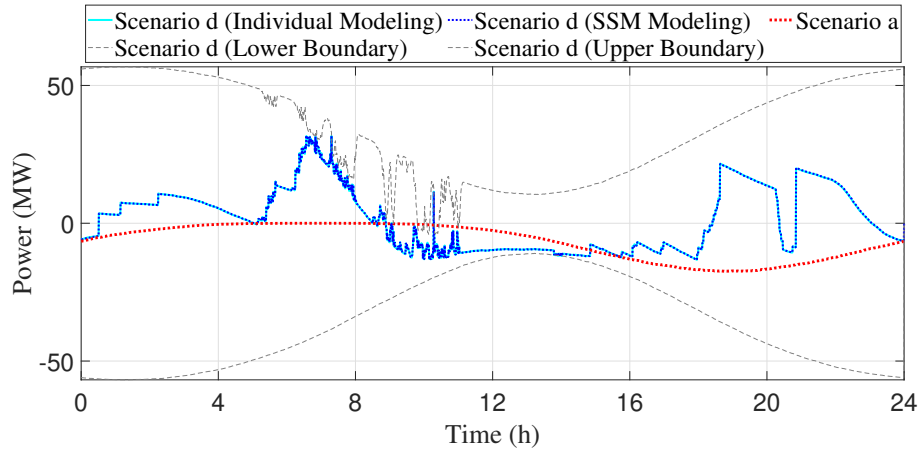


Figure 6.7 Power profiles of aggregated EVs for scenarios a and d

The frequency profiles for *Scenarios a, b, c* and *d* are compared in Fig. 6.5. It is seen that the participation of only TCLs, only EVs or both together, improves the frequency deviation and keep the system frequency within the desired range.

The power profile of the aggregated TCLs, the aggregated EVs and the CG for different *Scenarios* are shown in Fig. 6.6, Fig. 6.7 and Fig. 6.8, respectively. It is seen that in *Scenario a*, the steady state power profiles of the aggregated TCLs and EVs are not affected by frequency regulation commands. However, the CG tries to limit the frequency deviation by making fast adjustments to its output power. In *Scenario d*, aggregated TCLs are the first resource which respond to the frequency regulation command. During the regulation period, when the output power of the aggregated TCLs hits its lower or upper limits, the regulation capacity of the aggregated TCLs drops to zero. In this situation, the aggregated



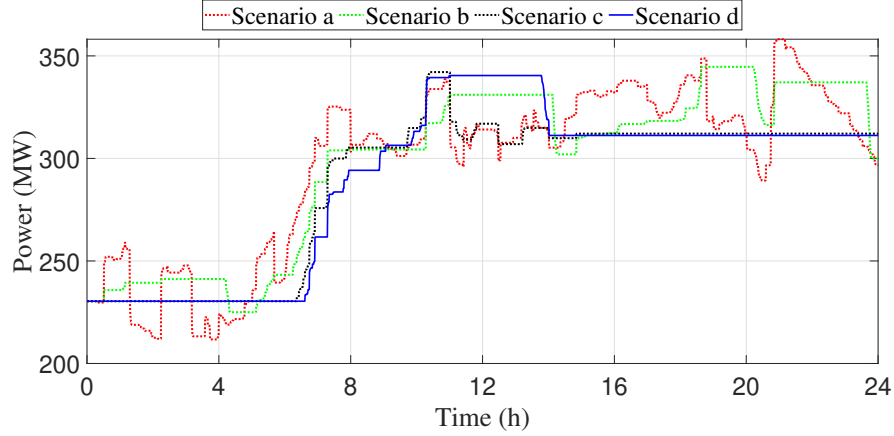


Figure 6.8 Power profiles of conventional generator for scenarios a, b, c and d

Table 6.2 Average number of switching actions

Scenario	TCL population	EV population
<i>Scenario a</i>	10.54	2
<i>Scenario b</i>	47.22	2
<i>Scenario c</i>	10.54	48.32
<i>Scenario d</i>	36.83	27.88

EVs contribute to compensate the remaining required power. If the regulation capacities provided by both aggregated TCLs and aggregated EVs are not sufficient to stabilize the system frequency, the CG will also participate.

It is seen from Fig. 6.8 that the proposed control structure can relieve the stress on the CG by mitigating the amount of required ramp adjustments, particularly for the case of *Scenario d*.

For *Scenario d*, Fig. 6.6 and Fig. 6.7 also show the power profile associated with the individual modeling of the TCLs and EVs, respectively. It can be depicted from these figures that the power profiles of the SSM-based aggregated TCLs and EVs are perfectly matched with those of the individual modeling.

For each scenario, the average number of switching actions of TCLs and EVs for one day are calculated as shown in Table 6.2. It is seen that for uncontrolled populations of TCLs and EVs in *Scenario a*, the average number of switching is 10.54 and 2, respectively. That means the uncontrolled population of TCLs repeat their temperature cycle roughly 5 times during one day ( $\approx 5$  "OFF" switching actions and  $\approx 5$  "ON" switching actions). However, the EVs in uncontrolled population change their switching states twice a day: once when they

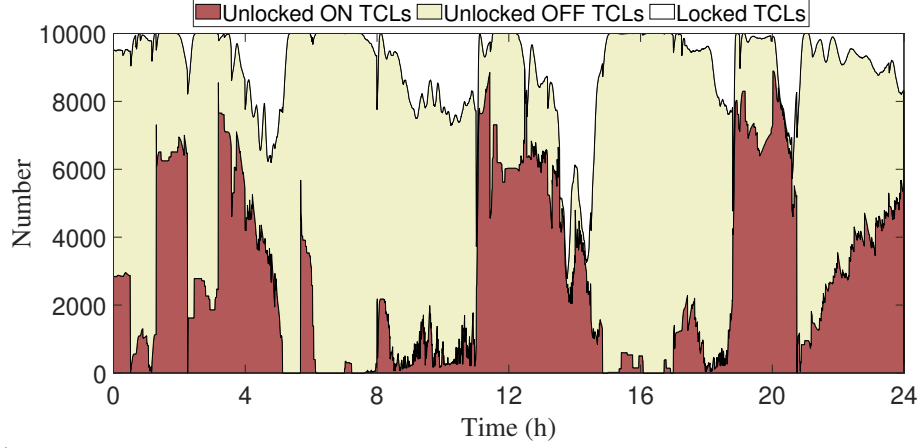


Figure 6.9 Number of TCLs with different switch states

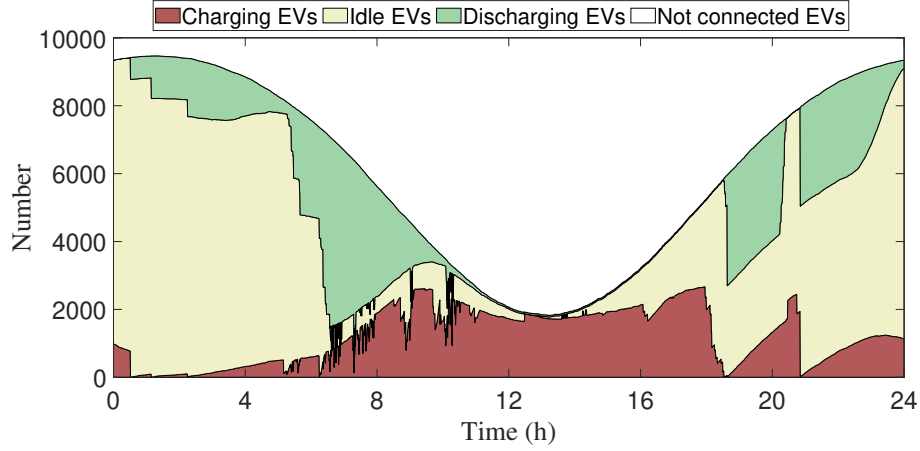


Figure 6.10 Number of EVs with different switch states

connect to the grid to start charging and once when they are fully charged or disconnected from grid before being fully charged. It is also seen that in *Scenario b* (TCL control only) the average number of switching actions for TCLs are more than those of *Scenario d* (TCL and EV control), which implies excessive dependence on TCLs. Similarly, in *Scenario c* (EV control only) the average number of switching actions for EVs are more than those of *Scenario d* (TCL and EV control), which implies excessive dependence on EVs. In *Scenario d*, both TCLs and EVs participate in regulation service with reduced average number of switching actions compared to *Scenario b* and *c*. This is of great importance particularly for EV population as it decreases the impact of excessive switching on battery life of EVs.

The distribution of TCLs and EVs between different switch states during the frequency control with *Scenario d* are shown in Fig. 6.9 and Fig. 6.10, respectively. It is seen that the

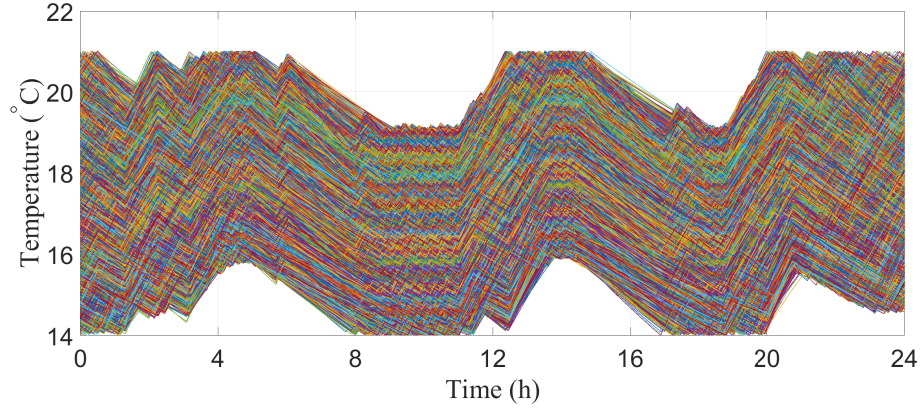


Figure 6.11 Indoor air temperature profiles of all TCLs for scenario c

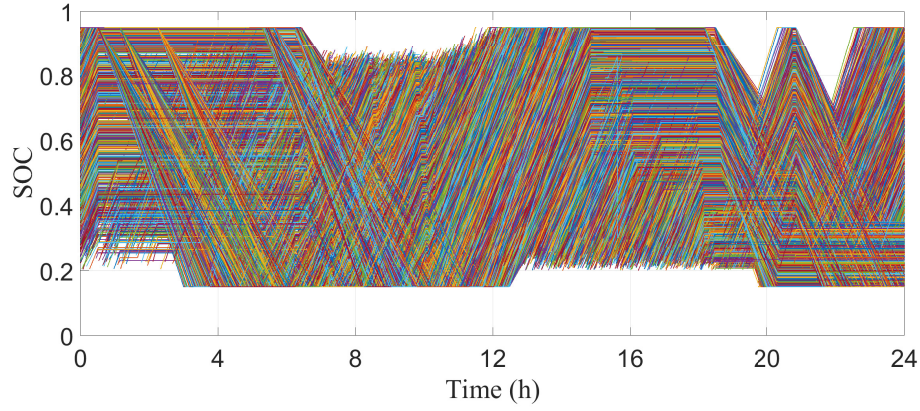


Figure 6.12 SOC of all EVs for scenario c

distribution curve for EVs has lower fluctuations than for TCLs as they are second resource to respond to regulation command which is when TCLs run out of regulation capacity. It is also seen that during a severe under frequency in the system (e.g. 7AM to 11AM), when the number of unlocked ON TCLs falls to zero, more EVs are switched to discharging state. Note that some EVs in charging state cannot be switched to idle or discharging states because they are in forced-charging state. When there are no available TCL or EV to respond to the regulation command, the conventional generator will contribute.

The indoor air temperatures of all TCLs for *Scenario d* are shown in Fig. 6.11 which reveals that, during the frequency regulation period, the indoor temperatures of all TCLs remains within the permissible dead-band  $[T_{tcl}^{set} - \delta_{tcl}^{db}/2, T_{tcl}^{set} + \delta_{tcl}^{db}/2]$ . This guarantees the end users' comfort requirements.

The SOC profiles of all EVs for *Scenario d* during the frequency regulation period are shown in Fig. 6.12. It can be seen from this figure that the SOC of all EVs remain within the permissible range (i.e.  $[0.15, 0.95]$ ). Hence, the energy constraints of the EV batteries are respected.

## 6.6 Conclusion

A new unified SSM-based aggregation-coordination approach has been proposed for the participation of large-scale TCLs and EVs in the Primary frequency control. The proposed aggregation-coordination approach offers an accurate regulation capacity estimation. Furthermore, the coordination is performed with a low communication burden. The simulations have been conducted for a community-level microgrid including 10,000 TCLs, 10,000 EVs, a conventional generator and a wind generation system. From the simulation, it has been shown that the proposed approach can accurately capture the aggregated behaviour of a large population of TCLs and EVs and can efficiently counteract the frequency excursions. In the proposed control structure, the short cycling of TCLs are minimized, the energy requirements of the EVs are guaranteed and the energy constraints of the EV batteries are respected.

## CHAPTER 7    ARTICLE 4: ADMM-BASED HIERARCHICAL SINGLE-LOOP FRAMEWORK FOR EV CHARGING SCHEDULING CONSIDERING POWER FLOW CONSTRAINTS

This chapter is the reproduction of an article that has been submitted to IEEE Transactions on Transportation Electrification on 2022/12/12.

- S. Kiani, K. Sheshyekani, and H. Dagdougui, "ADMM-Based Hierarchical Single-loop Framework for EV Charging Scheduling Considering Power Flow Constraints," in *IEEE Transactions on Transportation Electrification*, December 2022, submitted for publication.

### 7.1 Abstract

This paper presents a hierarchical distributed framework for optimal electric vehicle charging scheduling (EVCS). The proposed hierarchical EVCS structure includes distribution system operator (DSO) at the top layer, EV aggregators (EVAs) at the middle layer, and electric vehicles (EVs) charging stations at the bottom layer. A single-loop iterative algorithm is developed to solve the EVCS problem by combining the alternating direction method of multipliers (ADMM) and the distribution line power flow model (DistFlow). Using the single-loop structure, the primal variables of all agents are updated simultaneously at every iteration resulting in a reduced number of iterations and faster convergence. The developed framework is employed to provide charging cost minimization at the EV charging stations level, peak load shaving at the EVAs level, and voltage regulation at the DSO level. In order to further improve the performance of the optimization framework, a neural network-based load forecasting model is implemented to include the uncertainties related to non-EV residential load demand. The efficiency and the optimality of the proposed EVCS framework are evaluated through numerical simulations, conducted for a modified IEEE 13 bus test feeder which includes five EVAs each supplying 60 residential buildings (RBs) and their corresponding EVs.

### 7.2 Introduction

In recent years, transportation electrification has become one of the key solutions to tackle global climate change [132]. However, the large-scale penetration of electric vehicles (EVs) introduces a significant load increase to the power system. Inappropriate management of EVs load may lead to several negative impacts on the existing electric network, including new load

peaks, increased power fluctuations, overloading of lines, and voltage limit violations [89]. Owing to the controllable nature of EV loads and recent advancements in vehicle-to-grid (V2G) technology, these negative consequences can be mitigated by adopting a proper EV charging scheduling (EVCS) strategy.

To date, various EVCS strategies have been developed which can be generally categorized into centralized and distributed approaches. In centralized approaches, a central entity, e.g., distribution system operator (DSO), is responsible to collect and process the information of the whole EV network. Considering all decisions are made at a single point, centralized algorithms are known to have better accuracy and controllability [12]. However, the communication and computation burden for data collection, data processing, and control signal dispatching make them less efficient, especially for large-scale EV fleets. In order to improve both communication and computation efficiencies of centralized EVCS strategies, various control approaches have been developed majority of them focusing on employing some sort of reduced EV aggregation models [62, 64, 111, 130]. Within this concept, an EV aggregator (EVA) is defined as a middle agent who is in charge of controlling the smart interactions between the EV fleet and the DSO. Although the aforementioned approaches are successful in improving the efficiency of centralized EVCS strategies, they still suffer from a variety of security issues such as their vulnerability to single point failure and end-user data privacy concerns.

Contrary to centralized EVCS strategies, distributed approaches decompose the main problem into several sub-problems and distribute them over several agents (e.g., EVs, EVAs, and DSO) with some possible coupling in the constraints or/and objective functions [11]. These small-scale sub-problems are solved simultaneously but independently by each agent through a distributed and iterative procedure. As a result, distributed EVCS strategies are not only immune to single point failure, but also preserve the EV users' privacy since they do not require to exchange private information about EVs (e.g., battery capacity, energy consumption, and arrival and departure times, etc.) with the higher-level agent. Depending on the configuration of the communication network, distributed strategies are divided into bilayer and trilayer structures. The former consists of either EVA and EVs or DSO and EVAs while the latter includes all participating agents (e.g EVs, EVAs, and DSO).

Considering the bilayer structure, authors in [90] have used gradient projection algorithm to obtain the optimal charging profile of EVs for valley filling. A consensus-based primal-dual perturbation algorithm for a distributed consensus problem has been proposed in [91], which is applicable for EV charging coordination. A regularized primal-dual sub-gradient (RPDS) algorithm has been developed in [92] for solving multi-agent optimization problems

with coupled objectives and constraints. Although the developed RPDS shows an excellent convergence performance, the relative errors for optimal solution are significant. As an improvement, a novel shrunk primal-dual subgradient (SPDS) algorithm has been developed in [93], which significantly decreases the convergence errors by eliminating the need for regularization. A bilayer distributed EVCS has been developed in [94] by transforming the centralized formulation into two optimization phases via the lexicographic ordering method. However, the two phases are solved sequentially (not in parallel), which does not allow the practical implementation of the approach. More recently, considerable attention has been given to the alternating direction method of multipliers (ADMM) as a decomposition method due to its fast convergence and reasonable precision. In [89], the ADMM has been used to solve the bilayer optimization problem with the objectives of valley filling for EVA and charging cost minimization for EVs. A bilayer online ADMM has been proposed in [95], which is suitable for optimization problems with cost and constraints that evolve over time.

Considering the trilayer structure, authors in [96] have developed an ADMM-based EVCS strategy with the aim of maximizing the comfort of EV users. While the proposed model has a trilayer structure, no optimization objectives are considered for the EVA and DSO layers. In [97], a trilayer robust EVCS strategy has been developed to minimize the total operating cost of the system by coordinating the DSO and EVAs. Although the proposed model is effective in reducing operating costs, it is not flexible because of the strict assumption on the objective function of the DSO, while ignoring the objective function of the EVAs. Authors in [98] addressed this issue by taking into account the objectives and constraints of all agents. However, their approach suffers from a significant communication burden and a slow convergence rate. The trilayer EVCS structures proposed in [99–101] include two bilayer iterative loops which are linked together as a nested-loop structure. Despite including various stakeholders, these developed approaches are still time-consuming and are not computationally efficient as a result of using nested-loop hierarchical structures. As a solution, authors in [102] proposed a hierarchical distributed multi-agent framework in which the local optimization problems of all agents are solved simultaneously in a single iterative loop. However, the developed framework does not include the distribution network model and the power flow constraints.

Within the context alluded above, it is seen that the previously developed bilayer structures do not utilize the full potential of the EVCS as the optimization problem of the agent(s) in one layer (either EVs, EVAs, or DSO layer) is missing. On the other hand, while the trilayer structures have more degree of flexibility, they suffer from a number of issues, some of which are summarized below. First, the majority of trilayer EVCS methods developed so far use nested-loop structure, with the inner iterative loop (e.g., between EVs and EVAs)

being inside the outer iterative loop (e.g., between EVAs and DSO). In each iteration of the outer loop, the inner loop runs several times and starts over at the next iteration. This structure is not computationally efficient as the outer loop agents must wait for the sub-optimal solution of the inner loop agents before updating their primal variable and moving on to the next iteration. Consequently, the convergence time of the nested-loop EVCS algorithms is significantly higher compared to that of single-loop algorithms. Second, most of the trilayer EVCS methods do not consider the power flow constraints such as voltage fluctuation limits and maximum line currents. While there are few studies that consider the distribution network model in the nested-loop structures, to the best of authors' knowledge, power flow constraints have not so far been taken into account in single-loop structures. Finally, a precise knowledge about the non-EV residential load balance is essential for EVCS strategies. Hence, the short-term forecast of non-EV load demand/generation profile of the buildings can provide EV fleet managers with useful information to optimize their operational strategies. While accurate load forecasting is a challenging task due to its dependency on end-user behavior and various external factors (e.g., weather condition, occupancy, etc.); it is often overlooked in the EVCS strategies by assuming a deterministic load profile for the consumers [133]. Given the shortcomings of the existing research, in this paper, we propose an ADMM-based hierarchical single-loop EVCS (ADMM-HS-EVCS) framework that combines ADMM and the distribution line power flow model (DistFlow). The designed trilayer EVCS framework is general in the sense that any desired local objectives and constraints can be considered for the agents in each layer, as long as the optimization problems remain feasible and convex. The key contributions of this paper are summarized as follows:

- In order to decrease the amount of frequent communications between each optimization layer, a trilayer single-loop EVCS structure, scalable to large-scale EV fleets is proposed. Using a single-loop structure, the primal variables of all agents are updated simultaneously at every iteration resulting in a reduced number of iterations and faster convergence.
- The underlying physical system is taken into account using the distribution line power flow model (DistFlow) [107]. DistFlow is chosen due to its adequacy for modeling radial distribution networks, which is the typical network configuration to which EV fleets are connected.
- A load forecasting model based on Artificial Neural Network (ANN) is developed to take into account the uncertainties related to the uncontrollable load balance of residential buildings. In addition to the historical load data, other external features such as weather and occupancy data are included as inputs to enhance the performance of the forecast model.



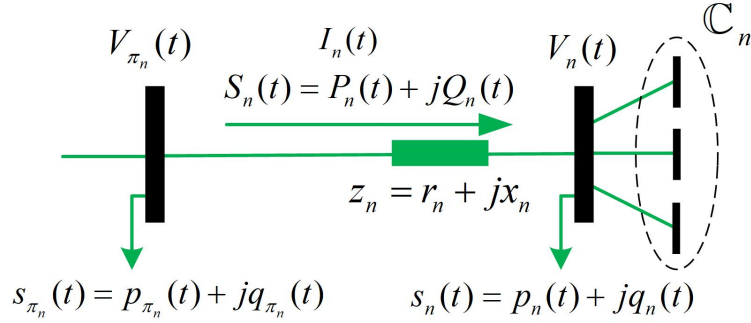


Figure 7.1 Distribution line power flow model (DistFlow)

The remainder of the paper is structured as follows. Section 7.3 introduces the mathematical models for the distribution network and EV charging infrastructure. In Section 7.4, the general EVCS optimization problem is defined, a convex approximation of the DistFlow model is introduced, and the proposed ADMM-based hierarchical single-loop EV charging scheduling (ADMM-HS-EVCS) framework is presented. Furthermore, an ANN-based load forecasting model is developed to estimate the non-EV load of residential buildings. Section 7.5 presents the simulation results and verifies the effectiveness of the proposed EVCS model by defining various performance metrics. Finally, the conclusions are drawn in Section 7.6.

## 7.3 System Modeling

### 7.3.1 Distribution Network Model

Consider a radial distribution network which is modeled as a directed graph  $G = (\mathbb{N}, \mathbb{L})$ , where  $\mathbb{N} := \{1, \dots, N\}$  represents the set of network buses and  $\mathbb{L} := \{1, \dots, L\}$  represents the set of network lines ( $L = N - 1$ ) [107, 108]. The substation bus is indexed by  $n = 1$  and each bus  $n \in \mathbb{N} \setminus \{1\}$  has a unique parent bus  $\pi_n$  and a set of children buses  $\mathbb{C}_n$  as shown in Fig. 7.1. At each moment  $t \in \mathbb{T} := \{1, \dots, T\}$ , for each bus  $n \in \mathbb{N}$ , its voltage and apparent power are represented by  $V_n(t)$  and  $s_n(t) = p_n(t) + jq_n(t)$ , respectively. For each line  $(\pi_n, n) \in \mathbb{L}$ , its impedance and apparent power flow are denoted by  $z_n = r_n + jx_n$  and  $S_n(t) = P_n(t) + jQ_n(t)$ , respectively. In order to simplify the equations, we use the vector notation  $\mathbf{y} := (y(t), y(t+1), \dots, y(t+T-1))$  for all time dependent variables.

The classic DistFlow equations can be utilized to calculate the power flow, line currents, and bus voltages of the system as below [107],

$$\mathbf{P}_n = \mathbf{p}_n + r_n \mathbf{i}_n + \sum_{m \in \mathbb{C}_n} \mathbf{P}_m \quad (7.1a)$$

$$\mathbf{Q}_n = \mathbf{q}_n + x_n \mathbf{i}_n + \sum_{m \in \mathbb{C}_n} \mathbf{Q}_m \quad (7.1b)$$

$$\mathbf{v}_{\pi_n} - \mathbf{v}_n = 2(r_n \mathbf{P}_n + x_n \mathbf{Q}_n) - (r_n^2 + x_n^2) \mathbf{i}_n \quad (7.1c)$$

$$\mathbf{v}_n \mathbf{i}_n = \mathbf{P}_n^2 + \mathbf{Q}_n^2 \quad (7.1d)$$

where  $\mathbf{i}_n = |\mathbf{I}_n|^2$  and  $\mathbf{v}_n = |\mathbf{V}_n|^2$ . For the substation bus  $n = 1$ , the voltage is assumed to be constant, while for other buses, the voltage magnitude limits are given as follows,

$$\underline{\mathbf{V}} \leq \mathbf{V}_n \leq \overline{\mathbf{V}} \quad n \in \mathbb{N} \setminus \{1\} \quad (7.2a)$$

$$\mathbf{V}_1 = \mathbf{V}_{ref} \quad (7.2b)$$

### 7.3.2 EV Charging Infrastructure Model

In this work, a trilayer EVCS structure consisting of DSO, EVAs, and EVs is considered. The set of EVAs and its cardinality are shown by  $\mathbb{N}^{eva}$  and  $N^{eva}$ , respectively. The set of EVs managed by  $EVA_j \in \mathbb{N}^{eva}$  are represented by  $\mathbb{N}_j^{ev}$  and its cardinality is  $N_j^{ev}$ . Therefore, the  $i_{th}$  EV managed by  $EVA_j$  can be shown by  $EV_{i,j} \in \mathbb{N}_j^{ev}$ . It is also assumed that each  $EV_{i,j}$  belongs to a unique residential building  $RB_{i,j}$ .

Considering the EV battery model, in discrete-time setting, the energy variation of a plugged-in EV can be described as follows [62],

$$E_{i,j}^{ev}(t+1) = E_{i,j}^{ev}(t) + \Delta t \cdot \eta_{i,j} \cdot p_{i,j}^{ev}(t) \quad (7.3)$$

where  $\eta_{i,j}$  and  $p_{i,j}^{ev}(t)$  are charging efficiency and charging power of  $EV_{i,j}$ , respectively.  $\Delta t$  is the time step and is considered to be 30 mins throughout the paper ( $\Delta t = 0.5$ ).

The active load demand of the residential building  $RB_{i,j}$  is denoted by  $p_{i,j}^{rb}(t)$  and is calculated as follows,

$$p_{i,j}^{rb}(t) = p_{i,j}^{unc}(t) + p_{i,j}^{ev}(t) \quad (7.4a)$$

$$p_{i,j}^{unc}(t) = p_{i,j}^l(t) - p_{i,j}^{sol}(t) \quad (7.4b)$$

where  $p_{i,j}^{unc}(t)$  is the uncontrollable active power balance of the building defined as the non-EV active power consumption  $p_{i,j}^l(t)$ , minus the generated active power from solar panels  $p_{i,j}^{sol}(t)$ . Considering V2G capability of EVs and generated power from solar panels,  $p_{i,j}^{rb}(t)$  can acquire both positive or negative values based on the power flow direction between the building and the grid.

Based on the electrical model defined for residential buildings (RBs), the total active and reactive power consumption at bus  $j$ , where  $EVA_j$  is located, are calculated as follows,

$$\mathbf{p}_j^{eva} = \mathbf{p}_j^{unc} + \mathbf{p}_j^{ev} \quad (7.5a)$$

$$\mathbf{q}_j^{eva} = \mathbf{q}_j^{unc} = \sum_{i \in \mathbb{N}_j^{ev}} \mathbf{q}_{i,j}^l \quad (7.5b)$$

where  $\mathbf{p}_j^{unc} = \sum_{i \in \mathbb{N}_j^{ev}} \mathbf{p}_{i,j}^{unc}$  is the aggregated uncontrollable active power balance at bus  $j$ ,  $\mathbf{p}_j^{ev} = \sum_{i \in \mathbb{N}_j^{ev}} \mathbf{p}_{i,j}^{ev}$  is the aggregated EV charging power at bus  $j$ , and  $\mathbf{q}_{i,j}^l$  is the reactive power consumption of  $RB_{i,j}$ .

Considering both power and energy requirement of EVs, the constraints of EV charging power,  $p_{i,j}^{ev}(t)$ , are defined as follows [89],

$$\underline{\mathbf{p}}_{i,j}^{ev} \leq \mathbf{p}_{i,j}^{ev} \leq \overline{\mathbf{p}}_{i,j}^{ev} \quad (7.6a)$$

$$\underline{\mathbf{R}}_{i,j} \leq \mathbf{A}_{i,j} \mathbf{p}_{i,j}^{ev} \leq \overline{\mathbf{R}}_{i,j} \quad (7.6b)$$

$$\underline{\mathbf{S}}_{i,j} \leq \mathbf{B}_{i,j} \mathbf{p}_{i,j}^{ev} \leq \overline{\mathbf{S}}_{i,j} \quad (7.6c)$$

The first set of constraints, (7.6a), defines the maximum and minimum EV charging/discharging power limits during the optimization horizon. The second set of constraints, (7.6b), defines the energy requirement of the EV during each connection session; and the last set of constraints, (7.6c), represents the EV battery capacity limits for each individual time slot during each connection session. The derivation of the parameters  $\underline{\mathbf{p}}_{i,j}^{ev}$ ,  $\overline{\mathbf{p}}_{i,j}^{ev}$ ,  $\mathbf{A}_{i,j}$ ,  $\underline{\mathbf{R}}_{i,j}$ ,  $\overline{\mathbf{R}}_{i,j}$ ,  $\mathbf{B}_{i,j}$ ,  $\underline{\mathbf{S}}_{i,j}$  and  $\overline{\mathbf{S}}_{i,j}$  depends on the EV driving behavior and the charging strategy chosen for EVCS problem. For more details on how to derive these parameters for different charging strategies, we refer the readers to [22]. In this study, we make the following assumptions for the EVCS problem:

- The arrival time, departure time, and energy requirement for the trip are known.
- The EV plugs into the charger after arrival time and stays connected until departure time. During the connection session, the EV is able to be in charging, discharging (V2G), or idle states.

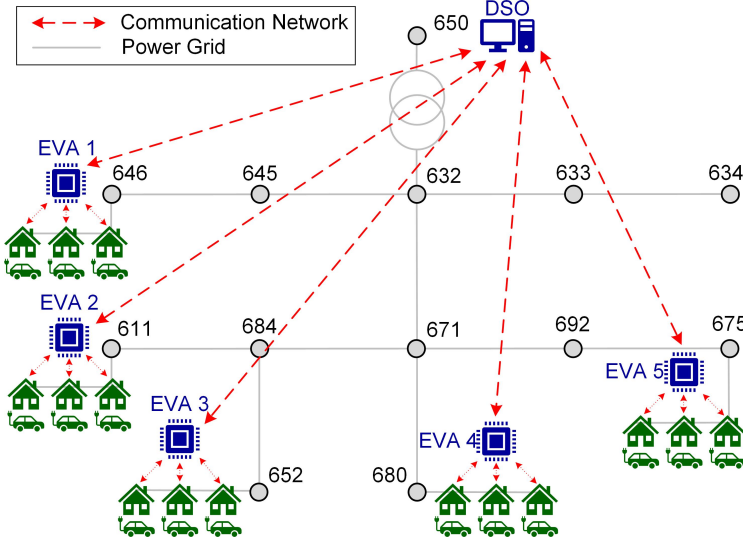


Figure 7.2 IEEE 13 bus test feeder with the proposed ADMM-HS-EVCS framework

For simplicity of notion, the feasible set of charging constraints for all EVs as follows,

$$\mathbb{Y}_{EV} := \{p_{i,j}^{ev}(t) \mid (7.3), (7.4), (7.6) \quad \forall i \in \mathbb{N}_j^{ev}, \forall j \in \mathbb{N}^{eva}, t \in \mathbb{T}\} \quad (7.7)$$

## 7.4 EV Charging Scheduling Problem Formulation

### 7.4.1 EVCS Optimization Problem

The structure of the distribution network and the proposed EVCS framework are shown in Fig. 7.2. The hierarchical EVCS structure includes DSO at the top layer, EVAs at the middle layer, and EVs at the bottom layer. The optimization problem for the whole network is written as follows:

$$\begin{aligned} V := \min_{\mathbf{V}, \mathbf{I}, \mathbf{P}, \mathbf{Q}} & \mathbf{F}^{dso}(\mathbf{p}) + \sum_{j \in \mathbb{N}^{eva}} \mathbf{F}_j^{eva}(\mathbf{p}_j^{eva}) + \sum_{j \in \mathbb{N}^{eva}} \sum_{i \in \mathbb{N}_j^{ev}} \mathbf{F}_{i,j}^{ev}(\mathbf{p}_{i,j}^{ev}) \\ s.t. & \mathbf{p}_{i,j}^{ev} \in \mathbb{Y}_{EV}, (7.1), (7.2), (7.5) \end{aligned} \quad (7.8)$$

where  $\mathbf{F}^{dso}$ ,  $\mathbf{F}^{eva}$ , and  $\mathbf{F}^{ev}$  are the optimization objective functions for DSO, EVAs and EVs, respectively.

Collecting the information of the whole system and solving (7.8) centrally by DSO alone is not computationally efficient, especially for a large distribution network with a large-scale EV fleet. Therefore, we propose an ADMM-based hierarchical EVCS framework to solve

(7.8) in a distributed manner between all participating agents (DSO, EVAs, and EVs). Using ADMM, the global optimization problem is decomposed into smaller sub-problems which are solved independently by each agent. This method converges to the optimal solutions through an iterative exchange of incentive signals between connected agents. As it is seen in Fig. 7.2, the DSO communicates only with EVAs, and EVAs communicate only with their own EVs. All sub-problems are solved locally and simultaneously in a single iterative loop which decreases the convergence time and communication burden compared to nested-loop hierarchical approaches. We call this framework ADMM-Based Hierarchical Single-loop EVCS or ADMM-HS-EVCS. The detailed formulation of the proposed model is presented in Subsection 7.4.4.

Note that ADMM is only applicable to the convex optimization problems, however, (7.8) is a non-convex problem due to the quadratic equality constraint (7.1d). One approach to make the problem (7.8) convex is to use the linearized version of the DistFlow model (LinDistFlow) by dropping all terms related to losses and assuming that bus voltage drops and line power flows are approximately linearly related to power injections [134]. By removing  $r_n \mathbf{i}_n$ ,  $x_n \mathbf{i}_n$  and  $(r_n^2 + x_n^2) \mathbf{i}_n$  terms from (7.1), the non-convex equality (7.1d) will be eliminated. Although this approach is successful in making (7.8) convex, it increases the model error due to negligence of line losses. To address this issue, a line loss approximation is presented in Subsection 7.4.2 which improves the accuracy of the DistFlow model while maintaining a linear set of equations. Using this approach, the line losses are explicitly parameterized and integrated into the DistFlow model.

In order to further enhance the performance of the proposed ADMM-HS-EVCS model, the uncertainties related to the uncontrollable power balance of residential buildings including non-EV power consumption and solar power generation have to be taken into account. This can be done through employing various load forecasting methods. In this paper, an ANN-based load forecasting is developed using the information acquired from the previously observed load data and other external inputs such as weather data and occupancy data. Subsection 7.4.3 presents the details of the ANN-based load forecasting model.

### 7.4.2 Lossy DistFlow approximation

Considering the distribution network graph, the following  $L \times N$  connection matrices are defined,

$$\mathbf{F}_{l,n} = \begin{cases} 1 & f(l) = n, l \in \mathbb{L}, n \in \mathbb{N} \\ 0 & otherwise \end{cases} \quad (7.9a)$$

$$\mathbf{T}_{l,n} = \begin{cases} 1 & t(l) = n, l \in \mathbb{L}, n \in \mathbb{N} \\ 0 & otherwise \end{cases} \quad (7.9b)$$

where  $f(l)$  and  $t(l)$  indicate the starting bus and ending bus of the directed line  $l$ , respectively.

In addition, the line-bus incidence matrix  $\tilde{\mathbf{M}}_{L \times N}$  is defined as,

$$\tilde{\mathbf{M}} = \mathbf{F} - \mathbf{T} = [m_1 \quad \mathbf{M}] \quad (7.10)$$

where  $m_1$  is the column corresponding to the substation bus and  $\mathbf{M}_{L \times L}$  is the reduced line-bus incidence matrix.

Using the connection matrices, at each moment  $t \in \mathbb{T}$ , the matrix-vector formulation of (7.1a)-(7.1c) can be rewritten as follows,

$$\mathbf{P} = \mathbf{T}\mathbf{p} + Dg(\mathbf{r})\mathbf{i} + \mathbf{T}\mathbf{F}^T\mathbf{P} \quad (7.11a)$$

$$\mathbf{Q} = \mathbf{T}\mathbf{q} + Dg(\mathbf{x})\mathbf{i} + \mathbf{T}\mathbf{F}^T\mathbf{Q} \quad (7.11b)$$

$$\mathbf{M}(\mathbf{v} - \mathbf{v}_1) = 2(Dg(\mathbf{r})\mathbf{P} + Dg(\mathbf{x})\mathbf{Q}) - Dg(\mathbf{r}^2 + \mathbf{x}^2)\mathbf{i} \quad (7.11c)$$

where  $\mathbf{v}_{L \times 1}$  is the vector of square voltage of all buses except the substation bus;  $\mathbf{v}_1$  is defined as  $\mathbf{v}_1 = v_1 \mathbf{1}_{L \times 1}$ ; and  $Dg(\hat{\mathbf{y}})$  is a diagonal function which returns a square matrix with vector  $\hat{\mathbf{y}}$  on the diagonal.

Substituting (7.11a) and (7.11b) in (7.11c), the matrix-vector from DistFlow equations is obtained as follows,

$$\mathbf{v} = \mathbf{v}_1 + 2\mathbf{M}^{-1}(Dg(\mathbf{r})\mathbf{B}\mathbf{T}\mathbf{p} + Dg(\mathbf{x})\mathbf{B}\mathbf{T}\mathbf{q}) + \mathbf{M}^{-1}\mathbf{C}\mathbf{i} \quad (7.12)$$

where,

$$\begin{aligned}\mathbf{B} &= (Dg(\mathbf{1}_{L \times 1}) - \mathbf{T}\mathbf{F}^T)^{-1} \\ \mathbf{C} &= 2(Dg(\mathbf{r})\mathbf{B}Dg(\mathbf{r}) + Dg(\mathbf{x})\mathbf{B}Dg(\mathbf{x})) - Dg(\mathbf{r}^2 + \mathbf{x}^2)\end{aligned}\quad (7.13)$$

The linear lossless DistFlow (LinDistFlow) formulation can be obtained by neglecting the non-linear quadratic term  $\mathbf{M}^{-1}\mathbf{C}\mathbf{i}$ , which reflects the power losses in the network lines.

In order to derive the linear lossy DistFlow approximation of (7.12), first, we need to expand the quadratic current term in (7.1),

$$i_n = I_n I_n^* = \frac{V_{\pi_n}^2 + V_n^2 - 2V_{\pi_n}V_n \cos(\theta_{\pi_n} - \theta_n)}{r_n^2 + x_n^2} \quad (7.14)$$

As suggested by [135], we can define a new controlled parameter  $0 \leq \alpha_n \leq 1$  to write  $V_{\pi_n}V_n$  as a convex combination of squared voltage magnitudes at two ends,

$$V_{\pi_n}V_n \approx \alpha_n(V_{\pi_n}^2 - V_n^2) + V_n^2 \quad (7.15)$$

Assuming bus voltage angles are close to each other,  $\cos(\theta_{\pi_n} - \theta_n) \approx 1$ , and substituting (7.15) in (7.14), the convex approximation of line current can be obtained as follow,

$$i_n \approx (1 - 2\alpha_n) \frac{V_{\pi_n}^2 - V_n^2}{r_n^2 + x_n^2} \quad (7.16)$$

The matrix-vector formulation of (7.16) is written as,

$$\mathbf{i} \approx [Dg(\mathbf{1}_{L \times 1}) - 2Dg(\alpha_n)]\mathbf{M}(\mathbf{v} - \mathbf{v}_1)Dg(\mathbf{r}^2 + \mathbf{x}^2)^{-1} \quad (7.17)$$

The value of  $\alpha_n$  can be determined by substituting (7.1d) in (7.16) as follows,

$$\alpha_n \approx -\frac{(P_n^2 + Q_n^2)(r_n^2 + x_n^2)}{2V_n^2(V_{\pi_n}^2 - V_n^2)} + \frac{1}{2} \quad (7.18)$$

By defining  $\mu_n = (2V_n^2(V_{\pi_n}^2 - V_n^2))^{-1}$ ,  $\beta(n) = (P_n^2 + Q_n^2)(r_n^2 + x_n^2)$  and  $\gamma_0 = \frac{1}{2}$ , (7.18) can be reformulated as,

$$\alpha_n \approx -\mu_n \cdot \beta(n) + \gamma_0 \quad (7.19)$$

In order to further simplify the problem formulation, we keep  $\mu_n = \mu$  constant for all the network lines and allow the  $\gamma_0$  to change from  $\frac{1}{2}$  to assist the linearization. Therefore, for any given range of  $\alpha_n \in [\underline{\alpha}, \bar{\alpha}]$ ,  $\alpha_n$  can be calculated as follows,

$$\begin{aligned}\alpha_n &\approx -\mu \cdot \beta(n) + \gamma \\ \mu &= \frac{\bar{\alpha} - \underline{\alpha}}{\max_{n \in \mathbb{N}}(\beta(n)) - \min_{n \in \mathbb{N}}(\beta(n))} \\ \gamma &= \bar{\alpha} + \mu \cdot \min_{n \in \mathbb{N}}(\beta(n))\end{aligned}\tag{7.20}$$

### 7.4.3 ANN-based load forecasting model

In this paper, an ANN-based load forecasting model is used to predict the day-ahead aggregated uncontrollable load balance of residential buildings. ANN is chosen for its accuracy and superior performance in extracting and mapping complex and nonlinear correlations between input and output variables compared to linear regression-based methods [136]. We consider a Multi-Layered Perceptron (MLP) network consisting of various input features, a few hidden layers, and one output layer which are all connected in a feed-forward manner.

The selection of nature and number of input features, historical data range, training algorithm, number of hidden layers and neurons in each layer is subjective and depends on cross-validation errors. The best-suited values for various parameters of the neural network architecture can be determined by comparing obtained load forecast errors for each EVA. For the training of the network, among various backpropagation algorithms, Levenberg-Marquardt (LM) algorithm is employed due to its efficiency in training small and median size patterns [137].

### Selection of Input Features

It is assumed that each EVA is equipped with a smart meter measuring the total uncontrollable power balance at each bus,  $p_j^{unc}(t)$ , every 30 minutes. In addition to load data, other external features such as weather data and dummy data such as calendar data are used to enhance the performance of the forecast model.

In order to reflect the relationship between the residential power balance and the weather conditions, meteorological features including dew point temperature, dry-bulb temperature, humidity, cloud coverage, wind speed, visibility, horizontal solar irradiance and weather condition index are taken into consideration. The weather condition index is categorized as clear



Table 7.1 ANN input features

Input feature	Description
$T_{dp}(t)$	Dew point temperature [ $^{\circ}C$ ]
$T_{db}(t)$	Dry-bulb temperature [ $^{\circ}C$ ]
$H(t)$	Humidity [%]
$CC(t)$	Cloud coverage [%]
$V_w(t)$	Wind speed [m/s]
$VIS(t)$	Visibility [Km]
$HSI(t)$	Horizontal solar irradiance [W/m <sup>2</sup> ]
$WCI(t)$	Weather condition index [1,...,6]
$p_j^{unc}(t - \Delta t_d)$	Power demand of the previous day* [KW]
$p_j^{unc}(t - 2\Delta t_d)$	Power demand of the second previous day* [KW]
$p_j^{unc}(t - 3\Delta t_d)$	Power demand of the third previous day* [KW]
$p_j^{unc}(t - 7\Delta t_d)$	Power demand of the previous week* [KW]
$S_{id}(t)$	Season ID [1,...,4]
$W_{id}(t)$	Week ID [1,...,52]
$D_{id}(t)$	Day ID [1,...,7]
$H_{id}(t)$	Hour ID [1,...,24]
$HH_{id}(t)$	Half hour ID [1,...,48]

\*  $\Delta t_d = 48\Delta t = 24h$

(1), partially cloudy (2), overcast (3), rainy (4), rain-overcast (5), rain-partially cloudy (6). The weather data can be gathered from the nearest weather station and depending on the geographical locations, EVAs may share similar weather conditions.

In addition to weather data, it is also very beneficial to consider the occupancy data in each EVA as it influences the consumption load pattern. Since such information is not measured, correlated load patterns from previous days including the load data from the previous day, the second previous day, the third previous day, and the previous week are used as input features. Furthermore, in order to better capture intraday, daily, weekly, monthly, and seasonal occupancy patterns, various dummy calendar pointers including season ID, week number, day of the week, hour of the day and half hour ID are considered. The description of all input features is presented in Table 7.1.

#### 7.4.4 ADMM-based Hierarchical Single-loop EV Charging Scheduling (ADMM-HS-EVCS)

Assuming  $\mathbf{p}_j = \mathbf{p}_j^{eva} \forall j \in \mathbb{N}^{eva}$ , ADMM can be utilized to distribute the centralized optimization problem (7.8) between the DSO and the EVAs as below (see [19] for more details on ADMM),

- *EVA Update:*

$$(\mathbf{p}_j^{eva^{k+1}}, \mathbf{p}_{i,j}^{ev^{k+1}}) := \underset{\mathbf{p}_j^{eva}, \mathbf{p}_{i,j}^{ev}}{\operatorname{argmin}} \left( \mathbf{F}_j^{eva}(\mathbf{p}_j^{eva}) + \sum_{i \in \mathbb{N}_j^{ev}} \mathbf{F}_{i,j}^{ev}(\mathbf{p}_{i,j}^{ev}) + \frac{\rho}{2} \|\mathbf{p}_j^{eva} - \mathbf{p}_j^k + \mathbf{u}_j^k\|_2^2 \right) \quad (7.21)$$

s.t.  $\mathbf{p}_{i,j}^{ev} \in \mathbb{Y}_{EV}, (7.5), \forall j \in \mathbb{N}^{eva}$

- *DSO update:*

$$\mathbf{p}_j^{k+1} := \underset{\mathbf{p}_j}{\operatorname{argmin}} \left( \mathbf{F}^{dso}(\mathbf{p}) + \frac{\rho}{2} \sum_{j \in \mathbb{N}^{eva}} \|\mathbf{p}_j^{eva^{k+1}} - \mathbf{p}_j + \mathbf{u}_j^k\|_2^2 \right) \quad (7.22)$$

s.t. (7.12), (7.13), (7.2), (7.17), (7.20),  $\forall j \in \mathbb{N}^{eva}$

- *Incentive signal update:*

$$\mathbf{u}_j^{k+1} = \mathbf{u}_j^k + (\mathbf{p}_j^{eva^{k+1}} - \mathbf{p}_j^{k+1}) \quad (7.23)$$

where  $\rho$  is the penalty factor and  $\mathbf{u}_j$  is the vector of Lagrangian multipliers (incentive signal). At each iteration  $k$ , all EVAs solve (7.21) in parallel and send their sub-optimal solutions to DSO. Then, DSO solves (7.22) by considering the power flow constraints. Finally, DSO updates  $\mathbf{u}_j$  by (7.23) and send it back to EVAs. This iterative procedure continues until the ADMM converges to an optimal solution.

It is to be noted that solving (7.21) by each EVA is not computationally efficient as EVAs are responsible to solve their own optimization problems as well as all optimization problems of their corresponding EVs. In addition, the private information of EVs needs to be communicated to their parent EVA which does not preserve the privacy of end-users. In order to address these issues, (7.21) can be further decomposed and distributed between EVAs and their corresponding EVs. Substituting (7.5a) in (7.21), the first update of the ADMM can be rewritten as follows,

$$(\mathbf{p}_j^{ev^{k+1}}, \mathbf{p}_{i,j}^{ev^{k+1}}) := \underset{\mathbf{p}_j^{ev}, \mathbf{p}_{i,j}^{ev}}{\operatorname{argmin}} \left( \mathbf{F}_j^{eva}(\mathbf{p}_j^{ev}) + \sum_{i \in \mathbb{N}_j^{ev}} \mathbf{F}_{i,j}^{ev}(\mathbf{p}_{i,j}^{ev}) + \frac{\rho}{2} \|\mathbf{p}_j^{ev} + \mathbf{p}_j^{unc} - \mathbf{p}_j^k + \mathbf{u}_j^k\|_2^2 \right) \quad (7.24)$$

s.t.  $\mathbb{Y}_{EV}, (7.5), \forall j \in \mathbb{N}^{eva}$

Considering the right-hand side of (7.24), the first expression is a function of  $\mathbf{p}_j^{ev}$  and the second expression is a function of  $\mathbf{p}_{i,j}^{ev}$  which is separable between the EVs. Therefore, equation (7.24) is in the form of *sharing problem*.

By introducing  $\bar{\mathbf{p}}_j^{ev} = \frac{\mathbf{p}_j^{ev}}{\mathbb{N}_j^{ev}}$  and defining new variable  $\hat{\mathbf{p}}_j^{ev} = \bar{\mathbf{p}}_j^{ev}$ , ADMM can be applied once again to further distribute the optimization problem in (7.24) between the EVA and the EVs as follows,

- *EV update:*

$$\begin{aligned} \mathbf{p}_{i,j}^{ev^{k+1}} &:= \underset{\mathbf{p}_{i,j}^{ev}}{\operatorname{argmin}} \left( \mathbf{F}_{i,j}^{ev}(\mathbf{p}_{i,j}^{ev}) + \frac{\rho_j}{2} \|\mathbf{p}_{i,j}^{ev} - \mathbf{p}_{i,j}^{ev^k} + \bar{\mathbf{p}}_j^{ev^k} - \hat{\mathbf{p}}_j^{ev^k} + \mathbf{v}_j^k\|_2^2 \right) \\ s.t. \quad &\mathbb{Y}_{EV} \end{aligned} \quad (7.25)$$

- *EVA update:*

$$\begin{aligned} \hat{\mathbf{p}}_j^{ev^{k+1}} &:= \underset{\hat{\mathbf{p}}_j^{ev}}{\operatorname{argmin}} \left( \mathbf{F}_j^{eva}(\mathbb{N}_j^{ev} \hat{\mathbf{p}}_j^{ev}) + \frac{\rho}{2} \|\mathbb{N}_j^{ev} \hat{\mathbf{p}}_j^{ev} + \mathbf{p}_j^{unc} - \mathbf{p}_j^k + \mathbf{u}_j^k\|_2^2 + \frac{\mathbb{N}_j^{ev} \rho_j}{2} \|\hat{\mathbf{p}}_j^{ev} - \bar{\mathbf{p}}_j^{ev^{k+1}} - \mathbf{v}_j^k\|_2^2 \right) \\ s.t. \quad &(7.5) \end{aligned} \quad (7.26)$$

- *Incentive signal update:*

$$\mathbf{v}_j^{k+1} = \mathbf{v}_j^k + (\bar{\mathbf{p}}_j^{ev^{k+1}} - \hat{\mathbf{p}}_j^{ev^{k+1}}) \quad (7.27)$$

where  $\rho_j$  and  $\mathbf{v}_j$  are the penalty factor and vector of Lagrangian multipliers for  $EVA_j$ , respectively. At each iteration,  $\bar{\mathbf{p}}_j^{ev}$  is updated as follows,

$$\bar{\mathbf{p}}_j^{ev^{k+1}} = \frac{\mathbf{p}_j^{ev^{k+1}}}{\mathbb{N}_j^{ev}} \quad (7.28)$$

Note that using the proposed algorithm, all sub-problems are solved locally and simultaneously by DSO, EVAs, and EVs in a single iterative loop. The whole procedure of the proposed ADMM-based hierarchical single-loop EVCS (ADMM-HS-EVCS) is summarized in Algorithm 1. At each iteration  $k$ , (7.25) is solved by all EVs in parallel and the results are sent to EVAs. Then, based on the received information, all EVAs update  $\bar{\mathbf{p}}_j^{ev}$  using (7.28) and calculate the EVA level sub-optimal solutions by (7.26) in parallel. Next, each EVA updates  $\mathbf{v}_j$  and  $\mathbf{p}_j^{eva}$  by (7.27) and (7.5) and sends the updated values to its corresponding EVs and the DSO, respectively. Finally, the DSO level optimization problem is solved by

**Algorithm 2:** ADMM-HS-EVCS

```

 $k \leftarrow 1;$ 
 $stop \leftarrow 0;$ 
while  $stop == 0$  do
  for  $j = 1 : N^{eva}$  do in parallel
    for  $i = 1 : N_j^{ev}$  do in parallel
      Calculate  $\mathbf{p}_{i,j}^{ev^{k+1}}$  by (7.25) and send it to  $EVA_j$ 
    end
    Update  $\bar{\mathbf{p}}_j^{ev^{k+1}}$  by (7.28)
    Calculate  $\hat{\mathbf{p}}_j^{ev^{k+1}}$  by (7.26)
    Update  $\mathbf{v}_j^{k+1}$  by (7.27) and send it to  $EV_{i,j}, \forall i \in \mathbb{N}_j^{ev}$ 
    Update  $\mathbf{p}_j^{eva^{k+1}}$  by (7.5) and send it to  $DSO$ 
  end
  Calculate  $\mathbf{p}_j^{k+1}, \forall j \in \mathbb{N}^{eva}$  by (7.22) and send it to  $EVA_j$ 
  Update  $\mathbf{u}_j^{k+1}, \forall j \in \mathbb{N}^{eva}$  by (7.23) and send it to  $EVA_j$ 
  Update primal and dual residuals by (7.29) and (7.30)
  if (7.31) is True then
     $stop \leftarrow 1;$ 
  end
   $k \leftarrow k + 1;$ 
end

```

(7.22) and the value of  $\mathbf{u}_j$  is updated by (7.23). This single-loop iterative procedure between the DSO, EVAs and EVs continues until the ADMM converges to an optimal solution.

### Convergence Criteria

The convergence criteria of the ADMM can be defined based on the primal and dual residuals [19]. These residuals are calculated for the proposed algorithm as below,

- *Primal residuals:*

$$\mathbf{r}_j^{ev^k} = \bar{\mathbf{p}}_j^{ev^k} - \hat{\mathbf{p}}_j^{ev^k}, \quad \forall j \in \mathbb{N}^{eva} \quad (7.29a)$$

$$\mathbf{r}_j^{eva^k} = \mathbf{p}_j^{eva^k} - \mathbf{p}_j^k, \quad \forall j \in \mathbb{N}^{eva} \quad (7.29b)$$

- *Dual residuals:*

$$\mathbf{s}_{i,j}^{ev^k} = -\rho_j \left( \mathbf{p}_{i,j}^{ev^k} - \mathbf{p}_{i,j}^{ev^{k-1}} \right), \quad (7.30a)$$

$$\forall i \in \mathbb{N}_j^{ev}, \forall j \in \mathbb{N}^{eva}$$

$$\mathbf{s}_j^{eva^k} = -\rho \left( \hat{\mathbf{p}}_j^{ev^k} - \hat{\mathbf{p}}_j^{ev^{k-1}} \right), \quad (7.30b)$$

$$\forall j \in \mathbb{N}^{eva}$$

$$\mathbf{s}_j^{dso^k} = -\rho \left( \mathbf{p}_j^k - \mathbf{p}_j^{k-1} \right), \quad (7.30c)$$

$$\forall j \in \mathbb{N}^{eva}$$

with  $\mathbf{s}_j^{ev^k} = [\mathbf{s}_{1,j}^{ev^k}, \dots, \mathbf{s}_{N_j^{ev},j}^{ev^k}]$  the stopping criteria are:

$$\|\mathbf{r}_j^{ev^k}\|_2^2 \leq \epsilon_{pri}^{ev}, \quad \forall j \in \mathbb{N}^{eva} \quad (7.31a)$$

$$\|\mathbf{r}_j^{eva^k}\|_2^2 \leq \epsilon_{pri}^{eva}, \quad \forall j \in \mathbb{N}^{eva} \quad (7.31b)$$

$$\|\mathbf{s}_j^{ev^k}\|_2^2 \leq \epsilon_{dual}^{ev}, \quad \forall j \in \mathbb{N}^{eva} \quad (7.31c)$$

$$\|\mathbf{s}_j^{eva^k}\|_2^2 \leq \epsilon_{dual}^{eva}, \quad \forall j \in \mathbb{N}^{eva} \quad (7.31d)$$

$$\|\mathbf{s}_j^{dso^k}\|_2^2 \leq \epsilon_{dual}^{dso}, \quad \forall j \in \mathbb{N}^{eva} \quad (7.31e)$$

where  $\epsilon_{pri}^{ev}$ ,  $\epsilon_{pri}^{eva}$ ,  $\epsilon_{dual}^{ev}$ ,  $\epsilon_{dual}^{eva}$  and  $\epsilon_{dual}^{dso}$  are the corresponding feasibility tolerances. Note that the primal residuals reflect the mismatch of the coupling variables at each iteration while the dual residuals describe the stability of the iterations.

## 7.5 Case studies and simulation results

In this section, the performance of the proposed ADMM-HS-EVCS framework is studied for the modified IEEE 13 bus test feeder. As it is seen in Fig. 7.2, the test system is single phase balanced system that includes five EVAs at bus 646, 611, 652, 680, and 575. Each EVA is supplying 60 residential buildings (RBs) and their corresponding EVs. Bus 650 is considered as the substation bus where the DSO is located. Based on the U.S. National Household Travel Survey (NHTS), the driving behavior and the energy requirement of the EVs are modeled by defining distribution functions for their arrival time, departure time, initial SOC, and desired SOC [127]. These distribution functions are listed in Table 7.2.

Table 7.2 EV fleet parameters

Parameter	Description	Value*
$t^{in}$	Arrival time [h]	$N(-6.5, 3.4) \in [0.0, 5.5]$ $N(17.5, 3.4) \in [5.5, 24]$
$t^{out}$	Departure time [h]	$N(8.9, 3.4) \in [0.0, 20.9]$ $N(32.9, 3.4) \in [20.9, 24]$
$SOC^{in}$	Initial SOC	$N(0.3, 0.05) \in [0.2, 0.4]$
$SOC^{out}$	Desired SOC	$N(0.8, 0.03) \in [0.7, 0.9]$

$N(\mu, \sigma) \in (\alpha, \beta)$  represents the normal distribution with the mean value of  $\mu$  and the standard deviation of  $\sigma$  with  $(\alpha, \beta)$  being the variation range.

### 7.5.1 Case studies

In order to study the effectiveness of the proposed optimization framework, the following charging scenarios are defined:

I) *Uncoordinated charging (UC)* : EVs start to charge with the maximum charging power ( $\bar{p}_{i,j}^{ev}$ ) right after their arrival and stop charging when they reach the desired SOC value.

II) *Semi-coordinated charging (SC)*: EVs charge with constant charging power throughout the connection session. The constant charging power is determined by dividing the required amount of energy by the connection session duration. Based on the duration of the connection session, the constant charging power may be equal to or less than the maximum charging power.

III) *Optimized charging (ADMM-HS-EVCS)*: The charging session of EVs is controlled based on the proposed optimization algorithm. In this scenario, the EVs are also able to inject energy back into the grid using V2G capability.

Note that the proposed EVCS framework in Section 7.4.4 is general and can be implemented for a wide range of convex optimization objectives. Without the loss of generality, in the remainder of this paper, we assume the following optimization objectives for each layer:

- The purpose of DSO is to regulate the nodal voltages while respecting the power flow constraints. Accordingly,  $\mathbf{F}^{dso}$  is defined by,

$$\mathbf{F}^{dso} = \sum_{n \in \mathbb{N} \setminus \{1\}} \|\mathbf{V}_n - \mathbf{V}_{ref}\|_2^2 \quad (7.32)$$

Table 7.3 Simulation parameters

Parameter	Description	Value
$\underline{p}_{i,j}^{ev}, \overline{p}_{i,j}^{ev}$	EV power limits [kW]	4,-4
$\overline{E}_{i,j}^{ev}$	EV battery maximum capacity [kWh]	25.5
$\eta_{i,j}$	Charging efficiency	0.93
$N$	Number of network buses	13
$L$	Number of network lines	12
$\underline{\alpha}, \overline{\alpha}$	DistFlow linearization parameters	0.483, 0.499
$V_{ref}$	Voltage reference [p.u.]	1
$\underline{V}, \overline{V}$	Bus voltage limits [p.u.]	0.97,1.03
$\rho, \rho_j$	Penalty factors	2
$\Delta t$	Time step [h]	0.5
$T$	Time horizon	48
$\epsilon_{pri}^{ev}, \epsilon_{pri}^{eva}$	Primal feasibility tolerances	0.1
$\epsilon_{dual}^{ev}, \epsilon_{dual}^{eva}, \epsilon_{dual}^{dso}$	Dual feasibility tolerances	0.1

- The purpose of EVAs is to minimize the peak load on their supplying buses which can be formulated as,

$$\mathbf{F}_j^{eva} = \|\overline{\mathbf{p}}_j^{unc} - \mathbf{p}_j^{unc} - (\mathbb{N}_j^{ev} \hat{\mathbf{p}}_j^{ev})\|_2^2 \quad (7.33)$$

where  $\overline{p}_j^{unc} = \frac{1}{T} \sum_{t=t_0}^{t_0+T-1} p_j^{unc}(t)$  is the temporal average of the uncontrollable power balance at bus j.

- EVs aim at minimizing their charging cost using the following objective function,

$$\mathbf{F}_{i,j}^{ev} = \boldsymbol{\Omega}^T \mathbf{p}_{i,j}^{ev} \quad (7.34)$$

where  $\boldsymbol{\Omega}$  is the wholesale electricity price which is obtained from [138] and depicted in Fig. 7.3. The details of all simulation parameters are shown in Table 7.3. All the simulations are processed by MATLAB on a PC with 1.8 GHz Intel Core i7-8550U CPU and 16.00 GB of RAM. CVX is used to solve the convex optimization problems [139].

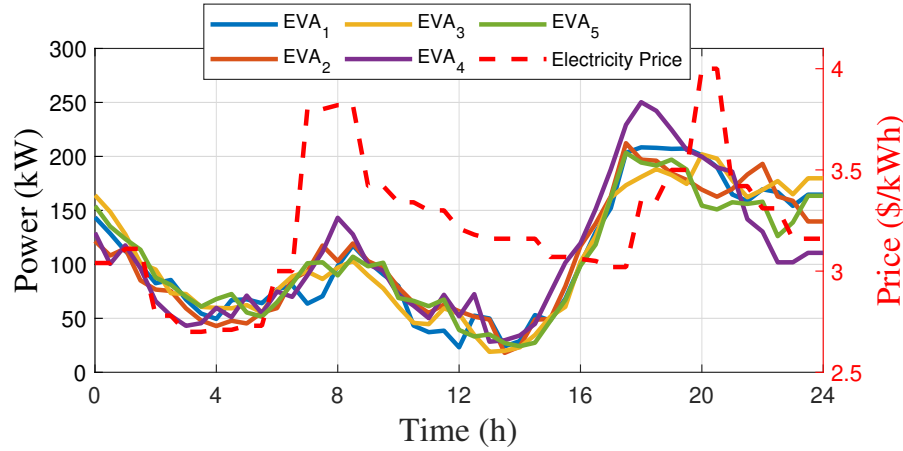


Figure 7.3 Left: predicted uncontrollable power balance of EVAs  
Right: wholesale electricity price

### 7.5.2 Simulation results

#### ANN-based load forecasting model

In order to validate the performance of the load forecasting model, three years of data with a resolution of 30 minutes are used. The load profile dataset of residential buildings is from the Australian electricity company (Ausgrid) [140]. The weather data is collected from [141] for the city of Sidney. The available dataset is divided into three sets for training (70%), testing (15%), and validation (15%). As previously mentioned in section 7.4.3, the selection of the number of hidden layers and neurons in each layer is determined as a trade-off between the forecast accuracy and the training time. In this study, two and three layer structures having 10, 24, and 48 neurons at each hidden layer are considered. The network is built using “fitnet” function of MATLAB. For each architecture, the mean absolute percentage error (MAPE), the root mean square error (RMSE), the training time, and the number of epochs are compared in Table 7.4.

Considering two layer architectures, the best value of MAPE and RMSE for all EVAs is obtained by defining 48 neurons in the hidden layer, with average values of 8.23% and 4.84 kWh, respectively. However, the average training time (235 s) is considerably higher compared to 10-neurons (28 s) and 24-neurons (84 s) architectures. Considering three layer architectures, it is seen that the introduction of an additional hidden layer in 10-24-neurons architecture further improves the accuracy of the model compared to the two layer architectures with the same number of neurons. However, the average training time is significantly increased for 24-48-neurons architecture (530 s) due to the large number of neurons in hidden layers. As



Table 7.4 Performance of the load forecasting model

		Two layers			Three layers	
		10	24	48	10-24	24-48
$EVA_1$	MAPE (%)	10.25	9.12	8.95	<b>8.87</b>	8.68
	RMSE (kWh)	6.06	5.29	5.01	<b>5.16</b>	4.76
	Time (s)	16	98	268	<b>86</b>	435
	Epochs	117	201	145	<b>146</b>	61
$EVA_2$	MAPE (%)	8.74	8.40	7.89	<b>7.99</b>	7.48
	RMSE (kWh)	5.58	5.26	4.82	<b>5.01</b>	4.41
	Time (s)	22	50	317	<b>125</b>	597
	Epochs	158	91	173	<b>193</b>	82
$EVA_3$	MAPE (%)	8.56	8.02	7.77	<b>7.85</b>	7.77
	RMSE (kWh)	5.31	4.87	4.68	<b>4.75</b>	4.57
	Time (s)	34	85	124	<b>98</b>	587
	Epochs	232	184	69	<b>182</b>	77
$EVA_4$	MAPE (%)	9.83	9.17	8.61	<b>8.87</b>	8.48
	RMSE (kWh)	5.55	5.16	4.77	<b>4.92</b>	4.52
	Time (s)	32	59	237	<b>56</b>	540
	Epochs	220	98	130	<b>88</b>	71
$EVA_5$	MAPE (%)	8.80	8.32	7.93	<b>7.98</b>	7.81
	RMSE (kWh)	5.62	5.26	4.92	<b>5.06</b>	4.94
	Time (s)	36	128	231	<b>110</b>	492
	Epochs	250	236	236	<b>147</b>	65
Average	MAPE (%)	9.23	8.60	8.23	<b>8.31</b>	8.04
	RMSE (kWh)	5.62	5.16	4.84	<b>4.98</b>	4.64
	Time (s)	28	84	235	<b>95</b>	530
	Epochs	195	162	151	<b>151</b>	71

a result, we consider the three layer 10-24-neurons architecture to be the optimal choice in terms of accuracy and training time. Using this architecture, the load forecasting regression plots for all EVAs are depicted in Fig. 7.4. It is seen that the actual values are closely scattered around the fitted lines which validates the accuracy of the proposed load forecasting algorithm. The predicted uncontrollable power balance profiles supplied by each aggregator are shown in Fig. 7.3.

### ADMM-based Hierarchical Single-loop EV Charging Scheduling (ADMM-HS-EVCS)

In this section, the simulation results of the proposed optimization charging framework are presented. The daily charging cost of all EVs under each scenario is shown in Fig. 7.5. It is seen that for both uncoordinated (UC) and semi-coordinated (SC) charging scenarios, the daily charging costs are very close to each other, with average values of 5.97\$ and 5.96\$, respectively. However, including the EV level optimization objective for ADMM-HS-EVCS, the daily charging costs are reduced by 37% to the average value of 3.75\$.

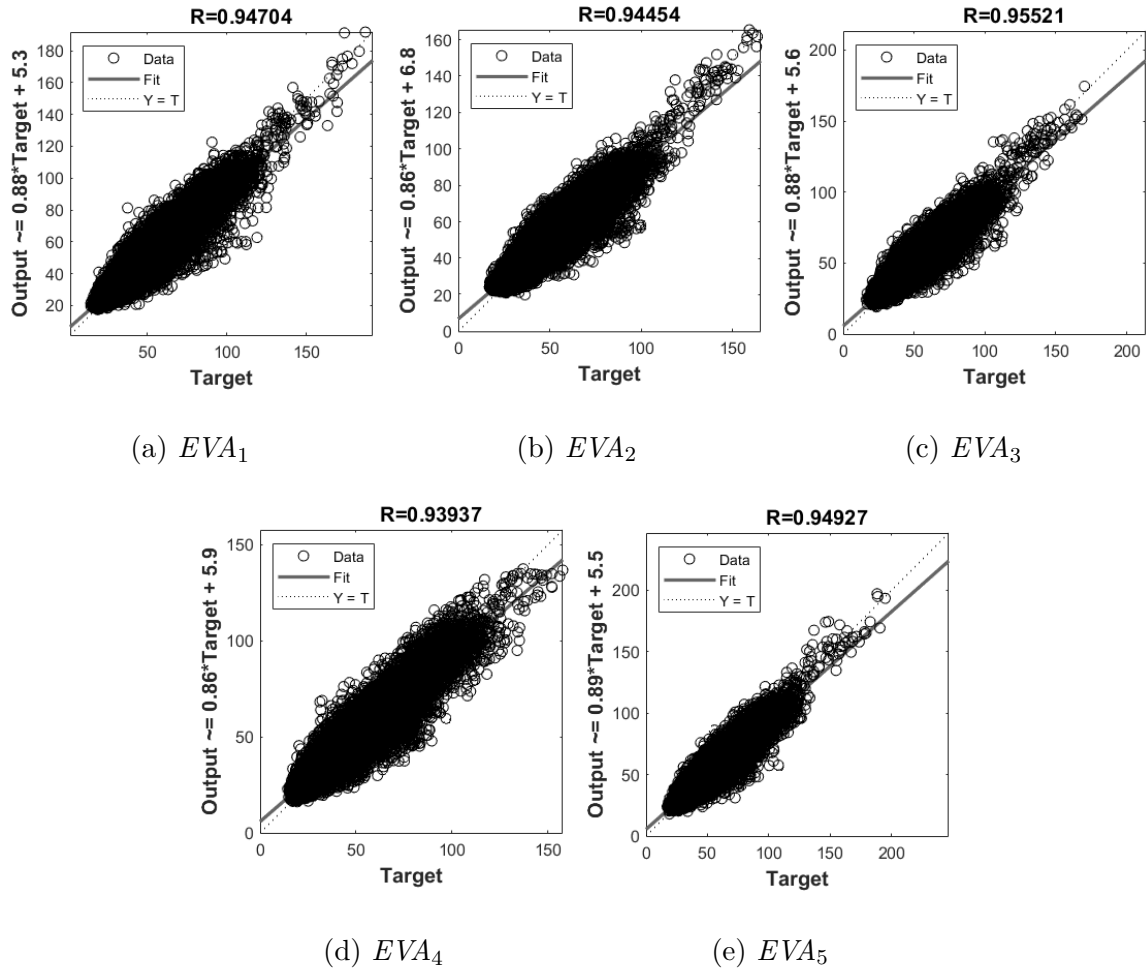


Figure 7.4 Load forecasting regression plots using the three layer 10-24 architecture

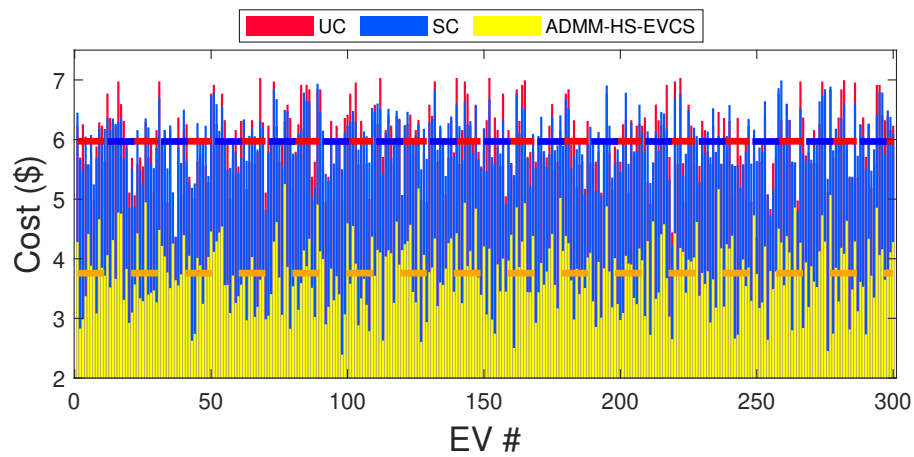


Figure 7.5 Daily EV charging costs

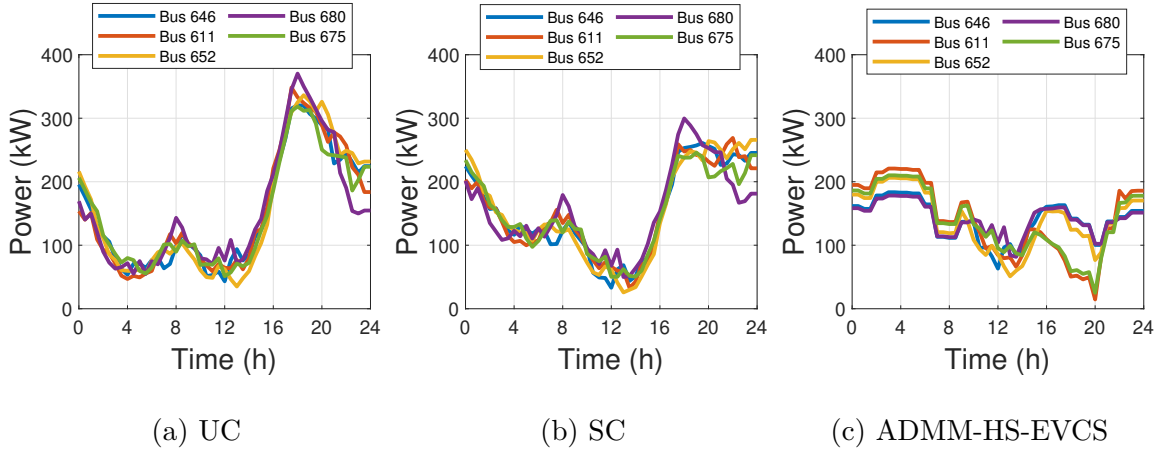


Figure 7.6 Power profile of the network buses

Table 7.5 Peak load shaving performance

	Metric	No EV	UC	SC	ADMM-HS-EVCS
$EVA_1$	PTP (kW)	185	277	228	<b>120</b>
	PTA	1.97	2.13	1.72	<b>1.31</b>
$EVA_2$	PTP (kW)	194	301	236	<b>206</b>
	PTA	2.02	2.31	1.76	<b>1.58</b>
$EVA_3$	PTP (kW)	182	301	240	<b>155</b>
	PTA	1.93	2.23	1.74	<b>1.47</b>
$EVA_4$	PTP (kW)	221	315	249	<b>96</b>
	PTA	2.32	2.42	1.94	<b>1.25</b>
$EVA_5$	PTP (kW)	179	267	195	<b>189</b>
	PTA	1.97	2.14	1.63	<b>1.53</b>
Average	PTP (kW)	192	292	229	<b>153</b>
	PTA	2.04	2.04	1.75	<b>1.42</b>

In order to investigate the peak load shaving performance (EVA level objective), the power profile of all network buses for each scenario is illustrated in Fig. 7.6. In addition, for each scenario, two evaluation metrics namely peak-to-peak (PTP) and peak-to-average (PTA) values are calculated by (7.35) and shown in Table 7.5.

$$PTP = \max_{t \in [t_0, t_0+T-1]} y(t) - \min_{t \in [t_0, t_0+T-1]} y(t) \quad (7.35a)$$

$$PTA = \frac{\max_{t \in [t_0, t_0+T-1]} y(t)}{\frac{1}{T} \sum_{t \in [t_0, t_0+T-1]} y(t)} \quad (7.35b)$$

where  $y(t)$  is the power profile associated with each scenario.

Comparing Fig. 7.6 (a) and Fig. 7.3 and their corresponding evaluation metrics from Table 7.5, it is seen that introducing the EV fleet with an uncoordinated charging (UC) scenario significantly increases the peak power during 16:00 and 20:00 for all EVAs. According to Table 7.2, this situation is caused by the arrival of EVs and their immediate charging needs under UC scenario. Considering Fig. 7.6 (b), while adopting the semi-coordinated (SC) charging approach relatively decreases the peak power, there is still a huge gap between the peak and valley points. As it is seen from Fig. 7.6 (c), the best peak shaving performance is obtained using ADMM-HS-EVCS where the EVs are allowed to have bidirectional power flow with the grid using V2G technology. In this scenario, average PTP and PTA values are 153 kW and 1.42, respectively (Table 7.5).

Considering Fig. 7.7, it can be seen that using ADMM-HS-EVCS to smooth out the power profile of network buses results in reduced power flows on all network lines. Peak power reduction is much more noticeable for the incoming main feeder line and the lines that are closer to the substation bus.

In order to investigate the voltage regulation performance (DSO level objective), the voltage profile of all network buses for each scenario is illustrated in Fig. 7.8. It is seen that the uncoordinated charging (UC) performs the worst of the three, resulting in voltage drops as low as 0.95 p.u.. Using the semi-coordinated (SC) charging approach, the minimum voltage of the system is increased to 0.96 p.u.; however, it is still out of the allowed limits. The best voltage regulation performance is obtained by using ADMM-HS-EVCS where all voltage profiles always remain inside the permissible range [0.97 1.03] p.u..

The convergence performance of the proposed single-loop ADMM framework is presented in Table 7.6 and is compared to the conventional nested-loop ADMM framework [98]. It is seen that the nested-loop algorithm converges to the optimal solution after 47 iterations of the outer loop each of which including, on average, 24 iterations of the inner loop (1128 iterations in total). This takes 7126 seconds to be executed. In contrast, the ADMM-HS-EVCS converges after only 73 iterations with a total execution time of 604 seconds. Therefore, the single-loop structure significantly improves the performance of the ADMM-

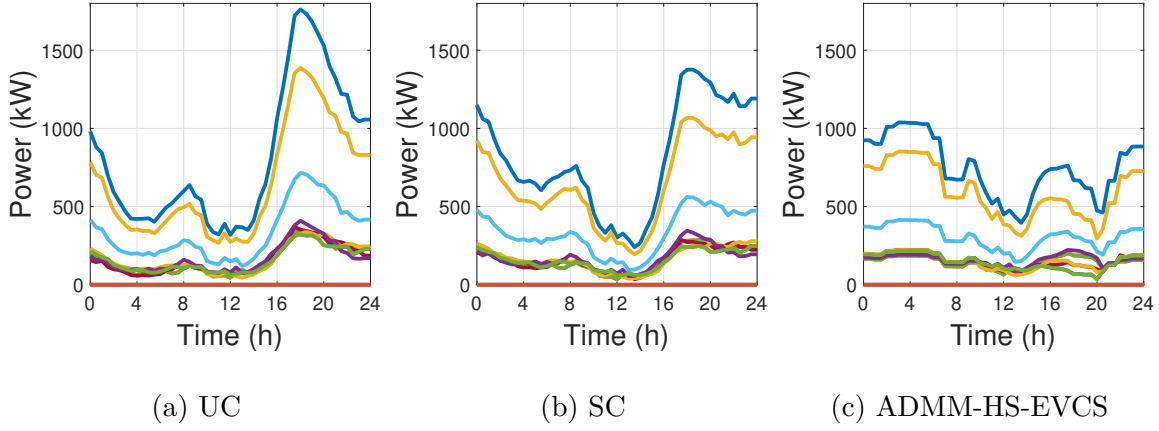


Figure 7.7 Power profile of the network lines

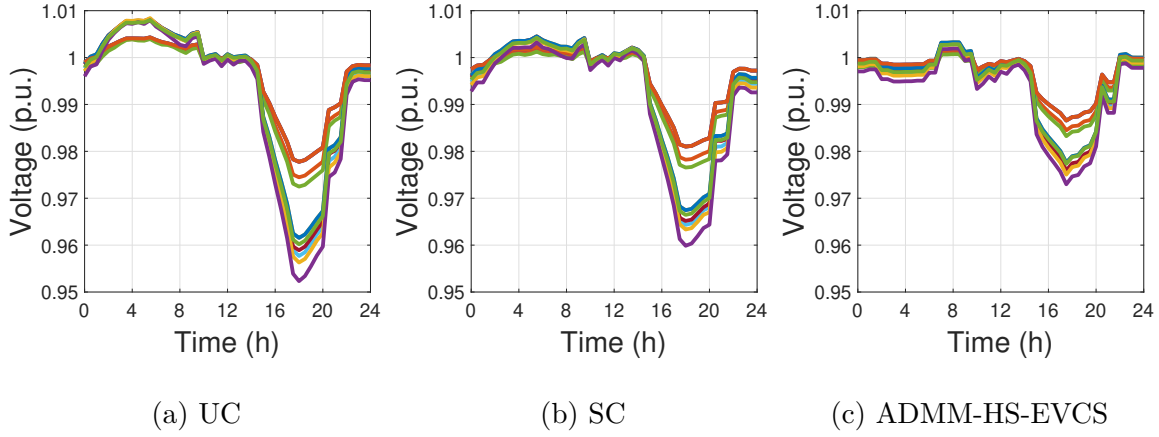


Figure 7.8 Voltage profile of the network buses

Table 7.6 Performance comparison of the proposed framework

	ADMM-HS-EVCS	ADMM (Nested-loop)
Convergence time (s)	604	7126
Outer loop iterations	N.A.	47
Inner loop iterations (mean)	N.A.	24
Total iterations	73	1128

based EVCS by reducing both the number of iterations and the convergence time. Note that the convergence times provided in Table 7.6 are obtained based on a sequential simulation using only one computing unit, while in reality, ADMM-HS-EVCS is proposed to be solved in parallel in a multi-agent environment.

## 7.6 Conclusion

A new distributed hierarchical framework has been proposed for optimal electric vehicle charging scheduling (EVCS). The hierarchical structure includes a single-loop iterative algorithm which is developed based on the alternating direction method of multipliers (ADMM) and distribution line power flow model (DistFlow). In addition, a load forecasting model using artificial neural network (ANN) is developed to predict the load demand of residential buildings. The proposed framework is simulated for a modified IEEE 13 bus test feeder which includes five EVAs each supplying 60 residential buildings (RBs) and their corresponding EVs.

From the simulation results, it has been found that the proposed ANN-based load forecasting model is able to predict the uncontrollable power balance of EVAs with the average MAPE and RMSE values of 8.31% and 4.98 kWh, respectively. The optimality of the proposed ADMM-HS-EVCS framework has been investigated by assigning distinct objective functions to each optimization layer. In terms of EV optimization layer, it has been shown that the daily charging costs have been reduced by 37% on average. Considering the EVA optimization layer, the proposed framework was able to obtain the optimal peak shaving performance with the average PTP and PTA values of 153 kW and 1.42, respectively. Regarding the DSO optimization layer, the proposed framework achieves the optimal voltage regulation performance where all voltage profiles always remain inside the permissible range,  $[0.97 \ 1.03]$ . Finally, it has been shown that the proposed single-loop structure is able to significantly improve the performance of the ADMM-based EVCS by reducing both the number of iterations and the convergence time.

Future work is concerned with the parallel implementation of the proposed framework in a true multi-agent environment including the communication network. This helps to investigate the effect of practical limitations such as packet loss, network congestion, bandwidth limitations, and communication delays.

## CHAPTER 8 GENERAL DISCUSSION

The primary goal of this thesis is to develop efficient centralized and distributed aggregation and optimization models for the participation of TCLs and EVs in the ancillary service of the smart grid. Given the shortcomings of the existing research, in this section, a general discussion surrounding the specific features of the proposed SSM-based and ADMM-based aggregation models is presented.

With reference to the SSM-based centralized aggregation model presented in Chapters 4 to 6, the main discussion elements are categorized as the service quality, accuracy, performance, and end-user integrity of the proposed model, as described below:

- **Service quality of the SSM**

**Frequency regulation:** The proposed SSM-based aggregation model can be utilized to provide frequency regulation service. It has been shown that the aggregation model is able to keep the system frequency within the permissible range even after severe power fluctuations in the system due to the following reasons: First, the coordinated participation of both TCLs and EVs increases the regulation capacity of the unified SSM-based aggregator presented in Chapter 6. Second, the incorporation of fast charging and fast discharging states in the extended EV-SSM given in Chapter 5 allows the EVs to participate in frequency regulation with higher power rates.

**Peak load shaving:** The proposed SSM can also be employed to provide effective peak load shaving service. With particular reference to aggregated EVs, the SSM is utilized to calculate a reference power trajectory and allow the aggregated EVs to follow the reference trajectory in real-time. This load following strategy is an efficient way for continuous regulation which allows the aggregator to provide a long period of peak load shaving service by forcing the EVs to be charged at off-peak periods so that the stored energy in the EV batteries support the grid during the on-peak periods. Due to the gradual load consumption variation in peak load shaving service, the contribution of EVs is mostly realized by regular power rates, even in the presence of fast charging.

- **Accuracy of the SSM**

To ensure the accuracy of the model, in addition to the estimated system state, the SSM is updated with measured user data every few minutes (2 to 8 minutes). As a result of this collect-and-correct procedure, the proposed SSM can accurately describe the aggregated behavior of the end-users while significantly reducing the communication requirement.

- **Performance of the SSM**

**Communication efficiency:** The communication efficiency of the proposed model is investigated by calculating two evaluation metrics for control and measurement signals, namely the maximum signal transmission times (MSTT) and the average signal transmission times (ASTT). According to these metrics, the proposed SSM is able to reduce the bi-directional communication burden between the aggregator and the end-users in both directions. Firstly, the reduced user data measurement rate decreases the measurement signal communication requirement. Secondly, the probabilistic control approach reduces the communication burden of the aggregator even further by broadcasting only one global probabilistic control signal to all TCLs or EVs rather than dispatching individualized control signals to each of them separately.

**Computation efficiency:** In order to evaluate the computation efficiency, the average execution time (AET) of the proposed SSM is calculated and compared to individual modeling. It is shown that with the SSM modeling, the AET per dispatch period is significantly reduced since the computation burden is mostly related to the number of state bins rather than the size of the population.

- **End-user integrity with SSM**

While exploiting the flexibility of the TCLs and EVs to provide grid-level services, the aggregation model must respect the integrity of end-users and their operational limitations such as comfort requirement, short cycling of the TCLs, and battery degradation of the EVs.

**Comfort requirement of end-users:** In order to meet the comfort requirement of TCL users during the regulation service, the SSM is designed in such a way that the indoor air temperature of all TCLs is always kept within the desired dead-band (i.e.,  $[T_{set} - \delta_{db}, T_{set} + \delta_{db}]$ ). Regarding the EV users, the SOC profile of all EVs always



remains within the predefined permissible range (i.e., [15%, 95%]), respecting the SOC constraint of the EV batteries. Meanwhile, all EVs are charged to their desired SOC value before plugging out in order to meet the energy requirement condition for their next trip.

**Short cycling of TCLs:** In order to avoid short cycling of TCLs caused by subsequent switching events in a short period of time, the SSM excludes the regulation capacity of the TCLs that are located at the state bins near the edge of the temperature dead-band. This consideration is necessary as these TCLs are recently switched by their hysteresis temperature cycle and should not be switched again by the aggregator control command for a certain period of time.

**Battery degradation of EVs:** The frequent charging and discharging cycles of EVs, particularly those with higher power rates, lead to excessive degradation of the EV batteries. The proposed SSM helps to avoid this situation in the following ways. First, using the extended EV-SSM presented in Chapter 5, the EVs only spend the bare minimum of time charging or discharging with high power rates. In other words, the fast charging and fast discharging states are the last state that EVs are switched *"to"* and the first state that EVs are switched *"from"*, when responding to power regulation command. Second, in the presence of the TCL population (unified SSM in Chapter 6), the priority of the controlled switching is given to TCLs; and EVs are reserved as the second resource to respond to the regulation command. This is of great importance as it reduces the average number of switching actions for EVs and, as a result, the impact of excessive switching on the battery life of EVs.

With reference to the ADMM-based distributed aggregation model presented in Chapter 7, the main discussion elements are categorized as the service quality, optimality and convergence, performance, and end-user integrity of the proposed model, as described below.

- **Service quality of the ADMM:**

The proposed hierarchical trilayer ADMM includes the DSO at the top layer, the EVAs at the middle layer and the EVs at the bottom layer. The underlying physical system is taken into account using the distribution line power flow model (DistFlow). DistFlow is chosen as it has been proven to be suitable for modeling radial distribution networks, which is the typical network configuration to which EV fleets are connected. While the developed framework is general and can be applied to any convex optimization

problem, in this paper, it is employed to provide charging cost minimization at the EV layer, peak load shaving at the EVA layer, and voltage regulation at the DSO layer. In addition to these optimization goals, as a result of smoothed power profile of all network buses, the line power flows are significantly reduced, particularly for the incoming main feeder line and the lines closest to the substation bus.

- **Optimality and convergence of the ADMM:**

The optimality conditions and convergence criteria of the ADMM are determined based on the primal and the dual residuals. The primal residual reflects the mismatch of the coupling variables at each iteration while the dual residual describes the stability of the iterations. These two residuals converge to zero as ADMM proceeds. Therefore, a reasonable termination criterion is that both residuals must be smaller than predefined feasibility thresholds. Note that the ADMM converges to the optimal solution only if both cost functions and constraint sets of all agents are convex.

- **Performance of the ADMM**

Using the single-loop iterative algorithm proposed for the trilayer ADMM framework, the primal variable of all agents is updated simultaneously at every iteration resulting in a reduced number of iterations and faster convergence compared to the nested-loop algorithms. This will decrease the amount of frequent communications between each optimization layer. Note that the convergence times provided in this thesis are obtained based on a sequential simulation using only one computing unit, while in reality, the developed ADMM framework is proposed to be solved in parallel in a multi-agent environment, which will further reduce the convergence time.

- **End-user integrity with ADMM**

In order to respect the integrity of end-users and their operational limitations during the ancillary service, the power and energy requirement of EVs are modeled by defining a series of inequality constraints. The first set of constraints defines the maximum and minimum EV charging/discharging power limits during the optimization horizon. The second set of constraints defines the energy requirement of the EV during each connection session and the last set of constraints represents the EV battery capacity limits for each individual time slot during each connection session. As a result, the SOC profile of all EVs always remains within the predefined permissible range and all EVs are charged to their desired SOC value before plugging out.

## CHAPTER 9 CONCLUSION AND RECOMMENDATIONS

### 9.1 Concluding Remarks

This thesis deals with the development of efficient centralized and distributed aggregation and optimization models to exploit the flexibility potential of large-scale TCL and EV populations. The proposed models are used to obtain specific user-level and grid-level objectives while preventing possible adverse effects on end-users' integrity.

The first proposed aggregation framework is based on the SSM and features a centralized structure to manage a population of TCLs for providing frequency regulation service. In the proposed control framework, the required power adjustment for frequency regulation is realized by coordinating the TCL aggregator and the conventional generator (CG) giving the priority to the TCLs. The proposed control strategy broadcasts the same control signal to all TCLs resulting in reduced communication requirement between the central aggregator and the individual TCLs. Simulations have been carried out for a community level power system involving 10,000 TCLs and a CG. It was found that the proposed control strategy can efficiently exploit the TCLs to counteract the frequency deviations. The role of CG in compensating for the inefficient reserve power of TCLs has been demonstrated. It has also been shown that the participation of TCLs will not affect the end users' comfort.

Next, a new extended SSM-based centralized EV aggregator has been proposed for the participation of large-scale EV population in frequency regulation and peak load shaving services. The urgent energy demand of fast-charging EVs is modeled and the flexibility of the EV aggregator is enhanced by enabling the EVs to participate in ancillary services with both regular and fast charging and fast discharging rates. From the simulation results, it has been found that the proposed aggregation model can efficiently counteract the frequency excursions while reducing the stress on the CG by decreasing its total ramp adjustments from 1026.98 MW to 292.43 MW. The frequency regulation service is achieved by accurate estimation of EVA regulation capacity with improved communicational and computational efficiencies. In particular, compared to individual modeling, the average signal transmission times (ASTT) of the control and measurement signals have been reduced by a factor of 97.17 and 32, respectively. In addition, using the proposed SSM, the maximum signal transmission times (MSTT) of the control signal has been reduced from 8568 to 1. Investigating the effectiveness of the proposed EVA for peak load shaving service, it has been found that the optimal flattened load curve can be obtained when the base power generation of the CG is about 91% of the mean value of the load curve. The performance of the proposed method

has also been evaluated for three distinct EV fleets with different driving behaviors and SOC levels. It has been demonstrated that for the EV fleets with lower energy demand where the EVs spend more time being connected to the grid, the performance of both frequency regulation and peak load shaving services is improved.

In order to achieve coordinated aggregation of TCLs and EVs, a new unified SSM-based centralized aggregation approach has been proposed. The proposed aggregation-coordination approach offers an accurate regulation capacity estimation. Furthermore, the coordination is performed with a low communication burden. The simulations have been conducted for a community-level microgrid including 10,000 TCLs, 10,000 EVs, a CG and a wind generation system. From the simulation, it has been shown that the proposed approach can accurately capture the aggregated behavior of a large population of TCLs and EVs and can efficiently counteract the frequency excursions. In the proposed control structure, the short cycling of TCLs is minimized, the energy requirements of the EVs are guaranteed and the energy constraints of the EV batteries are respected.

Finally, a new distributed hierarchical framework has been proposed for optimal electric vehicle charging scheduling (EVCS). The hierarchical structure includes a single-loop iterative algorithm which is developed based on the alternating direction method of multipliers (ADMM) and distribution line power flow model (DistFlow). In addition, a load forecasting model using artificial neural network (ANN) is developed to predict the load demand of residential buildings. The proposed framework is simulated for a modified IEEE 13 bus test feeder which includes five EVAs each supplying 60 residential buildings (RBs) and their corresponding EVs. From the simulation results, it has been found that the proposed ANN-based load forecasting model is able to predict the uncontrollable power of EVAs with the average MAPE and RMSE values of 8.31% and 4.98kWh, respectively. The optimality of the proposed framework has been investigated by assigning distinct objective functions to each optimization layer. In terms of EV optimization layer, it has been shown that the daily charging costs have been reduced by 37% on average. Considering the EVA optimization layer, the proposed framework was able to obtain the optimal peak shaving performance with the average PTP and PTA values of 153 kW and 1.42, respectively. Regarding the DSO optimization layer, the proposed framework achieves the optimal voltage regulation performance where all voltage profiles always remain inside the permissible range, [0.97 1.03]. Finally, it has been shown that the proposed single-loop structure is able to significantly improve the performance of the proposed framework by reducing both the number of iterations and the convergence time.

## 9.2 Future Work

The contributions of this thesis can be further extended as follows:

- Recently, EV manufacturers are shifting toward using hybrid energy storage systems (HESS) such as the combination of batteries and supercapacitors [142,143]. Given the higher energy efficiency, reliability, and reduced degradation cost of these systems, the integration of the HESS model within the proposed aggregation frameworks would be an interesting topic for future research.
- Contrary to fixed-frequency TCLs (FTCLs) that can only operate at two states (ON or OFF), the power consumption of inverter-based TCLs (ITCLs), such as AC units equipped with variable speed compressors, can be adjusted continuously. Given the higher flexibility of these loads, the integration of ITCLs within the proposed aggregation framework is suggested for future studies.
- Future work is also concerned with the real-world implementation of the proposed frameworks including the communication structure. This helps to investigate the effect of practical limitations such as packet loss, network congestion, bandwidth limitations, and communication delays. Furthermore, the practical parallel implementation of the proposed distributed framework in a true multi-agent environment is suggested.
- The aggregation models developed in Chapters 4 to 6 presume the existence of an agreement between the aggregator and end-users for compensating their participation in ancillary services. However, no investigation has been performed regarding the details of this agreement. While this issue is addressed in Chapter 7 by systematically incorporating the user profit goal in the optimization problem; in practice, the compensation mechanism based only on the power contribution may not be attractive enough for the users. Therefore, the proposed aggregation frameworks must be extended to include reimbursement strategies based on both the power contribution and the ability of the users to remain available, even if there is no power exchange with the grid.

## REFERENCES

- [1] “Czech transmission system operator (Čeps),” <https://www.ceps.cz/en/all-data>, accessed: 2020-05-30.
- [2] A. Radaideh, U. Vaidya, and V. Ajjarapu, “Sequential set-point control for heterogeneous thermostatically controlled loads through an extended markov chain abstraction,” *IEEE Transactions on Smart Grid*, vol. 10, no. 1, pp. 116–127, 2019.
- [3] M. Diekerhof, S. Schwarz, and A. Monti, “Distributed optimization for electro-thermal heating units,” in *2016 IEEE PES Innovative Smart Grid Technologies Conference Europe (ISGT-Europe)*, 2016, pp. 1–6.
- [4] M. Song, C. Gao, H. Yan, and J. Yang, “Thermal battery modeling of inverter air conditioning for demand response,” *IEEE Transactions on Smart Grid*, vol. 9, no. 6, pp. 5522–5534, 2018.
- [5] M. Song, C. Gao, M. Shahidehpour, Z. Li, S. Lu, and G. Lin, “Multi-time-scale modeling and parameter estimation of tcls for smoothing out wind power generation variability,” *IEEE Transactions on Sustainable Energy*, vol. 10, no. 1, pp. 105–118, 2019.
- [6] M. Liu and Y. Shi, “Optimal control of aggregated heterogeneous thermostatically controlled loads for regulation services,” in *2015 54th IEEE Conference on Decision and Control (CDC)*, 2015, pp. 5871–5876.
- [7] M. Diekerhof, F. Peterssen, and A. Monti, “Hierarchical distributed robust optimization for demand response services,” *IEEE Transactions on Smart Grid*, vol. 9, no. 6, pp. 6018–6029, 2018.
- [8] M. M. Islam, X. Zhong, Z. Sun, H. Xiong, and W. Hu, “Real-time frequency regulation using aggregated electric vehicles in smart grid,” *Computers & Industrial Engineering*, vol. 134, pp. 11 – 26, 2019.
- [9] C. Le Floch, E. C. Kara, and S. Moura, “Pde modeling and control of electric vehicle fleets for ancillary services: A discrete charging case,” *IEEE Transactions on Smart Grid*, vol. 9, no. 2, pp. 573–581, 2018.
- [10] B. M. Sanandaji, H. Hao, and K. Poolla, “Fast regulation service provision via aggregation of thermostatically controlled loads,” in *2014 47th Hawaii International Conference on System Sciences*, Jan 2014, pp. 2388–2397.

- [11] N. I. Nimalsiri, C. P. Mediwaththe, E. L. Ratnam, M. Shaw, D. B. Smith, and S. K. Halgamuge, "A survey of algorithms for distributed charging control of electric vehicles in smart grid," *IEEE Transactions on Intelligent Transportation Systems*, pp. 1–19, 2019.
- [12] A. Amin, W. U. K. Tareen, M. Usman, H. Ali, I. Bari, B. Horan, S. Mekhilef, M. Asif, S. Ahmed, and A. Mahmood, "A review of optimal charging strategy for electric vehicles under dynamic pricing schemes in the distribution charging network," *Sustainability*, vol. 12, no. 23, 2020. [Online]. Available: <https://www.mdpi.com/2071-1050/12/23/10160>
- [13] and Ning Lu, D. P. Chassin, and S. E. Widergren, "Modeling uncertainties in aggregated thermostatically controlled loads using a state queueing model," *IEEE Transactions on Power Systems*, vol. 20, no. 2, pp. 725–733, May 2005.
- [14] N. Lu and D. Chassin, "A state-queueing model of thermostatically controlled appliances," *IEEE Transactions on Power Systems*, vol. 19, no. 3, pp. 1666–1673, 2004.
- [15] S. Koch, J. Mathieu, and D. Callaway, "Modeling and control of aggregated heterogeneous thermostatically controlled loads for ancillary services," *Proc. PSCC*, pp. 1–7, 01 2011.
- [16] J. L. Mathieu, S. Koch, and D. S. Callaway, "State estimation and control of electric loads to manage real-time energy imbalance," *IEEE Transactions on Power Systems*, vol. 28, no. 1, pp. 430–440, Feb 2013.
- [17] N. I. Nimalsiri, C. P. Mediwaththe, E. L. Ratnam, M. Shaw, D. B. Smith, and S. K. Halgamuge, "A survey of algorithms for distributed charging control of electric vehicles in smart grid," *IEEE Transactions on Intelligent Transportation Systems*, vol. 21, no. 11, pp. 4497–4515, 2020.
- [18] M. Song, C. Gao, M. Shahidehpour, Z. Li, J. Yang, and H. Yan, "State space modeling and control of aggregated tcls for regulation services in power grids," *IEEE Transactions on Smart Grid*, vol. 10, no. 4, pp. 4095–4106, July 2019.
- [19] S. Boyd, N. Parikh, E. Chu, B. Peleato, and J. Eckstein, "Distributed optimization and statistical learning via the alternating direction method of multipliers," *Found. Trends Mach. Learn.*, vol. 3, no. 1, p. 1–122, jan 2011. [Online]. Available: <https://doi.org/10.1561/22000000016>

- [20] A. Nedic and A. Ozdaglar, “Distributed subgradient methods for multi-agent optimization,” *IEEE Transactions on Automatic Control*, vol. 54, no. 1, pp. 48–61, 2009.
- [21] D. P. Bertsekas and J. N. Tsitsiklis, *Parallel and Distributed Computation: Numerical Methods*. USA: Prentice-Hall, Inc., 1989.
- [22] J. Rivera, “Optimal charging of electric vehicles with renewable energy in smart grids,” 09 2015.
- [23] G. Chen, H. Zhang, H. Hui, N. Dai, and Y. Song, “Scheduling thermostatically controlled loads to provide regulation capacity based on a learning-based optimal power flow model,” *IEEE Transactions on Sustainable Energy*, vol. 12, no. 4, pp. 2459–2470, 2021.
- [24] K. Xie, H. Hui, and Y. Ding, “Review of modeling and control strategy of thermostatically controlled loads for virtual energy storage system,” *Protection and Control of Modern Power Systems*, vol. 4, no. 1, p. 23, Dec 2019. [Online]. Available: <https://doi.org/10.1186/s41601-019-0135-3>
- [25] Z. Li, W. Wu, and B. Zhang, “Coordinated state-estimation method for air-conditioning loads to provide primary frequency regulation service,” *IET Generation, Transmission & Distribution*, vol. 11, pp. 3381–3388(7), September 2017. [Online]. Available: <https://digital-library.theiet.org/content/journals/10.1049/iet-gtd.2017.0176>
- [26] M. Song, C. Gao, M. Shahidehpour, Z. Li, J. Yang, and H. Yan, “Impact of uncertain parameters on tcl power capacity calculation via hdmr for generating power pulses,” *IEEE Transactions on Smart Grid*, vol. 10, no. 3, pp. 3112–3124, 2019.
- [27] W. Zhang, J. Lian, C.-Y. Chang, and K. Kalsi, “Aggregated modeling and control of air conditioning loads for demand response,” *IEEE Transactions on Power Systems*, vol. 28, no. 4, pp. 4655–4664, 2013.
- [28] M. Liu and Y. Shi, “Model predictive control of aggregated heterogeneous second-order thermostatically controlled loads for ancillary services,” *IEEE Transactions on Power Systems*, vol. 31, no. 3, pp. 1963–1971, May 2016.
- [29] B. Biegel, P. Andersen, T. S. Pedersen, K. M. Nielsen, J. Stoustrup, and L. H. Hansen, “Smart grid dispatch strategy for on/off demand-side devices,” in *2013 European Control Conference (ECC)*, 2013, pp. 2541–2548.



- [30] Y. Chen, A. Bušić, and S. P. Meyn, “State estimation for the individual and the population in mean field control with application to demand dispatch,” *IEEE Transactions on Automatic Control*, vol. 62, no. 3, pp. 1138–1149, 2017.
- [31] N. A. Sinitsyn, S. Kundu, and S. Backhaus, “Safe protocols for generating power pulses with heterogeneous populations of thermostatically controlled loads,” *Energy Conversion and Management*, vol. 67, pp. 297–308, 2013. [Online]. Available: <https://www.sciencedirect.com/science/article/pii/S0196890412004591>
- [32] H. Hao, B. M. Sanandaji, K. Poolla, and T. L. Vincent, “Aggregate flexibility of thermostatically controlled loads,” *IEEE Transactions on Power Systems*, vol. 30, no. 1, pp. 189–198, 2015.
- [33] B. M. Sanandaji, T. L. Vincent, and K. Poolla, “Ramping rate flexibility of residential hvac loads,” *IEEE Transactions on Sustainable Energy*, vol. 7, no. 2, pp. 865–874, April 2016.
- [34] N. Lu and Y. Zhang, “Design considerations of a centralized load controller using thermostatically controlled appliances for continuous regulation reserves,” *IEEE Transactions on Smart Grid*, vol. 4, no. 2, pp. 914–921, 2013.
- [35] S. Esmail Zadeh Soudjani and A. Abate, “Aggregation and control of populations of thermostatically controlled loads by formal abstractions,” *IEEE Transactions on Control Systems Technology*, vol. 23, no. 3, pp. 975–990, 2015.
- [36] M. Liu, Y. Shi, and X. Liu, “Distributed mpc of aggregated heterogeneous thermostatically controlled loads in smart grid,” *IEEE Transactions on Industrial Electronics*, vol. 63, no. 2, pp. 1120–1129, 2016.
- [37] M. Song, G. Ciwei, J. Yang, Y. Liu, and G. Cui, “Novel aggregate control model of air conditioning loads for fast regulation service,” *Transmission Distribution IET Generation*, vol. 11, no. 17, pp. 4391–4401, 2017.
- [38] N. Lu, “An evaluation of the hvac load potential for providing load balancing service,” *IEEE Transactions on Smart Grid*, vol. 3, no. 3, pp. 1263–1270, Sep. 2012.
- [39] V. Trovato, S. H. Tindemans, and G. Strbac, “Leaky storage model for optimal multi-service allocation of thermostatic loads,” *IET Generation, Transmission & Distribution*, vol. 10, no. 3, pp. 585–593, 2016. [Online]. Available: <https://ietresearch.onlinelibrary.wiley.com/doi/abs/10.1049/iet-gtd.2015.0168>

- [40] S. Bashash and H. K. Fathy, “Modeling and control of aggregate air conditioning loads for robust renewable power management,” *IEEE Transactions on Control Systems Technology*, vol. 21, no. 4, pp. 1318–1327, 2013.
- [41] D. S. Callaway, “Tapping the energy storage potential in electric loads to deliver load following and regulation, with application to wind energy,” *Energy Conversion and Management*, vol. 50, no. 5, pp. 1389–1400, 2009. [Online]. Available: <https://www.sciencedirect.com/science/article/pii/S0196890408004780>
- [42] S. Kundu, N. Sinitsyn, S. Backhaus, and I. Hiskens, “Modeling and control of thermostatically controlled loads,” 2011. [Online]. Available: <https://arxiv.org/abs/1101.2157>
- [43] A. Radaideh and V. Ajjarapu, “Extracting expedient short term services from homogeneous group of thermostatically controlled loads,” in *2016 IEEE Power & Energy Society Innovative Smart Grid Technologies Conference (ISGT)*, 2016, pp. 1–5.
- [44] D. Wang, H. Jia, C. Wang, N. Lu, M. Fan, W. Miao, and Z. Liu, “Performance evaluation of controlling thermostatically controlled appliances as virtual generators using comfort-constrained state-queueing models,” *IET Generation, Transmission & Distribution*, vol. 8, pp. 591–599(8), April 2014. [Online]. Available: <https://digital-library.theiet.org/content/journals/10.1049/iet-gtd.2013.0093>
- [45] N. Mahdavi, J. H. Braslavsky, and C. Perfumo, “Mapping the effect of ambient temperature on the power demand of populations of air conditioners,” *IEEE Transactions on Smart Grid*, vol. 9, no. 3, pp. 1540–1550, 2018.
- [46] O. Erdiñç, A. Taşcıkaraoğlu, N. G. Paterakis, Y. Eren, and J. P. S. Catalão, “End-user comfort oriented day-ahead planning for responsive residential hvac demand aggregation considering weather forecasts,” *IEEE Transactions on Smart Grid*, vol. 8, no. 1, pp. 362–372, 2017.
- [47] N. Mahdavi, J. H. Braslavsky, M. M. Seron, and S. R. West, “Model predictive control of distributed air-conditioning loads to compensate fluctuations in solar power,” *IEEE Transactions on Smart Grid*, vol. 8, no. 6, pp. 3055–3065, 2017.
- [48] Y.-Y. Hong, J.-K. Lin, C.-P. Wu, and C.-C. Chuang, “Multi-objective air-conditioning control considering fuzzy parameters using immune clonal selection programming,” *IEEE Transactions on Smart Grid*, vol. 3, no. 4, pp. 1603–1610, 2012.

- [49] B. Zhang and J. Baillieul, "A packetized direct load control mechanism for demand side management," in *2012 IEEE 51st IEEE Conference on Decision and Control (CDC)*, 2012, pp. 3658–3665.
- [50] C. H. Wai, M. Beaudin, H. Zareipour, A. Schellenberg, and N. Lu, "Cooling devices in demand response: A comparison of control methods," *IEEE Transactions on Smart Grid*, vol. 6, no. 1, pp. 249–260, 2015.
- [51] C. Y. Chong and A. S. Debs, "Statistical synthesis of power system functional load models," in *1979 18th IEEE Conference on Decision and Control including the Symposium on Adaptive Processes*, vol. 2, 1979, pp. 264–269.
- [52] R. Malhame and C.-Y. Chong, "Electric load model synthesis by diffusion approximation of a high-order hybrid-state stochastic system," *IEEE Transactions on Automatic Control*, vol. 30, no. 9, pp. 854–860, 1985.
- [53] S. Bashash and H. K. Fathy, "Modeling and control insights into demand-side energy management through setpoint control of thermostatic loads," in *Proceedings of the 2011 American Control Conference*, 2011, pp. 4546–4553.
- [54] J. Hu, J. Cao, M. Z. Q. Chen, J. Yu, J. Yao, S. Yang, and T. Yong, "Load following of multiple heterogeneous tcl aggregators by centralized control," *IEEE Transactions on Power Systems*, vol. 32, no. 4, pp. 3157–3167, July 2017.
- [55] W. Zhang, K. Kalsi, J. Fuller, M. Elizondo, and D. Chassin, "Aggregate model for heterogeneous thermostatically controlled loads with demand response," in *2012 IEEE Power and Energy Society General Meeting*, 2012, pp. 1–8.
- [56] S. Lin, D. Liu, F. Hu, F. Li, W. Dong, D. Li, and Y. Fu, "Grouping control strategy for aggregated thermostatically controlled loads," *Electric Power Systems Research*, vol. 171, pp. 97–104, 2019. [Online]. Available: <https://www.sciencedirect.com/science/article/pii/S0378779619300616>
- [57] C.-Y. Chang, W. Zhang, J. Lian, and K. Kalsi, "Modeling and control of aggregated air conditioning loads under realistic conditions," in *2013 IEEE PES Innovative Smart Grid Technologies Conference (ISGT)*, 2013, pp. 1–6.
- [58] H. Zhao, Q. Wu, S. Huang, H. Zhang, Y. Liu, and Y. Xue, "Hierarchical control of thermostatically controlled loads for primary frequency support," *IEEE Transactions on Smart Grid*, vol. 9, no. 4, pp. 2986–2998, July 2018.

- [59] H. Hao, B. M. Sanandaji, K. Poolla, and T. L. Vincent, "A generalized battery model of a collection of thermostatically controlled loads for providing ancillary service," in *2013 51st Annual Allerton Conference on Communication, Control, and Computing (Allerton)*, 2013, pp. 551–558.
- [60] W. Zhang, J. Lian, C.-Y. Chang, K. Kalsi, and Y. Sun, "Reduced-order modeling of aggregated thermostatic loads with demand response," in *2012 IEEE 51st IEEE Conference on Decision and Control (CDC)*, 2012, pp. 5592–5597.
- [61] *Electric Vehicle outlook 2020*, BoombergNEF, 2020 (accessed October 11, 2020). [Online]. Available: <https://about.bnef.com/electric-vehicle-outlook/>
- [62] M. Wang, Y. Mu, Q. Shi, H. Jia, and F. Li, "Electric vehicle aggregator modeling and control for frequency regulation considering progressive state recovery," *IEEE Transactions on Smart Grid*, vol. 11, no. 5, pp. 4176–4189, 2020.
- [63] A. Langton and N. Crisostomo, "Vehicle-grid integration: A vision for zero-emission transportation interconnected throughout california's electricity system," *California Public Utilities Commission*, vol. 13, 2013.
- [64] M. Wang, Y. Mu, F. Li, H. Jia, X. Li, Q. Shi, and T. Jiang, "State space model of aggregated electric vehicles for frequency regulation," *IEEE Transactions on Smart Grid*, vol. 11, no. 2, pp. 981–994, 2020.
- [65] P. Paulraj, *Electric Vehicle Charging Levels, Modes and Types Explained: North America Vs. Europe Charging cables and plug types*, (accessed 05, May, 2020). [Online]. Available: <https://www.emobilitysimplified.com/2019/10/ev-charging-levels-modes-types-explained.html>
- [66] *Driver's Checklist: A Quick Guide to Fast Charging*, Chargepoint, (accessed 05, May, 2020). [Online]. Available: [https://www.chargepoint.com/files/Quick\\_Guide\\_to\\_Fast\\_Charging.pdf](https://www.chargepoint.com/files/Quick_Guide_to_Fast_Charging.pdf)
- [67] M. Shirk and J. Wishart, *Effects of electric vehicle fast charging on battery life and vehicle performance*, SAE Technical Paper, 2015. [Online]. Available: <https://doi.org/10.4271/2015-01-1190>
- [68] H. Zhang, Z. Hu, Z. Xu, and Y. Song, "Evaluation of achievable vehicle-to-grid capacity using aggregate pev model," *IEEE Transactions on Power Systems*, vol. 32, no. 1, pp. 784–794, 2017.

- [69] L. Gan, U. Topcu, and S. Low, "Optimal decentralized protocol for electric vehicle charging," in *2011 50th IEEE Conference on Decision and Control and European Control Conference*, 2011, pp. 5798–5804.
- [70] M. Liu, Y. Shi, and H. Gao, "Aggregation and charging control of phev in smart grid: A cyber-physical perspective," *Proceedings of the IEEE*, vol. 104, no. 5, pp. 1071–1085, 2016.
- [71] Z. Ma, S. Zou, L. Ran, X. Shi, and I. A. Hiskens, "Efficient decentralized coordination of large-scale plug-in electric vehicle charging," *Automatica*, vol. 69, pp. 35–47, 2016. [Online]. Available: <https://www.sciencedirect.com/science/article/pii/S0005109816000364>
- [72] K. Zhan, Z. Hu, Y. Song, N. Lu, Z. Xu, and L. Jia, "A probability transition matrix based decentralized electric vehicle charging method for load valley filling," *Electric Power Systems Research*, vol. 125, pp. 1–7, 2015. [Online]. Available: <https://www.sciencedirect.com/science/article/pii/S0378779615000802>
- [73] E. L. Karfopoulos and N. D. Hatziargyriou, "Distributed coordination of electric vehicles providing v2g services," *IEEE Transactions on Power Systems*, vol. 31, no. 1, pp. 329–338, 2016.
- [74] A. Y. S. Lam, K. Leung, and V. O. K. Li, "Capacity estimation for vehicle-to-grid frequency regulation services with smart charging mechanism," *IEEE Transactions on Smart Grid*, vol. 7, no. 1, pp. 156–166, 2016.
- [75] E. L. Karfopoulos, K. A. Panourgias, and N. D. Hatziargyriou, "Distributed coordination of electric vehicles providing v2g regulation services," *IEEE Transactions on Power Systems*, vol. 31, no. 4, pp. 2834–2846, 2016.
- [76] H. Yang, C. Y. Chung, and J. Zhao, "Application of plug-in electric vehicles to frequency regulation based on distributed signal acquisition via limited communication," *IEEE Transactions on Power Systems*, vol. 28, no. 2, pp. 1017–1026, 2013.
- [77] H. Liu, Z. Hu, Y. Song, J. Wang, and X. Xie, "Vehicle-to-grid control for supplementary frequency regulation considering charging demands," *IEEE Transactions on Power Systems*, vol. 30, no. 6, pp. 3110–3119, 2015.
- [78] J. Lin, K.-C. Leung, and V. O. K. Li, "Optimal scheduling with vehicle-to-grid regulation service," *IEEE Internet of Things Journal*, vol. 1, no. 6, pp. 556–569, 2014.

- [79] D. B. Richardson, "Electric vehicles and the electric grid: A review of modeling approaches, impacts, and renewable energy integration," *Renewable and Sustainable Energy Reviews*, vol. 19, pp. 247–254, 2013. [Online]. Available: <https://www.sciencedirect.com/science/article/pii/S1364032112006557>
- [80] P. Kou, D. Liang, L. Gao, and F. Gao, "Stochastic coordination of plug-in electric vehicles and wind turbines in microgrid: A model predictive control approach," *IEEE Transactions on Smart Grid*, vol. 7, no. 3, pp. 1537–1551, 2016.
- [81] S. Bashash and H. K. Fathy, "Transport-based load modeling and sliding mode control of plug-in electric vehicles for robust renewable power tracking," *IEEE Transactions on Smart Grid*, vol. 3, no. 1, pp. 526–534, 2012.
- [82] J. Meng, Y. Mu, H. Jia, J. Wu, X. Yu, and B. Qu, "Dynamic frequency response from electric vehicles considering travelling behavior in the great britain power system," *Applied Energy*, vol. 162, pp. 966–979, 2016.
- [83] Y. Cui, Z. Hu, and H. Luo, "Optimal day-ahead charging and frequency reserve scheduling of electric vehicles considering the regulation signal uncertainty," *IEEE Transactions on Industry Applications*, vol. 56, no. 5, pp. 5824–5835, 2020.
- [84] Z. Wang, P. Jochem, and W. Fichtner, "A scenario-based stochastic optimization model for charging scheduling of electric vehicles under uncertainties of vehicle availability and charging demand," *Journal of Cleaner Production*, vol. 254, p. 119886, 2020. [Online]. Available: <https://www.sciencedirect.com/science/article/pii/S0959652619347560>
- [85] A. Mercurio, A. Di Giorgio, and F. Purificato, "Optimal fully electric vehicle load balancing with an admm algorithm in smartgrids," in *21st Mediterranean Conference on Control and Automation*, 2013, pp. 119–124.
- [86] Z. Ma, D. Callaway, and I. Hiskens, "Decentralized charging control for large populations of plug-in electric vehicles: Application of the nash certainty equivalence principle," in *2010 IEEE International Conference on Control Applications*, 2010, pp. 191–195.
- [87] W.-J. Ma, V. Gupta, and U. Topcu, "On distributed charging control of electric vehicles with power network capacity constraints," in *2014 American Control Conference*, 2014, pp. 4306–4311.

- [88] M. G. Vayá, G. Andersson, and S. Boyd, “Decentralized control of plug-in electric vehicles under driving uncertainty,” in *IEEE PES Innovative Smart Grid Technologies, Europe*, 2014, pp. 1–6.
- [89] J. Rivera, C. Goebel, and H.-A. Jacobsen, “Distributed convex optimization for electric vehicle aggregators,” *IEEE Transactions on Smart Grid*, vol. 8, no. 4, pp. 1852–1863, 2017.
- [90] L. Gan, U. Topcu, and S. H. Low, “Optimal decentralized protocol for electric vehicle charging,” *IEEE Transactions on Power Systems*, vol. 28, no. 2, pp. 940–951, 2013.
- [91] T.-H. Chang, A. Nedić, and A. Scaglione, “Distributed constrained optimization by consensus-based primal-dual perturbation method,” *IEEE Transactions on Automatic Control*, vol. 59, no. 6, pp. 1524–1538, 2014.
- [92] J. Koshal, A. Nedić, and U. V. Shanbhag, “Multiuser optimization: Distributed algorithms and error analysis,” *SIAM Journal on Optimization*, vol. 21, no. 3, pp. 1046–1081, 2011. [Online]. Available: <https://doi.org/10.1137/090770102>
- [93] X. Huo and M. Liu, “Decentralized electric vehicle charging control via a novel shrunk primal-multi-dual subgradient (spmds) algorithm,” in *2020 59th IEEE Conference on Decision and Control (CDC)*, 2020, pp. 1367–1373.
- [94] H.-M. Chung, W.-T. Li, C. Yuen, C.-K. Wen, and N. Crespi, “Electric vehicle charge scheduling mechanism to maximize cost efficiency and user convenience,” *IEEE Transactions on Smart Grid*, vol. 10, no. 3, pp. 3020–3030, 2019.
- [95] Y. Zhang, E. Dall’Anese, and M. Hong, “Online proximal-admm for time-varying constrained convex optimization,” *IEEE Transactions on Signal and Information Processing over Networks*, vol. 7, pp. 144–155, 2021.
- [96] C.-K. Wen, J.-C. Chen, J.-H. Teng, and P. Ting, “Decentralized plug-in electric vehicle charging selection algorithm in power systems,” *IEEE Transactions on Smart Grid*, vol. 3, no. 4, pp. 1779–1789, 2012.
- [97] M. Mohiti, H. Monsef, and H. Lesani, “A decentralized robust model for coordinated operation of smart distribution network and electric vehicle aggregators,” *International Journal of Electrical Power & Energy Systems*, vol. 104, pp. 853–867, 2019. [Online]. Available: <https://www.sciencedirect.com/science/article/pii/S0142061518302333>

- [98] R. Verschae, H. Kawashima, T. Kato, and T. Matsuyama, "Coordinated energy management for inter-community imbalance minimization," *Renewable Energy*, vol. 87, pp. 922–935, 2016, optimization Methods in Renewable Energy Systems Design. [Online]. Available: <https://www.sciencedirect.com/science/article/pii/S096014811530135X>
- [99] S. Zou, I. Hiskens, and Z. Ma, "Consensus-based coordination of electric vehicle charging considering transformer hierarchy," *Control Engineering Practice*, vol. 80, pp. 138–145, 2018. [Online]. Available: <https://www.sciencedirect.com/science/article/pii/S0967066118304714>
- [100] C. Shao, X. Wang, X. Wang, C. Du, and B. Wang, "Hierarchical charge control of large populations of evs," *IEEE Transactions on Smart Grid*, vol. 7, no. 2, pp. 1147–1155, 2016.
- [101] B. Khaki, C. Chu, and R. Gadh, "A hierarchical admm based framework for ev charging scheduling," in *2018 IEEE/PES Transmission and Distribution Conference and Exposition (T&D)*, 2018, pp. 1–9.
- [102] B. Khaki, C. Chu, and R. Gadh, "Hierarchical distributed framework for ev charging scheduling using exchange problem," *Applied Energy*, vol. 241, pp. 461–471, 2019. [Online]. Available: <https://www.sciencedirect.com/science/article/pii/S0306261919304027>
- [103] *Hidden Markov model parameter estimates from emissions and states*, MathWorks, 2020 (accessed January 20, 2020). [Online]. Available: <https://www.mathworks.com/help/stats/hmmestimate.html>
- [104] J. Rivera, P. Wolfrum, S. Hirche, C. Goebel, and H.-A. Jacobsen, "Alternating direction method of multipliers for decentralized electric vehicle charging control," in *52nd IEEE Conference on Decision and Control*, 2013, pp. 6960–6965.
- [105] O. Sundstrom and C. Binding, "Optimization methods to plan the charging of electric vehicle fleets," in *International conference on control, communication and power engineering*, 2010, pp. 28–29.
- [106] Z. Ma, S. Zou, and X. Liu, "A distributed charging coordination for large-scale plug-in electric vehicles considering battery degradation cost," *IEEE Transactions on Control Systems Technology*, vol. 23, no. 5, pp. 2044–2052, 2015.



- [107] M. Baran and F. Wu, "Optimal sizing of capacitors placed on a radial distribution system," *IEEE Transactions on Power Delivery*, vol. 4, no. 1, pp. 735–743, 1989.
- [108] M. Baran and F. Wu, "Optimal capacitor placement on radial distribution systems," *IEEE Transactions on Power Delivery*, vol. 4, no. 1, pp. 725–734, 1989.
- [109] S. Kiani, K. Sheshyekani, and H. Dagdougui, "State space model of aggregated tcsls for frequency regulation with a low communication requirement," in *2020 IEEE Power & Energy Society General Meeting (PESGM)*, 2020, pp. 1–5, © 20XX IEEE. Reprinted, with permission.
- [110] X. Wu, J. He, Y. Xu, J. Lu, N. Lu, and X. Wang, "Hierarchical control of residential hvac units for primary frequency regulation," *IEEE Transactions on Smart Grid*, vol. 9, no. 4, pp. 3844–3856, July 2018.
- [111] S. Kiani, K. Sheshyekani, and H. Dagdougui, "An extended state space model for aggregation of large-scale evs considering fast charging," *IEEE Transactions on Transportation Electrification*, pp. 1–1, 2022, © 20XX IEEE. Reprinted, with permission.
- [112] T. B. Lee, *The story of cheaper batteries, from smartphones to Teslas*, 2020 (accessed October 10, 2020). [Online]. Available: <https://arstechnica.com/tech-policy/2020/09/the-story-of-cheaper-batteries-from-smartphones-to-teslas>
- [113] X. Duan, Z. Hu, and Y. Song, "Bidding strategies in energy and reserve markets for an aggregator of multiple ev fast charging stations with battery storage," *IEEE Transactions on Intelligent Transportation Systems*, pp. 1–12, 2020.
- [114] C. Dharmakeerthi, N. Mithulananthan, and T. Saha, "Impact of electric vehicle fast charging on power system voltage stability," *International Journal of Electrical Power & Energy Systems*, vol. 57, pp. 241 – 249, 2014. [Online]. Available: <http://www.sciencedirect.com/science/article/pii/S0142061513005218>
- [115] J. Deng, J. Shi, Y. Liu, and Y. Tang, "Application of a hybrid energy storage system in the fast charging station of electric vehicles," *IET Generation, Transmission Distribution*, vol. 10, no. 4, pp. 1092–1097, 2016.
- [116] M. Zhou, Z. Wu, J. Wang, and G. Li, "Forming dispatchable region of electric vehicle aggregation in microgrid bidding," *IEEE Transactions on Industrial Informatics*, p. 1, 2020.

- [117] C. S. Ioakimidis, D. Thomas, P. Rycerski, and K. N. Genikomsakis, "Peak shaving and valley filling of power consumption profile in non-residential buildings using an electric vehicle parking lot," *Energy*, vol. 148, pp. 148 – 158, 2018.
- [118] K. Kaur, M. Singh, and N. Kumar, "Multiobjective optimization for frequency support using electric vehicles: An aggregator-based hierarchical control mechanism," *IEEE Systems Journal*, vol. 13, no. 1, pp. 771–782, 2019.
- [119] I. Lymperopoulos, F. A. Qureshi, A. Bitlislioglu, J. Poland, A. Zanmarini, M. Mercan-goez, and C. Jones, "Ancillary services provision utilizing a network of fast-charging stations for electrical buses," *IEEE Transactions on Smart Grid*, vol. 11, no. 1, pp. 665–672, 2020.
- [120] A. Porras, R. Fernandez-Blanco, J. M. Morales, and S. Pineda, "An efficient robust approach to the day-ahead operation of an aggregator of electric vehicles," *IEEE Transactions on Smart Grid*, vol. 11, no. 6, pp. 4960–4970, 2020.
- [121] H. Chaudhry and T. Bohn, "A v2g application using dc fast charging and its impact on the grid," in *2012 IEEE Transportation Electrification Conference and Expo (ITEC)*, 2012, pp. 1–6.
- [122] C. D. White and K. M. Zhang, "Using vehicle-to-grid technology for frequency regulation and peak-load reduction," *Journal of Power Sources*, vol. 196, no. 8, pp. 3972–3980, 2011. [Online]. Available: <https://www.sciencedirect.com/science/article/pii/S0378775310019142>
- [123] C. Le Floch, E. C. Kara, and S. Moura, "PDE modeling and control of electric vehicle fleets for ancillary services: A discrete charging case," *IEEE Transactions on Smart Grid*, vol. 9, no. 2, pp. 573–581, 2018.
- [124] Q. Shi, H. Cui, F. Li, Y. Liu, W. Ju, and Y. Sun, "A hybrid dynamic demand control strategy for power system frequency regulation," *CSEE Journal of Power and Energy Systems*, vol. 3, no. 2, pp. 176–185, 2017.
- [125] C. Pradhan, C. N. Bhende, and A. K. Srivastava, "Frequency sensitivity analysis of dynamic demand response in wind farm integrated power system," *IET Renewable Power Generation*, vol. 13, no. 6, pp. 905–919, 2019.
- [126] W. Yao, J. Zhao, F. Wen, Y. Xue, and G. Ledwich, "A hierarchical decomposition approach for coordinated dispatch of plug-in electric vehicles," *IEEE Transactions on Power Systems*, vol. 28, no. 3, pp. 2768–2778, 2013.

- [127] Y. Guo, W. Liu, F. Wen, A. Salam, J. Mao, and L. Li, “Bidding strategy for aggregators of electric vehicles in day-ahead electricity markets,” *Energies*, vol. 10, no. 1, p. 144, Jan 2017. [Online]. Available: <http://dx.doi.org/10.3390/en10010144>
- [128] Y. Mu, J. Wu, N. Jenkins, H. Jia, and C. Wang, “A spatial-temporal model for grid impact analysis of plug-in electric vehicles,” *Applied Energy*, vol. 114, pp. 456–465, 2014. [Online]. Available: <https://www.sciencedirect.com/science/article/pii/S030626191300826X>
- [129] S. Qi, Z. Lin, J. Song, X. Lin, Y. Liu, M. Ni, and B. Wang, “Research on charging-discharging operation strategy for electric vehicles based on different trip patterns for various city types in china,” *World Electric Vehicle Journal*, vol. 13, no. 1, 2022. [Online]. Available: <https://www.mdpi.com/2032-6653/13/1/7>
- [130] S. Kiani, K. Sheshyekani, and H. Dagdougui, “A unified state space model for aggregation and coordination of large-scale tcsls and evs for frequency regulation,” *Electric Power Systems Research*, vol. 195, p. 107181, 2021. [Online]. Available: <https://www.sciencedirect.com/science/article/pii/S0378779621001620>
- [131] V. Trovato, F. Teng, and G. Strbac, “Role and benefits of flexible thermostatically controlled loads in future low-carbon systems,” *IEEE Transactions on Smart Grid*, vol. 9, no. 5, pp. 5067–5079, 2018.
- [132] H. Nazaripouya, B. Wang, and D. Black, “Electric vehicles and climate change: Additional contribution and improved economic justification,” *IEEE Electrification Magazine*, vol. 7, no. 2, pp. 33–39, 2019.
- [133] H. Fan, C. Duan, C.-K. Zhang, L. Jiang, C. Mao, and D. Wang, “Admm-based multi-period optimal power flow considering plug-in electric vehicles charging,” *IEEE Transactions on Power Systems*, vol. 33, no. 4, pp. 3886–3897, 2018.
- [134] L. Gan and S. H. Low, “Convex relaxations and linear approximation for optimal power flow in multiphase radial networks,” in *2014 Power Systems Computation Conference*, 2014, pp. 1–9.
- [135] E. Schweitzer, S. Saha, A. Scaglione, N. G. Johnson, and D. Arnold, “Lossy distflow formulation for single and multiphase radial feeders,” *IEEE Transactions on Power Systems*, vol. 35, no. 3, pp. 1758–1768, 2020.
- [136] H. Dagdougui, F. Bagheri, H. Le, and L. Dessaint, “Neural network model for short-term and very-short-term load forecasting in district buildings,” *Energy and*

- Buildings*, vol. 203, p. 109408, 2019. [Online]. Available: <https://www.sciencedirect.com/science/article/pii/S0378778819304505>
- [137] B. M. Wilamowski and H. Yu, “Improved computation for levenberg–marquardt training,” *IEEE Transactions on Neural Networks*, vol. 21, no. 6, pp. 930–937, 2010.
- [138] “California independent system operator- locational marginal price,” 2022. [Online]. Available: <http://oasis.caiso.com>
- [139] I. CVX Research, “CVX: Matlab software for disciplined convex programming, version 2.0,” <http://cvxr.com/cvx>, Aug. 2012.
- [140] Ausgrid, “Solar home electricity data,” 2013. [Online]. Available: <https://www.ausgrid.com.au/Industry/Our-Research/Data-to-share/Solar-home-electricity-data>
- [141] Visual Crossing Corporation, “Visual crossing weather,” 2010-2013. [Online]. Available: <https://www.visualcrossing.com/>
- [142] C. Zheng, Y. Wang, Z. Liu, T. Sun, N. Kim, J. Jeong, and S. W. Cha, “A hybrid energy storage system for an electric vehicle and its effectiveness validation,” *International Journal of Precision Engineering and Manufacturing-Green Technology*, vol. 8, no. 6, pp. 1739–1754, Nov 2021. [Online]. Available: <https://doi.org/10.1007/s40684-020-00304-5>
- [143] S. Verma, S. Mishra, A. Gaur, S. Chowdhury, S. Mohapatra, G. Dwivedi, and P. Verma, “A comprehensive review on energy storage in hybrid electric vehicle,” *Journal of Traffic and Transportation Engineering (English Edition)*, vol. 8, no. 5, pp. 621–637, 2021. [Online]. Available: <https://www.sciencedirect.com/science/article/pii/S2095756421000842>
- [144] D. P. Bertsekas, *Nonlinear Programming*. Athena Scientific, 2016.

## APPENDIX A    ALTERNATING DIRECTION METHOD OF MULTIPLIERS (ADMM)

In this Appendix, a revisit is made to the conventional ADMM algorithm [19] and ADMM solution for EV aggregation problem [22].

### ADMM Algorithm

The ADMM algorithm combines the dual decomposition and the augmented Lagrangian methods to create a fast and efficient distributed algorithm. The algorithm is formulated as below [19]:

$$\begin{aligned} & \text{minimize} && f(x) + g(z) \\ & \text{s.t.} && Ax + Bz = c \end{aligned} \tag{A.1}$$

with variables  $x \in \mathbb{R}^n$  and  $z \in \mathbb{R}^m$ , where  $A \in \mathbb{R}^{p \times n}$ ,  $B \in \mathbb{R}^{p \times m}$  and  $c \in \mathbb{R}^p$ . It is assumed that  $f$  and  $g$  are convex. The optimal value of this problem is denoted by,

$$p^* = \inf\{f(x) + g(z) \mid Ax + Bz = c\} \tag{A.2}$$

The augmented Lagrangian for (A.1) is derived as below:

$$L_\rho(x, y, z) = f(x) + g(z) + y^T(Ax + Bz - c) + \left(\frac{\rho}{2}\right)\|Ax + Bz - c\|_2^2 \tag{A.3}$$

where  $y$  is the dual variable or Lagrange multiplier and  $\rho > 0$  is the augmented Lagrangian parameter (penalty parameter).

ADMM consists of the following iterations,

$$x^{k+1} = \underset{x}{\operatorname{argmin}} L_\rho(x, z^k, y^k) \tag{A.4a}$$

$$z^{k+1} = \underset{z}{\operatorname{argmin}} L_\rho(x^{k+1}, z, y^k) \tag{A.4b}$$

$$y^{k+1} = y^k + \rho(Ax^{k+1} + Bz^{k+1} - c) \tag{A.4c}$$

The ADMM algorithm consists of an  $x$ -minimization step (A.4a), a  $z$ -minimization step (A.4b), and a dual variable update (A.4c) with a step size equal to the augmented Lagrangian parameter  $\rho$ . Using this algorithm,  $x$  and  $z$  are updated in an alternating or sequential fashion, which accounts for the term *alternating direction*. Separating the minimization over  $x$  and  $z$  into two steps is precisely what allows for decomposition when  $f$  or  $g$  are separable.

### Scaled Form

ADMM can be written in a slightly different form, which is sometimes more convenient, by combining the linear and quadratic terms in the augmented Lagrangian and scaling the dual variable [19]. Defining the residual  $r = Ax + Bz - c$ , we have

$$y^T r + \left(\frac{\rho}{2}\right) \|r\|_2^2 = \left(\frac{\rho}{2}\right) \|r + \left(\frac{1}{\rho}\right)y\|_2^2 - \left(\frac{1}{2\rho}\right) \|y\|_2^2 = \left(\frac{\rho}{2}\right) \|r + u\|_2^2 - \left(\frac{\rho}{2}\right) \|u\|_2^2 \quad (\text{A.5})$$

where  $u = (1/\rho)y$  is the *scaled dual variable*. Using the scaled dual variable, we can express ADMM as,

$$x^{k+1} = \underset{x}{\operatorname{argmin}} \left( f(x) + \left(\frac{\rho}{2}\right) \|Ax + Bz^k - c + u^k\|_2^2 \right) \quad (\text{A.6a})$$

$$z^{k+1} = \underset{z}{\operatorname{argmin}} \left( g(z) + \left(\frac{\rho}{2}\right) \|Ax^{k+1} + Bz - c + u^k\|_2^2 \right) \quad (\text{A.6b})$$

$$u^{k+1} = u^k + (Ax^{k+1} + Bz^{k+1} - c) \quad (\text{A.6c})$$

Defining the residual at iteration  $k$  as  $r^k = Ax^k + Bz^k - c$ , we see that

$$u^k = u^0 + \sum_{j=1}^k r^j \quad (\text{A.7})$$

is the running sum of the residuals.

### Optimality conditions and stopping criteria

The necessary and sufficient optimality conditions for the ADMM problem (A.1) are primal feasibility,

$$Ax^* + Bz^* - c = 0 \quad (\text{A.8})$$

and dual feasibility,

$$0 \in \partial f(x^*) + A^T y^* \quad (\text{A.9a})$$

$$0 \in \partial g(z^*) + B^T y^* \quad (\text{A.9b})$$

where,  $\partial$  denotes the sub-differential operator [19]. When  $f$  and  $g$  are differentiable, the sub-differentials  $\partial f$  and  $\partial g$  can be replaced by the gradients  $\nabla f$  and  $\nabla g$ , and  $\in$  can be replaced by  $=$ .

Since  $z^{k+1}$  minimizes  $L_\rho(x^{k+1}, z, y^k)$  by definition, we have

$$\begin{aligned} 0 &\in \partial g(z^{k+1}) + B^T y^k + \rho B^T (Ax^{k+1} + Bz^{k+1} - c) \\ &= \partial g(z^{k+1}) + B^T y^k + \rho B^T (r^{k+1}) \\ &= \partial g(z^{k+1}) + B^T y^{k+1} \end{aligned} \quad (\text{A.10})$$

This means that  $z^{k+1}$  and  $y^{k+1}$  always satisfy (A.9b), so attaining optimality comes down to satisfying (A.8) and (A.9a).

Since  $x^{k+1}$  minimizes  $L_\rho(x, z^k, y^k)$  by definition, we have

$$\begin{aligned} 0 &\in \partial f(x^{k+1}) + A^T y^k + \rho A^T (Ax^{k+1} + Bz^k - c) \\ &= \partial f(x^{k+1}) + A^T (y^k + \rho r^{k+1} + \rho B(z^k - z^{k+1})) \\ &= \partial f(x^{k+1}) + A^T y^{k+1} + \rho A^T B(z^k - z^{k+1}) \end{aligned} \quad (\text{A.11})$$

or equivalently,

$$\rho A^T B(z^{k+1} - z^k) \in \partial f(x^{k+1}) + A^T y^{k+1} \quad (\text{A.12})$$

This means that the quantity

$$s^{k+1} = \rho A^T B(z^{k+1} - z^k) \quad (\text{A.13})$$

can be viewed as a residual for the dual feasibility condition (A.9a). We will refer to  $s^{k+1}$  as the *dual residual* at iteration  $k + 1$ , and to  $r^{k+1} = Ax^{k+1} + Bz^{k+1} - c$  as the *primal residual* at iteration  $k + 1$ . These two residuals converge to zero as ADMM proceeds.

## Stopping criteria

The discussion above suggests that a reasonable termination criterion is that the primal and dual residuals be small, i.e.,

$$\|r^k\|_2^2 \leq \epsilon_{pri} \quad (\text{A.14a})$$

$$\|s^k\|_2^2 \leq \epsilon_{dual} \quad (\text{A.14b})$$

where  $\epsilon_{pri}$  and  $\epsilon_{dual}$  are feasibility tolerances for the primal and dual feasibility conditions (A.8) and (A.9a), respectively.

## Derivation of the ADMM solution for EV aggregation problem

In order to apply ADMM to the EV aggregation problem, the exchange problem (2.30) is reformulated as [22]:

$$\begin{aligned} & \underset{\mathbf{p}_i, \mathbf{z}}{\text{minimize}} && \sum_{i=0}^{N_{ev}} f_i(\mathbf{p}_i) + g(\mathbf{z}) \\ & \text{s.t.} && \mathbf{p}_i = \mathbf{z}_i, \quad i = 0, \dots, N_{ev} \end{aligned} \quad (\text{A.15})$$

where

$$g(\mathbf{z}) = \begin{cases} 0, & \text{if } \sum_{i=0}^{N_{ev}} \mathbf{z}_i = 0 \\ \infty, & \text{otherwise} \end{cases} \quad (\text{A.16})$$

Note that the formulation (2.30) and (A.15) are equivalent. In order to solve (A.15), the augmented Lagrangian function is defined as below:

$$L_\rho(\mathbf{p}, \mathbf{z}, \mathbf{y}) = \sum_{i=0}^{N_{ev}} f_i(\mathbf{p}_i) + g(\mathbf{z}) + \mathbf{y}^T(\mathbf{p} - \mathbf{z}) + \left(\frac{\rho}{2}\right) \|\mathbf{p} - \mathbf{z}\|_2^2 \quad (\text{A.17})$$

where  $\mathbf{y} = [\mathbf{y}_0, \dots, \mathbf{y}_{N_{ev}}]^T$  is the vector of the Lagrangian multipliers and  $\rho$  is the penalty parameter of the augmented term. In order to solve the problem we need to minimize over the primal variables  $\mathbf{p}$ ,  $\mathbf{z}$  and maximize over the Lagrangian variables  $\mathbf{y}$  [144]:

$$\max_{\mathbf{y}} \min_{\mathbf{p}, \mathbf{z}} L_\rho(\mathbf{p}, \mathbf{z}, \mathbf{y}) \quad (\text{A.18})$$



This problem can be solved using an iterative process:

$$\mathbf{p}^{k+1} = \underset{\mathbf{p}}{\operatorname{argmin}} L_{\rho}(\mathbf{p}, \mathbf{z}^k, \mathbf{y}^k) \quad (\text{A.19a})$$

$$\mathbf{z}^{k+1} = \underset{\mathbf{z}}{\operatorname{argmin}} L_{\rho}(\mathbf{p}^{k+1}, \mathbf{z}, \mathbf{y}^k) \quad (\text{A.19b})$$

$$\mathbf{y}^{k+1} = \underset{\mathbf{y}}{\operatorname{argmax}} L_{\rho}(\mathbf{p}^{k+1}, \mathbf{z}^{k+1}, \mathbf{y}) \quad (\text{A.19c})$$

By expanding (A.19a) we get,

$$\begin{aligned} \mathbf{p}^{k+1} &= \sum_{i=0}^{N_{ev}} f_i(\mathbf{p}_i) + \mathbf{y}^{kT}(\mathbf{p} - \mathbf{z}^k) + \left(\frac{\rho}{2}\right) \|\mathbf{p} - \mathbf{z}^k\|_2^2 \\ &= \sum_{i=0}^{N_{ev}} \left\{ f_i(\mathbf{p}_i) + \mathbf{y}_i^k(\mathbf{p}_i - \mathbf{z}_i^k) + \left(\frac{\rho}{2}\right) \|\mathbf{p}_i - \mathbf{z}_i^k\|_2^2 \right\} \end{aligned} \quad (\text{A.20})$$

The problem (A.20) is separable and we can write a single problem for each  $\mathbf{p}_i^{k+1}$ . The iterative solution then can be written as:

$$\mathbf{p}_i^{k+1} = \underset{\mathbf{p}_i}{\operatorname{argmin}} f_i(\mathbf{p}_i) + \mathbf{y}_i^k(\mathbf{p}_i - \mathbf{z}_i^k) + \left(\frac{\rho}{2}\right) \|\mathbf{p}_i - \mathbf{z}_i^k\|_2^2 \quad (\text{A.21a})$$

$$\mathbf{z}^{k+1} = \underset{\mathbf{z}}{\operatorname{argmin}} g(\mathbf{z}) - \mathbf{y}^{kT} \mathbf{z} + \left(\frac{\rho}{2}\right) \|\mathbf{p}^{k+1} - \mathbf{z}\|_2^2 \quad (\text{A.21b})$$

$$\mathbf{y}^{k+1} = \underset{\mathbf{y}}{\operatorname{argmax}} \mathbf{y}^T(\mathbf{p}^{k+1} - \mathbf{z}^{k+1}) \quad (\text{A.21c})$$

The update of  $\mathbf{z}$  has an analytical solution and a gradient algorithm can be used to solve the  $\mathbf{y}$  update. Let us derive these solutions:

**Solution of  $\mathbf{z}^{k+1}$ :** taking into account the definition of  $g(\mathbf{z})$  in (A.16), we can formulate the optimization problem:

$$\begin{aligned} &\underset{\mathbf{z}_i}{\operatorname{minimize}} \quad \sum_{i=0}^{N_{ev}} \left\{ -\mathbf{y}_i^k \mathbf{z}_i + \left(\frac{\rho}{2}\right) (\mathbf{p}_i^{k+1} - \mathbf{z}_i)^2 \right\} \\ &\text{s.t.} \quad \sum_{i=0}^{N_{ev}} \mathbf{z}_i = 0 \end{aligned} \quad (\text{A.22})$$

The Lagrangian of this problem is:

$$L(\mathbf{z}, \lambda) = \sum_{i=0}^{N_{ev}} L(\mathbf{z}_i, \lambda) = \sum_{i=0}^{N_{ev}} \left\{ -\mathbf{y}_i^k \mathbf{z}_i + \left(\frac{\rho}{2}\right) (\mathbf{p}_i^{k+1} - \mathbf{z}_i)^2 + \lambda \mathbf{z}_i \right\} \quad (\text{A.23})$$

where  $\lambda$  is the Lagrangian multiplier. Using the KKT conditions and adding up the gradients of Lagrangian in terms of  $\mathbf{z}_i$ ,

$$\nabla_{\mathbf{z}_i} L(\mathbf{z}_i, \lambda) = 0 \quad \rightarrow \quad \mathbf{z}_i = \mathbf{p}_i^{k+1} + \frac{\mathbf{y}_i^k}{\rho} - \frac{\lambda}{\rho} \quad (\text{A.24a})$$

$$\nabla_{\lambda} L(\mathbf{z}, \lambda) = 0 \quad \rightarrow \quad \sum_{i=0}^{N_{ev}} \mathbf{z}_i = 0 \quad (\text{A.24b})$$

With (A.24a) and (A.24b):

$$\sum_{i=0}^{N_{ev}} \left\{ \mathbf{p}_i^{k+1} + \frac{\mathbf{y}_i^k}{\rho} - \frac{\lambda}{\rho} \right\} = 0 \quad (\text{A.25})$$

Solving for  $\lambda$  we get:

$$\lambda = \rho(\bar{\mathbf{p}}^{k+1} + \frac{\bar{\mathbf{y}}^k}{\rho}) \quad (\text{A.26})$$

where  $\bar{\mathbf{p}}^{k+1} = 1/(N_{ev} + 1) \sum_{i=0}^{N_{ev}} \mathbf{p}_i^{k+1}$  and  $\bar{\mathbf{y}}^{k+1} = 1/(N_{ev} + 1) \sum_{i=0}^{N_{ev}} \mathbf{y}_i^{k+1}$ . Using (A.26) and (A.24a) we can find the closed form of update  $\mathbf{z}_i$  as below,

$$\mathbf{z}_i^{k+1} = \mathbf{p}_i^{k+1} - \bar{\mathbf{p}}^{k+1} + \frac{\mathbf{y}_i^k}{\rho} - \frac{\bar{\mathbf{y}}^k}{\rho} \quad (\text{A.27})$$

or in vector form,

$$\mathbf{z}^{k+1} = \mathbf{p}^{k+1} - \mathbf{1}\bar{\mathbf{p}}^{k+1} + \frac{\mathbf{y}^k}{\rho} - \mathbf{1}\frac{\bar{\mathbf{y}}^k}{\rho} \quad (\text{A.28})$$

where  $\mathbf{1}$  is the identity matrix.

**Solution of  $\mathbf{y}^{k+1}$ :** by setting  $\nabla_{\mathbf{y}} L_{\rho}(\mathbf{p}^{k+1}, \mathbf{z}^{k+1}, \mathbf{y}) = 0$  we have:

$$\nabla_{\mathbf{y}} L_{\rho}(\mathbf{p}^{k+1}, \mathbf{z}^{k+1}, \mathbf{y}) = (\mathbf{p}^{k+1} - \mathbf{z}^{k+1}) \quad (\text{A.29})$$

using the gradient method,

$$\mathbf{y}^{k+1} = \mathbf{y}^k + \rho(\mathbf{p}^{k+1} - \mathbf{z}^{k+1}) \quad (\text{A.30})$$

Note that the step size of the gradient descent method  $\rho$  is exactly the same as the penalty parameter of the augmented term  $\rho$ . In this way, the first condition of the dual feasibility is always fulfilled and the convergence is guaranteed [19].

Substituting the  $\mathbf{z}^{k+1}$  solution (A.27) in the  $\mathbf{y}^{k+1}$  solution (A.30) gives:

$$\mathbf{y}^{k+1} = \rho(\mathbf{1} \frac{\bar{\mathbf{y}}^k}{\rho} + \mathbf{1} \bar{\mathbf{p}}^{k+1}) \quad (\text{A.31})$$

Note that the elements of  $\mathbf{y}$  have the same value:

$$\mathbf{y} = \mathbf{1} y_i \quad (\text{A.32a})$$

$$\bar{\mathbf{y}} = y_i \quad (\text{A.32b})$$

therefore,

$$\mathbf{y}_i^{k+1} = \rho(\frac{\mathbf{y}_i^k}{\rho} + \bar{\mathbf{p}}^{k+1}) = \mathbf{y}_i^k + \rho \bar{\mathbf{p}}^{k+1} \quad (\text{A.33})$$

Considering the latter, the  $\mathbf{z}^{k+1}$  solution (A.27) can be rewritten as follows,

$$\mathbf{z}_i^{k+1} = \mathbf{p}_i^{k+1} - \bar{\mathbf{p}}^{k+1} \quad (\text{A.34})$$

and finally,  $\mathbf{p}_i^{k+1}$  from (A.21a) becomes:

$$\mathbf{p}_i^{k+1} = \underset{\mathbf{p}_i}{\operatorname{argmin}} f_i(\mathbf{p}_i) + \mathbf{y}_i^k(\mathbf{p}_i) + (\frac{\rho}{2}) \|\mathbf{p}_i - \mathbf{p}_i^k + \bar{\mathbf{p}}^k\|_2^2 \quad (\text{A.35})$$

Using  $\mathbf{u} = (1/\rho)\mathbf{y}$ , the scaled form of (A.35) is derived as follows,

$$\mathbf{p}_i^{k+1} = \underset{\mathbf{p}_i}{\operatorname{argmin}} f_i(\mathbf{p}_i) + (\frac{\rho}{2}) \|\mathbf{p}_i - \mathbf{p}_i^k + \bar{\mathbf{p}}^k + \mathbf{u}^k\|_2^2 \quad (\text{A.36})$$

Equations (A.36), (A.34), and (A.33) jointly present the scaled form of ADMM solution for the exchange problem (A.15).

## APPENDIX B LIST OF PUBLICATIONS

### Journal papers

- [J1] **S.Kiani**, K. Sheshyekani, and H. Dagdougui, "A unified state space model for aggregation and coordination of large-scale TCLs and EVs for frequency regulation," *Electric Power Systems Research*, vol. 195, p. 107181, 2021.
- [J2] **S.Kiani**, K. Sheshyekani, and H. Dagdougui, "An Extended State Space Model for Aggregation of Large-scale EVs Considering Fast Charging," in *IEEE Transactions on Transportation Electrification*, doi: 10.1109/TTE.2022.3179311.
- [J3] **S.Kiani**, K. Sheshyekani, and H. Dagdougui, "ADMM-Based Hierarchical Single-loop Framework for EV Charging Scheduling Considering Power Flow Constraints," in *IEEE Transactions on Transportation Electrification*, December 2022, submitted for publication.

### Conference papers

- [C1] **S.Kiani**, K. Sheshyekani, and H. Dagdougui, "State Space Model of Aggregated TCLs for Frequency Regulation with a Low Communication Requirement," *2020 IEEE Power & Energy Society General Meeting (PESGM)*, 2020, pp. 1-5, doi: 10.1109/PESGM41954.2020.9281513.
- [C2] **S.Kiani**, K. Sheshyekani, and H. Dagdougui, "Real-time Aggregation of Large-scale EVs Considering Fast Charging," *2021 IEEE Transportation Electrification Conference & Expo (ITEC)*, 2021, pp. 1-6, doi: 10.1109/ITEC51675.2021.9490152.